Search for Color Transparency in $A(e, e'p)$ at High Momentum Transfer

Thesis by

Thomas G. O'Neill

In Partial Fulfillment of the Requirements

For the Degree of

Doctor of Philosophy

California Institute of Technology

Pasadena, California

1994

(Submitted February 21, 1994)

To my family

and

Alice

ACKNOWLEDGEMENTS

I would like to thank the members of the NE-18 collaboration for their contributions to making the experiment a success. Special thanks go to Eric Belz, Rolf Ent, Wolfgang Lorenzon, and Naomi Makins for their work in the set up and analysis of the experiment. I also acknowledge the good work of Carl Hudspeth, Bob Eisle, the beam operators, and other SLAC staff members.

I am especially grateful to my adviser Brad Filippone. Brad has provided me with countless hours of guidance and discussion, and I have profitted greatly from his suggestions and also from observing his methods. My graduate tenure was made much easier by the knowledge that my adviser had my best interests in mind.

Finally I would like to thank all of the friends who have offered support throughout my graduate studies. I am particularly indebted to my family, who helped me get here, and to Alice Householder, who put up with me once I did.

Abstract

Rates for $A(e, e'p)$ on the nuclei ^{2}H, C, Fe, and Au have been measured at momentum transfers Q^2 = 1, 3, 5, and 6.8 $(\mathrm{GeV/c})^2$. We extract the nuclear transparency T, a measure of the importance of final state interactions (FSI) between the outgoing proton and the recoil nucleus. Some calculations based on perturbative QCD predict an increase in T with momentum transfer, a phenomenon known as Color Transparency. No statistically significant rise is seen in the present experiment.

Contents

List of Figures

List of Tables

I. INTRODUCTION

In 1982 Mueller and Brodsky [1] independently proposed that in wide angle exclusive processes, the initial and final state interactions (ISI and FSI) of hadrons in nuclei would vanish at high energies. This effect, based on arguments using perturbative QCD (pQCD), is called "Color Transparency" (CT), in reference to the disappearance of the "color" forces between the hadrons and nuclei. The onset of CT with increasing energy can be tested by measurement of the nuclear transparency T, the ratio of the measured cross section to the cross section expected in the limit of complete CT (*i.e.*, no ISI or FSI). At low energies, $T < 1$ because of absorption or deflection of the hadrons by ISI and FSI with the nucleus. At energies below the onset of CT, T should be independent of Q^2 (assuming a constant proton-nucleus cross section). As the energy increases and pQCD processes begin to dominate the scattering, however, T should increase to unity. Some recent models of CT (see Figure 1, for example) exhibit significant increases in T for Q^2 as low as $5\,(\mathrm{GeV/c})^2$ [2–6]. Measurement of an unambiguous increase in T could indicate the energy scale at which QCD becomes perturbative in exclusive processes. We present measurements of T for the reaction $A(e,e'p)$ on ^{2}H, C, Fe, and Au nuclei at momentum transfers $Q^2 = 1$, 3, 5, and $6.8\,(\mathrm{GeV/c})^2$.

The following sections present a general overview of the theoretical and experimental questions of interest in the current experiment. First, in Section I.A there are descriptions of the formalism used for the analysis of $A(e,e'p)$ and of the results of previous $A(e,e'p)$ experiments. Following this, in Section I.B there is a discussion of the current theoretical and experimental knowledge of CT. Finally, in Section I.C there is a brief description of the current experiment.

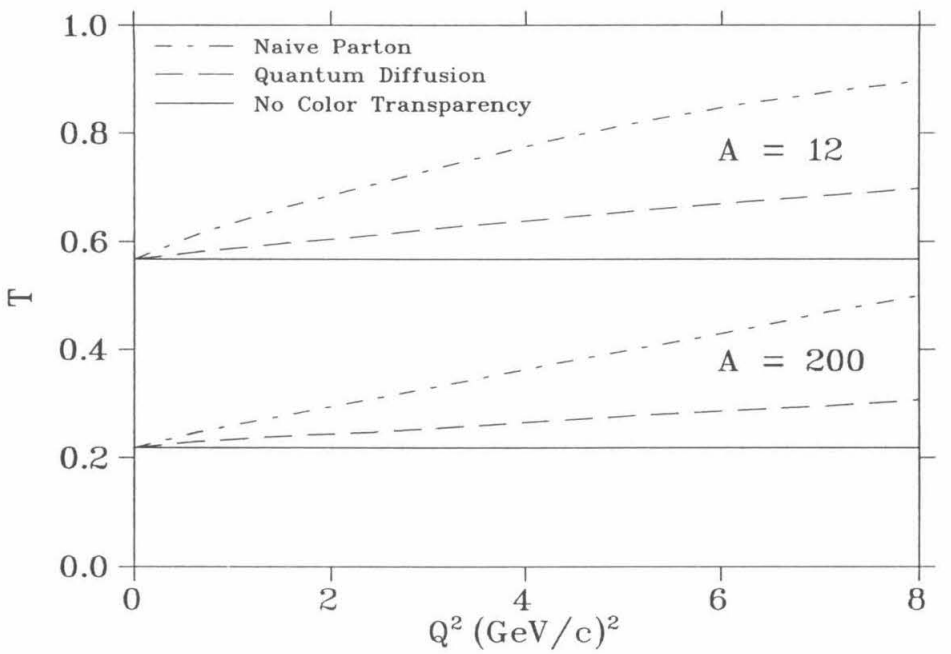

FIG. 1. **Farrar** *et al.* **[2]** T **prediction for** $A(e,e'p)$ **on** $A = 12$ **(upper curves) and 200 (lower curves), calculated in the absence of Color Transparency (solid line) or with the naive parton (dashed line) and quantum diffusion (dash-chain line) Color Transparency models [2]. The CT models are described in Sections I.B.3 and V.D. For comparison, the highest** Q^2 **in the present experiment is 6.8** $(\mathrm{GeV/c})^2$.

I.A. The $A(e, e'p)$ Reaction

Some of the best information about the structure of the nucleus has been derived using lepton-nucleus scattering. Experiments using leptonic probes have several advantages over those using hadronic probes. Leptons couple to the nucleus through the relatively weak electromagnetic interaction, while hadrons also experience the strong force. The electromagnetic interaction is calculable through low-order diagrams of the precision-tested theory of QED. By contrast QCD, the theory of the strong interaction, is not as well-tested and its perturbative expansion does not converge quickly (or at all) at the energies of interest. Furthermore, the ISI and FSI of a weakly-coupled leptonic probe are much smaller than those of a hadronic probe, minimizing the distortions to the measured structure. Finally, due to the small coupling, the structure is measured throughout the nuclear volume, rather than just at the surface.

Early information about nuclear structure was provided by *inclusive* electron-nucleus scattering. The dependence of the $A(e, e')$ cross section on the energy loss at intermediate Q^2 exhibits, among other structure, a broad "quasielastic" peak due to the direct knockout of an individual nucleon from the nucleus (see Figure 2). The width of the peak is the result of the distribution of nucleon momenta inside the nucleus. Approximate nucleon momentum distributions can be extracted from the data through, for example, the study of the distribution in the scaling variable y [7].

Semi-exclusive measurements such as $A(e, e'p)$ allow a more complete characterization of the scattering. Four-momentum conservation can be used to infer the 4-momentum of the ejected proton before the interaction (up to distortions due to higher-order couplings—known as radiative effects—and the proton's FSI). The distribution in the proton initial energy shows direct evidence of the distinct levels predicted by the nuclear shell model. The simultaneous measurement of the proton initial momentum allows the extraction of the momentum distribution not just for

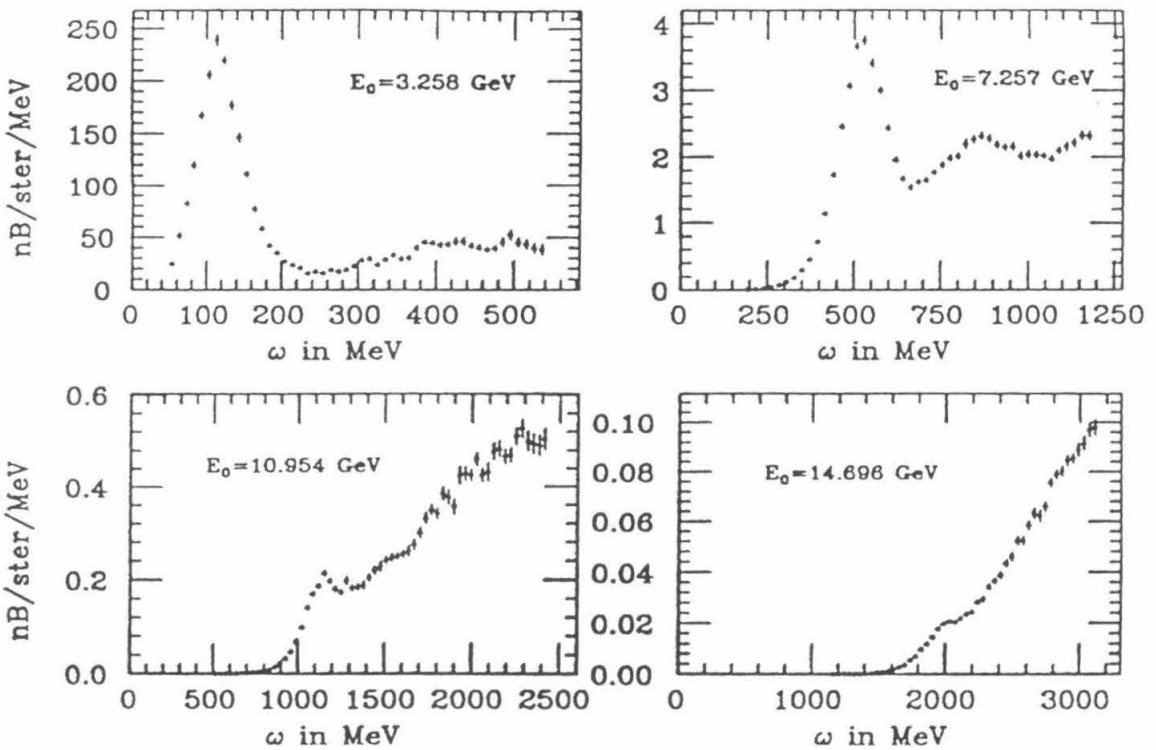

FIG. 2. **Differential cross section** $d\sigma/d\Omega/d\nu$ **for** ^{3}He(e,e') **at** $E = 3.3$–$14.7\,$GeV **and** $\theta_{k'} = 8°$ **[8]. In the figure, the energy loss** ν **is called** ω**. The data exhibit a bump at** $\nu \simeq 100$, 500, 1100, 2000 MeV $[Q^2 \simeq 0.2,\ 0.95,\ 2.1,\ 3.6\,(\mathrm{GeV/c})^2]$ **due to quasielastic nucleon knock-out. The strength at larger** ν **is due to excitation of a nucleon to the** $\Delta(1236)$ **resonance and other inelastic channels. At** $Q^2 \gtrsim 1\,(\mathrm{GeV/c})^2$**, the quasielastic peak disappears into the side of the rapidly rising background from deep inelastic scattering.**

the entire nucleus, but for each nuclear shell. Thus the exclusive reaction allows much more accurate tests of the single-particle description of the nucleus and better differentiation between competing models of nuclear structure.

I.A.1. The Plane Wave Impulse Approximation

The simplest $A(e,e'p)$ reaction is electron-proton elastic scattering. Figure 3 shows the Born-level diagram (with time going from left to right) and establishes the kinematics for this process. The momentum transfer is $Q^2 \equiv -q_\mu q^\mu$ and the 4-momentum transfer is

$$q^\mu \equiv k^\mu - k'^\mu = (\nu, \mathbf{q}). \tag{1.1}$$

The circle at the photon-proton vertex, indicating the unspecified details of the coupling, is suppressed in the following diagrams.

The Born-level cross section for this process is:

$$\frac{d\sigma}{d\Omega} = \left(\frac{d\sigma}{d\Omega}\right)_{Mott} \frac{E'}{E}\left(\frac{G_E^2 + \tau G_M^2}{1+\tau} + 2\tau G_M^2 \tan^2\frac{\theta}{2}\right) \tag{1.2}$$

where the reference cross section for a structureless, non-recoiling target is

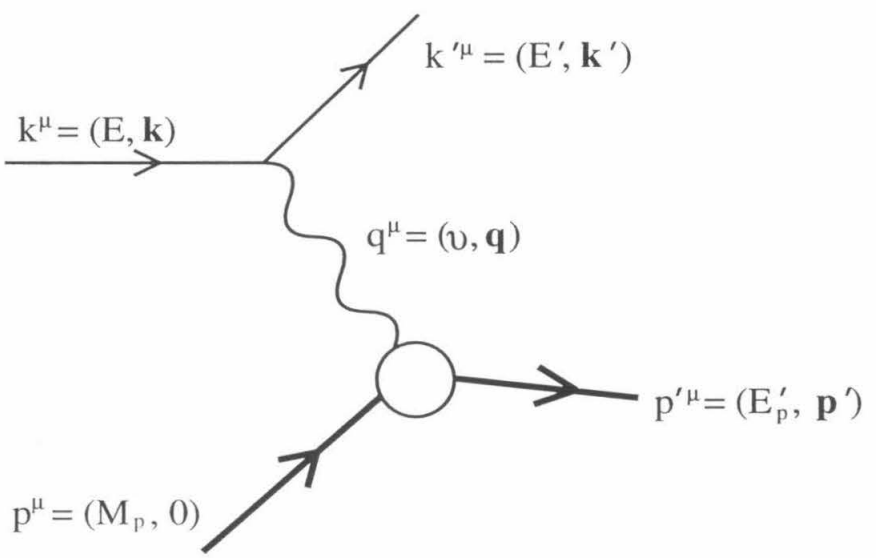

FIG. 3. **Born-Level ^{1}H$(e,e'p)$. Here k^μ, k'^μ, p^μ, and p'^μ are the 4-momenta of the incoming electron, the outgoing electron, the incoming proton, and the outgoing proton, respectively.**

$$\left(\frac{d\sigma}{d\Omega}\right)_{Mott} = \frac{\alpha^2 \cos^2 \frac{\theta}{2}}{4E^2 \sin^4 \frac{\theta}{2}}. \tag{1.3}$$

Here $\alpha = e^2/4\pi\hbar c$ is the fine-structure constant, $\Omega = (\theta, \phi)$ is the laboratory solid angle of the scattered electron, and $\tau = Q^2/4M^2$. The effect of the structure of the proton is specified by the electric and magnetic form factors, $G_E(Q^2)$ and $G_M(Q^2)$, with approximate values given by the dipole form:

$$G_E^p \simeq \left(1 + \frac{Q^2}{0.71\,(\mathrm{GeV/c})^2}\right)^{-2}, \tag{1.4}$$

$$G_M^p \simeq \mu_p G_E^p. \tag{1.5}$$

Here μ_p is the magnetic moment of the proton.

For *nuclear* targets ($A > 1$) at quasielastic kinematics and high energies [$Q^2 \gtrsim 1\,(\mathrm{GeV/c})^2$], the Plane Wave Impulse Approximation (PWIA) is expected to dominate the $A(e, e'p)$ reaction mechanism. The PWIA assumes k, k', p, and p' are undistorted plane waves (no Coulomb distortions, ISI, or FSI) and that the proton detected in the final state absorbed the entire momentum transfer. The Born-level PWIA is shown in Figure 4.

In the PWIA, the proton is treated as being essentially free ("quasi-free") before the reaction, except that it is bound with separation energy E_s and moving with momentum $\mathbf{p}$:

$$p^\mu \equiv (M_p - E_s - T_{A-1}, \mathbf{p}). \tag{1.6}$$

The initial momentum $\mathbf{p}$ is the result of the Fermi motion of the nucleons. The separation energy E_s is the energy it would take to remove the proton from the nucleus to infinity without recoil (*i.e.*, $T_{A-1} = 0$). In the quasifree knockout reaction the proton loses an additional energy T_{A-1} to the recoil of the $A - 1$ system. In the PWIA, the scattering ejects the proton from the nucleus without ISI or FSI. (The reaction is "quasi-elastic".)

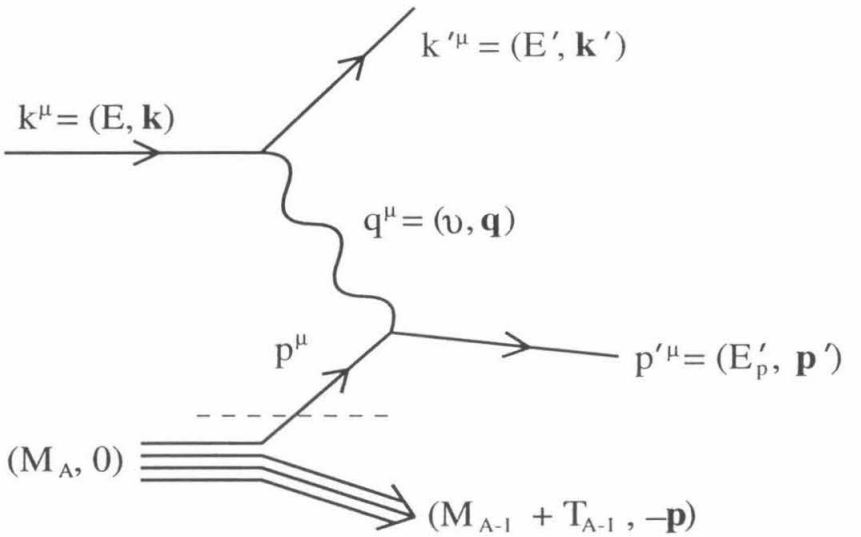

FIG. 4. $A(e,e'p)$ **in the Born-level PWIA. The part of the Feynman diagram above the dashed line is equivalent to Figure 3, except that the proton initial 4-momentum** p^μ **is given by Equation 1.6.**

In the Born-level PWIA, p^μ can be reconstructed from the experimentally determined 4-momenta: $p^\mu = p'^\mu - q^\mu$. Thus, E_s and $\mathbf{p}$ can be measured by the missing energy

$$E_m \equiv \nu - E'_p + M_p - T_{A-1} \tag{1.7}$$

and missing momentum

$$\mathbf{p}_m \equiv \mathbf{p}' - \mathbf{q} \tag{1.8}$$

not accounted for in the detected particles [9]. In reality, the relations $E_m = E_s$ and $\mathbf{p}_m = \mathbf{p}$ are modified by FSI and radiative (higher-order) effects, which entail the exchange or emission of additional (and unobserved) 4-momentum (cf. Equations 4.5 and 4.6). Even in the absence of these effects, E_m and $\mathbf{p}_m$ would measure E_s and $\mathbf{p}$

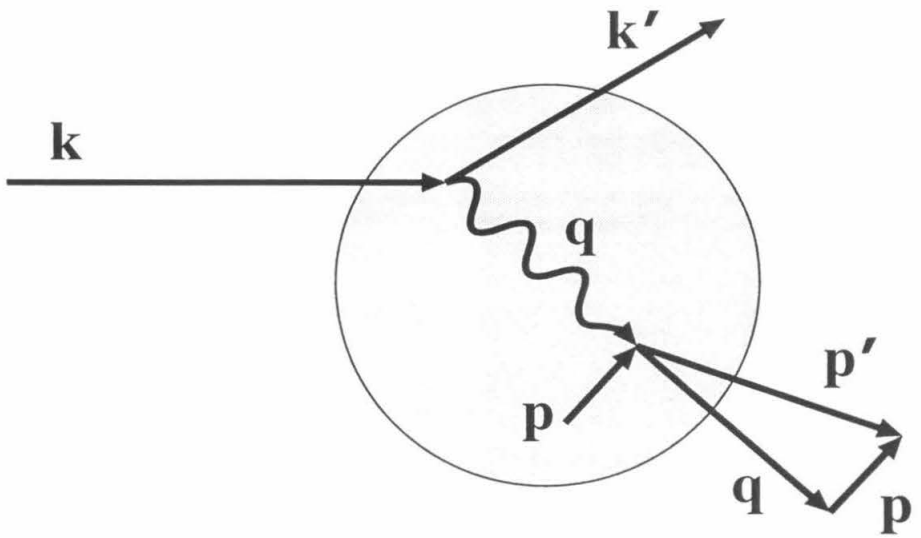

FIG. 5. **Schematic $A(e,e'p)$ showing effect of proton intial 3-momentum on kinematics. Note the propagation length $\sim \hbar/Q$ of the photon is in reality much smaller than the size of the nucleus (which is indicated in gray).**

only up to the experimental resolution. Thus, the experimentally determined quantities E_m and $\mathbf{p}_m$ can only be considered to be approximations to the actual separation energy E_s and initial momentum $\mathbf{p}$. Note that in place of $\mathbf{p}_m$, some authors [9] refer to the momentum $\mathbf{p}_B = -\mathbf{p}_m$ of the recoil $A-1$ system.

We adopt a convention where p_m, the magnitude of $\mathbf{p}_m$, is assigned a positive (negative) sign if $\mathbf{p}'$ is at a larger (smaller) angle with respect to the beam in the electron scattering plane than is $\mathbf{q}$. (For example, Figure 5 shows a kinematics where $p_m < 0$. Note this convention is opposite to that used in [9].)

Because of its separation energy E_s and Fermi motion $\mathbf{p}$ in the nucleus, the proton is off-shell. De Forest [10] and others [9] give a prescription for extending the nucleon current to off-shell kinematics in the Born-level PWIA, resulting in the cross section:

$$\frac{d^6\sigma}{dE'd\Omega_{k'}dE'_p d\Omega_{p'}} = p'E'_p\sigma_{ep}S(E_s,\mathbf{p}). \tag{1.9}$$

Here $\Omega_{k'}$ and $\Omega_{p'}$ are the solid angles of the outgoing electron and proton, respectively. The additional four degrees of freedom with respect to Equation 1.2 are from the unconstrained proton initial 4-momentum.

The nuclear structure is characterized by the spectral function $S(E_s,\mathbf{p})$, the probability density for finding a proton with separation energy E_s and 3-momentum $\mathbf{p}$. The normalization of $S(E_s,\mathbf{p})$ is given by the spectroscopic sum rule:

$$\int S(E_s,\mathbf{p})d^3\mathbf{p}dE_s = Z, \tag{1.10}$$

where Z is the nuclear charge. The off-shell electromagnetic interaction is specified by σ_{ep}, the square of the electron-proton elastic scattering amplitude. Equation (1.9) illustrates the intuitive idea that the quasielastic cross section should be the product of the probability $S(E_s,\mathbf{p})$ of finding a proton with 4-momentum p^μ and the probability σ_{ep} of scattering from it (multiplied by a Jacobian).

In the reaction, the $A-1$ system may experience an excitation to any possible bound or unbound state $|A-1^*>$. Because the Born-level cross section, Equation 1.9, ignores the final state of the $A-1$ system, it can be considered to be the closure sum over $|A-1^*>$. Data from the Saclay ^{12}C$(e,e'p)$ experiment [11] indicate that the rate is confined to low-lying $A-1$ states included in $E_m < 100$ MeV (see Section I.A), so the use of this cross section is appropriate.

One goal of many $A(e,e'p)$ experiments is comparison of the experimental cross sections with those predicted using the PWIA cross section (or a refinement thereof) and a single-particle description of the nuclear structure, given by the Independent Particle Shell Model (IPSM). In the IPSM, the spectral function is the sum of the contribution from each shell:

$$S(E_s,\mathbf{p}) = \sum_i N_i|\varphi_i(\mathbf{p})|^2 L_i(E_s), \tag{1.11}$$

where N_i is the occupation number of orbital i ($\sum_i N_i = Z$), $L_i(E_s)$ is the energy profile due to the finite lifetime of the one-hole state, and $\varphi_i(\mathbf{p})$ is the bound-state wave function. Except for the the least-bound shell, which may be partially filled, $N_i = 2j_i + 1$, where j_i is the total angular momentum of orbital i. It is customary in the analysis of $A(e, e'p)$ data to calculate the $\varphi_i(\mathbf{p})$ in a Woods-Saxon nuclear potential with shell-dependent adjustable parameters (see Appendix E).

I.A.2. Previous $A(e,e'p)$ Data

The quasielastic proton knockout reaction has been studied for Q^2 up to $0.79\,(\mathrm{GeV/c})^2$ and nuclei ranging from the lowest masses (^{2}H, ^{3}H, ^{3}He) up to ^{208}Pb [9,12–14]. The theory outlined in the previous section, with some refinements, has had great success in explaining many features of the observed data. But there still are unresolved issues, such as the failure of the spectroscopic sum rule, that can be explored by measuring the reaction at higher Q^2. The measured quantities most relevant to the current experiment are the nuclear spectral function $S(E_m, p_m)$ and the spectroscopic factors.

The spectral function is measured using Equation 1.9. First, the counts are binned in E_m and p_m using Equations 1.7 and 1.8. Then $S(E_m, p_m)$ is extracted by dividing the cross section measured in an (E_m, p_m) bin, corrected for experimental acceptances, by σ_{ep}. Distortions due to radiative effects are removed in a generalization of the radiative correction procedure used in elastic $^1\mathrm{H}(e,e')$ scattering. Other distortions from proton FSI and Coulomb distortions of the particle waves are *not* removed from the data, so the measured $S(E_m, p_m)$ are referred to as "effective" spectral functions. Instead, the data is compared to the prediction in the Distorted Wave Impulse Approximation (DWIA) which includes these effects [9]. The resulting $S(E_m, p_m)$ can be converted into proton energy and momentum distributions by integration over d^3p_m and dE_m, respectively. The treatment of radiation and distortions in the current experiment is somewhat different (see Section V.A).

Figure 6 shows E_m spectra measured on ^{12}C at Saclay [11]. The E_m acceptance extends up to $\sim 60\,\mathrm{MeV}$. The data clearly exhibit the presence of the $1p$ and $1s$ energy levels predicted in the nuclear shell model. The narrow $1p$ peak at 16 MeV exhibits substructure at $E_m = 18$ and 21 MeV due to the final state of the $A-1 = {}^{11}$B recoil nucleus. The states have rapidly decreasing relative strengths: the $\frac{3}{2}^-$ ground

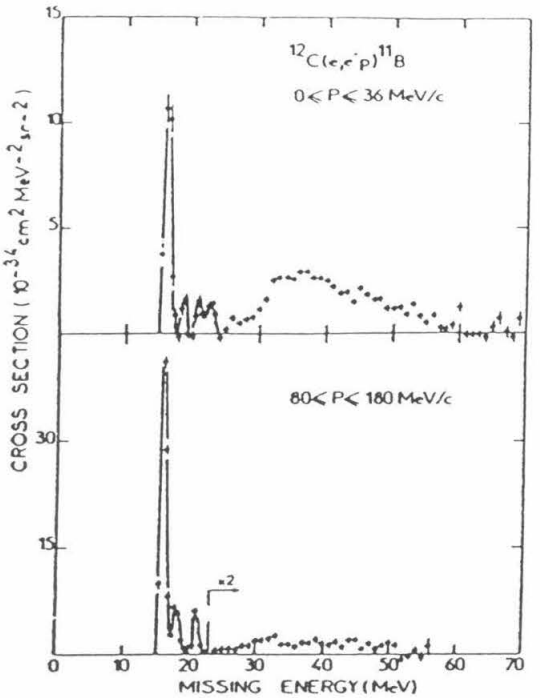

FIG. 6. E_m **spectra from** $^{12}\mathrm{C}(e,e'p)$ **at Saclay [11]; (a)** $0 \leq p_m \leq 36\,\mathrm{MeV}$**, (b)** $80 \leq p_m \leq 180\,\mathrm{MeV}$

state has 74%, the $\frac{1}{2}^-$ (2.12 MeV) excited state has 13%, the $\frac{3}{2}^-$ (5.02 MeV) has 9%, and higher excitations have 4% [9]. This indicates that all of the rate involves the low-lying $A-1$ states which are included in $E_m < 100\,\mathrm{MeV}$. The 20-MeV width of the $1s$ shell at $E_m = 38\,\mathrm{MeV}$ is due to the short lifetime of the $1s$ hole state.

The identification of these peaks with the nuclear shell model states is confirmed by the clear $l = 1$ and $l = 0$ nature of the momentum distributions measured for the shells, shown in Figure 7, and the good agreement with the p_m distributions calculated in the DWIA using the IPSM spectral function (Equation 1.11). The $\varphi_i(\mathbf{p})$ and $L_i(E_s)$ used in the IPSM $S(E_s, \mathbf{p})$ are based on charge distributions from elastic electron-nucleus scattering and separation energies from $(p, 2p)$ [11,15]. The good agreement between the $^{12}\mathrm{C}(e,e'p)$ data and the DWIA calculation demonstrates that the single-particle model simultaneously explains the three different data sets.

Another feature of Figure 7 is that the PWIA and DWIA calculations differ in

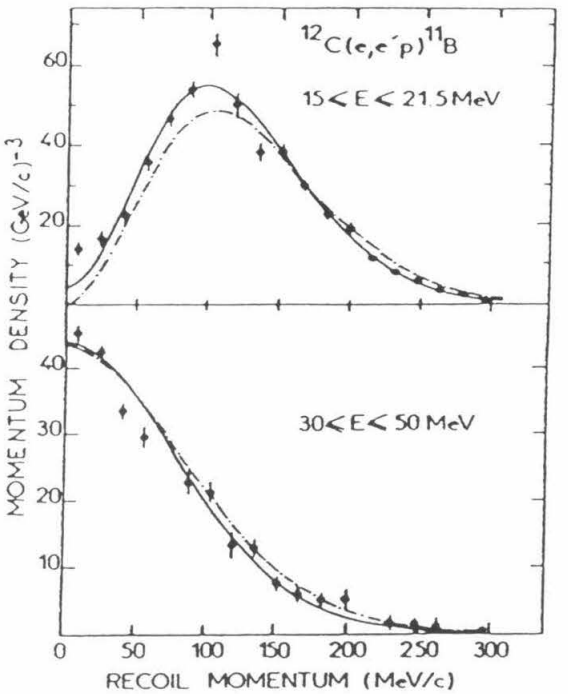

FIG. 7. $1s$ **and** $1p$ p_m **distributions from** $^{12}\mathbf{C}(e,e'p)$ **at Saclay [11]. The solid and dashed lines are DWIA and PWIA calculations respectively, with normalizations fit to the data.**

magnitude and shape. This distortion of the p_m distribution is due to the FSI of the proton, which are generally calculated with an optical-model of the proton-nucleus potential [9,13]. The DWIA calculations are sensitive to the scattering kinematics [9] and can be subject to large theoretical uncertainties [13].

The existing $A(e,e'p)$ data have good agreement with the shape of the DWIA/IPSM calculation, but are consistently lower in magnitude. The discrepancy is seen for the entire nucleus in the incomplete ($\sim$ 70%) saturation of the spectroscopic sum rule (Equation 8), as shown in Figure 8. The discrepancy persists up to $A = ^{208}$Pb, the heaviest nucleus measured [13]. The measured fraction of the sum rule strength is closely related to the nuclear transparency T, except that it is corrected for absorption in the proton FSI. Thus, the value expected for standard FSI is unity. By contrast, for the nuclear transparency, the expected value is less than one. The

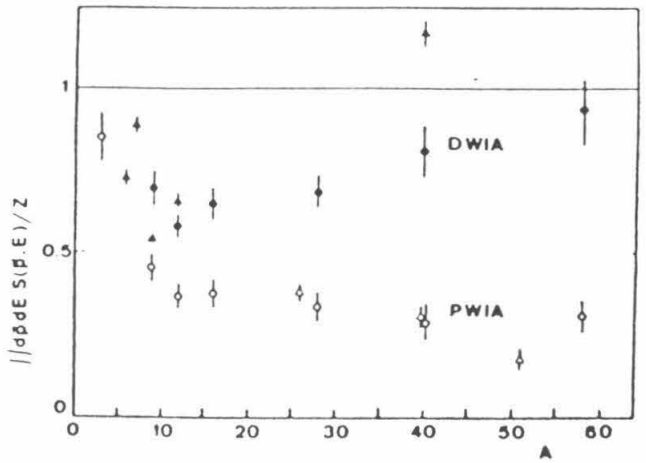

FIG. 8. $A(e,e'p)$ **results for the spectroscopic sum rule, from reference [9].**

connection between the nuclear transparency T and the measured fraction of the sum rule strength is elaborated in Section V.B.

Part of the sum rule discrepancy may be due to performing the integrals over the finite ranges of p_m and E_m imposed by experimental acceptances. Experiments with larger acceptance ranges exhibit smaller discrepancies [9]. In particular, one must be careful to take account of the large $\sim 15\%$ strength at $|p_m| > p_f$ (where p_f is the Fermi momentum) due to short-range correlations in the initial state. See Section V.B for the treatment of these issues in the current experiment. Another problem is uncertainties in the model of the proton FSI due to Pauli blocking, medium modifications, and nucleon-nucleon correlations [16]. Most of these uncertainties should be smaller at $Q^2 \gtrsim 1\,(\mathrm{GeV/c})^2$ [17].

A possible explanation for the remaining discrepancy is that the virtual photon can couple to more than one nucleon because for $Q^2 < 0.8\,(\mathrm{GeV/c})^2$ its wavelength $\hbar c/Q$ is comparable to the nucleon radius $R_N \simeq 0.8\,\mathrm{fm}$. The expectation that the interaction should be single-particle in nature at higher Q^2 is consistent with the observation of y scaling at $Q^2 \gtrsim 1\,(\mathrm{GeV/c})^2$ [18]. However it has been argued [14]

that the multi-nucleon contributions for $50 \leq E_m \lesssim 100\,\mathrm{MeV}$ may increase at higher Q^2.

It is clear that the $A(e,e'p)$ reaction changes character at $Q^2 \gtrsim 1\,(\mathrm{GeV/c})^2$. First, it becomes more truly a reaction involving a single nucleon and, as Q^2 increases, the virtual photon resolves not just individual nucleons but also individual partons therin. As a consequence there is the onset of the dominance of inelastic scattering in the inclusive $A(e,e')$ reaction, as shown in Figure 2.

In addition, treatment of the FSI should simplify at $Q^2 \gtrsim 1\,(\mathrm{GeV/c})^2$ where, due to the shorter de Broglie wave length of the outgoing proton, the FSI are dominated by nucleon-nucleon scattering. In Section V it is shown that at such high Q^2, the FSI produce a reduction in the proton flux without much distortion in the shape of $S(E_m, p_m)$. Given the theoretical uncertainties in the low-Q^2 distortion calculations [13], it is important to verify the low-Q^2 $S(E_m, p_m)$ with higher-Q^2 measurements.

Furthermore, since the strong coupling constant α_s decreases with increasing Q^2, one expects QCD to enter the perturbative regime. Hence, the internal dynamics and FSI of the struck proton could change dramatically at $Q^2 > 1\,(\mathrm{GeV/c})^2$, possibly leading to entirely new effects such as Color Transparency.

For all of these reasons, it is imperative to test the $A(e,e'p)$ quasielastic scattering mechanism at $Q^2 > 1\,(\mathrm{GeV/c})^2$. The current experiment represents the extension of these measurements by nearly an order of magnitude to $Q^2 = 6.8\,(\mathrm{GeV/c})^2$.

I.B. Color Transparency

The arguments leading to CT involve three assumptions. First, observing an exclusive reaction requires the hadrons to have fluctuated to a small size—referred to as a point like configuration (PLC)—at the time of the interaction. Second, the PLC experiences a reduced interaction with the nucleus, a phenomenon known as color screening. Third, the hadrons remain small while they propagate out of the nucleus. The three assumptions are discussed in the following sections, with special attention paid to the $A(e,e'p)$ reaction. The process is shown in Figure 9 for the reaction $A(e,e'p)$ with $A = {}^1\mathrm{H}$ and $A > 1$.

I.B.1. Selection of Point Like Configuration

The first assumption can be supported by a simple pQCD model. As Q^2 increases and QCD becomes perturbative, the lowest order diagrams dominate the (quasi) elastic scattering. Such a diagram is shown in Figure 10 for the case of electron-proton elastic scattering in the Breit frame where $q^\mu = (0, Q\hat{\mathbf{z}})$ (choosing $z \parallel \mathbf{Q}$).

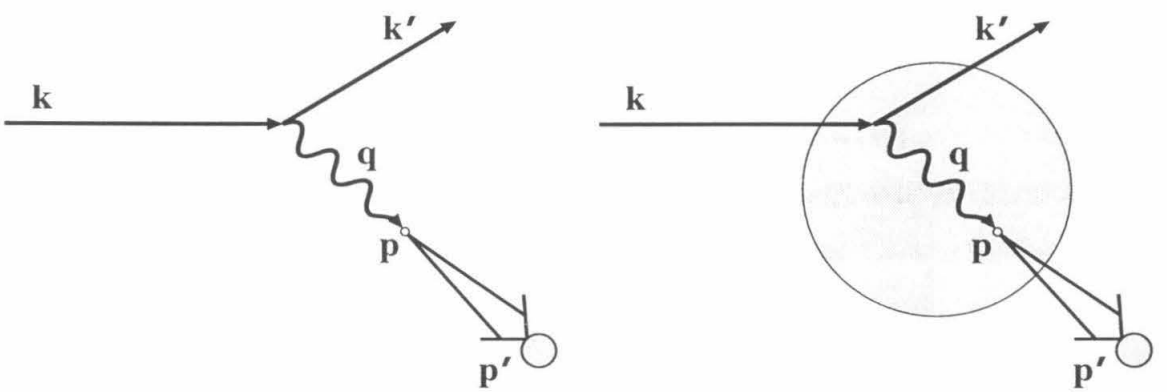

FIG. 9. **Schematic indicating the 3-momenta involved in** ${}^1\mathbf{H}(e,e'p)$ **and** $A(e,e'p)$.

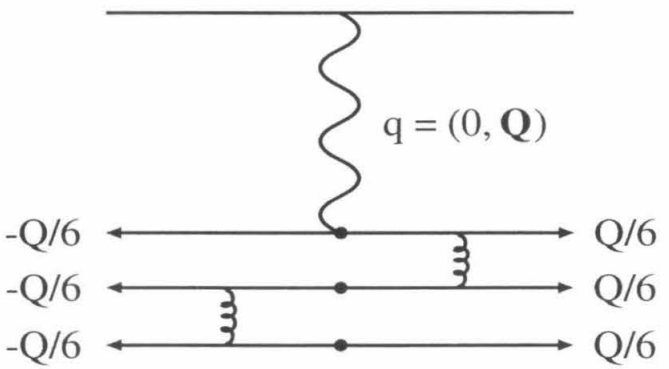

FIG. 10. **Lowest-order elastic scattering. To lowest order in α_s, the scattering involves the minimum possible number of partons (3) and gluon exchanges (2). The scattering is shown in the Breit frame, where the proton momentum is changed in sign but not in magnitude, and $\nu = 0$. The quark lines are labeled by the momentum components along Q. For definiteness the quarks are shown as having typical momentum values (Bjorken $x = 1/3$) before and after the collision. (After Jennings and Miller [3].)**

Unless the struck quark shares the momentum transfer with the other quarks, the proton fragments and the reaction is inelastic. Hence, elastic scattering requires the exchange of two gluons (in the lowest order) of 4-momentum $\sim (0, Q\hat{\mathbf{z}})$ and off-shell mass $\sim Q$. By the uncertainty principle, the gluons have a lifetime of $\sim \hbar/cQ$ and a range of $\sim \hbar/Q$. Thus an elastic interaction only occurs if the proton happens to have fluctuated to a PLC of transverse extent $b \lesssim \hbar/Q$ before the interaction. At large Q^2, b can be much smaller than R_h, the equilibrium radius of the hadron. (Small longitudinal extent is guaranteed by Lorentz contraction.)

Implicit in the simple model is the roughly equal distribution of momentum between the quarks. In the Feynman mechanism, however, the proton fluctuates to a state where almost all of the momentum is carried by a single parton of 4-momentum

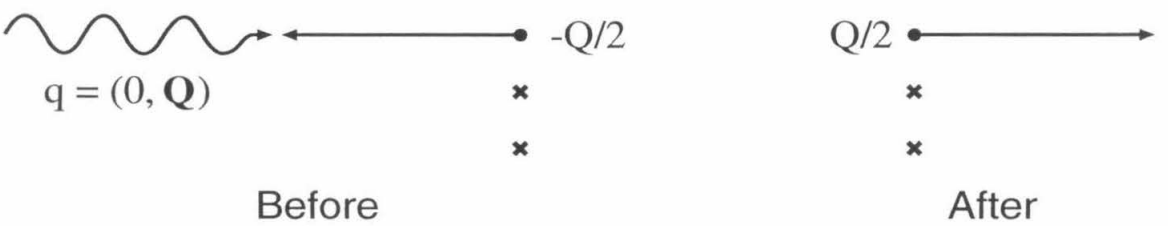

FIG. 11. **The Feynman mechanism for elastic scattering. As in Figure 10, the scattering is shown in the Breit frame and the quark lines are labeled by the longitudinal momenta. Crosses indicate the "wee" partons, which carry almost none of the longitudinal momentum.**

$\sim (0, -\mathbf{Q}/2)$ (see Figure 11). The momentum is reversed in the scattering, restoring the proton to its initial state without any gluon exchanges. At high Q^2 this diagram is suppressed, however, because the large acceleration of the struck quark produces gluon radiation (in analogy with electromagnetic radiation from accelerated electrons), making the interaction inelastic.

This reasoning leads to the most general argument supporting the formation of a PLC: the radiation of gluons is only suppressed if the color-neutral proton fluctuates to a PLC with no residual color fields (in analogy with the vanishing of the radiation field of a zero-size electric dipole). This argument does not require the exchange of a small number of gluons between the partons, and therefore can apply at energies lower than the onset of pQCD. Unfortunately, it is not known what Q^2 is high enough for gluon radiation to prevent elastic scattering from non-PLCs.

The selection of the PLC may be responsible for the constituent counting rule scaling behavior predicted by pQCD and observed in many exclusive processes for $Q^2 \gtrsim 5\,(GeV/c)^2$. Consider a reaction involving two (possibly composite) particles in both the initial and final state, with a total of N constituents before and after

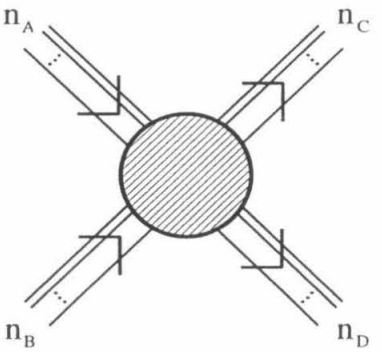

FIG. 12. **The $A+B \to C+D$ exclusive reaction. Particle X (= A, B, C, or D) has n_X elementary constituents ($n_X = 1$ is allowed). The total number of constituents is $N = n_A + n_B + n_C + n_D$.**

the interaction (see Figure 12). If the momenta involved are much greater than the particle masses, then constituent counting predicts the cross section scales [19]:

$$\frac{d\sigma}{dQ^2} \simeq \frac{f(\Theta_{CM})}{s^{N-2}} = \frac{f(\Theta_{CM})/\sin^{2N-4}(\Theta_{CM}/2)}{(Q^2)^{N-2}}. \tag{1.12}$$

Here s is the Mandelstam invariant and $f(\Theta_{CM})$ is a function of the center of mass angle Θ_{CM}. The relation $Q^2 = s\sin^2(\Theta_{CM}/2)$ is used.

In the PLC-dominated mechanism, the factor $1/Q^2$ for each additional constituent represents the geometric probability $\sim (b/R_h)^2$ that its transverse separation from the location of the scattering is $< b = \hbar/Q$. (The factor $1/Q^2$ arises for the outgoing constituents as well because the probability of a PLC fluctuating back to a full-sized hadron is the same as that of the full-sized hadron fluctuating to the PLC.) Equation 1.12 appears to explain the scaling observed at $\Theta_{CM} = 90°$ and $s \gtrsim 2\,(\mathrm{GeV/c})^2$ for the reactions $^1\mathrm{H}(p,2p)$ and $^2\mathrm{H}(\gamma,p)n$ (see Figure 16 and reference [20]). For electron-hadron scattering, the scaling results in

$$F_h(Q^2) \sim \frac{1}{(Q^2)^{n_h-1}} \tag{1.13}$$

where $F_h(Q^2)$ is the elastic form factors of a hadron with n_h constituents. This scaling is observed in the data of Figure 13 for $Q^2 \gtrsim 5\,(GeV/c)^2$. In the case of elastic electron-proton scattering, relevant to the current experiment, the scaling can be seen as the limit of the dipole form (Equations 1.4 and 1.5) of the electric and magnetic form factors:

$$\lim_{Q^2\to\infty} G_M^p/\mu_p = \lim_{Q^2\to\infty} G_E^p = \frac{[0.71\,(\mathrm{GeV/c})^2]^2}{Q^4}. \tag{1.14}$$

The onset of the scaling behavior is not conclusive evidence of the onset of pQCD. The dispersion sum rule approach argues that the observed scaling is accidental and that the true scaling does not set in until higher Q^2. For example, Bakulov and Radushkin [21] claim that the Feynman mechanism dominates the pion form factor for values of Q^2 up to $10\,(\mathrm{GeV/c})^2$.

I.B.2. Color Screening

In QCD the color field of a color neutral object vanishes as the size of the object is reduced. This occurs because the fields of the individual quarks and gluons cancel each other as the size is reduced, in analogy with the electric dipole in QED. Thus, the interaction of the PLC with the nucleus vanishes as its transverse extent b becomes small. In pQCD for small b, two-gluon exchange is the dominant scattering mechanism and the PLC-nucleon cross section is [27]:

$$\sigma_{PLC,N} \simeq \sigma_{h,N}\frac{b^2}{R_h^2}, \tag{1.15}$$

where $\sigma_{h,N}$ is the standard hadron-nucleon cross section and R_h is the radius of the free hadron. The cross section vanishes as $b \to 0$, in contrast with black-disk scattering where the cross section is $\pi(b^2 + R_N^2) \to \pi R_N^2$.

Although the two-gluon approximation is probably not very accurate for $Q^2 \leq 7\,(\mathrm{GeV/c})^2$, there is evidence that Equation 1.15 is valid over a wider kinematic

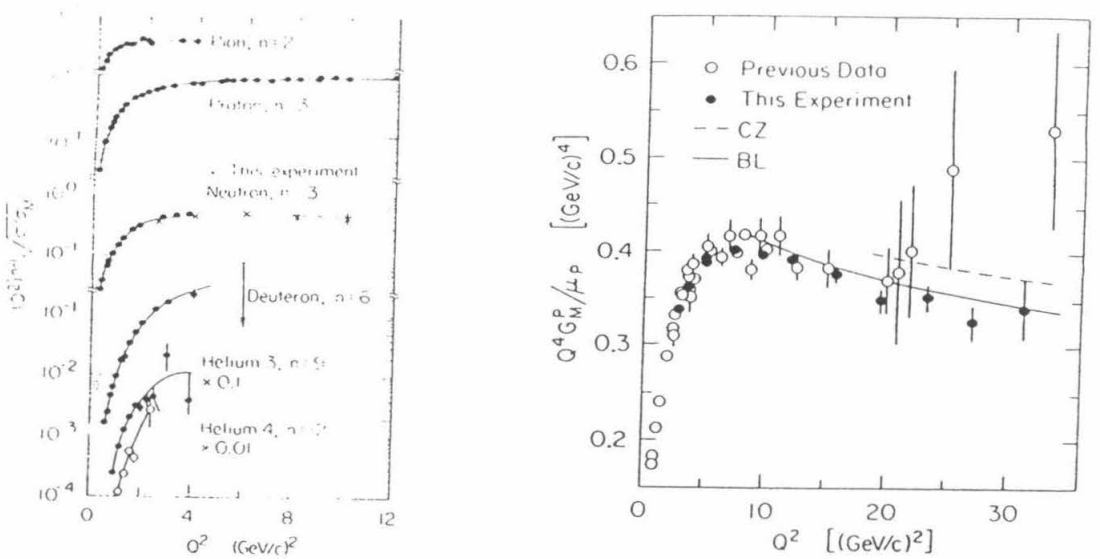

FIG. 13. **Constituent scaling in hadron form factors. The left-hand figure, taken from reference [22], exhibits approximate dimensional scaling (Equation 1.13) at $Q^2 \gtrsim 5\,(GeV/c)^2$ for the pion, proton, and neutron. More recent proton data is shown in the right hand figure, taken from reference [23].**

range than pQCD. For example, Povh and Hüfner [24] independently arrived at an analogous form through the study of hadron-proton cross section data. They deduce the RMS hadron radius R_h from the elastic scattering slope parameter,

$$b_{hp} = \frac{d}{dt} \ln \left(\frac{d\sigma_{hp}^{el}}{dt} \right) = \frac{1}{3}(R_h^2 + R_p^2), \tag{1.16}$$

where $d\sigma_{hp}^{el}/dt$ is the differential elastic cross section and $t = Q^2$ is the Mandelstam invariant. The proton and pion radii are found to be $R_p = \sqrt{3b_{pp}/2} = 0.82 \pm 0.01$ fm, $R_{\pi+} = \sqrt{3b_{\pi p} - R_p^2} = 0.64 \pm 0.01$ fm, and $R_{\pi-} = 0.65 \pm 0.01$ fm, consistent with the measured electromagnetic radii. They find that the total cross section is given by

$$\sigma_{hp}^{tot} \simeq \frac{1}{9} g R_h^2 R_p^2 = g(b_{hp} - \frac{1}{2} b_{pp}) \frac{1}{2} b_{pp}, \tag{1.17}$$

equivalent to Equation 1.15. The data are consistent with this linear b_{hp} dependence

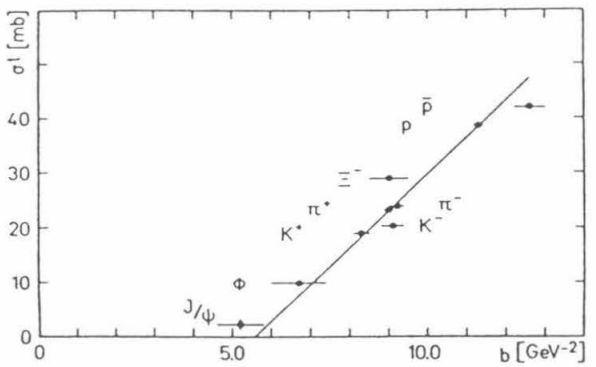

FIG. 14. **Data for total cross sections σ_{hp}^{tot} vs. the experimental slope parameters b for hadron-proton reactions at c.m. energy $\sqrt{s} \leq 16\,\mathrm{GeV}$.**

for R_h between 0.84 (for $\bar{p}p$) and 0.20 fm (for $J/\psi p$) (see Figure 14). Note that the radii relevant to the elastic and total cross sections are the equilibrium radii and are not reduced by the formation of a PLC because the elastic slope parameters are measured at $t \simeq 0$ and because the total cross sections do not represent exclusive processes.

Direct evidence of color screening has been seen in the Fermilab experiment E665 [25] in the same Q^2 range as NE-18. The experiment measured $A(\mu, \mu'\rho^0)$ and $A(\mu, \mu'\phi)$ production on deuterium, carbon, calcium, and lead in deep-inelastic kinematics. In a simple model of the scattering, the photon fluctuates to a virtual quark-antiquark pair with transverse extent $b \sim 1/Q$ (where Q^2 is the muon momentum transfer) before it enters the nucleus, where it is scattered on-shell through an "elastic" interaction with a nucleon. The distance travelled by the meson before obtaining full size is $l_h \simeq \hbar\nu/c^4 m_V \Delta m$ [26] where the energy loss is $\nu \simeq 200\,\mathrm{GeV}$, the ρ^0 or ϕ mass is $m_V \sim 1\,\mathrm{GeV/c^2}$, and the typical level splitting of quarkonium is $m_V \sim 0.7$–$1\,\mathrm{GeV/c^2}$ (based on the mass differences of the ρ^0 or ϕ excitations). The formation length is large $\sim 40\,\mathrm{fm}$ because the proper time of formation, $\sim \hbar/c^3\Delta m \sim 0.2\,\mathrm{fm/c}$,

is subject to a large time dilation, $\sim \nu/c^2 m_V \sim 200$.

The data were taken at the Fermilab Tevatron muon beam line with an average beam energy of 470 GeV. The outgoing muon and meson were detected in the E665 spectrometer. Exclusive meson production was selected by requiring the detection of the scattered muon and exactly two oppositely charged hadrons (from the meson decay). Because the recoil nucleon was not detected, kinematic cuts were used to select the incoherent scattering off of individual nucleons (describe above) from coherent scattering from the entire nucleus. The data show an increase in T and a decrease in the A-dependence with increasing Q^2, consistent with the onset of Color Transparency. Thus, hadron-nucleon reactions exhibit color screening in the Q^2 range of NE-18. Note that this does not imply that Color Transparency occurs in $A(e,e'p)$ and $A(p,2p)$ because for these reactions the PLC would be produced—if at all—by a different mechanism. Furthermore l_h in E665 is larger than expected in $A(e,e'p)$ and $A(p,2p)$ experiments at the same Q^2 because of the large time dilation.

Frankfurt, Miller, and Strikman [27] find additional support for the phenomenon of color screening in the observation of precocious Bjorken scaling in deep inelastic lepton-proton scattering, jet production in deep inelastic lepton-nucleus scattering (which suggests that Equation 1.15 may be valid for $b \lesssim 0.25\,\mathrm{fm}^2$), and high energy diffractive processes.

I.B.3. Lifetime of Point Like Configuration

The PLC takes a finite proper time to fluctuate back to its full size. Because the PLC is moving at momentum Q, time dilation guarantees that at some Q^2 the PLC will be able to propagate out of the nucleus before returning to full size.

The earliest quantitative models for the lifetime of the PLC were advanced by Farrar *et al.* [2] (see Figure 1). The simplest is the "naive parton" model, which

assumes that the quarks expand back to their usual separation at the speed of light, taking a time $\tau \simeq R_h/c$. The PLC can propagate through a length

$$l_h \simeq \gamma\tau c \tag{1.18}$$

of the nucleus with reduced cross section, where $\gamma = E'_h/M_h$ is the time dilation Lorentz factor. If the hadron is a nucleon, $R_h = R_N \simeq 0.8\,\mathrm{fm}$, and the PLC can have a significantly enhanced probability of escaping the nucleus, even for modest values of γ.

The naive parton model ignores the basic quantum behavior of the system. For example, the virtual gluons and sea quarks can fluctuate back into existence at radii $\sim R_h$ on a smaller time scale. The more realistic "quantum diffusion" model assumes the expansion takes a total time given by the average value of the dominant pQCD energy denominator, $\gamma\tau = <\hbar/(E'_{h^*} - E'_h)>$. Here E'_h and E'_{h^*} are the energy of the hadron and its intermediate state.

The key point in this model is that the PLC is not the ground state of the free hadron hamiltonian (which has a much larger radius), and therefore represents a fluctuation to a state with $M_{PLC} > M_h$. By the energy-time uncertainty principle, this off-shell state can propagate a distance:

$$l_h \simeq \frac{\hbar c}{E'_{PLC} - E'_h} \simeq \frac{2\hbar p'}{c^2 \Delta M^2}, \tag{1.19}$$

where p' is the momentum of the outgoing hadron (and of the PLC) and $\Delta M^2 \equiv M^2_{PLC} - M^2_h$. The right-hand approximation is valid for $p'/c \gg M_{PLC}, M_h$. The authors use $\Delta M^2 = 0.7\,(\mathrm{GeV/c})^2$, which corresponds to $\tau \simeq 0.5\,\mathrm{fm/c}$. (For easier comparison with the naive parton model result, $\gamma = E'_h/M_h$ has been used instead of $\gamma = E'_{PLC}/M_{PLC}$.)

The other model of PLC expansion length commonly used to predict CT effects, due to Jennings and Miller [3], is closely related. The authors expand the PLC in

a hadronic basis, $|PLC>=\sum|h^*><h^*|PLC>$, where the sum is over hadronic excitations $|h^*>$ with the same quantum numbers. Because the PLC is produced by cancellations between the $|h^*>$ wave functions, the propagation distance l_h is then given by the phase decoherence distance of the state $|PLC(t)>=\sum e^{(i/\hbar)\mathbf{p'}_{h^*}\cdot\mathbf{r}}|h^*><h^*|PLC(t=0)>$. Here the $|h^*>$ are assumed to have equal energy E'_h, so $p'_{h^*}=\sqrt{p'^2+M_p^2-M_{h^*}^2}$. Assuming the PLC is dominated by the nucleon $|N>$ and a low-lying nucleonic excitation $|N_1>$ of mass M_1 and momentum p'_1, the decoherence distance is:

$$l_h=\frac{\pi\hbar}{2(p'-p'_1)}\simeq\pi\hbar E'_p c^3\frac{1}{M_1^2-M_p^2}. \tag{1.20}$$

The result is similar to Equation 1.19. The underlying physics is basically equivalent, except that here the intermediate state is assumed to have the same energy as the outgoing proton, and so it is the position-momentum uncertainty principle that applies.

One of the largest differences between models of CT in $A(e,e'p)$ is the value of ΔM^2 or M_1 assumed. Larger l_h (smaller ΔM^2, M_1) indicate that CT can set in at smaller Q^2. The CT predictions use $\Delta M^2=0.7$–$1.1\,\mathrm{GeV/c^2}$ [6] or $M_1=1.23$–$1.77\,\mathrm{GeV/c^2}$ [3]. Clearly these ranges are only estimates.

A complication to this picture that has apparently been overlooked in the published theories is the possible dependence of M_{PLC} on Q^2. Specifically, as Q^2 increases and $b\lesssim\hbar/Q$ decreases, the overlap $<PLC|N>$ of the PLC with the ground state also decreases. Therefore, in the hadronic basis, the overlap $<PLC|h^*>$ with higher-mass states must increase. Thus, the M_{PLC} may increase with Q^2, lessening the PLC lifetime τ and the size of the CT-induced transparency increase.

I.B.4. Color Transparency Experiments

Due to the difficulty of performing realistic QCD calculations at the relevant energy scales, there is no theoretical consensus on either the Q^2 value at which the production of the PLC begins to dominate elastic scattering or the dominant mass scale M_{PLC} (or M_1) of the PLC configuration. Thus, these values must be constrained by experimental searches for the onset of CT.

The first experiment to investigate CT was performed by Carroll *et al.* [28], using simultaneous measurements of $A(p,2p)$ and $H(p,2p)$ reaction rates at Brookhaven National Laboratory. To determine T they divided the $A(p,2p)$ rate by the rate expected in the limit of full CT. This rate was given by the product of the measured proton momentum distribution and the $H(p,2p)$ rate, corrected for the theoretical variation of the elastic cross section and the difference in the experimental acceptances for the two reactions. Their results showed T increasing for incident proton momenta from 4.5 to 9.5 GeV/c, but then decreasing from 9.5 to 13 GeV/c (Figure 15). Because of the subsequent decrease, the increase at lower momenta cannot be taken as an unambiguous signal of CT. Ralston and Pire have noted that the free proton-proton cross section oscillates about the s^{-10} behavior predicted by the pQCD constituent counting rule, indicating the interference of a soft process with the pQCD amplitude [29]. If the soft process is suppressed in the nuclear environment, this would lead to the observed bump in T at 9.5 GeV/c [29] (see Figure 16). In contrast, the electron-proton interaction is well-understood and its cross section varies smoothly as a function of Q^2. Thus the $A(e,e'p)$ reaction allows an important independent measurement of the Q^2 dependence of CT.

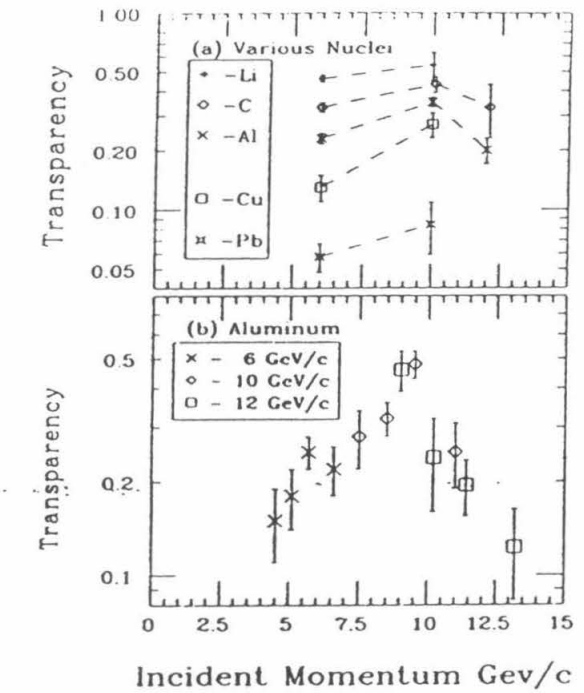

FIG. 15. T measured in $A(p, 2p)$ [28]. The graphs show (a) the transparency vs. beam momentum for nuclear targets, (b) the transparency vs. effective beam momentum for the aluminum target. The effective beam momentum is given by the actual beam momentum, coupled with the measured fermi momentum along the beam.

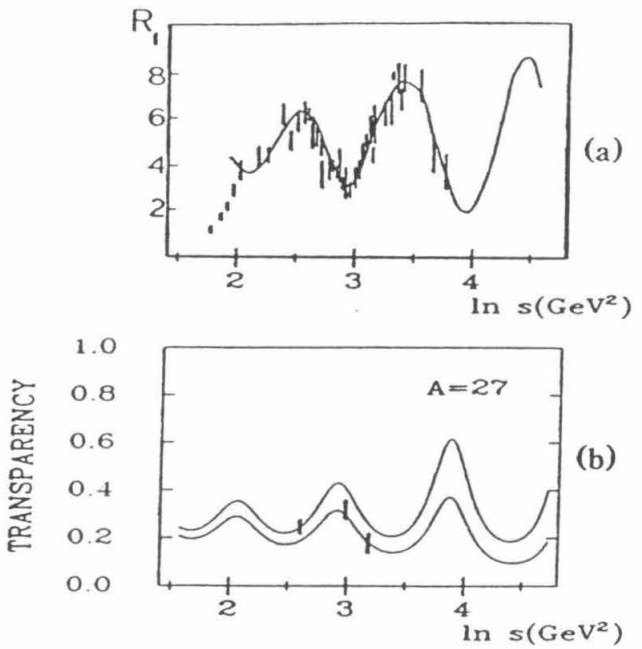

FIG. 16. **Correlation of T and $d\sigma/dt$ in $A(p,2p)$. From reference [29], the graphs show (a) the energy dependence of $R_1(s) = \text{const} \times s^{10} d\sigma/dt$ for high-energy pp elastic scattering at $90°$ c.m. angle [30] compared to a model including the interference of a soft Landshoff-scattering process with the pQCD amplitude, (b) the prediction for oscillating transparency for $A = 27$ compared with the Carroll *et al.* [28] aluminum data.**

I.C. Overview of the Experiment

Experiment NE-18 measured $A(e, e'p)$ scattering at quasielastic kinematics for $A = {}^2$H, C, Fe, and Au and $Q^2 = 1$, 3, 5, and 6.8 (GeV/c)^2. Elastic H$(e, e'p)$ was also measured as a test of systematics.

The experiment was performed in End Station A at the Stanford Linear Accelerator (SLAC) using the electron beam from the Nuclear Physics Injector (see Figure 17). Electrons and protons were detected in coincidence by the 1.6 GeV/c and 8 GeV/c magnetic spectrometers, respectively. A schematic of the experiment is shown in Figure 18.

The kinematics used in the analysis are summarized in Table 1. For the nuclear targets, multiple proton angle settings were used in "perpendicular kinematics" to measure the desired range of p_m (see Figure 5 or Section III.F).

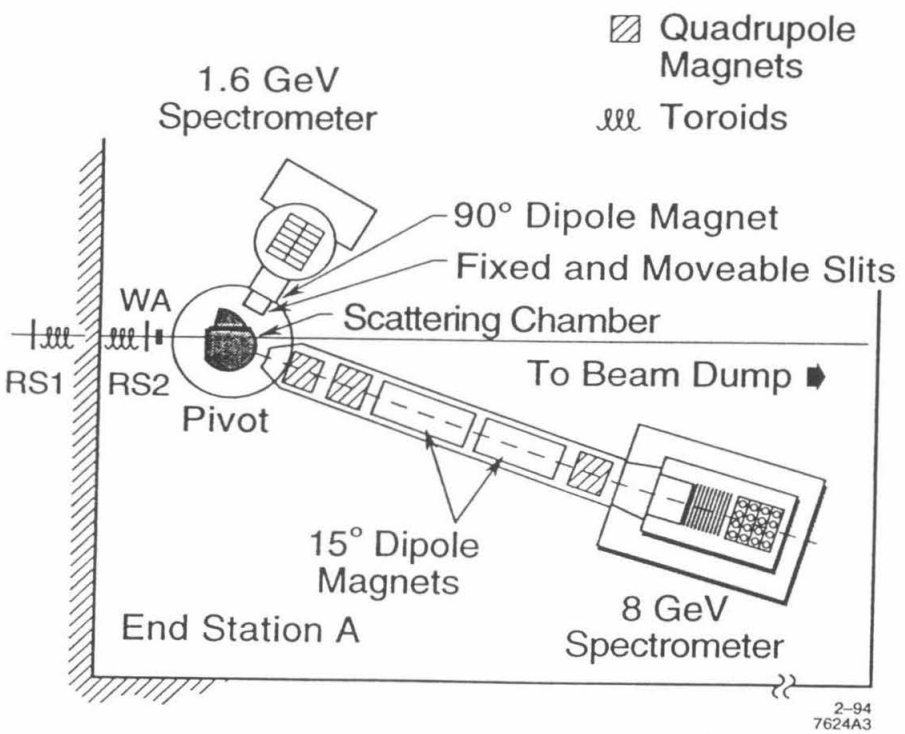

FIG. 17. **Plan view of End Station A.**

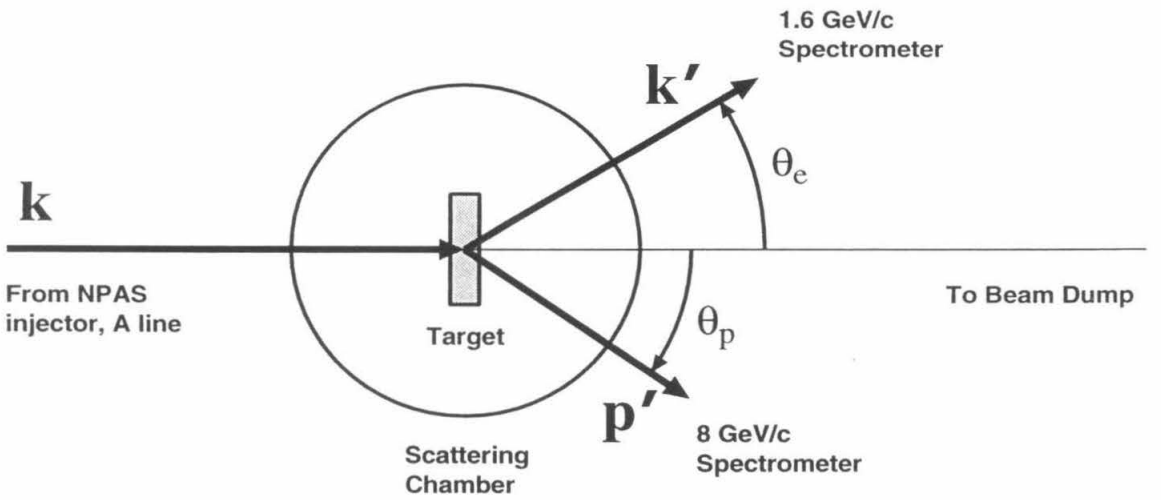

FIG. 18. **Schematic of experiment NE-18**

TABLE 1. Approximate NE-18 Kinematics. Here E is the beam energy, E' and θ_{16} are the momentum and angle settings of the 1.6 GeV/c spectrometer (used to detect electrons), and p' and θ_8 are the momentum and angle settings of the 8 GeV/c spectrometer (used to detect protons). The exact kinematics are given in Table 6.

Q^2	E	E'	θ_{16}	p'	θ_8
$(\mathrm{GeV/c})^2$	(GeV)	(GeV)	(degrees)	(GeV/c)	(degrees)
1	2.0	1.4	36	1.20	35.0–54.6
3	3.2	1.5	48	2.45	27.7–33.3
5	4.2	1.5	53	3.54	18.5–22.6
7	5.1	1.5	57	4.49	15.9–17.3

To identify coincidences, the time difference between the electron and proton triggers is converted into a time difference Δt_{p-e} between the electron and proton at the target by removing the effects of path length through the spectrometer and scintillator response time (Section III.D). The coincidence rate inferred from the Δt_{p-e} distribution is corrected for the absorption of outgoing protons in the target and spectrometer materials.

The electron and proton particle tracks measured in the spectrometers are converted to 3-momentum at the target by using matrix models of the spectrometer optics. These yield the approximate 4-momentum of the proton before the collision via Equations 1.7 and 1.8. The spectral function $S(E_m, p_m)$ is extracted as discussed earlier (in Section I.A.2).

Using model spectral functions fit to this and previous data, the PWIA is used to predict the rate measured in the absence of FSI. We define the nuclear transparency T as the ratio of the measured coincidence rate to the calculated PWIA rate. Comparison of T at $Q^2 = 1,3\,(\mathrm{GeV/c})^2$ (where CT is not expected to occur) with the value expected using conventional nuclear physics tests the saturation of the spectroscopic sum rule. Also, the Q^2 dependence of T is used to test for the presence of Color Transparency. In the limit of complete CT, T is expected to increase to unity.

II. EXPERIMENTAL APPARATUS

II.A. Electron Beam

The current experiment was performed in End Station A at SLAC using the electron beam from the Nuclear Physics Injector [31]. The beam energy was E = 2.015–5.120 GeV/c (see Table 6). Average currents were 0.1–15 μA, delivered in 1–2 μs pulses at a rate of 120 Hz. The beam was transported to End Station A through the A-Line of the beam switch yard. The energy spread of the beam is defined by slits following eight momentum-analyzing dipole magnets (see Table 2).

Two ferromagnetic toroids roughly 10 m upstream of the target measured the beam charge. The toroids were calibrated at least once an hour by passing a known charge through a wire that passed through them. The charge measured by the two

TABLE 2. Full width $2\Delta E/E$ of the energy defining slits during the different experimental kinematics (cf. Table 6). An entry of "*" in the target (or angle) column indicates that the corresponding slit width was used for all targets (or angles), except for the two exceptions in the second half of the table. These exceptions, which effect the resolution but not the count rates, are ignored in the calculation of the PWIA prediction for the experiment (Section IV.A).

Q^2 (GeV/c)^2	Target	θ_8 (degrees)	$2\Delta E/E$ (%)
1.04,1.16,3.06,3.23	*	*	0.3
1.21	4 cm ^{2}H	*	0.2
5.00,5.14,6.77,6.85	*	*	0.4
1.16	4 cm ^{1}H	43.29	0.2[a]
5.00	6% C	20.88	0.3

[a]only 1 out of 6 of the runs

toroids agreed to within 1%. Beam position and angle on target were controlled by a position monitor and steering magnet closed-loop feedback system (the Beam Control System). The beam size was roughly 0.2 cm high and 1 cm wide. The beam delivery and monitoring have not changed substantially since SLAC experiment NE-11, described in reference [32].

II.B. Targets

The targets, listed in Table 3, were mounted on remotely moveable target ladders in a sealed vacuum scattering chamber. There were two target ladders, one holding the solid targets, and the other the cryogenic and "dummy" targets. Thin aluminum entrance and exit windows, described in Table 4, allowed the beam and scattered particles to pass through with minimum energy loss and multiple scattering. The targets were positioned at normal incidence to the beam.

The standard SLAC cryogenic liquid targets (^{1}H and ^{2}H) were used. The liquid was contained in thin Aluminum target cells made of Coors aluminum beer can stock. The liquid was circulated at a flow rate of 2 m/s, with pressure and temperature monitored by pressure transducers and platinum resistors. These were used to calculate the target density.

The small ($< 1\%$) contribution to the coincidence rate by the 0.0762 mm and 0.1219 mm thick upstream and downstream end caps was measured using replica empty cells (the dummy targets) with aluminum walls at the same positions but 9.5 times thicker. In the analysis, the inferred endcap coincidence rate is subtracted from the measured endcap plus liquid rate.

TABLE 3. Target characteristics. Targets are referred to by their nominal lengths (liquid and dummy targets) or radiator thicknesses (solid targets). Purity of solid targets is effectively 100%. The lengths and thicknesses of the liquid targets are given after applying the expected 0.996 shrinkage factor in cooling to 21 K. The dummy targets are two aluminum sheets of equal thickness at the positions of the endcaps of the liquid targets.

Name	Material	Density (g/cm^3)	Length (cm)	Thickness (% r.l.)	Purity (%)
4 cm ^{1}H	Liquid H_2	0.0705	4.011	0.461	99.94
4 cm ^{2}H	Liquid D_2	0.1701	4.011	0.557	99.68
15 cm ^{2}H	Liquid D_2	0.1701	15.680	2.176	99.68
2% C	^{12}C	2.193	0.4097	2.104	
6% C	^{12}C	2.193	1.1730	6.024	
6% Fe	^{56}Fe	7.829	0.1064	6.019	
12% Fe	^{56}Fe	7.829	0.2098	11.87	
6% Au	^{197}Au	19.157	0.0206	6.137	
12% Au	^{197}Au	19.157	0.04013	11.96	
4,15 cm dummy	Al 3004 and	2.72	1.270	1.461	
	Al 5052	2.68	0.6096	0.691	

II.C. The Magnetic Spectrometers

Electrons were detected in the 1.6 GeV/c magnetic spectrometer [33] and protons in the 8 GeV/c spectrometer [34]. Both are vertical bend spectrometers with focusing in momentum and scattering angle, yielding good ($\sim$ 0.1%) resolution in particle 3-momentum. The optics focus point-to-point from target to momentum focal plane in the bend plane and parallel-to-point in the horizontal plane. Scintillator planes in both spectrometers were used to determine the time of particle passage, allowing the

TABLE 4. Target-related materials. The wire array measures beam position, and is used by the Beam Control System. The length and thickness listed are averaged over the wires and the gaps between them. The hymen and chamber windows provide the vacuum isolation of the scattering chamber. The endcaps and cell wall are the ends and side of the aluminum can encasing a liquid target. The cell wall thickness includes the contribution of the liquid target flow guide. The mylar insulation provides thermal isolation of the cryogenic liquid targets. The endcaps, cell wall, and insulation do not apply to solid targets.

Object	Material	Density	Length (mm)	Thickness (% r.l.)
Wire Array	Al	2.70	0.03990	0.0449
Entrance Hymen	Al	2.70	0.02540	0.0286
Upstream Endcap[a]	Al 5052	2.68	0.07620	0.0864
Downstream Endcap[a]	Al 3004	2.72	0.12192	0.1403
Cell Wall[a]	Al 3004	2.72	0.12700	0.1461
Insulation[a]	Mylar	1.39	0.06350	0.0221
1.6 Chamber Window	Al 5052	2.68	0.12700	0.1440
1.6 Air Gap	Air	0.00121	132.588	0.0434
1.6 Entrance Window	Mylar	1.39	0.35560	0.1237
8 Chamber Window	Al 5052	2.68	0.3048	0.3457
8 Air Gap	Air	0.00121	160.02	0.0524
8 Entrance Window	Al 5052	2.68	0.25400	0.2881

[a]Cryogenic liquid targets only

selection of coincident electrons and protons.

II.C.1. 1.6 GeV/c Spectrometer

The 1.6 GeV/c spectrometer, described in more detail elsewhere [33,32], is a 90° vertical bend dipole spectrometer (see Figure 19). It has a maximum momentum of 1.5 GeV/c, a solid angle $\Delta\Omega \simeq 3$ msr, and a momentum bite of $\pm 6\%$. Note that the quadrupoles used to increase the solid angle for SLAC experiment NE-11 (reference [32]) were not used in the present experiment.

After passing through the dipole magnet, electrons pass through a 1.5 m long gas Čerenkov counter filled with CO_2 at atmospheric pressure (see Figures 20 and 21). Following this, they pass through two crossed layers (XD and YD) of 0.5 cm thick, 11.1 cm wide plastic scintillators, 3 pairs (A, B, C) of X-Y drift chambers, another hodoscope pair (XU and YU), and two rows (PA and PB) of 10.8 cm-thick (6.4 radiation lengths) lead glass shower counter blocks.

Each drift chamber had two planes of 31 X wires and two planes of 21 Y wires spaced at 2 cm intervals. These provided an effective wire spacing of 1 cm and a coverage of approximately 40 cm by 60 cm. For paired wire hits, the drift time information allowed location of the track to a resolution of around ± 0.3 mm. The Čerenkov and shower counter provide electron identification and pion rejection, and the hodoscopes provide trigger and timing information. The scintillators and segmented shower counter also provide position information used to remove tracking ambiguities. The 1.6 GeV/c spectrometer detector package was the same as in SLAC experiment NE-11, except that all of the scintillators had photomultiplier tubes (PMT) on both sides for better timing resolution.

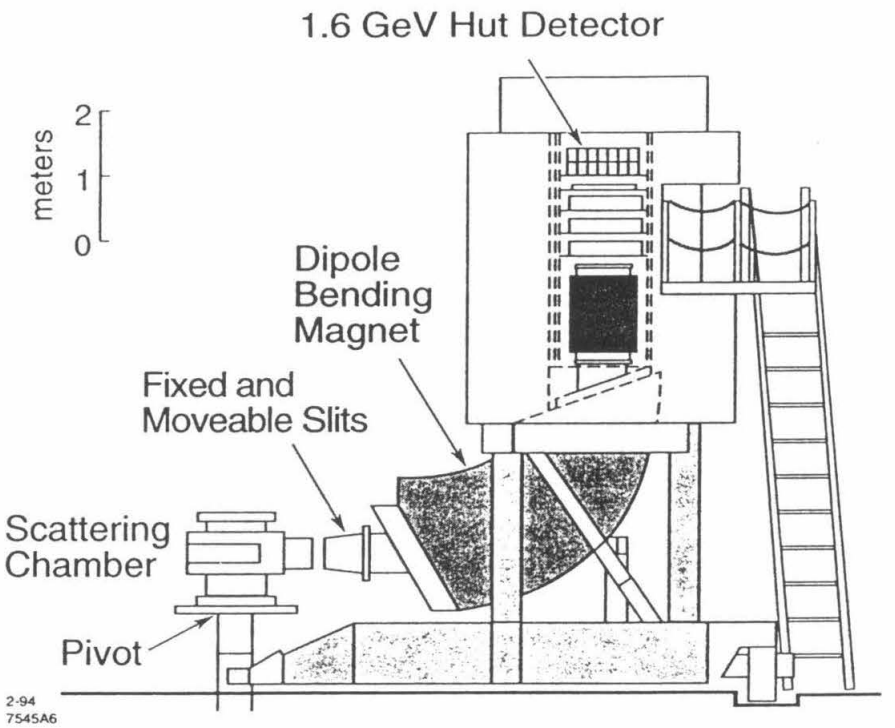

FIG. 19. Exterior side view of the 1.6 GeV/c spectrometer, as configured for the present experiment. The momentum analysis is provided by a 90° dipole bending magnet, with optical properties optimized by the use of rotated entrance and exit pole faces and other pole tip shaping [31]. The detectors are above the exit of the dipole magnet, inside the concrete shielding hut.

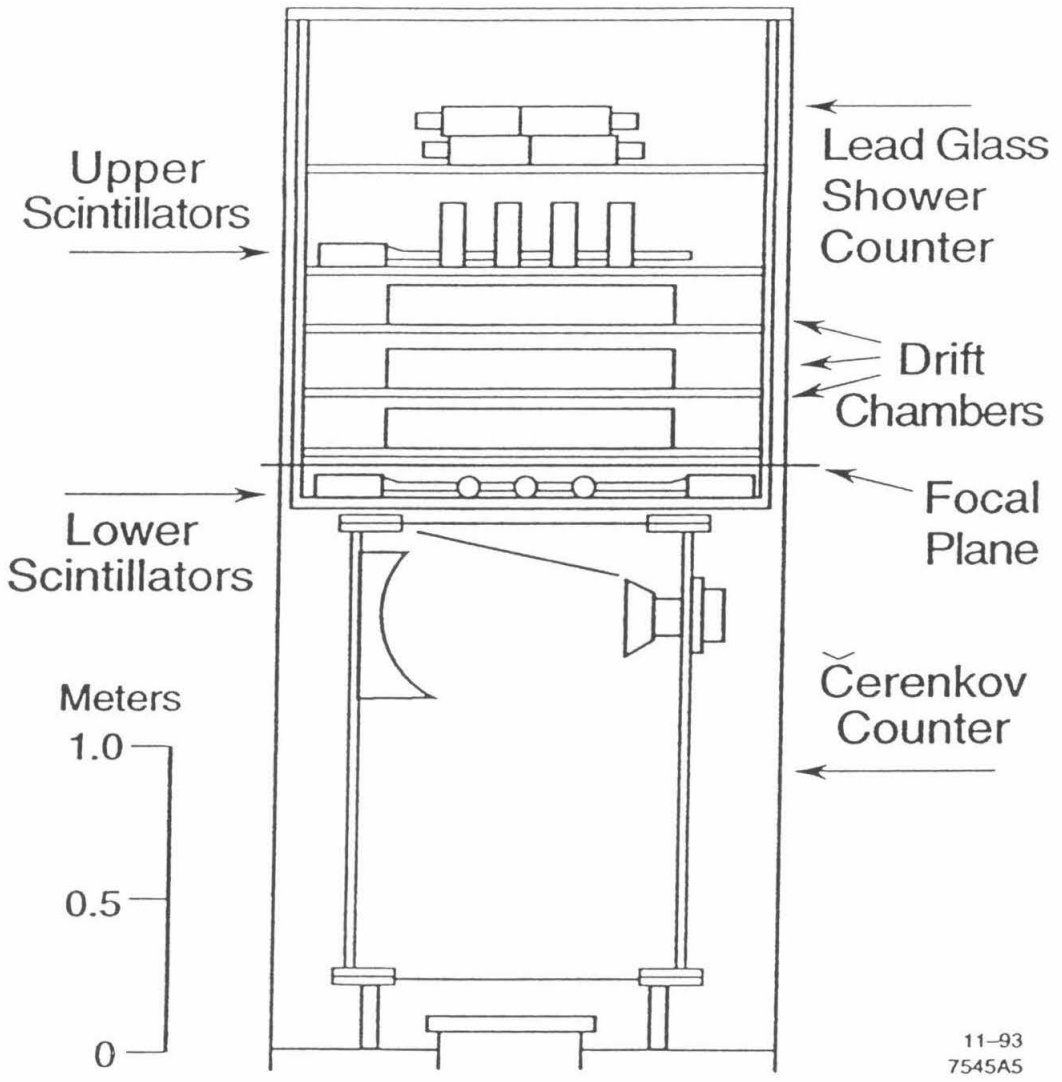

FIG. 20. Side view of 1.6 GeV/c spectrometer detector hut with Y_{16} increasing to the left. Particles are incident from the bottom. The light guides of the YU scintillators, shown bent in the figure, were straightened before the experiment (see text for a description of the detectors).

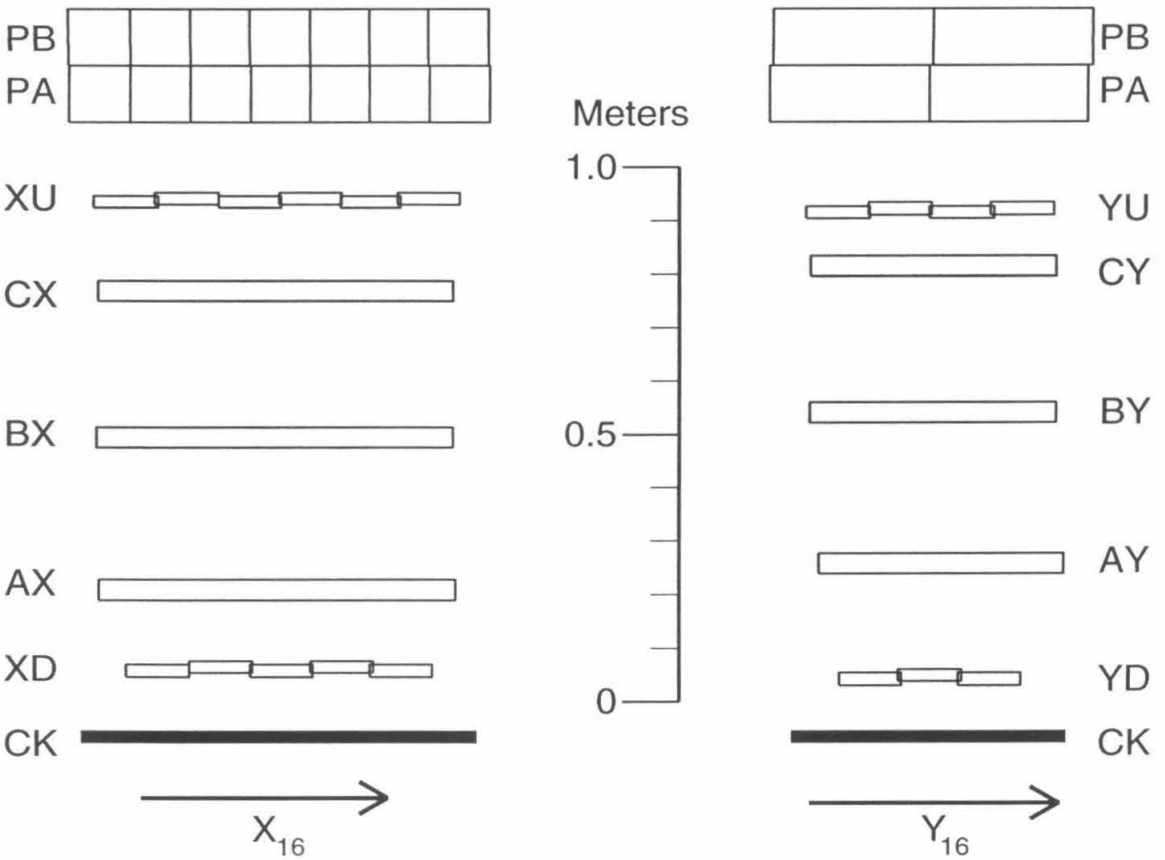

FIG. 21. **Side views of the 1.6 GeV/c detector hut showing the sizes and positions of the detectors to scale. With the exception of the lead glass shower counters, the *thicknesses* of the detectors are not to scale.**

II.C.2. 8 GeV/c Spectrometer

The 8 GeV/c is a 30° vertical bend $QQDDQ$ magnetic spectrometer (Q = Quadrupole and D = Dipole, see Figure 22). It is discussed in more detail in reference [20], which describes an experiment that took data with the 8 GeV/c spectrometer in the same configuration (see also references [32,34]). In order to increase the angular acceptance of the 8 GeV/c spectrometer, the polarities of the first two quadrupoles were reversed from the standard configuration. In this large acceptance tune, the spectrometer has a maximum momentum of 4.5 GeV/c and a factor of > 4 larger solid angle. See Figures 23 and 24 for raytrace diagrams showing the optics of the large acceptance tune.

The detector package also differed significantly from previous experiments (see Figures 25 and 26). The first detector encountered by a proton in the shielded hut was a 3.1 m long gas Čerenkov counter, which was filled with atmospheric Freon 114 ($n = 1.00140$) at the $Q^2 = 5,7\,(\mathrm{GeV/c})^2$ kinematics but evacuated at $Q^2 = 1,3\,(\mathrm{GeV/c})^2$. Intended to provide π^+ identification, it was not necessary in the analysis because the pion rate was only $\lesssim 10\%$ of the accidental coincidence rate (see Section III.A). Following the Čerenkov were the front layer of plastic scintillators (SF), ten multi-wire proportional chambers, two planes of scintillator hodoscope (NBS), and two more scintillator layers (SM, SR). The lead glass shower counter used in previous experiments was removed.

For optimal timing resolution, the scintillators were read out on both sides by PMTs (see Figure 26). The three scintillator planes were refurbished and repositioned before the current experiment. The refurbishment included the replacement of all scintillator material with new Bicron BC-420 fast scintillator material, and the replacement of the PMTs with fast (1.5 ns rise time) Amperex XP2020 phototubes from the decommissioned MARK-III detector at SLAC.

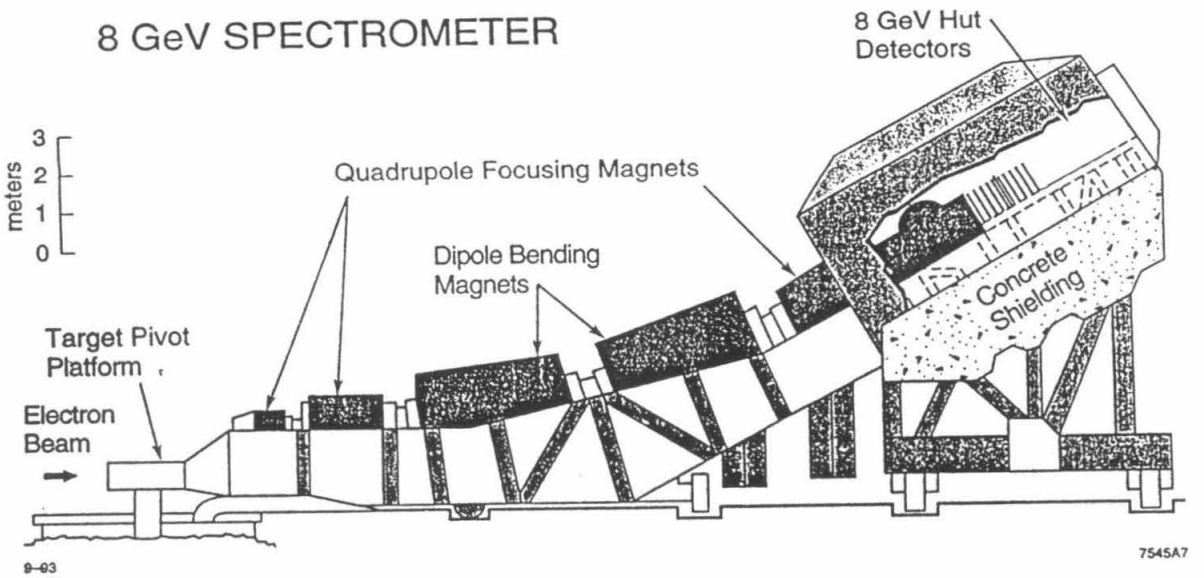

FIG. 22. **Exterior side view of 8 GeV/c spectrometer, as configured for the present experiment. The momentum analysis is provided by the two dipole magnets, with focussing provided by the three quadrupoles. The detectors are above and to the right of the exit of the dipole magnet, inside the concrete shielding hut.**

The SF plane was completely replaced. The eight new scintillators are 0.9525 cm thick, 6 cm wide, and 45 cm long. The scintillators are vertically oriented, layered along the horizontal direction with 2 mm overlap. Light guides with alternating bend directions prevent position conflicts between adjacent readout PMTs. The layer included two of the old 21.6 cm-wide SF scintillators, one on either end, to increase the acceptance for SLAC experiment E-140X, which was run just before NE-18. The SF layer was placed in a new frame and mounted in front of the wire chambers.

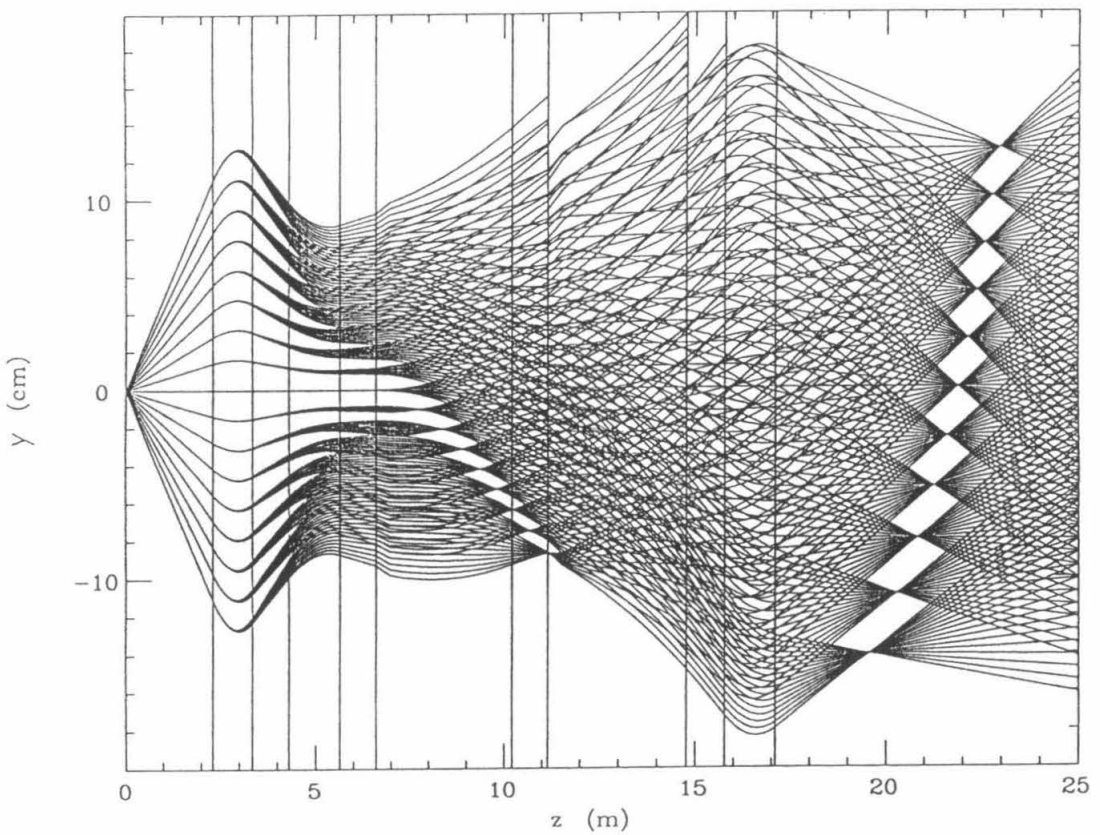

FIG. 23. **Vertical (bend) plane magnetic optics of the 8 GeV/c spectrometer's large acceptance tune. Rays are started at Φ from -48 to 48 mr in 6 mr increments (bottom through top sets of curves at $Z < 2$ m) and δ from -5% to 5% in 1% increments (bottom through top set of rays at the tilted momentum focal plane at $Z \simeq 22$ m). The rays are propagated forward using the optics model described in Section IV.G and are cut off if they intersect an aperture.**

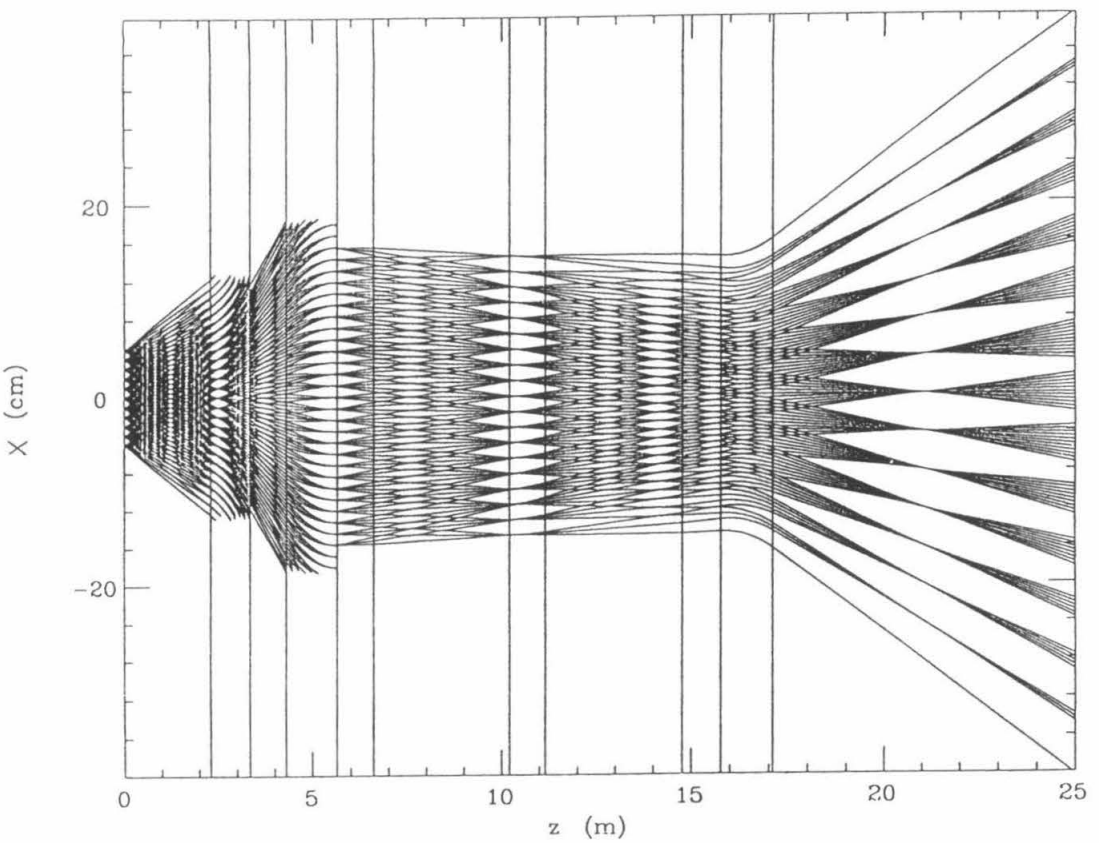

FIG. 24. **Horizontal plane magnetic optics of the 8 GeV/c spectrometer's large acceptance tune. Rays are started at** X **from** -5 **to** $5\,\mathrm{cm}$ **in** $1\,\mathrm{cm}$ **increments and** $\Theta = -28$ **to** $28\,\mathrm{mr}$ **in** $4\,\mathrm{mr}$ **increments (bottom through top set of rays at the angle focal plane at** $Z \simeq 21\,\mathrm{m}$**). See Figure 23 for details.**

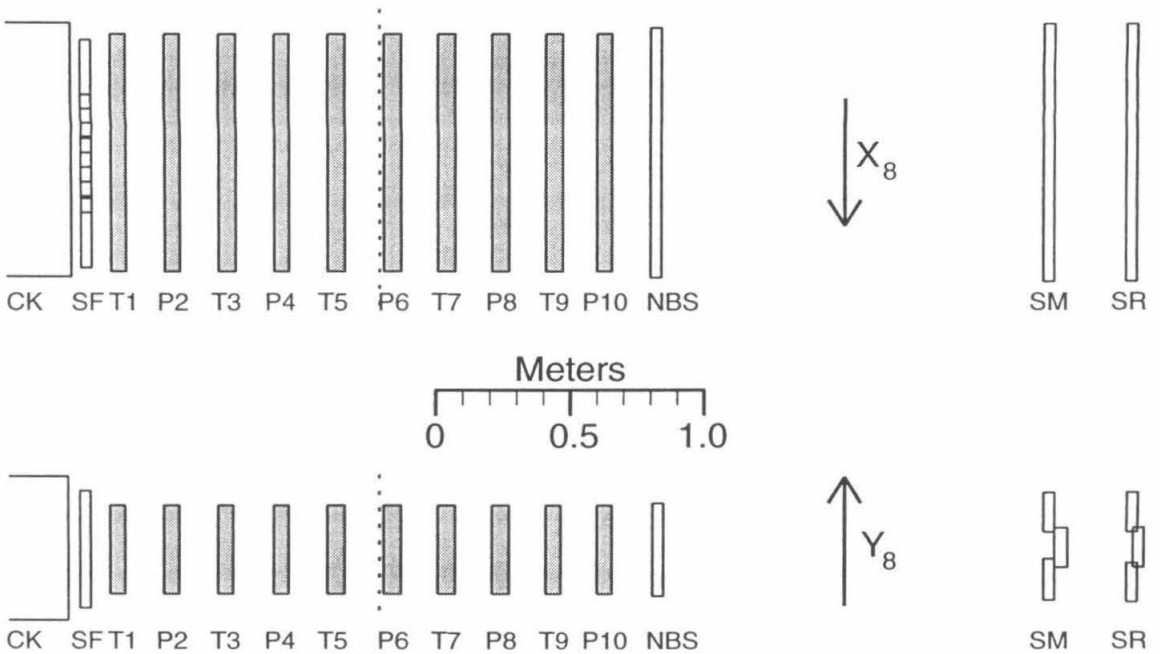

FIG. 25. **Top and side views of the 8 GeV/c spectrometer detector stack, to scale (detector thicknesses are exaggerated). The scintillator planes SF, SM, and SR were used to identify charged particles and record their time of passage. The 10 planes of multiwire proportional chamber (shown in gray) were used to measure the particles' focal plane coordinates. In the top view, Y_8 (not shown) is out of the page, and in the bottom view X_8 is out of the page. In both views, Z_8 is to the right, with $Z_8 = 0$ indicated by the dashed line (see Table 19). Protons enter from the left. Note the stack is inclined at 30° from horizontal.**

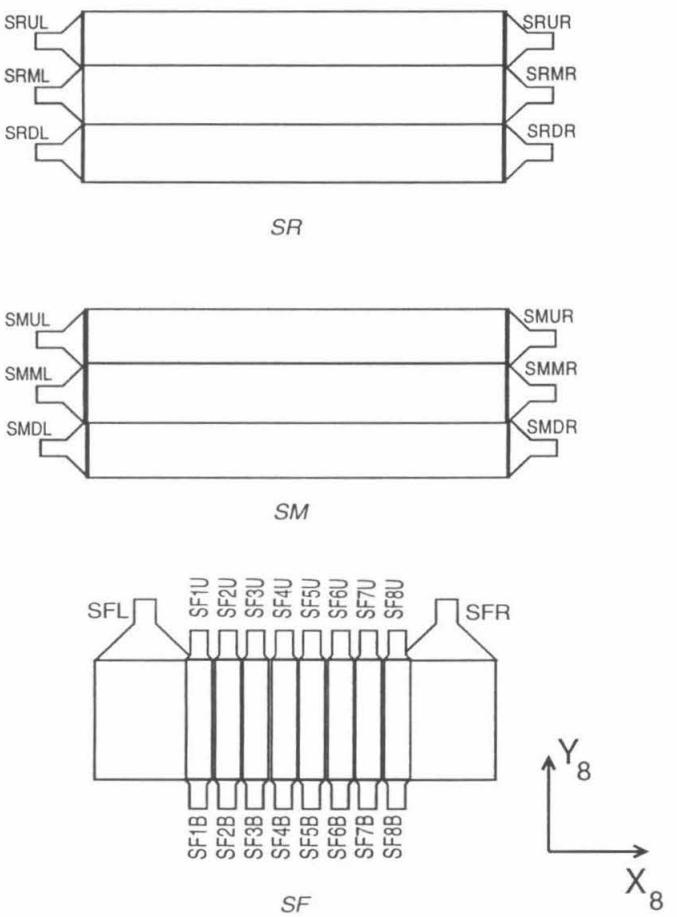

FIG. 26. **Schematic diagram of the 8 GeV/c scintillator timing planes as they would appear from the front of the detector hut, approximately to scale. The horizontal-by-vertical dimensions of the SF, SM and SR planes are** 89.1 cm × 45.0 cm, 101.6 cm × 41.6 cm **and** 101.6 cm × 42.4 cm, **respectively.**

The replacement of the scintillator material reduced the thickness of the SM and SR planes to 1.27 cm. The scintillators were 15.24 cm wide and 1.016 m long. They were oriented in the horizontal direction, with at least 1 cm overlap. The two planes were mounted at the back of the hut, separated by 29.3 cm along the central ray. The repositioning of the three scintillator planes increased the distance between the SF and SR to 386 cm. This allowed for particle identification using particle velocity from Time-of-Flight (Section III.A). As with the Čerenkov counter above, this particle identification was not necessary for the analysis.

The multiple-wire proportional chambers (MWPC's) and NBS hodoscope are essentially unchanged from SLAC experiment NE-11 [32]. The wire chambers (MWPC's) were operated in proportional mode, with the ion cascades provided by a gas mixture of 65.75% argon, 30.0% isobutane, 0.25% Freon 13B1 and 3.0% methylal. The anode wires were arrayed in planes orthogonal to the central trajectory (the Z_8 axis). The angle of the wires from the Y_8 axis, in order of increasing distance into the hut, were 90, -30, 90, 30, 90, -30, 90, 30, 90, and $-30°$ (see Figure 27). The five chambers at 90°, called the "P" chambers, had horizontally-oriented (along X_8) wires for measuring vertical track position and angles. These alternated with the "T" chambers which were used to measure the horizontal position and angle. The names P and T refer to the sensitivity of the chambers to the proton momentum p' and scattering angle (θ'_p), respectively. The wire spacing in the chambers was 2 mm, although the effective spacing in the T chambers was 4 mm because adjacent wires were electrically connected. The MWPC readout gate was 80 ns wide.

The NBS hodoscope consisted of 22 vertical and 20 horizontal scintillators, and was used to help remove tracking ambiguities. Each scintillator had a single PMT, the signals from which were fed into latches with a 15 ns gate.

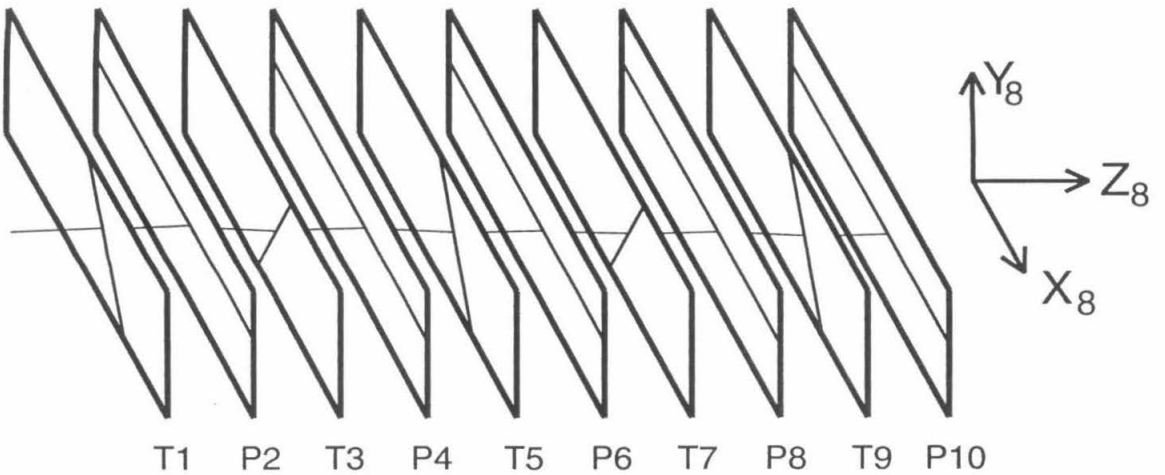

FIG. 27. **Oblique view of the 8 GeV/c wire chambers showing the alternating wire angles. The wires shown are those registering a hit during the event, and a track is shown connecting them. (The apparent variations in the track angle are artificially induced by the projection used.)**

II.D. Trigger Electronics

The detection electronics of either spectrometer signaled the presence of an event by generating a candidate trigger, called a pretrigger. Due to data-acquisition rate limitations, only one pretrigger per beam pulse was allowed to generate a trigger, leading to the read-out of the spectrometer's ADCs, TDCs, latches, scalers, and wire chamber information. If either spectrometer generated a trigger during a given beam pulse, both were read out (see Figures 28 and 30).

The NE-18 trigger electronics were designed under the assumption of a modest electron rate in the 1.6 GeV/c and a potentially large rate in the 8 GeV/c. The 1.6 GeV/c triggered on the first electron identified in a beam spill. The 8 GeV/c triggered on the first proton following a 1.6 GeV/c trigger, including true coincidences.

In the 1.6 GeV/c spectrometer (see Figure 28), two complimentary electron pretriggers were used to provide maximum efficiency. The module $\mathcal{M}_{el,low}$ required a signal in the Čerenkov, as well as at least two of the following: a) a signal in the XU or YU, b) a signal in XD or YD, c) a signal in the PA shower counter greater than a "low" threshold. The pretrigger $\mathcal{M}_{el,high}$ required signals in at least three of the four hodoscopes, a PA shower signal greater than a "high" threshold, and a total (PA + PB) shower signal greater than another threshold. The electron pretrigger $\mathcal{P}_{el}$ is the OR of these. There was also a prescaled pion pretrigger $\mathcal{P}_{\pi,pre}$ used to measure the π^- background. Both spectrometers shared the random pretrigger $\mathcal{P}_{ran}$, which was generated periodically to allow the determination of ADC pedestal values in both spectrometers. With the exception of adjustments and recalibrations, the 1.6 GeV/c trigger and readout electronics were essentially unchanged since NE-11.

In the 8 GeV/c (see Figures 29 and 30) the passage of a charged particle is marked by the firing of the proton module, $\mathcal{M}_{prot}$, a 3-way coincidence between the three scintillator planes (SF, SM, SR). Candidate coincidence events are identified by the pretrigger $\mathcal{P}_{coin}$, which resulted when $\mathcal{M}_{prot}$, occurred during a 100 ns gate opened by the 1.6 GeV/c $\mathcal{P}_{el}$ pretrigger (see Section III.D for more detail). The pretrigger $\mathcal{P}_{longcoin}$ was similar except with a 3.1 μs gate. The purpose of this pretrigger was to record any 8 GeV/c $\mathcal{M}_{prot}$ single that followed a 1.6 GeV/c singles trigger in the same beam gate.

The module $\mathcal{M}_{2/3}$ fired when at least 2 of SF, SM, SR had signals. This was ANDed with the beam gate, prescaled by a factor $\epsilon_{pre} = 2^{-8} - 2^{-10}$, to create the pretrigger $\mathcal{P}_{2/3,pre}$. The prescaling was necessary so that the high $\mathcal{M}_{2/3}$ rate (up to 8 per spill) did not create a high computer dead-time. For the data on the hydrogen targets the $\mathcal{M}_{2/3}$ rate was lower and $\epsilon_{pre} = 1$ was used. The $\mathcal{P}_{2/3,pre}$ events were used to determine the efficiencies of the scintillator planes.

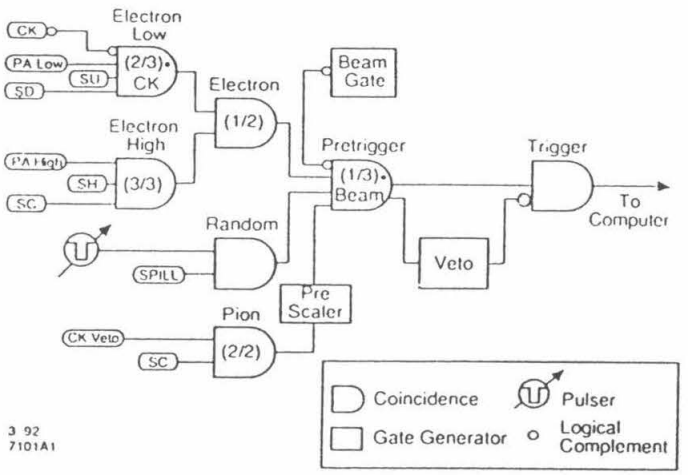

FIG. 28. **The formation of the 1.6 GeV/c trigger. The labelled inputs are: "CK" = discriminator on Čerenkov signal, "PA Low", "PA High" = discriminators (with different thresholds) on analog sum of PA signals, "SU" = logic sum of XU and YU discriminators, "SD" = logic sum of XD and YD discriminators, "SC" = logic sum of XU, YU, XD, and YD discriminators, "SH" = discriminator on analog sum of PA and PB signals. "SPILL" = beam gate, and "CK Veto" = not CK. The beam gate is included as a veto to the trigger module to prevent triggers in between beam gates.**

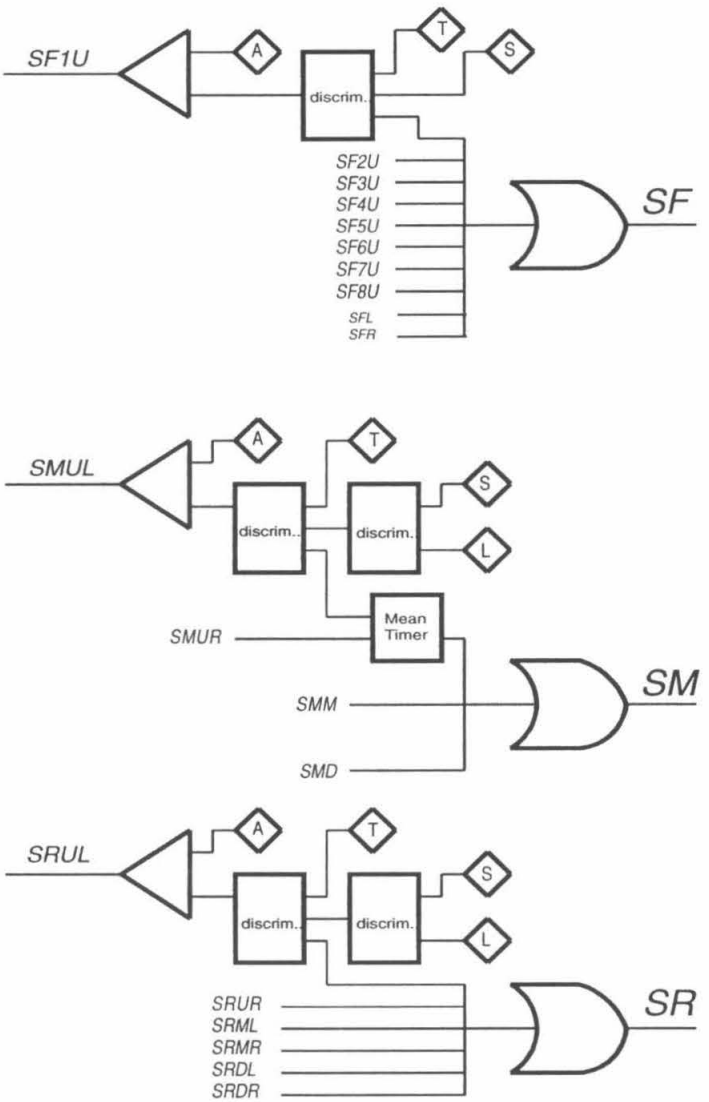

FIG. 29. **The 8 GeV/c SF, SM, and SR signal electronics. The full electronics diagram is displayed for only one PMT in each scintillator plane. Only the upper SF detectors contributed to the SF summed signal. For our purposes, the mean timers in the SM electronics can effectively be treated as an AND gate (2/2 coincidence module).**

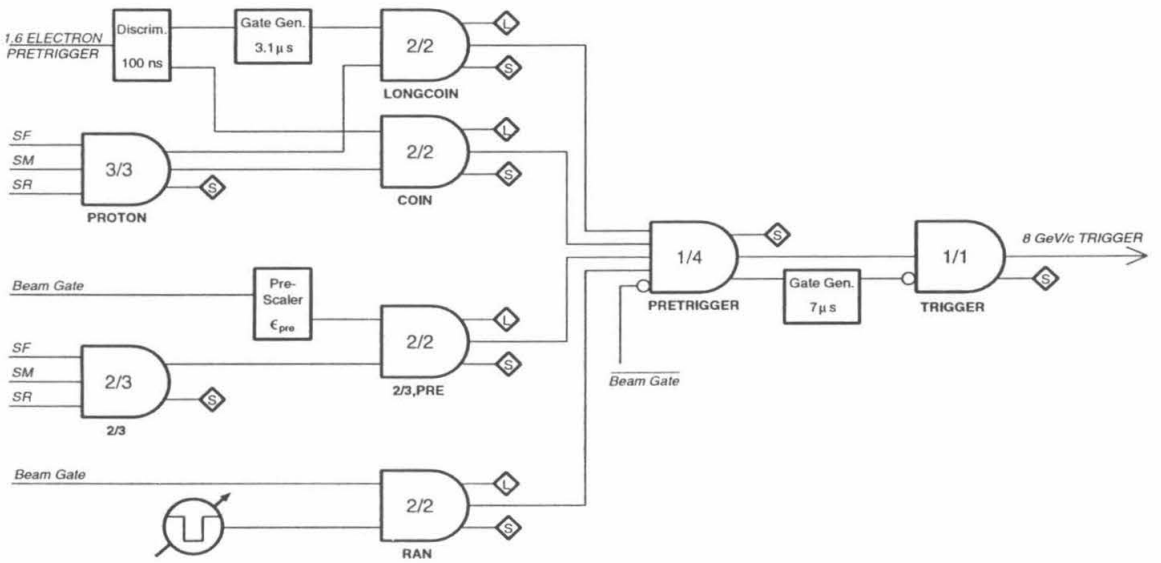

FIG. 30. 8 GeV/c trigger electronics. The formation of the pretriggers is described in the text. The 7 μs-wide gate generator into the trigger veto input allows only the first pretrigger in an event to cause a trigger. The trigger signal is fanned out to a scaler, TDC starts, ADC gates (30–90 ns wide), latch gates (5–80 ns wide), the MWPC readout gate (80 ns wide), the computer interrupt, and the 1.6 GeV/c coincidence TDC.

III. ANALYSIS

III.A. Particle Identification

As discussed in Section III.D, the subtraction of accidentals ensures that the measured coincidence rate includes only electron-proton events. Thus no further particle identification is strictly necessary. However, rejection of contamination by other particle types, especially in the 1.6 GeV/c spectrometer, can reduce the size of the accidental subtraction and of the statistical errors in the measured $S(E_m, p_m)$ and T.

The π^- rate in the 1.6 GeV/c spectrometer was up to 500 times the e^- rate. Rejection of events with a Čerenkov ADC value below channel 60 reduced the π^- contamination by a factor of ~ 300. The e^- efficiency of this cut was measured to be $99.93 \pm 0.03\%$, using electrons identified with a tight cut on the shower counter.

In the runs with high $\pi : e$ ratio, most extra tracks in the 1.6 GeV/c spectrometer were due to pions. In events with multiple tracks and an electromagnetic shower detected in the lead glass array, the track associated with the shower was chosen (see Section III.B). Events were not rejected if there was no electromagnetic shower, however, because of the highly variable e^- inefficiency (1% – 5%). Some of the reasons for the high e^- inefficiency were variable gain in the PMT of one of the counters (PA4) and an ADC malfunction similar to that of the 1.6 GeV/c scintillator ADCs described in Appendix D.3. The two layers of the shower counter were offset to reduce the alignment of the cracks, but electrons passing in between counters in the first layer (PA) experienced enhanced shower leakage in the second (PB). The cause of the PA4 variable gain was not identified. The ADC malfunction was characterized by the appearance of the same large value in all of the channels of the 3 ADC modules measuring the shower counter signals. As in the case of the scintillator PMT malfunction, it is thought that these events were caused by problems with the gate input signal.

The 8 GeV/c PROTON module provided minimal particle identification since an SF-SM-SR 3-way scintillator coincidence would fire on any charged particle in the 8 GeV/c spectrometer hut. Tests with additional particle identification by TOF measurements of the velocity in the hut (at $Q^2 = 1,3\,(\mathrm{GeV/c})^2$) and with the Freon gas Čerenkov detector (at $Q^2 = 5,7\,(\mathrm{GeV/c})^2$) demonstrated that the non-proton contamination was always small. (In the Čerenkov counter, a signal indicated the passage of a pion, while there would be no signal for a proton.) Thus, no further particle identification was used in the analysis of the 8 GeV/c data.

III.B. Track Identification

The drift chamber and wire chamber information in the 1.6 GeV/c and 8 GeV/c spectrometers, respectively, are used to measure the positions and angles of the detected particles at the focal plane. The identification and selection of the particle tracks are performed by modified versions of the existing 1.6 GeV/c and 8 GeV/c tracking software.

The 1.6 GeV/c tracking software begins by identifying which wires recorded hits during the readout gate. When a pair of adjacent wires fired and had consistent drift time information, the drift times are used to infer the position of the track. For an unpaired wire, the position of the wire is used. The number of unpaired wires was as high as 30–40% in some runs. For a pair with inconsistent drift times, the position is chosen randomly between them. The software then generates candidate tracks by grouping nearly-colinear hit positions in the three chambers. The focal plane coordinates of the tracks are given by linear regression. Because the X and Y wire planes are orthogonal, this procedure results in separate, uncoupled tracks in both directions (see Figure 31). In events with multiple tracks, deciding which X track is associated with a given Y track is the task of the track purging software. The purging software is also responsible for identifying and discarding spurious tracks, based on the information provided by the other detectors (see Appendix B for details).

The 8 GeV/c tracking software works on similar principles. In this case, there is no drift time information, and the hit position is given by the centroid of adjacent wires that fired during the 80 ns readout gate. (In the P chambers the hit locations are randomized to $\pm 1/2$ wire spacing at no cost to the resolution. This is done to prevent the otherwise discrete nature of the possible track angles from causing spikes in the dY_8 and Φ_8 spectra. Such spikes would make the cross section sensitive to small changes in the value of the Φ_8 cut used in the analysis.) If a sequence of more

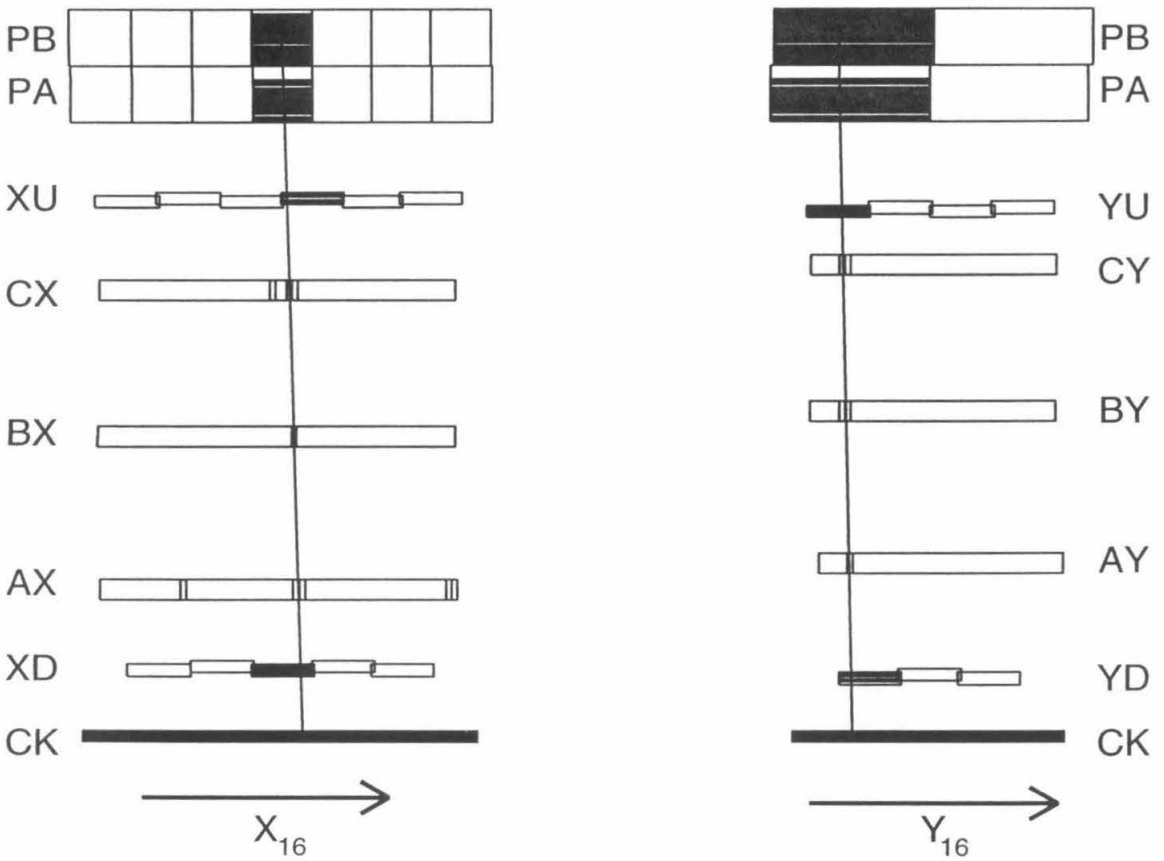

FIG. 31. Typical track in the 1.6 GeV/c spectrometer. Detectors with signals are colored in. The thin rectangles in the drift chambers indicate hit positions of the particle track. Note the presence in the X chambers of hits not associated with the particle track. These mark the positions of dead or hot wires.

than two adjacent wires fired in a given chamber, the position used is given by the pair with the best χ^2 for the track. The software identifies candidate tracks in the P chambers first, and then identifies the associated tracks in the T chambers. Because the different T chambers had different wire angles (see Figure 27), hit positions are all converted into X_8 values through the use of the P tracks (see Figure 32). In most cases P and T tracks from different particles are inconsistent, so the ambiguity in matching P and T tracks was much smaller than in matching X and Y tracks in the 1.6 GeV/c. The combined P and T track is required to include hits in ≥ 3 P chambers and ≥ 3 T chambers, for a total of ≥ 7 hits. If no tracks are found, this condition is relaxed to ≥ 2 T, ≥ 2 P, and ≥ 6 total. The purging software is similar to that used for the 1.6 GeV/c, and is detailed in Appendix B.

A tracking efficiency correction for each spectrometer accounts for inefficiencies in the chambers and in the tracking routine. For events with no final track in a given spectrometer, the correction is determined by measuring the area of the coincidence peak in the trigger time difference TDC (because tracking information is used to calculate the timing corrections, Δt_{p-e} cannot be calculated for these events). The resulting values were 1.01–1.03 in the 1.6 GeV/c spectrometer and 1.00 in the 8 GeV/c spectrometer, with errors of ± 0.01 (see Tables 10 and 10).

The final three purges in either spectrometer are used to choose the final track when more than one track survives the other purges. In either spectrometer, this is usually necessary in $\lesssim 1\%$ of the events, although there are runs where it is necessary for up to $\sim 10\%$ of the events. It is expected that most of these cases the software either chooses the correct track or a track with (E_m, p_m) within the range $\mathcal{R}$ used to measure the transparency. Rather than estimate a correction factor for these events, we include an extra systematic error of 1% for each spectrometer.

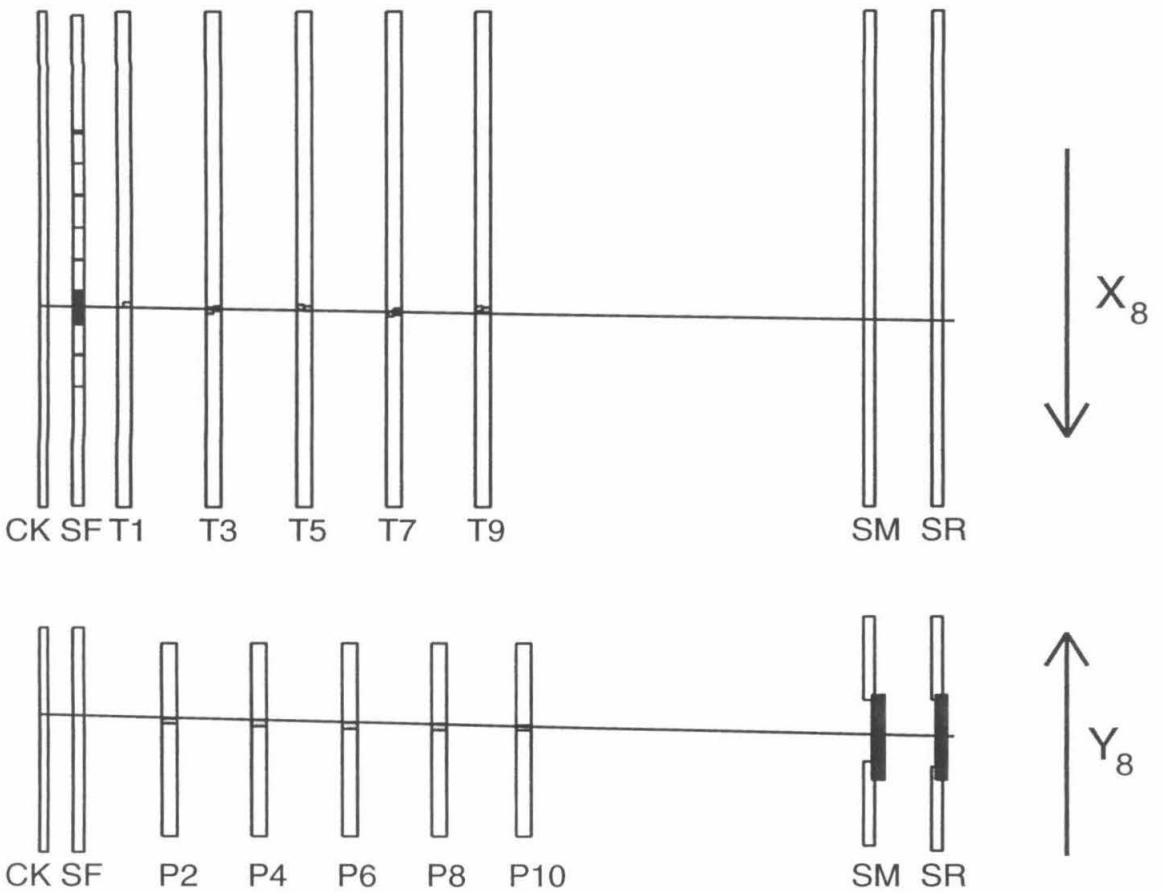

FIG. 32. **Typical track in the 8 GeV/c spectrometer. Overhead and side view of the 8 GeV/c detector hut, with a compressed Z_8 scale to exaggerate the track angle (compare with Figure 25). Positions of track hits are shown in gray.**

III.C. 3-Momentum Reconstruction

The track focal plane coordinates measured in each spectrometer are converted into 3-momentum at the target by using a third-order matrix model of the spectrometer's magnetic optics. The matrix model was derived using the measured correlations between the momenta and angles in the ^{1}H(e,e'), ^{1}H$(e,e'p)$, and ^{2}H$(e,e'p)$ reactions. The behavior of the optics at the edge of the acceptance was constrained with data taken at momenta or angles away from the nominal values. The resulting optics model agreed reasonably well with those derived from a fit to a Transport [35] model of the spectrometers (see Section IV.G).

In each spectrometer, the momenta are reconstructed using a third-order matrix that maps from the position and angle of a particle track in the hut to the initial 3-momentum at the target. Usually this matrix (or a second-order version) is given by fitting to rays generated with the forward Transport model of the spectrometer (see Section IV.G). For this experiment, however, the matrix elements were inferred solely from the kinematic correlations seen in ^{1}H(e,e') and $A(e,e'p)$ data. These were then compared with the Transport-based matrix as a consistency check.

Although some of the correlations were fitted using Minuit, most were fit by eye in order to discount the false correlations and centroid values caused by the radiative tail, the spread in beam energy, and multiple scattering. These effects were the principle sources of uncertainty in the determination of the matrix elements. For example, the radiative tail contributes differently in p_m, E_m, and W^2 (the invariant mass, squared) spectra, and the fitted peak position depends on how close to the elastic value the data are cut. In some ^{1}H$(e,e'p)$ spectra the effect of the beam energy spread on the correlations in one spectrometer was removed by inferring the beam energy with the other.

The ^{1}H$(e,e'p)$ data provided strong constraints on the matrix elements because

the measured centroids for E_m and p_m should be 0 exactly, and should also have no correlations with any hut quantity. Additional constraints were obtained from the ^{2}H$(e,e'p)$ data, where E_m should reconstruct to the deuteron binding energy (2.2 MeV). Finally, it is worth noting that the determination of most of these matrix elements was performed iteratively, to ensure that any matrix element changes did not destroy good agreement for earlier-determined elements.

The first step was optimizing the matrix elements used to measure Z_{targ}, since this could be done without knowing any other matrix elements. (See Tables 18 and 19 for the coordinate systems used.) This was accomplished using singles data taken on the 15 cm dummy cell, which consists of two aluminum targets with known positions and separations. The matrix elements were adjusted to generate two peaks at the correct positions with the best resolution (roughly 4 cm in both spectrometers, depending on the angle).

Next, the Φ matrix elements were determined to an estimated uncertainty of 5 mr. The Φ_{16} acceptance is limited to $\pm$46.3 mr by slits placed in front of the 1.6 GeV/c dipole. The angular magnification $(\Phi|X)_{16}$ was chosen to reproduce this width. The Φ_8 matrix elements were adjusted to produce $p_{m,y} = 0$ for ^{1}H$(e,e'p)$ scattering. (Here $p_{m,y}$ is the out-of-plane component of $\mathbf{p}_m$.) The Φ matrix elements in both spectrometers were then adjusted to ensure that $p_{m,y} = 0$, independent of the measured values of Φ_{16}, Φ_8.

The dispersive (δ) matrix elements were then determined to an uncertainty of about 0.2%. The first constraint was that the measured E_m in ^{1}H$(e,e'p)$ and ^{2}H$(e,e'p)$ should be 0 and 2.2 MeV, independent of any focal plane coordinate. The 3-momenta of the electron and proton are directly (ignoring radiation) correlated in ^{1}H$(e,e'p)$. Thus, for example, an E_m–$dX_{8,16}$ correlation may be caused by either a $(\delta|dX\ldots)_{16}$ matrix element (where "..." can be anything) or a $(\delta|dX\ldots)_8$ matrix element. The ambiguity is resolved through the use of ^{2}H$(e,e'p)$, which has a much weaker kine-

matic correlation between the electron and proton (*i.e.*, $|p_m| > 0$ is allowed). The δ matrix elements were also constrained through the use of ^{1}H(e,e') and ^{1}H$(e,e'p)$ data taken at non-central momenta, by ensuring that the position of the elastic stripes changed accordingly. For these data, we assume that the spectrometer magnet field configuration is linear with the NMR reading (to better than 0.1%).

Finally, the scattering angle $\Delta\Theta$ is determined using ^{1}H$(e,e'p)$ data where the angle of each spectrometer was stepped in both directions from its central value. (Here "central" refers to the standard kinematics, where ^{1}H$(e,e'p)$ events arrive at the center of both spectrometers.) For these data, the elastic stripes should be in the correct location (for the electron, this is $W^2 = M_p^2$), independent of the focal plane coordinates. The measured $\Delta\Theta_{16}$ and $\Delta\Theta_8$ were further constrained by ensuring that $p_m = 0$ in all of the ^{1}H$(e,e'p)$ data. The estimated uncertainty in the scattering angles is less than 2 mr.

Although the spectrometer magnets were run through a "de-gaussing" cycle whenever their strength was lowered, there were still $\sim 0.1\%$ history-dependent variations in the magnetic field strengths. Hence it was necessary at each Q^2 to use ^{1}H$(e,e'p)$ and ^{2}H$(e,e'p)$ to re-determine the "offset" matrix elements to remove the effects of these variations on the measurement of E_m and p_m. The offset matrix elements are those—namely $(\delta|1)$, $(\Delta\Theta|1)$, and $(\Phi|1)$—which do not depend on the focal plane coordinates.

III.D. Coincidence Identification

The pretrigger $\mathcal{P}_{coin}$ resulted when an 8 GeV/c proton $\mathcal{M}_{prot}$ occurred during a 100 ns coincidence gate opened by the 1.6 GeV/c electron pretrigger $\mathcal{P}_{el}$. The time difference Δt_{8-16} between the two spectrometers' triggers was measured by the 8 GeV/c coincidence TDC. This is converted into a time difference Δt_{p-e} between the electron and proton at the target by removing the effects of path length through the spectrometer and scintillator response time (see Figure 33). The path length corrections are made using the Transport model, adjusted to produce the best resolution. The scintillator response times are determined using measurements of the Time-of-Flight between scintillators for particles of known velocity. The calculation of Δt_{p-e} is detailed in Appendix D. Figure 33, which shows the uncorrected and corrected time differences for one of the worst cases cases, illustrates the utility of this approach.

The FWHM of the coincidence peak was $\sim$ 0.6 ns (see, for example, Figure 34). The true to accidental ratio is typically $\geq$ 10:1, but at one kinematics is as bad as 1:1. The rate of true coincidences is determined by subtracting the rate of accidentals (measured away from the coincidence peak) from the rate within $\pm$2 ns of the coincidence peak, and then correcting for true coincidences outside this 4 ns window.

For the measurement of transparency, we need the number of true coincidences N_{true} in a range $\mathcal{R}$ of (E_m, p_m) (see Figure 35). Let N_{peak} be the number of counts in $\mathcal{R}$ with $|\Delta t_{p-e}| < \Delta t_{peak}/2$, where $\Delta t_{peak} = 4$ ns is the width of the coincidence window. The number of true coincidences is given by subtracting the inferred number of accidentals under the peak:

$$N_{true} = N_{peak} - \frac{\Delta t_{peak} N^{\mathcal{F}}_{win} N_{acc}}{\Delta t_{win} N^{\mathcal{F}}_{acc}}. \tag{3.1}$$

For improved determination of the accidental subtraction, the number of accidentals under the peak is deduced from a large window -20 ns $< \Delta t_{p-e} < -6$ ns (of width $\Delta t_{win} = 14$ ns) where the accidental background is flat.

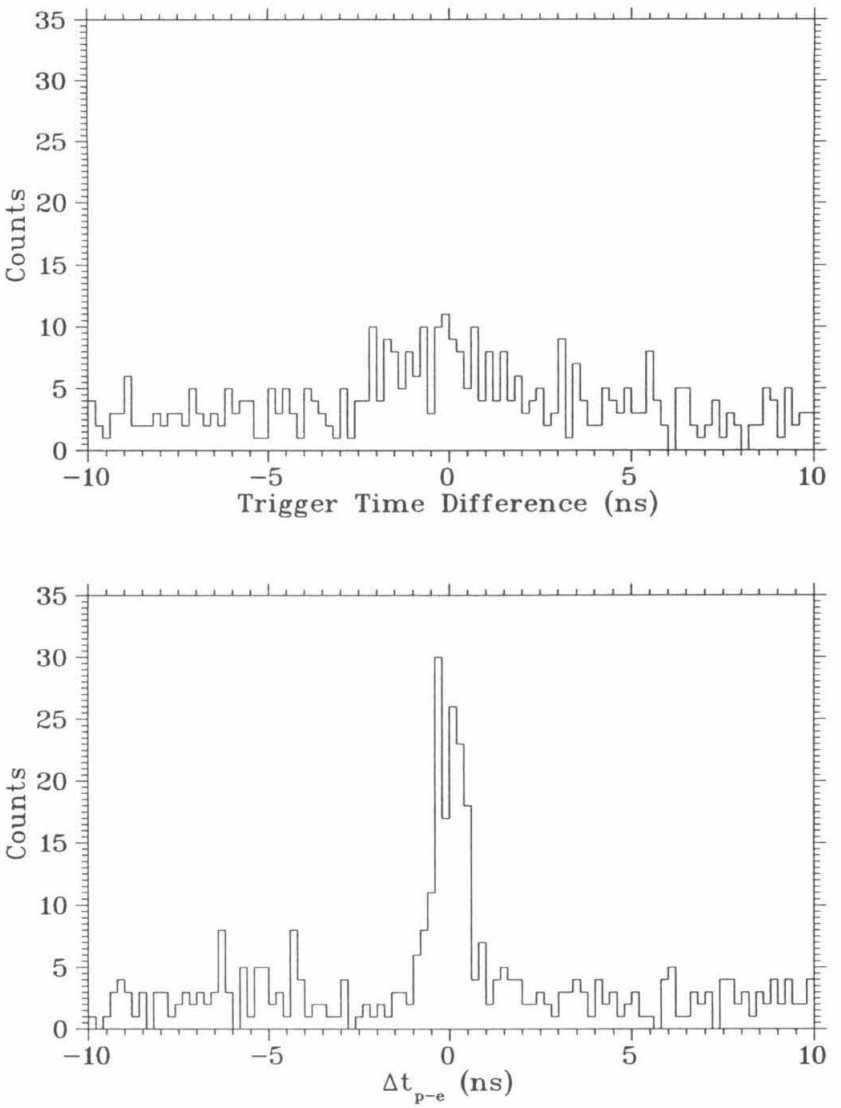

FIG. 33. **Coincidence time for ^{197}Au at $Q^2 = 7\,(\mathrm{GeV/c})^2$ before (top) and after (bottom) corrections for flight path and scintillator response times.**

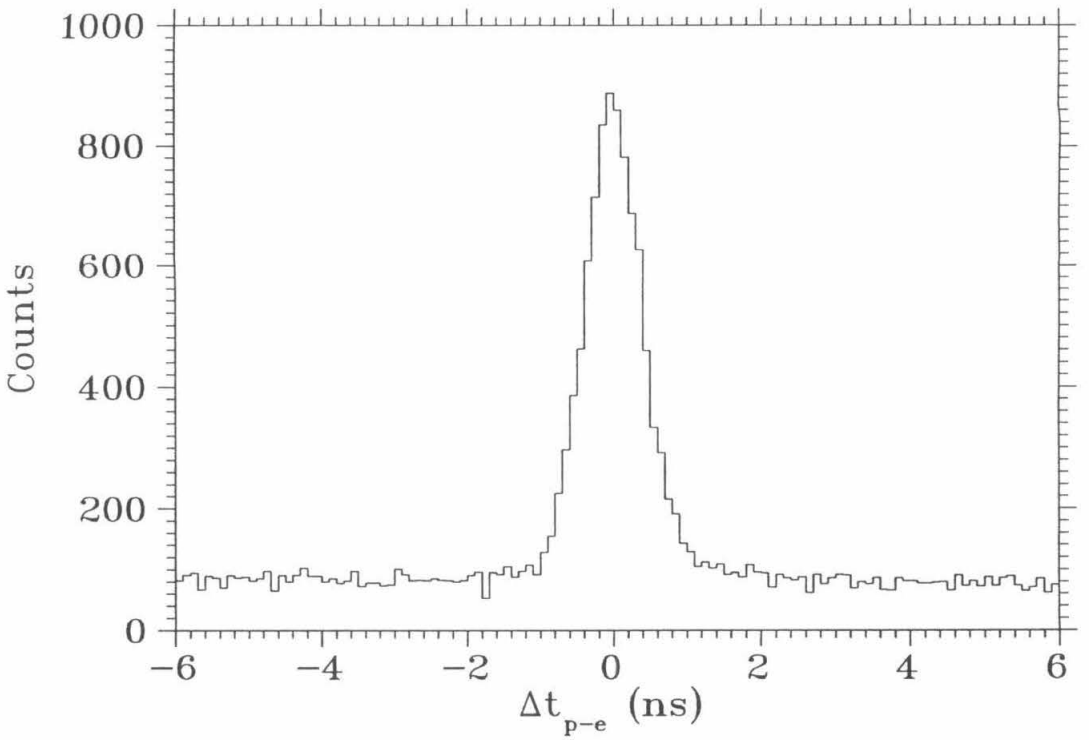

FIG. 34. Δt_{p-e} **for** ^{12}**C at** $Q^2 = 1\,(\mathrm{GeV/c})^2$

The number of counts in the Δt_{win} window and the range $\mathcal{R}$ can be small (especially in the spectral function measurement described in Section V.A). The determination of the background subtraction is improved by using the number of counts $N^{\mathcal{F}}_{win}$ in the "full" (E_m, p_m) range $\mathcal{F}$ ($-100 < E_m < 220\,\mathrm{MeV}$ and $|p_m| < 320\,\mathrm{MeV/c}$), and then multiplying by the fraction $N_{acc}/N^{\mathcal{F}}_{acc}$ of these that should be in $\mathcal{R}$. For best accuracy, $N_{acc}/N^{\mathcal{F}}_{acc}$ is determined using almost the entire Δt_{p-e} accidental range (see Figure 36). Specifically, $N^{\mathcal{F}}_{acc}$ is the number of accidentals in $\mathcal{F}$ with $|\Delta t_{p-e}| > 5\,\mathrm{ns}$, and N_{acc} is the number of these inside $\mathcal{R}$. Thus there should be $N^{\mathcal{F}}_{win} N_{acc}/N^{\mathcal{F}}_{acc}$ accidentals in the range $\mathcal{R}$ in the accidental timing window Δt_{win}. This value, multiplied by $\Delta t_{peak}/\Delta t_{win}$, is the estimated number of accidentals in the coincidence window Δt_{peak} (see Equation 3.1). When calculating the error in the background subtraction,

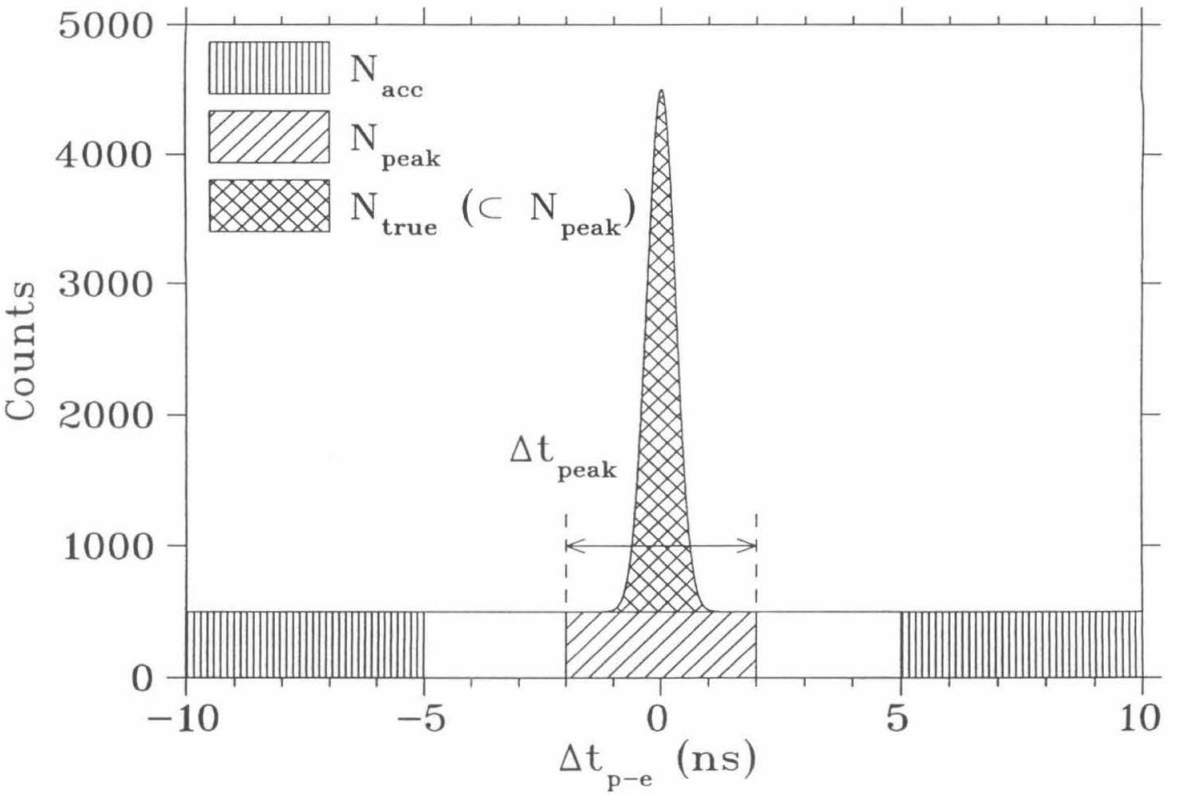

FIG. 35. **Histogram of Δt_{p-e} for $(E_m, p_m) \in \mathcal{R}$**

the correct binomial error in $N_{acc}/N_{acc}^{\mathcal{F}}$ must be used when $\mathcal{R} \sim \mathcal{F}$ because then $N_{acc}^{\mathcal{F}} \sim N_{acc}$.

A coincidence identification efficiency correction of 1.015 ± 0.010 (1.000 ± 0.010 for the ^{1}H target) is applied to correct for true coincidences outside of the Δt_{peak} timing window. This is measured using a $\Delta t_{peak} = 8$ ns window, and verified by comparison with the number of coincidences calculated from the 8 GeV/c trigger time difference TDC. The efficiency includes a correction for the small number of true coincidences in the underflow channel of the 8 GeV/c coincidence TDC, as described in Appendix D

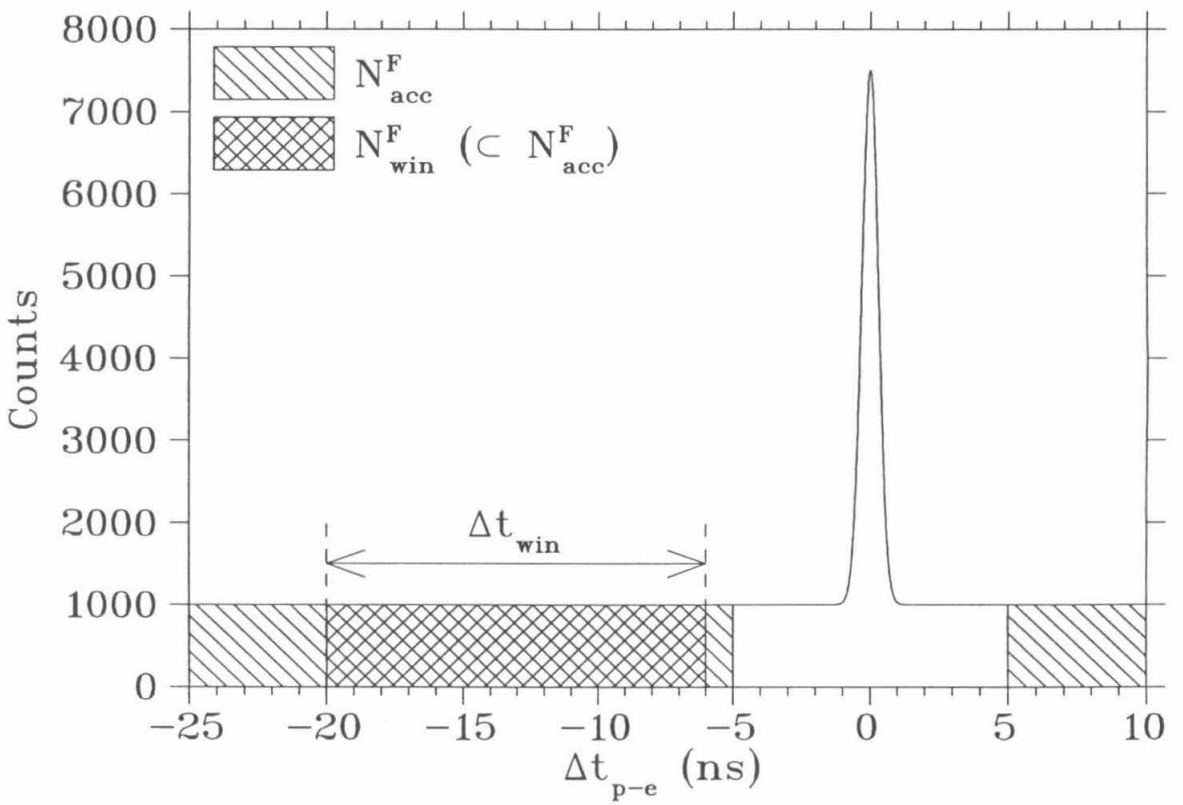

FIG. 36. **Histogram of Δt_{p-e} for $(E_m, p_m) \in \mathcal{F}$**

III.E. Reconstruction of E_m and p_m

The E, E', and p' measured in the experiment are affected by ionization energy loss and Coulomb acceleration. The PWIA calculation also simulates these effects on an event-by-event basis (see Section IV.A). The measured and PWIA values are corrected for the typical magnitude of these effects in order to improve the resolution of the measurement of E_m and p_m. Any bias introduced by the use of typical values is common to the data and the PWIA calculation, and so does not effect the measured transparency. The effects of energy loss and Coulomb acceleration are *added* to E and *subtracted* from E' and p' to obtain the correct values at the time of the scattering. The energy loss is calculated using the measured angles and assuming the interaction occurred at the center of the target. The correction for the Coulomb acceleration is the average Coulomb potential energy inside the nucleus (modelled as a uniform sphere of charge).

III.E.1. Ionization Energy Loss

The energy loss is calculated using the material thicknesses given in Tables 3 and 4. In cases of non-normal incidence, thicknesses are increased by the appropriate geometrical factors calculated using the measured angles and assuming the interaction occurred at the center of the target. Ionization energy loss in each material is modelled by the most probable value [36,37]:

$$\Delta E_{mp} = \left(0.15354 \frac{\text{MeV-cm}^2}{\text{g}}\right) \frac{Zt}{A\beta^2} \left[\ln\left(\frac{m_e c^2}{I^2}\right) + 2\ln\left(\frac{P}{m_e c}\right) + \ln\left(\frac{At}{\beta^2}\right) - \beta^2 - \delta\right], \tag{3.2}$$

where Z, A, and t are the charge, mass number, and thickness (length times density ρ) of the traversed material and βc is the speed of the traversing particle. The ionization constant $I = 21.8$ eV for the liquid ^{1}H and ^{2}H targets and 166 eV for Al

windows. For other elements, we use $I = 16Z^{0.9}$ eV [38]. We neglect the density effect δ for protons. For the highly-relativistic electrons, inserting the asymptotic form of δ reduces Equation 3.2 to [36]:

$$\Delta E_{mp} = \left(0.15354 \frac{\text{MeV-cm}^2}{\text{g}}\right) \frac{Zt}{A} \left[19.2551 + \ln\left(\frac{t}{\rho}\right)\right]. \tag{3.3}$$

The width $\xi = (0.15354\,\text{MeV-cm}^2/\text{g})(Zt/A\beta^2)$ [36] of the Landau tail in each arm is less than 0.2 MeV for all kinematics, so use of the most probable value is quite accurate. (Ideally, the average energy loss should be used instead of the most probable value. The difference is negligible because of the small width ξ.) The energy loss in each arm is $\Delta E_{mp} \lesssim 3.5\,MeV$.

III.E.2. Coulomb Acceleration

The Coulomb attraction of the nucleus accelerates the electron before scattering and decelerates it after scattering. The change in energy of the electron is given by the addition or subtraction of the Coulomb potential energy $V_C(r)$ of the recoil nucleus, modeled as a uniform sphere of radius R_0 (given in Table 5). Using an energy scale with $V_C(r) = 0$ at $r = \infty$, the potential energy inside the nucleus (at $r < R_0$) is,

$$V_C(r) = -\frac{(Z-1)e^2}{4\pi\epsilon_0 R_0}\left(\frac{3}{2} - \frac{r^2}{2R_0^2}\right), \tag{3.4}$$

where e is the electron charge. The contribution of the struck proton to the potential energy is ignored, with negligible error. Note that electron screening is also negligible: inside the nucleus, the Coulomb potential energy of the electron cloud is less than 10^{-4} that of the nucleus. No correction is applied in the $Z = 1$ nuclei ^{1}H and ^{2}H.

Inserting $< r^2 > = 3R_0^2/5$ for the uniform sphere, one finds the average Coulomb potential energy:

$$< V_C(r) > = -\frac{6}{5}\frac{(Z-1)e^2}{4\pi\epsilon_0 R_0} = -\frac{6}{5}\frac{(Z-1)\alpha\hbar c}{R_0}. \tag{3.5}$$

TABLE 5. Equivalent uniform nuclear radius R_0 from elastic electron-nucleus charge distributions [39], the average Coulomb acceleration from Equation 3.5, and the fractional effect of the Coulomb acceleration on the elastic electron-proton Born cross section at the $Q^2 = 1\,(\mathrm{GeV/c})^2$ kinematics.

A	R_0 (fm)	$<V_C(r)>$ (MeV)	$\Delta\sigma/\sigma$
^{12}C	3.23	0.3	-0.0008
^{56}Fe	4.85	8.9	-0.0233
^{197}Au	6.88	19.6	-0.0505

The resulting values, which are used for the correction to the scattering kinematics, are listed in Table 5. The table also lists the effect of the acceleration of the incoming electron on the scattering cross section for the $Q^2 = 1\,(\mathrm{GeV/c})^2$ solid target kinematics. The effect becomes smaller as Q^2 increases, and is approximately half as large at $Q^2 = 7$. The effect is relevant because the corrected kinematics are used to calculate the off-shell cross section σ_{ep} when weighting the data (see Equation 5.3).

III.F. Kinematic Settings

The kinematic settings are listed in Table 6. For the nuclear targets, data were taken at near-elastic kinematics, with energies adjusted to allow for the binding energy of the proton in the nucleus. For a fixed $\mathbf{q}$ and $|p_m|$ less than the Fermi momentum p_f, the protons scatter into a cone of opening angle $\sim 2\arctan(p_f/q)$ (see Equation 3.7, below). The coverage of $\mathbf{p}_m$ was achieved in nearly perpendicular kinematics, by setting the central $p' = q$ and varying the angle of the 8 GeV/c spectrometer. At higher Q^2 the proton cone becomes smaller and fewer angle settings are needed.

To maximize the cross section (by minimizing θ_{16}) for a given Q^2, the central 1.6 GeV/c momentum E' was chosen close to its maximum value of 1.5 GeV/c. For the $Q^2 \simeq 1\,(\mathrm{GeV/c})^2$ data, a lower value (~ 1.4) was used to satisfy the constraint $\theta_{16} > 35°$ imposed by the extent of the scattering chamber's exit window.

Because nuclei have $S(E_m, p_m) = 0$ for $E_m \lesssim 0$, best use of the E_m acceptance

TABLE 6. Detailed NE-18 kinematics using definitions of Table 1.

Q^2	Targets	E	E'	θ_{16}	p'	θ_8
$(\mathrm{GeV/c})^2$		(GeV)	(GeV)	(degrees)	(GeV/c)	(degrees)
1.04	2% C	2.015	1.39	35.5	1.20	35, 37.8, 40.6, 43.4, 46.2, 49.0, 51.8, 54.6
1.04	6% Fe, 12% Au					43.4, 46.2, 49.0, 51.8, 54.6
1.16	4 cm ^{1}H		1.40	37.3	1.24	43.3
1.21	4 cm ^{2}H		1.36	38.8	1.28	39.1, 41.3, 43.5, 46.7
3.06	2% C, 6% Fe, 6% Au	3.188	1.47	47.7	2.45	27.7, 30.5, 33.3[a]
3.06	4 cm ^{2}H					27.7
3.23	4 cm ^{1}H			49.0	2.49	26.5
5.00	6% C, 6% Fe, 12% Au	4.212	1.47	53.4	3.54	18.5[b], 20.9, 22.6[a]
5.00	15 cm ^{2}H					19.5
5.14	4 cm ^{1}H			54.2	3.56	19.6
6.77	6% C, 6% Fe, 12% Au	5.120	1.47	56.6	4.49	15.9[a], 16.7, 17.3[a]
6.77	15 cm ^{2}H					15.9
6.85	4 cm ^{1}H			57.0		15.9

[a]C, Fe only

[a]C only

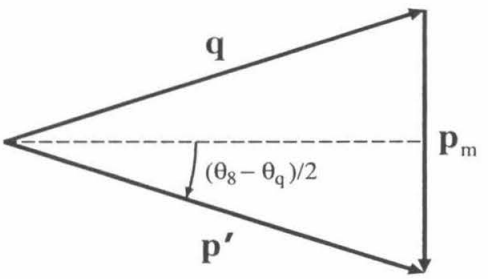

FIG. 37. **Central p_m for a given θ_8. For clarity, $\theta_8 - \theta_q$ is grossly exaggerated compared to the actual experimental kinematics.**

is made by centering it at $E_m > 0$. From Equation 1.7, the E_m value for central kinematics is,

$$E_{m,central} = \nu - \sqrt{Q^2 + \nu^2 + M_p^2} + M_p. \tag{3.6}$$

Here the approximation $T_{A-1} = 0$ (exact at $p_m = 0$, and still very accurate at $|p_m| \simeq p_f$) and nearly perpendicular kinematics ($p'^2 = q^2 = Q^2 + \nu^2$) were used. The result is easily inverted to allow calculation of ν from Q^2 and the desired $E_{m,central}$. The $E_{m,central}$ values used in the present experiment were approximately 50, 30, 20, and 10 MeV at $Q^2 \simeq 1, 3, 5, 7\,(\mathrm{GeV/c})^2$, although $E_{m,central} \simeq 10$ MeV was used for the ^{2}H target at $Q^2 = 1.21\,(\mathrm{GeV/c})^2$. The broader E_m acceptance at high Q^2 allowed the choice of smaller $E_{m,central}$, maximizing the acceptance near the peak of $S(E_m, p_m)$. Once ν is given by Equation 3.6, the central proton kinematics are given by $\mathbf{p}' = \mathbf{q}$. The limit on the central momentum of the 8 GeV/c, $p' < 4.5\,(\mathrm{GeV/c})^2$ prevented data-taking at $Q^2 > 6.77\,(\mathrm{GeV/c})^2$.

Assuming $p' = q$, the central p_m value for a given 8 GeV/c angle setting is given by (see Figure 37):

$$p_{m,central} = 2p' \tan\left(\frac{\theta_8 - \theta_q}{2}\right). \tag{3.7}$$

To ensure overlapping (E_m, p_m) acceptance at consecutive θ_8 settings, one must account for the strong correlation in the E_m and p_m acceptances. The two-dimensional (E_m, p_m) acceptance is given by plotting the size of the detection volume contributing to each (E_m, p_m) bin. This is given by the "phase space" integral:

$$I_{PS} = \int_{E_m, p_m} dE' d\Omega_{k'} dE'_p d\Omega_{p'} A_{16}(E', \Omega_{k'}) A_8(E'_p, \Omega_{p'}). \tag{3.8}$$

The acceptance functions of the two spectrometers, $A_{16}(E', \Omega_{k'})$ and $A_8(E'_p, \Omega_{p'})$, give the probability that the coincidence kinematics being integrated over would be accepted. The acceptance functions are set to zero outside of the acceptance cuts applied to the data (see Section V), and so are technically functions of $(\delta, \Delta\Theta, \Phi)$ as well. Here the distinction between (E', Ω) and $(\delta, \Delta\Theta, \Phi)$ is that between the true and the measured momenta. The integration region is over *all* kinematics with (E_m, p_m) inside the bin, and the presence of the acceptance functions insures that only the experimentally relevant kinematics contribute.

The integral I_{PS} is given by a Monte Carlo calculation including the effects of ionization energy loss, multiple scattering, spectrometer acceptances, and spectrometer resolutions. Examples of the (E_m, p_m) coverage are given in Figures 38 and 39.

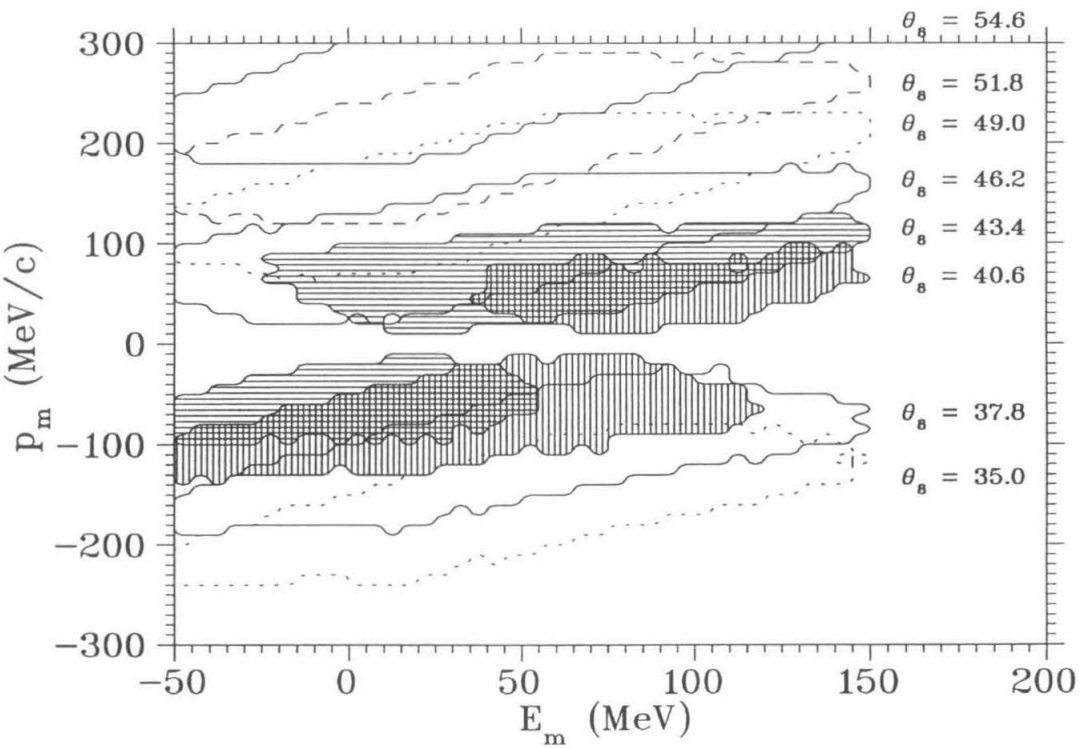

FIG. 38. **Coverage of (E_m, p_m) at $Q^2 = 1$ (GeV/c)^2 for each carbon θ_8 setting, indicated by contours where the acceptance I_{PS} reaches 10% of its maximum value. The $\theta_8 = 40.6$ and $\theta_8 = 43.4$ contours are shaded in to emphasize the continuity of acceptance across $p_m = 0$, where the volume integral $d_m^p = p_m^2 dp_m$ vanishes.**

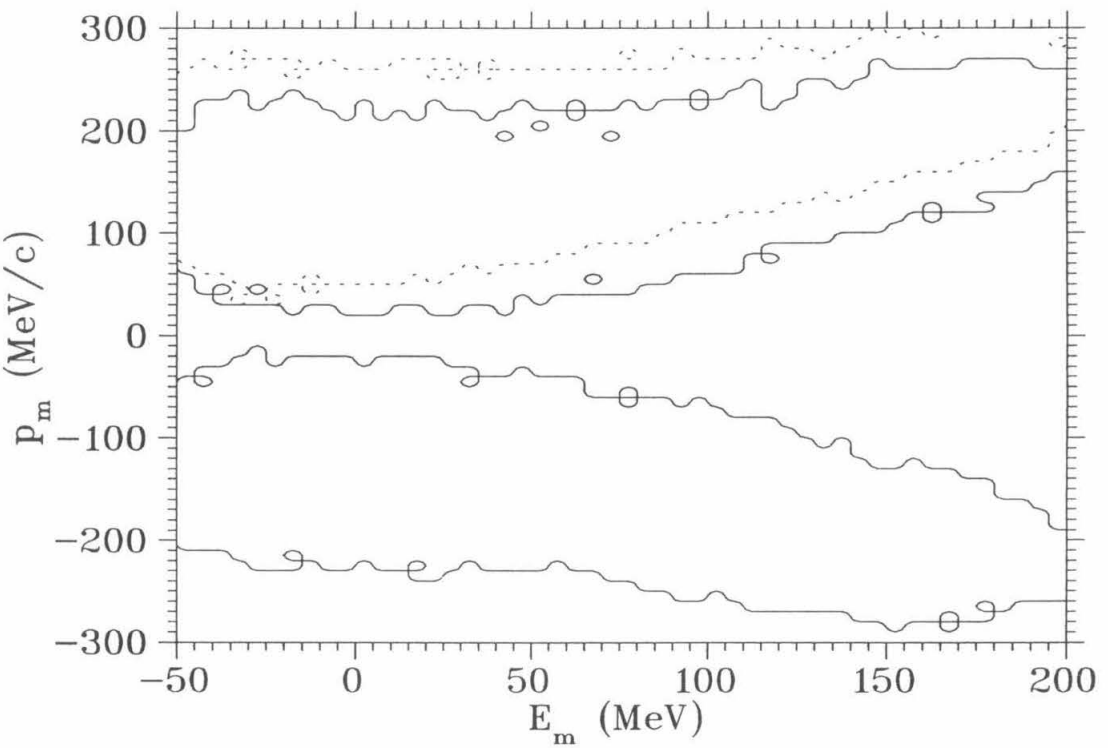

FIG. 39. **Coverage of (E_m, p_m) at $Q^2 = 6.8\,(\mathrm{GeV/c})^2$ for the two extreme carbon angle settings, $\theta_8 = 15.9$ (solid line) and 17.3 (dotted line).**

III.G. Efficiency Corrections

The count rates used in the extraction of $S(E_m, p_m)$ and $T(Q^2)$ must be corrected for the electron-proton coincidence detection inefficiency. The correction includes contributions from the tracking inefficiency in both spectrometers, the coincidence timing inefficiency, and the absorption of protons in the target and 8 GeV/c spectrometer materials. For convenience, the tracking inefficiency is defined to include all single-arm particle identification inefficiencies, such as trigger inefficiencies and, in the 1.6 GeV/c spectrometer, the inefficiency of the cut on the Čerenkov ADC. Most of the efficiency corrections are derived in other sections. This section describes the correction for the absorption of protons and summarizes all of the efficiency results.

III.G.1. Absorption of Protons in Target and 8 GeV/c Materials

Protons are absorbed and deflected in strong interactions with the nuclei of the material in between the struck nucleus and the back of the 8 GeV/c detector stack. Because the proton trigger requires an SF-SM-SR coincidence, the proton is not detected unless it reaches the rear (SR) scintillator plane. The proton absorption correction is derived from the measured thicknesses of the intervening materials and the known proton-nucleus cross sections. For the hydrogen target, the correction is consistent with the ratio of ^{1}H$(e, e'p)$ to ^{1}H(e, e') counts.

The probability of absorption of a proton in a thickness X (= length $\times$ density) of material is

$$A = 1 - e^{X/\lambda}, \tag{3.9}$$

where λ is the proton mean free path. Because of the strong forward peaking of the elastic cross section, many elastic scatterings do not remove the proton from the detector volume. This is especially true for elastic scatterings in the detector hut.

Thus, the correction used is intermediate between the two extremes given by $\lambda = \lambda_C$ and $\lambda = \lambda_I$. Here λ_C and λ_I are the mean free paths between collisions (elastic or inelastic) and between inelastic interactions, respectively. The values used are from [38].

Tables 7 through 10 detail the calculation of the absorption correction. The average absorption is given (to high accuracy) by the value for a scattering at target center, $x = y = z = 0$, into the center of the 8 GeV/c solid angle, $(\theta, \phi)_{p'} = (\theta_8, 0)$. The thicknesses of the target-related materials traversed by the proton (Tables 7 and 8) varies with θ_8. The resulting variation in the absorption is negligible ($< 0.3\%$), however, because at every kinematics, either the absorption in the target is small ($\lesssim 1\%$) or the maximum range of θ_8 is small ($\lesssim 1°$). Thus, a typical value of θ_8 (44, 28, 19, and 16°) is used to calculate A at each Q^2 [1, 3, 5, 7 $(\mathrm{GeV/c})^2$].

The total absorption is calculated as $1 - \prod_i (1 - A_i)$, where $(1 - A_i)$ is the transmission through each absorbing material i. The total A_I and A_C differ by 3–4%. Hence, the average of the two is used for the absorption correction, with a fractional systematic error of $\pm 2\%$.

As a consistency check, the transmission for the hydrogen target is measured directly as the ratio of the number of coincidences (corrected for the 8 GeV/c tracking efficiency and dead time contribution and also for the coincidence timing efficiency) to the number of 1.6 GeV/c electron singles. Radiative tail events are discarded with a cut on the elastic stripe in the 1.6 GeV/c, ensuring near-exact kinematic correlation of the electron and proton. (Note that if the effect of proton internal bremsstrahlung on the electron kinematics is small enough, the cut may not exclude all radiative tail events. However, the total fraction of events outside the 8 GeV/c momentum acceptance is estimated to be $< 0.1\%$.) Then the $(\delta, \Delta\Theta, \Phi)$ illumination of the 8 GeV/c spectrometer is restricted to the central, unit-acceptance, region through cuts on $(\Delta\Theta, \Phi)$ in the 1.6 GeV/c spectrometer. Proton absorption is indicated by

TABLE 7. Proton absorption in liquid target materials.

Target	Density	λ_I	λ_C	Q^2	length	thickness	A_I	A_C
	(g/cm^3)	(g/cm^2)	(g/cm^2)	$(GeV/c)^2$	(cm)	(g/cm^2)	(%)	(%)
4 cm ^{1}H	0.0705	50.8	43.3	1	2.79	0.197	0.39	0.45
				3	2.27	0.160	0.31	0.37
				5	2.12	0.150	0.29	0.34
				7	2.09	0.147	0.29	0.34
4 cm ^{2}H	0.1701	54.7	45.7	1	2.79	0.474	0.86	1.03
				3	2.27	0.386	0.70	0.84
15 cm ^{2}H				5	8.29	1.410	2.55	3.04
				7	8.16	1.387	2.50	2.99
Al Endcap	2.72	106.4	70.6	1	0.169	0.461	0.43	0.65
				3	0.138	0.376	0.35	0.53
				5	0.129	0.351	0.33	0.50
				7	0.127	0.345	0.32	0.49
Mylar Insulation	1.39	60.2	85.7	1–7	0.006	0.009	0.01	0.01

^{1}H(e,e') events that did not result in an 8 GeV/c track. Note that the measurement does not depend on the efficiency of the 1.6 GeV/c spectrometer. The measured values are consistent with those predicted using Equation 3.9 (see Figure 40).

III.G.2. Summary

This section summarizes efficiency corrections applied in the analysis of $S(E_m, p_m)$ and $T(Q^2)$. For each correction, the associated systematic error is also given. The tracking efficiency corrections given in Table 10 are described in Section III.B. The

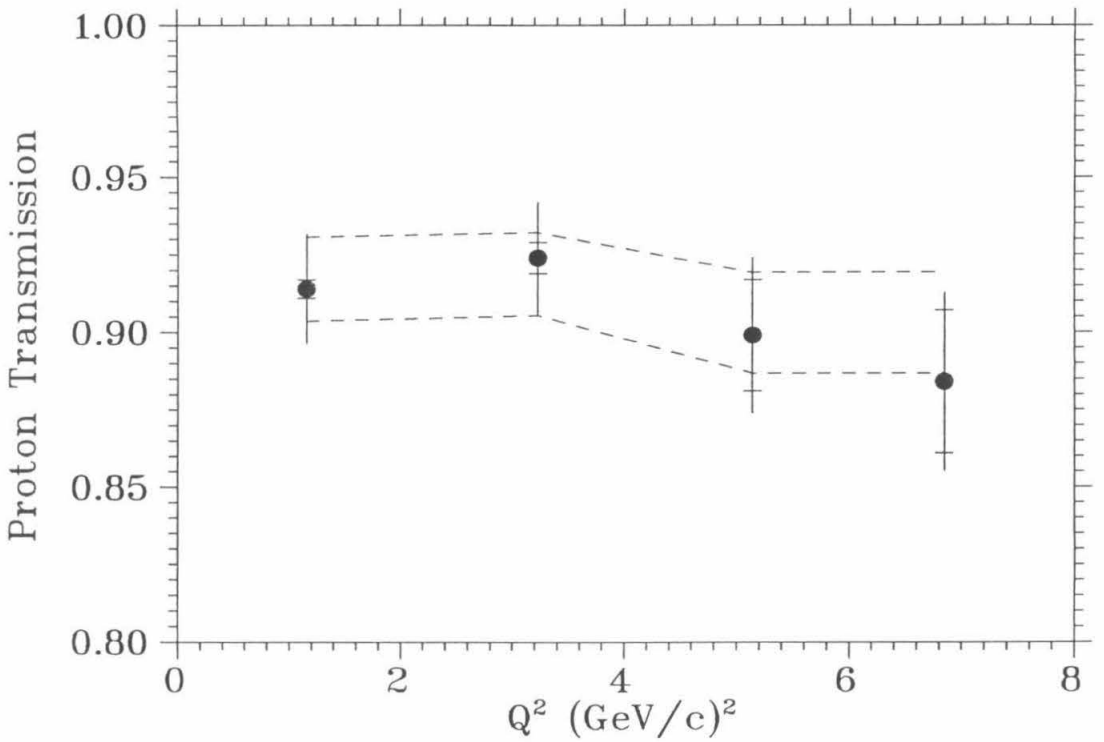

FIG. 40. **Proton absorption efficiency for hydrogen. The data points are measured as the efficiency-corrected ratio of ^{1}H$(e,e'p)$ coincidences to 1.6 GeV/c ^{1}H(e,e') singles with a kinematic cut to restrict the 8 GeV/c illumination. The inner error bars are statistical only and the outer error bars include the systematic errors in quadrature. The two curves are the transmission calculated using the inelastic (upper curve) and the total (lower curve) nuclear scattering lengths λ_I and λ_C.**

TABLE 8. Proton absorption in solid targets.

Target	Density (g/cm^3)	λ_I (g/cm^2)	λ_C (g/cm^2)	Q^2 $(GeV/c)^2$	length (cm)	thickness (g/cm^2)	A_I (%)	A_C (%)
2% C	2.193	86.3	60.2	1	0.285	0.625	0.72	1.03
				3	0.232	0.509	0.59	0.84
6% C				5	0.620	1.360	1.56	2.23
				7	0.610	1.338	1.54	2.20
6% Fe	7.829	131.9	82.8	1	0.0740	0.579	0.44	0.70
				3	0.0603	0.472	0.36	0.57
				5	0.0563	0.441	0.33	0.53
				7	0.0553	0.433	0.33	0.52
12% Au	19.157	190.4	113.7	1	0.0279	0.534	0.28	0.47
6% Au				3	0.0117	0.223	0.12	0.20
12% Au				5	0.0212	0.407	0.21	0.36
12% Au				7	0.0209	0.400	0.21	0.35

proton absorption correction is derived in Section III.G.1. The coincidence identification efficiency is discussed in Section III.D.

TABLE 9. Proton absorption in 8 GeV/c spectrometer

Absorber	Material	Density (g/cm^3)	λ_I (g/cm^2)	λ_C (g/cm^2)	length (cm)	thickness (g/cm^2)	A_I (%)	A_C (%)
Chamber Exit[a] and 8 GeV/c Entrance Windows	Al 5052	2.68	106.4	70.6	0.056	0.15	0.14	0.21
Čerenkov Entrance and Exit Windows	Al	2.70	106.4	70.6	0.08	0.22	0.21	0.31
Čerenkov Mirror	Lucite	1.2	83.6	59.2	0.64	0.77	0.92	1.29
Čerenkov Gas[b]	$C_2Cl_2F_4$	0.0049	106	70.6	310	1.52	1.42	2.13
Wire Chambers	Fe foil	7.9	131.9	82.8	0.026	0.21	0.16	0.25
SF scintillators	Polystyrene	1.03	82.0	58.4	0.95	0.98	1.19	1.66
NBS scintillators	Polystyrene	1.03	82.0	58.4	1.27	1.31	1.58	2.22
SM scintillators	Polystyrene	1.03	82.0	58.4	1.27	1.31	1.58	2.22
Air Gaps	Air	0.001205	90.0	62.0	410	0.49	0.54	0.79
Total[c] for $Q^2 = 1,3\,(\mathrm{GeV/c})^2$							6.16	8.64
Total[c] for $Q^2 = 5,7\,(\mathrm{GeV/c})^2$							7.50	10.58

[a]Scattering chamber exit included in table for compactness.

[b]$Q^2 = 5,7\,(\mathrm{GeV/c})^2$ only

[c]Solid targets (does not include additional 0.01 from mylar insulation)

TABLE 10. Tracking efficiency and proton absorption corrections. The 1.6 GeV/c and 8 GeV/c tracking efficiencies and the proton coincidence identification have an error of ± 0.01 each. The fractional error on the proton absorption is ± 0.02.

	Q^2	Tracking		Coincidence	Proton
A	$(\mathrm{GeV/c})^2$	1.6 GeV/c	8 GeV/c	Identification	Absorption
^{1}H	1, 3	1.00	1.00	1.00	1.09
	5, 7	1.00	1.00	1.00	1.11
^{2}H	1, 3	1.01	1.00	1.015	1.09
	5	1.01	1.00	1.015	1.14
	7	1.02	1.00	1.015	1.14
^{12}C	1	1.01	1.00	1.015	1.09
	3	1.02	1.00	1.015	1.09
	5, 7	1.03	1.00	1.015	1.13
^{56}Fe, ^{197}Au	1	1.01	1.00	1.015	1.08
	3	1.02	1.00	1.015	1.08
	5, 7	1.03	1.00	1.015	1.11

IV. THE PLANE WAVE IMPULSE APPROXIMATION CALCULATION

Extraction of the spectral function and the nuclear transparency are performed assuming the scattering can be modelled in the Plane Wave Impulse Approximation with an Independent Particle Shell Model $S(E_s, \mathbf{p})$. The transition from the Born-level cross section (Equation 1.9) to higher orders is made through the addition of the effects of internal radiation (see Section IV.E). This allows direct comparison in both the transparency and spectral function measurements between the PWIA calculation and the data.

The present calculation improves on simple the PWIA/IPSM approximation through the addition of effects due to Coulomb distortions of the electron waves (Section IV.F). The calculation also includes effects due to the experimental apparatus such as external radiation, ionization energy loss, multiple scattering, spectrometer acceptances, and spectrometer resolutions.

It is worth discussing higher-order corrections to the PWIA that are not included in the calculation. These effects are difficult to calculate but are expected to be small for the low-Q^2 kinematics of previous $A(e, e'p)$ experiments, and so were not corrected for. Fortunately, they are even smaller for $Q^2 \gtrsim 1\,(\mathrm{GeV/c})^2$.

Dispersion corrections and exchange terms involve the coupling of the virtual photon to the entire A or $A-1$ nucleus, and so must scale like the electron-nucleus elastic form factor. Due to the large extent of the nucleus, the form factor drops rapidly for $Q^2 \gtrsim 1\,(\mathrm{GeV/c})^2$. Here dispersion corrections refer to two-photon exchange processes ($\sim \alpha^4$) leaving the nucleus in an excited state before the knockout of the detected proton [9]. Exchange terms refer to one-photon processes where the virtual photon knocks out the $A-1$ system instead of the detected proton [9]. This is further suppressed at high Q^2 because it involves nucleons with initial momentum $\sim q$, where the spectral function has extremely little strength.

Multi-nucleon processes are expected to decrease for $Q^2 > 1\,(\mathrm{GeV/c})^2$ due to the decreasing wavelength of the virtual photon (see Section I.A.2). However, Lourie *et al.* argue that the enhancement in the measured rate at $50 < E_m \lesssim 100\,\mathrm{MeV}$ due to multi-nucleon knockout may be increased at high Q^2 [14]. The issue can be resolved through a comparison of the PWIA/IPSM calculation and the data (see Section V.A).

In meson exchange currents, the photon couples to a virtual meson (produced by the nuclear strong interaction) or to a nucleon undergoing a strong interaction with another nucleon (dynamic correlations). This includes isobar contributions, where the nucleon is excited to a virtual resonance. For inclusive $A(e,e')$, these contributions peak in the dip region and are $\lesssim 4\%$ at quasielastic kinematics even for $Q^2 \simeq 0.18\,(\mathrm{GeV/c})^2$ [9].

IV.A. Overview of the Calculation

The PWIA calculation is performed by a Monte Carlo simulation that begins with events generated according to Equation (1.9) and includes the effects of internal radiation. Coulomb distortion, and the experimental apparatus.

The first step in the calculation is the degradation of the energy of the incoming electron by ionization energy loss and radiation (internal and external). Internal radiation is calculated in the equivalent radiator approximation, modified to exactly reproduce the theoretical E' [40] and E_m [41] dependences. Trial values of scattered electron and proton kinematics are chosen, and accepted with a probability proportional to Equation 1.9. The outgoing electron and proton energies are then degraded by radiation and ionization energy loss. The outgoing electron and proton are then traced through the magnets of the 1.6 and 8 GeV/c spectrometers using the Transport-based models of the spectrometers. If the models predict both particles will be accepted, their momenta are reconstructed and recorded. The calculation is

described in more detail below.

IV.B. The Born-Level Plane Wave Impulse Approximation Cross Section

This section describes the values of σ_{ep} and $S(E_s, \mathbf{p})$ used to evaluate Equation 1.9, the $A(e, e'p)$ cross section in the Born-level PWIA.

In principle, one would need to know the off-shell nuclear current in order to calculate σ_{ep}. At present, however, this is not possible and there is some ambiguity in the choice of σ_{ep}. We use the De Forest prescription, $\sigma_{ep} = \sigma_1^{cc}$ [10], which accounts for the differences in the on- and off-shell kinematics and satisfies 4-momentum and current conservation. Other forms for σ_{ep}, including the on-shell value, have been tested, with little ($\leq 2\%$) effect on the measured T.

For the hydrogen values of $\mathbf{p} = 0$ and $E_s = 0$, σ_1^{cc} reduces to the free-nucleon cross section (Equation 1.2), divided by the recoil factor E'/E and flux term E'/M [10]. The full elastic cross section results from integrating Equation (1.9) over the 4-dimensional delta function in the hydrogen spectral function.

For the $S(E_s, \mathbf{p})$ of ^{1}H and ^{2}H we use a 4-dimensional delta-function and the Bonn potential momentum-space wave function [42], respectively. For the solid targets we use the Independent Particle Shell Model (Equation 1.11). In this case, $L_i(E_s)$ is a Lorentzian energy profile (with a cut-off at the one-proton removal energy, see Appendix E) and $\varphi_i(\mathbf{p})$ is the bound-state wave function in a Woods-Saxon nuclear potential with shell-dependent parameters. The Lorentzian and Woods-Saxon parameters, based on from fits to spectral functions extracted from previous $A(e, e'p)$ experiments [9], are given in Tables 24 and 25. The carbon spectral function is taken from the Saclay ^{12}C$(e, e'p)$ experiment [11] shown in Figures 6 and 7. Since there is no $A(e, e'p)$ data on iron and gold, their spectral functions are based on the $S(E_m, p_m)$ measured at Saclay on ^{58}Ni [11] and at NIKHEF on ^{208}Pb [13]. The momentum dis-

tributions for Fe and Au are modified to improve agreement with the distributions measured in the current experiment.

For the proton elastic form factors G_E^p and G_M^p used in σ_1^{cc}, we assume the dipole (Equation 1.4) and Gari-Krümplemann [43] forms, respectively, as suggested by SLAC experiment NE-11 [44]. The form factor model-dependence is estimated to be $\leq 2\%$ by comparing elastic cross section calculated with different form factor parameterizations.

IV.C. Kinematics and Luminosity

The calculation generates events in a region of $dE'd\Omega_{k'}dE'_pd\Omega_{p'}$ with 6-fold volume V_{kin}. The region includes the entire acceptance range of the spectrometers. When radiation is being simulated, the region's upper E' and E'_p boundaries are increased by ω_{max} (see Section IV.D) to allow the outgoing particles to radiate down into the spectrometer's momentum acceptance.

The program generates trial events with a flat distribution in V_{kin}. An event is accepted with a probability given by $d^6\sigma/dE'd\Omega_{k'}dE'_pd\Omega_{p'}$ (Equation 1.9) divided by a constant value σ_{max}, so the accepted events are distributed according to the quasielastic cross section. Here $\sigma_{max} \geq$ the maximum value of $d^6\sigma/dE'd\Omega_{k'}dE'_pd\Omega_{p'}$ in V_{kin}. The integrated luminosity $\mathcal{L}_{PWIA} = \int Ldt$ of the calculation is needed to convert to count rates. It is most easily found by realizing that the trial events are effectively generated with the cross section σ_{max} (*i.e.*, if the quasielastic cross section were constant at σ_{max}, every trial event would pass the cross section test). Thus, the integrated luminosity is simply:

$$\mathcal{L}_{PWIA} = \frac{N_{trial}}{V_{kin}\sigma_{max}} \tag{4.1}$$

where N_{trial} is the number of trial kinematics.

To increase computing speed this procedure is modified for all targets except ^{197}Au. For hydrogen, the spectral function is a delta function in energy and 3-momentum, which is impractical to simulate. The calculation circumvents this issue by generating events according to the elastic cross section, Equation 1.2, instead of the quasielastic cross section. For the nuclei ^{2}H, C, Fe, which are highly peaked in E_s, it is convenient to generate events in E_s instead of E'. In this case the relevant cross section is (cf. Equation 1.9):

$$\frac{d^6\sigma}{dE_s d\Omega_{k'} dE'_p d\Omega_{p'}} = p' E'_p \sigma_{ep} S(E_s, \mathbf{p}) \left| \frac{dE'}{dE_s} \right| \tag{4.2}$$

where

$$-\left(\frac{dE'}{dE_s}\right)^{-1} = 1 + \frac{\mathbf{p} \cdot \mathbf{k}'}{\sqrt{M_{A-1}^2 + p^2}}. \tag{4.3}$$

The calculation performs the E_s integral directly by choosing a shell i (weighted by N_i) and then sampling E_s according to $L_i(E_s)$. Proper weighting is then given by an accept-reject test with probability proportional to (cf. Equation 1.11):

$$\frac{d^5\sigma}{d\Omega_{k'} dE'_p d\Omega_{p'}} = p' E'_p \sigma_{ep} |\varphi_i(\mathbf{p})|^2 \left| \frac{dE'}{dE_s} \right|. \tag{4.4}$$

IV.D. External Radiation

The emission of real (bremsstrahlung) photons in external radiation (Figure 41) changes the kinematics of the detected particles. In a single arm experiment, this process distributes the counts along a radiative tail in E', and can significantly lower the count rate by moving counts to below the spectrometer momentum acceptance. In a coincidence experiment one can observe not just the magnitude, but also the direction of the radiation. In the PWIA, the 4-momentum p^μ of the initial proton equals the missing 4-momentum $p_m^\mu \equiv k'^\mu + p'^\mu - k^\mu$. But if real photons are emitted, there is an unknown additional missing 4-momentum ω^μ in the final state: $p^\mu + k^\mu =$

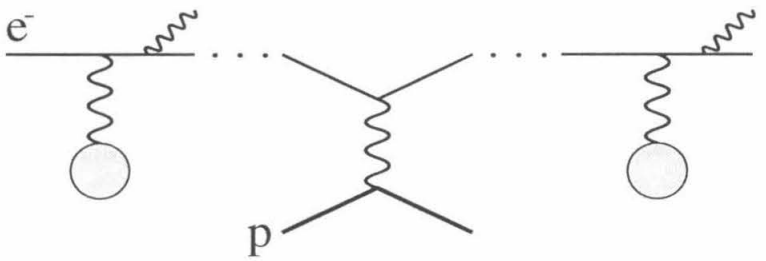

FIG. 41. **One-photon external radiation in ^{1}H(e,e'). The incoming and outgoing electrons experience bremsstrahlung interactions in the electromagnetic fields of target nuclei (indicated by gray circles). Because of the large distances separating the interactions and the high Q^2 of the electron-proton scattering, the three diagrams shown are incoherent.**

$p'^{\mu} + k^{\mu} + \omega^{\mu}$. Thus, $p_m^{\mu} = p^{\mu} - \omega^{\mu}$ and the measured missing energy and momentum are now:

$$E_m = E_s + \omega \tag{4.5}$$

$$\mathbf{p}_m = \mathbf{p} - \boldsymbol{\omega}. \tag{4.6}$$

This leads to the observed tails in the E_m-p_m plane. In the present experiment the tails can move either $\mathbf{k}'$ or $\mathbf{p}'$ outside the spectrometer acceptances. It is therefore necessary for the calculation to include the effects of radiation on the kinematics of the detected particles. (Note that the distribution of the photons themselves is irrelevant, except through their effect on the detected kinematics.) The following two sections detail how this is accomplished.

External radiation refers to the emission of bremsstrahlung photons by the incoming and outgoing electrons in the fields of the target nuclei (see Figure 41). The more massive outgoing proton is subject to much smaller accelerations, and emits

a negligible amount of radiation. R. A. Early [45] solved numerically, in the complete screening approximation, for the probability $I_b(\omega, t)$ that an electron of energy E would radiate an energy ω in passing through a thickness of t radiation lengths. Note that $I_b(\omega, t)$ is the probability of emitting any number of photons, with energy totalling ω. The present calculation uses Y. S. Tsai's fit [46],

$$I_b(\omega, t)d\omega = \frac{1}{\Gamma(1+bt)}\left(\frac{\omega}{E}\right)^{bt}\frac{bt}{\omega}\phi\left(\frac{\omega}{E}\right)d\omega \tag{4.7}$$

$$\phi\left(\frac{\omega}{E}\right) = 1 - \frac{\omega}{E} + \frac{3}{4}\left(\frac{\omega}{E}\right)^2, \tag{4.8}$$

with the t values given in Tables 3 and 4 (multiplied by geometric factors for non-orthogonal incidence). Tsai's fit is below Early's result by a fraction that varies between about $t/10$ and $t/5$ as ω varies between 0 and $0.8E$ for $t < 0.1$ [45]. For example, the deviation at $\omega \simeq 0$ is $\sim 1\%$ for a $t = 10\%$ radiator. The discrepancy increases for $\omega > 0.8E$, but this is always outside the experimental acceptance (see the discussion of ω_{max}, below).

The resulting error in the calculated count rate is dominated by the $t/10$ deviation at $\omega \ll E$. As a result of this discrepancy, Equation 4.7 does not integrate to 1 (the probability is not normalized):

$$\int_0^E I_b(\omega, t)d\omega = \frac{1}{\Gamma(1+bt)}\left[\frac{8 + 7bt + 8(bt)^2}{4(1+bt)(2+bt)}\right] \simeq 1 - t/10. \tag{4.9}$$

This is a small effect ($< 2\%$) and the total radiator thickness t does not vary much for events inside the acceptance. Thus the calculated rate is simply renormalized through division by Equation 4.9 evaluated for an event at the center of the target and at central kinematics. After this correction the deviation of the total PWIA count rate from the Early result is estimated to be $< 0.2\%$.

Equation 4.7 is valid in the Born approximation, where each electron-nucleus collision releases at most one photon. For a heavy nucleus like ^{197}Au, with $Z\alpha \sim 1$,

diagrams with multiple photons also become important. However, we will argue in Appendix F.3 that the equation, which includes the effects of multiple *collisions*, approximately incorporates the effects of diagrams with multiple *photons*.

In the $t \to 0$ limit, one recovers $\phi(\omega/E)$, the shape of the bremsstrahlung spectrum from a single collision:

$$I_b^{1-\gamma}(\omega, t)d\omega = \frac{bt}{\omega}\phi\left(\frac{\omega}{E}\right)d\omega. \tag{4.10}$$

The quantity b in Equation 4.7 is given by [46]:

$$b = \frac{4}{3}\left\{1 + \frac{1}{12}\left[\frac{Z+1}{ZL_{rad} + L'_{rad}}\right]\right\} \tag{4.11}$$

where Z is the charge of the external radiator nucleus. We use the Thomas-Fermi-Moliere model for L_{rad} and L'_{rad} [46]:

$$L_{rad} = \ln(184.15Z^{-1/3}) \tag{4.12}$$

$$L'_{rad} = \ln(1194Z^{-2/3}). \tag{4.13}$$

The resulting values of b agree with those calculated using Tsai's recommended values of L_{rad} and L'_{rad} [46] to better than 0.1% for Hydrogen, and almost exactly for ^{12}C and heavier nuclei.

Because Equation 4.7 becomes inaccurate at large ω, the PWIA calculation only includes events with ω less than a chosen cut-off $\omega = \omega_{max} < 0.8E$. This is justified because events with such large ω are outside of the E_m cuts used in the analysis (see Equation 4.5 and Section V.B). For nuclear targets, $\omega_{max} = 200\,\text{MeV}$. For ^{1}H, where the (e, e') cross section is also of interest, larger values of ω_{max} are used, ensuring that the radiative tail is computed correctly beyond the momentum acceptance of the 1.6 GeV/c spectrometer. For $Q^2 = 1, 3, 5, 7\,\text{GeV/c}^2$, the ^{1}H values are $\omega_{max} = 300, 700, 1200, 1300\,\text{MeV/c}$.

The photons are emitted nearly parallel to the electron momentum, with an angular spread of $\Delta\theta_\omega = m_e/E < 0.4\,\mathrm{mr}$ for electron energies of $E \geq 1.4\,\mathrm{GeV}$. The deflection of the electron, roughly $\omega\Delta\theta_\omega/E$, is $\lesssim 0.05\,\mathrm{mr}$ for the photon energies of interest, $\omega < 200\,\mathrm{MeV}$. Thus, the calculation uses the angle peaking approximation, where the radiation changes the magnitude but not the direction of the electron.

IV.E. Internal Radiation

The Born-level PWIA describes the electron-proton interaction as the exchange of a single virtual photon (see Figures 3 and 4). Higher-order diagrams, involving multiple photons, are referred to as internal radiative corrections. The diagrams involving a single radiative photon, shown for $\mathrm{H}(e,e')$ in Figures 42 and 43, have been calculated by Mo and Tsai [40]. The diagrams in Figure 42 describe an elastic scattering, with the exchange of a *virtual* radiative photon. These graphs are simply additional contributions to the elastic cross section, increasing it by $\sim 10\%$ without changing the kinematics. The diagrams in Figure 43 describe an *inelastic* scattering, with the emission of a *real* photon. This process, called internal bremsstrahlung, produces radiative tails as discussed at the beginning of Section IV.D.

In the spirit of the PWIA, for the radiative correction to the *quasielastic* $A(e,e'p)$ cross section (Equation 1.9) the correction for $^1\mathrm{H}(e,e'p)$ *elastic* scattering at the same E and θ is used. The recoil nucleus is treated as a spectator, which does not participate in the high-Q^2 scattering and therefore is not involved in the exchange or radiation of hard photons. In particular, recall from Section I.A.1 that the PWIA quasielastic cross section, Equation 1.9, implicitly includes a closure sum over the final state of the $A-1$ system. The sum includes inelastic channels, such as internal bremsstrahlung from the recoil nucleus. The Coulomb attraction of the recoil nucleus, involving the exchange of soft photons, is treated in Section IV.F.

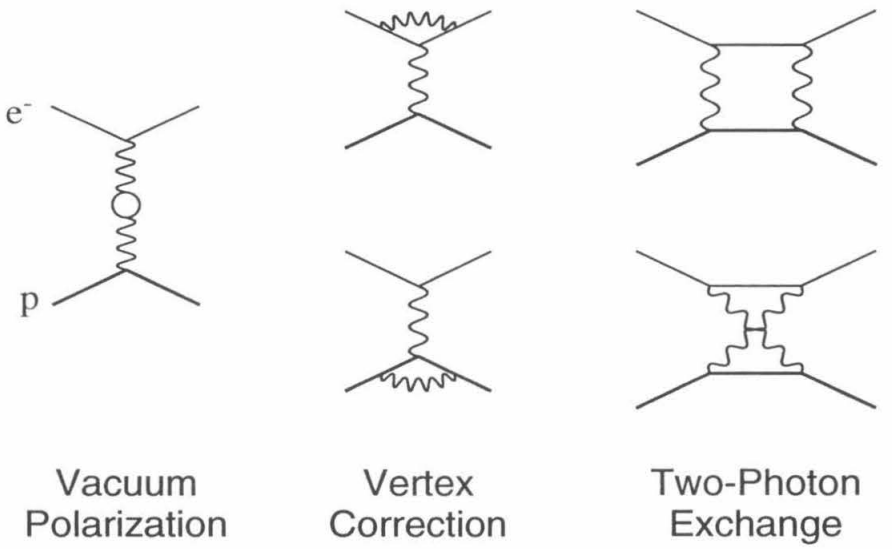

FIG. 42. **One-photon internal virtual radiation in ^{1}H(e,e'). Internal radiation diagrams involving an additional virtual photon, coherent with the electron-proton scattering.**

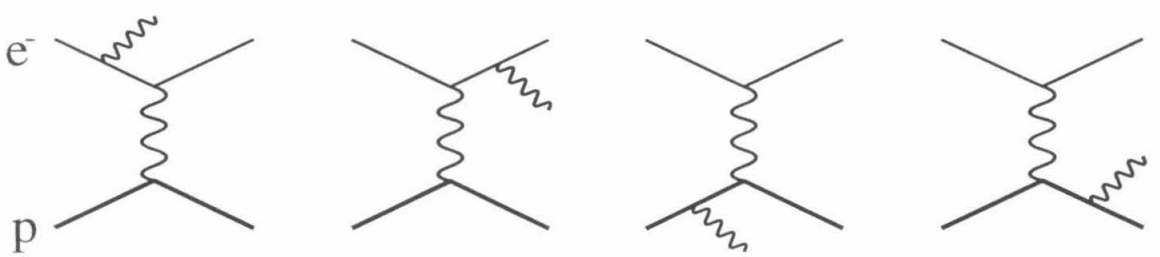

FIG. 43. **One-photon internal bremsstrahlung in ^{1}H(e,e'). Diagrams involving the emission of a single real photon, coherent with the electron-proton scattering.**

Mo and Tsai [40] calculated the count rate in an H$(e,e')p$ experiment for $E'_{el} - \Delta E' < E' < E'_{el}$ assuming the emission of a single radiative photon. (This is the "one-photon" approximation, correct to order α^4; see Equation F8). Exponentiation approximates the effect of higher-order diagrams to all orders [40]:

$$\left(\frac{d\sigma}{d\Omega}\right)_{\Delta E'} \equiv \int_{E'_{el}-\Delta E'}^{E'_{el}} dE' \left(\frac{d^2\sigma}{d\Omega dE'}\right) = e^{\delta_{E'}} \left(\frac{d\sigma}{d\Omega}\right)_{Born}. \tag{4.14}$$

Here the Born-level (order α^2) cross section $(d\sigma/d\Omega)_{Born}$ is given by Equation 1.2. The correction factor δ is given by Mo and Tsai [40], Equation II.6, with the addition of the Schwinger correction and vacuum polarization from quark and heavy lepton vacuum polarization loops [47]. These additions are necessary for consistency with SLAC NE-11, on which the present calculation's form factors are based. The $1/\omega$ character of the internal bremsstrahlung leads (see Appendix F.3) to the following $\Delta E'$ dependence:

$$e^{\delta_{E'}} = N_{E'}(\Delta E')^{\lambda_{E'}}, \tag{4.15}$$

where $N_{E'}$ and $\lambda_{E'}$ are functions of E and $\theta_{k'}$ only. Mo and Tsai give a formula for $\delta_{E'}$ which is valid for $\Delta E' \ll E'/(1 + 2E/M_p)$ [48].

In an $A(e,e'p)$ experiment, one is also interested in the number of counts within the experimental range of E_m. Wasson *et al.* [41] have repeated the Mo and Tsai work for the case of coincidence kinematics. In this case, one finds the analogous result:

$$\left(\frac{d\sigma}{d\Omega}\right)_{\Delta E_m} = e^{\delta_{E_m}} \left(\frac{d\sigma}{d\Omega}\right)_{Born} = N_{E_m}(\Delta E_m)^{\lambda_{E_m}} \left(\frac{d\sigma}{d\Omega}\right)_{Born}. \tag{4.16}$$

One finds that the exponent $\lambda_{E_m} = \lambda_{E'}$ at all kinematics. This is because $\delta_{E'}$ and δ_{E_m} are both integrals of Equation F7, except with different integration regions.

The present calculation simulates the internal radiation through the equivalent radiator approximation, modified to exactly reproduce the above E' and E_m cut dependences. The standard equivalent radiator approximation simulates the internal

bremsstrahlung by passing the incoming and outgoing electron through two imaginary external radiators, both with $bt = \lambda^{EQ}$:

$$\lambda^{EQ} = \frac{\alpha}{\pi}\left[\ln\left(\frac{Q^2}{m_e^2}\right) - 1\right]. \tag{4.17}$$

Note that for internal bremsstrahlung b and t are separately meaningless (cf. Equation 4.7). The value is typically $\lambda^{EQ} \sim 3.5$ (see Table 26).

The present calculation uses this method to simulate the effects of internal radiation on the count rates and kinematics of $A(e, e'p)$. There are two refinements, however. First, as the scattering energy increases, a few percent of the radiation becomes peaked near the scattered proton direction [41]. (The large acceleration of the proton in the scattering begins to overcome the suppression of radiation by its high mass.) Thus, the scattered proton is also passed through an equivalent external radiator, with bt values between 0.00037 [at $Q^2 = 1\,(\mathrm{GeV/c})^2$] and 0.00524 [$Q^2 = 7\,(\mathrm{GeV/c})^2$] (see Table 26). Second, the three equivalent radiators have different thicknesses. (The equality of the incoming and outgoing electron radiators in the standard equivalent radiator approximation is only valid in the limit of no target recoil [41].) The thicknesses are adjusted to simultaneously reproduce the theoretical cut dependences in both E' and E_m:

$$\left(\frac{d\sigma}{d\Omega}\right)^{PWIA}_{\Delta E'} = N_{E'}(\Delta E')^{\lambda_{E'}}\left(\frac{d\sigma}{d\Omega}\right)_{Born}, \tag{4.18}$$

$$\left(\frac{d\sigma}{d\Omega}\right)^{PWIA}_{\Delta E_m} = N_{E_m}(\Delta E_m)^{\lambda_{E_m}}\left(\frac{d\sigma}{d\Omega}\right)_{Born}. \tag{4.19}$$

Both conditions must be satisfied because events are *simultaneously* subject to the $\Delta E'$ range given by the 1.6 GeV/c momentum acceptance and the ΔE_m range applied in the analysis.

The selection of the λ values used in the calculation is described in Appendix F.4. Figure 44 demonstrates the success of the equivalent radiator technique.

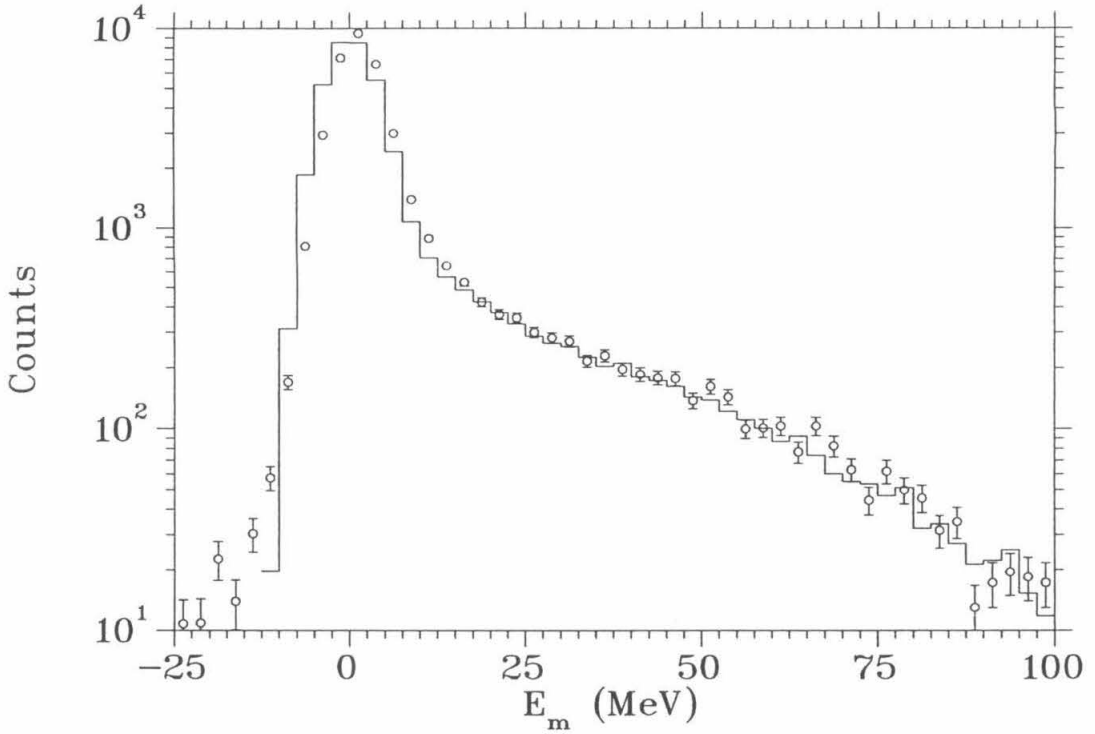

FIG. 44. E_m **distribution of** $^1\mathbf{H}(e,e'p)$ **at** $Q^2 = 1\,(\mathrm{GeV/c})^2$**. Comparison of data (points with error bars) and calculation (histogram). Error bars are statistical only.**

To reproduce the internal radiative tails, the equivalent radiator approximation must correctly simulate the effect of the radiation on **k**, **k**′, and **p**′. This is discussed in Appendix F.5. Appendix F.3 illuminates some issues surrounding internal radiation through the use of the one-photon approximation.

IV.F. Multiple Scattering, Energy Loss, and Coulomb Acceleration

The calculation simulates multiple scattering, energy loss, and Coulomb acceleration based on the position and angles of the scattering in each event. After the calculation, the reaction kinematics are then corrected for the *average* value of these

effects (Section III.E).

Multiple scattering and energy loss calculations are performed using the material thicknesses given in Tables 3 and 4. The location of the scattering is chosen uniformly along the length of the target and inside the transverse extent of the beam spot. In cases of non-normal incidence, the thicknesses are increased by the appropriate geometrical factors. Multiple scattering of the incoming and outgoing particles in the target and spectrometer materials is simulated in the gaussian approximation, which is accurate for 98% of the multiple scattering distribution [38]. The approximation is sufficient, given the small value of the RMS angular deflection $\theta^{rms} < 5\,\mathrm{mr}$ in each arm.

Ionization energy loss in each material is accounted for by subtraction of the most probable value ΔE_{mp} from E, E', and E'_p. Values are given by Equation 3.3 for electrons and Equation 3.2 for protons. The width $\xi < 0.2\,\mathrm{MeV}$, so it is ignored. Changes in ΔE_{mp} due to variations in the location and angles of the scattering are more important, and are correctly simulated.

The Coulomb attraction results from radiative diagrams, neglected in SectionIV.E, where the electron exchanges soft photons with the recoil $A-1$ system. In a Complete Distorted Wave Impulse Approximation model of the scattering, the attraction gives rise to the Coulomb distortion of the $t = \pm\infty$ plane wave fronts. The main effect of the Coulomb acceleration is a change in the scattering cross section caused by the change in scattering kinematics. Note the potential used to calculate the IPSM wave function $\varphi_i(\mathbf{p})$ includes the Coulomb potential energy of the $A-1$ system (see Appendix E). Thus, the Coulomb acceleration of the struck proton is already accounted for in the separation energy E_s

The calculation simulates the change in the energy of the electron by the addition or subtraction of the Coulomb potential energy of the recoil nucleus at the point of the interaction (Equation 3.4). The position of the scattering is chosen randomly

inside the nucleus, which is modelled as a uniform sphere. This procedure neglects the localization of the charge in discrete nucleons and the shell-dependence of the radial wave function. These approximations are well justified, however.

The model does not include hard interactions with $\hbar/Q \lesssim 1\,\mathrm{fm}$, which resolve individual nucleons. However, since the elastic cross section is strongly peaked at small Q^2, these interactions have vanishing probability. At small Q^2, $E' \simeq E$ and the proton structure is not resolved, so the cross section (Equation 1.2) reduces to the Mott cross section (Equation 1.3):

$$\left(\frac{d\sigma}{d\Omega}\right) \simeq \left(\frac{d\sigma}{d\Omega}\right)_{Mott} \simeq \frac{4\alpha^2 E^2}{Q^4}. \tag{4.20}$$

Here the small angle approximation and $Q^2 \simeq E^2\theta^2$ have been used. The cross section for $Q > Q_{min} = \hbar/1\,\mathrm{fm}$ is then:

$$\sigma_{Q>Q_{min}} = 2\pi \int_{Q_{min}/E}^{\infty} \left(\frac{d\sigma}{d\Omega}\right) \sin(\theta) d\theta \simeq \frac{4\pi\alpha^2}{Q^2_{min}} = 0.00067\,\mathrm{fm}^2, \tag{4.21}$$

or $6.7\,\mu\mathrm{b}$. The probability is greatest for ^{197}Au, with density $\rho_A = 3A/4\pi R_0^3 = 0.144\,\mathrm{fm}^{-3}$ and thickness $\sim \rho_A R_0 = 1\,\mathrm{fm}^{-2}$: $\sigma_{Q>Q_{min}}\rho_A R_0 \simeq 0.00067$. Hence the localization of charge has an insignificant effect.

The error introduced by choosing $\mathbf{r}$ from a uniform sphere instead of each shell's radial wave function is greatest by far in ^{197}Au, which has both the largest Z/R_0 and the largest variation in $< r^2 >$ between shells. The smallest and largest values are $< r^2_{1s} > = 6.6\,\mathrm{fm}^2$ and $< r^2_{1h^{11/2}} > = 35.4\,\mathrm{fm}^2$, while the uniform sphere has $< r^2 > = 28.4\,\mathrm{fm}^2$. The error in $< V_C(r) >$ is greatest for the $1s$ shell: 3.8 MeV. For the incoming electron, this would produce a 1% change in the elastic cross section at $Q^2 = 1\,(\mathrm{GeV/c})^2$ (or less at higher Q^2). Since the majority of shells have $< r_i^2 >$ much closer to $< r^2 >$, the error in the transparency is estimated to be $< 0.2\%$.

For finite impact parameters $r_\perp$, the Coulomb interaction also produces small deflections in the particle trajectories. Because the deflection is small it can be

approximated by integrating the transverse force along the undeflected trajectory (the straight line approximation). The deflection is less than or order of that for tangential trajectories with $r_\perp = R_0$:

$$\Delta p_\perp = \frac{1}{\beta c}\int_{-\infty}^{0} dr_{||} F_\perp = -\frac{Z\alpha\hbar}{\beta r_\perp}. \tag{4.22}$$

The integral is shown for the incoming electron. The outgoing electron and proton experience deflections of the same magnitude. The largest value occurs in Au, $\Delta p_\perp = -16.5\,\mathrm{MeV}/\beta c$. The deflection may be thought of as another contribution to the experimental p_m resolution. Inclusion of the deflection did not have a statistically significant ($< 0.5\%$) effect on the PWIA rate at the $Q^2 = 1\,(\mathrm{GeV/c})^2$ Au kinematics. This kinematics should be the most sensitive because the smaller experimental momenta result in larger ($\sim$ 10 mr) angular deflections. The width of the PWIA momentum distribution was increased negligibly (1.3%) by including the deflections. Because of its small effect, the deflection was not included in the PWIA calculation used in the present analysis.

On the other hand, the Coulomb deflection produces an observable increase in the PWIA count rate by bending non-impacting trajectories into the nucleus, an effect that is included in the PWIA calculation. The increase is easily calculated by conservation of angular momentum for rays that just graze the nucleus. The angular momentum of the incoming electron at $r_{||} = -\infty$ is $r_\perp k$ and at $r_{||} = 0$ is $R_0[k - V_C(R_0)]$. Equating these, one finds $r_\perp = R_0[1 - V_C(R_0)/k] > R_0$. The count rate scales as $r_\perp^2$, so it is increased by a factor $[1 - V_C(R_0)/k]^2$. The increase is largest (1.016) for Au at $Q^2 = 1\,(\mathrm{GeV/c})^2$.

IV.G. Spectrometer Acceptance Monte Carlos

The PWIA calculation requires models of the spectrometers in order to correctly simulate the experimental acceptances and resolutions. Monte Carlo models from earlier experiments [32,49] were modified to account for changes in the apparatus. In the Monte Carlos, the spectrometer optics are modelled with second-order Transport matrices [35] based on surveyed positions, wire-float measurements, and previous data. The 8 GeV/c optics model is not as well-constrained as the 1.6 GeV/c model because this was one of the earliest experiments using the 8 GeV/c in the large-acceptance tune, which is more sensitive to the strengths of the first two quadrupoles. The Monte Carlo uses beam-pipe aperture checks at strategic locations in the magnets to determine the spectrometer acceptance. The effects of multiple scattering, tracking resolution, and detector extents are also included.

Inverse matrix elements, allowing conversion from focal plane coordinates to target coordinates, were fit to "data" generated by the Monte Carlo. The inverse matrix elements were varied to minimize the RMS difference between the reconstructed (resolution-blurred) and generated (actual) target coordinates. In previous SLAC experiments, these matrix elements were used to reconstruct the data. In the current experiment, the data reconstruction matrix elements were derived independently through the use of kinematic correlations in $A(e,e'p)$ (Section III.C). The data-based and Transport-based reconstruction matrices agreed very well for the 1.6 GeV/c spectrometer, but not as well for the 8 GeV/c.

The inconsistencies indicate that the 8 GeV/c Transport model is not a complete description of the magnetic optics. The inconsistency is best demonstrated by comparison of the focal plane distributions of the data with those generated by the PWIA calculation (which includes the Monte Carlo model of the spectrometer). In the 1.6 GeV/c spectrometer, these distributions are consistent with each other up

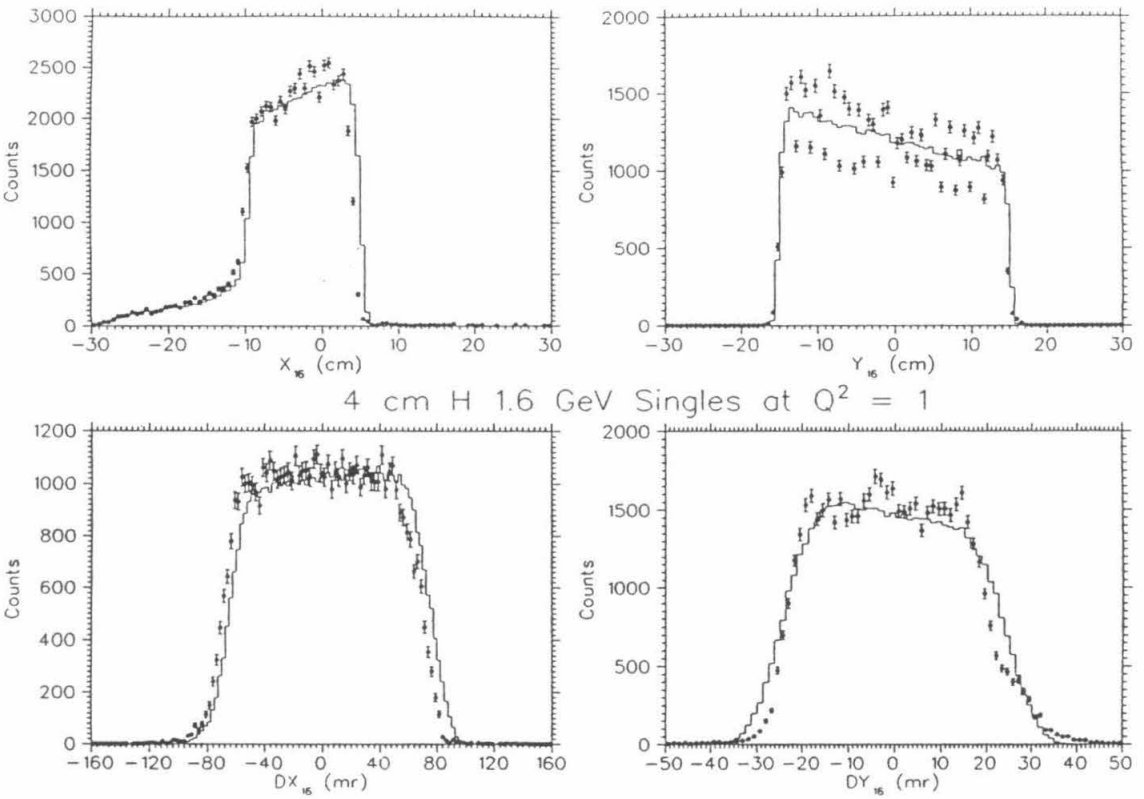

FIG. 45. **Distributions of the 1.6 GeV/c spectrometer focal plane coordinates for the ^{1}H(e,e) reaction at $Q^2 = 1\,(\mathrm{GeV/c})^2$. The points are the data and the histogram is the PWIA prediction for the same integrated luminosity.**

to shifts, which are accounted for with matrix element offsets (see Figure 45). The spikes in the Y_{16} spectrum are due to discrete track positions for unpaired wires. The discrepancy in dY_{16} is acceptable because dY_{16} is not important in the reconstruction. The other coordinates X_{16}, dX_{16}, and Y_{16} dominate the measurement of δ, Φ, and $\Delta\Theta$ respectively.

In the 8 GeV/c spectrometer, one can see good agreement (up to shifts) in X_8, dX_8, and Y_8 (Figure 46). However, the calculation's dY_8 distribution is roughly 2.5% too narrow. This disagreement is due to a problem with the optics model and not with the aperture sizes, because the height of the other distributions (hence

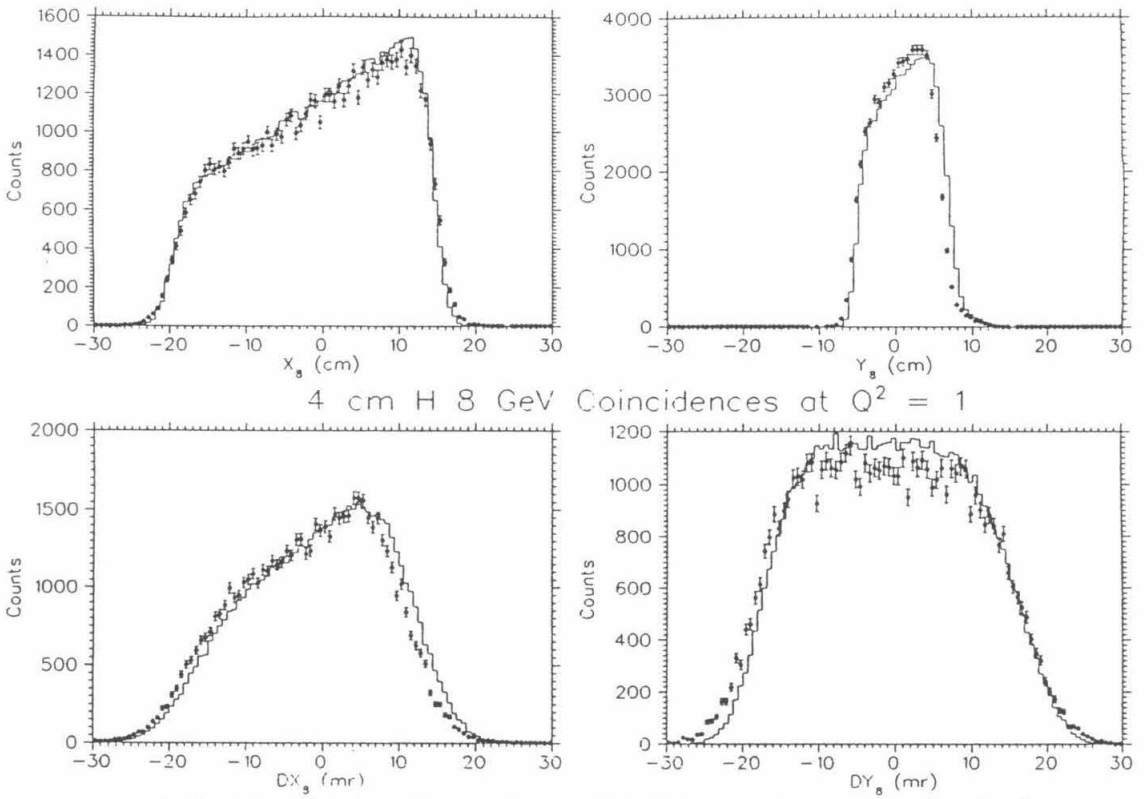

FIG. 46. **Distributions of the 8 GeV/c spectrometer focal plane coordinates for the ^{1}H$(e,e'p)$ reaction at $Q^2 = 1\,(\mathrm{GeV/c})^2$. The points are the data and the histogram is the PWIA prediction for the same integrated luminosity.**

the total acceptance) are correct and the disagreement persists when the 8 GeV/c illumination is restricted by placing cuts on the electron kinematics in the 1.6 GeV/c. The coordinates X_8 and dX_8 are sensitive to $\Delta\Theta$, Y_8 to δ, and dY_8 to Φ. (The width of Y_8 is determined not by the acceptance, but by the extent of the elastic stripe. The small disagreement in widths is probably due to too much tracking-resolution broadening in the spectrometer Monte Carlo.) In order to account for the limitations in the 8 GeV/c Transport model, we introduce several correction factors.

The Transport-based inverse matrix elements are reconstructed from the spectrometer Monte Carlo focal plane coordinates. This way, the resolution of the Monte

Carlo is not artificially degraded by differences between the forward and reverse optics models. In the 8 GeV/c, the Monte Carlo reconstruction matrices are subjected to two *ad hoc* modifications. The resulting inconsistency between the forward and reverse Monte Carlo matrix elements is necessary in order to compensate for the dY_8 inconsistency described above and for the presence of a large third-order term in the $\Delta\Theta$ data reconstruction matrix. The dY_8 inconsistency is handled by the use of a modified Φ reconstruction:

$$\Phi_8^{MC,new} = 1.025\Phi_8^{MC}. \tag{4.23}$$

Furthermore, the $\Delta\Theta$ reconstruction matrix elements are replaced by those derived from kinematic correlations in the data (Section III.C):

$$(\Delta\Theta|...)_8^{MC,new} = (\Delta\Theta|...)_8^{data}. \tag{4.24}$$

Without this change, the presence of the third-order term in the data reconstruction but not in the Monte Carlo reconstruction creates a 3-4% dependence of the H$(e, e'p)$ cross section on the $\Delta\Theta_8$ cut. These modifications and the uncertainty in their origin are the main source of the 5% systematic error in the understanding of the acceptances.

V. RESULTS

Extraction of the spectral function $S(E_m, p_m)$ and the nuclear transparency T are performed assuming the scattering can be modelled by the calculation discussed in Section IV, based on the Plane Wave Impulse Approximation with an Independent Particle Shell Model $S(E_s, \mathbf{p})$. The calculation improves on the PWIA in several ways, but it does not include any effects from Initial and Final State Interactions. In Section V.A the measured $S(E_m, p_m)$ are compared with the results of the PWIA calculation in order to demonstrate the success of the PWIA and to check the input IPSM $S(E_s, \mathbf{p})$. The good agreement of the data and the calculation then justifies the extraction of T as the ratio of the data and PWIA rates.

For $|p_m| < 250\,\mathrm{MeV/c}$ the FSI are modelled in the analysis as producing a uniform suppression of the count rate by the measured value of T. Monte Carlo calculations of the experiment, including the FSI in a semi-classical cascade model using the free nucleon-nucleon cross section, indicate that the FSI distortions to the measured $S(E_m, p_m)$ are $\lesssim 5\%$ for $|p_m| < p_f$ [50]. This is because the average angular deflection in elastic NN interactions is $\gtrsim 5°$, much larger than the spectrometer acceptances. (In fact the deflection is $\sim 20°$ at $Q^2 = 1\,(\mathrm{GeV/c})^2$, where the elastic cross section is largest.) The large deflection is due to the large average t of the elastic differential cross section and to Pauli blocking of small-t collisions. Note that inelastic events occur at $E_m > m_\pi$ and are not accepted.

In extracting $S(E_m, p_m)$ and $T(Q^2)$, the acceptance of both spectrometers was restricted to $|\delta| < 5\%$, $|\Delta\Theta| < 15\,\mathrm{mr}$, and $|\Phi| < 40\,\mathrm{mr}$ where the acceptance functions $A_{16}(E', \Omega_{k'})$ and $A_8(E'_p, \Omega_{p'})$ are large.

V.A. Extraction of $S(E_m, p_m)$

In principle, the spectral function $S(E_s, p)$ could be extracted by dividing the measured six-fold differential cross section by σ_1^{cc} (Equation 1.9). In practice, finite measurement statistics do not allow binning the data in six dimensions. An alternate approach involves binning the data in only E_m and p_m and dividing by the rate that would be measured if $S(E_m, p_m)$ were equal to one.

Specifically, in the PWIA, the number of true coincidences measured in a bin during a run of integrated luminosity $\mathcal{L} = \int Ldt$ is:

$$N_{true}(E_m, p_m) = \mathcal{L} \int_{E_m, p_m} dE' d\Omega_{k'} dE'_p d\Omega_{p'} [p' E'_p \sigma_1^{cc} S(E_m, p_m)] A_{16}(E', \Omega_{k'}) A_8(E'_p, \Omega_{p'}). \tag{5.1}$$

Here the term in brackets is the differential cross section, Equation 1.9. The integration region is over *all* kinematics with (E_m, p_m) inside the bin.

If the value of $S(E_m, p_m)$ is approximately constant across the bin, it can be pulled out of the integral. Also, due to the large range of kinematics that can contribute to the same (E_m, p_m) bin, the term $p' E'_p \sigma_1^{cc}$ can vary by factors of two in the integral. Contributions of these variations to the statistical error in $S(E_m, p_m)$ is minimized by applying this term as a weight to the data counts. That is, the relevant values of this term are not the average over all possible kinematics, but the values actually observed for each event. Then the spectral function can be extracted as:

$$S(E_m, p_m) \simeq \frac{1}{\mathcal{L} I_{PS}} \sum_{true} \frac{1}{p' E'_p \sigma_1^{cc}} = \frac{1}{\mathcal{L} I_{PS}} N_{true}^{weighted}. \tag{5.2}$$

Here $N_{true}^{weighted}$ is given below and the phase space integral I_{PS} is given by Equation 3.8. In principle, the inverse of the acceptance functions could also be applied directly as weights to the data, further reducing the statistical error. This is not done because the increased weighting of counts with small acceptances would amplify the systematic errors due to mismatch between the model and actual acceptances.

For a measurement of the spectral function, Equation 3.1 is used with a range $\mathcal{R}$ corresponding to a single (E_m, p_m) bin. The weight is applied to counts in $\mathcal{R}$ when calculating N_{true}, N_{peak}, and N_{acc}:

$$N^{weighted} = \sum_{counts} \frac{1}{p' E'_p \sigma_1^{cc}}. \tag{5.3}$$

It is not necessary to weight counts when calculating $N_{win}^{\mathcal{F}}$ and $N_{acc}^{\mathcal{F}}$. Because of the small bin size, the unweighted $N_{acc} \ll N_{acc}^{\mathcal{F}}$ and binomial weighting is not used in the calculation of the statistical error.

Equation 5.2 can be used to extract a value of $S(E_m, p_m)$ at one θ_8 setting. In the (E_m, p_m) bins where more than one θ_8 can be used, the best statistics are obtained by combining the $S(E_m, p_m)$ measurements with weights given by the counting statistics. Unfortunately, direct averaging of $S(E_m, p_m)$ values calculated independently at each θ_8 is made difficult by the unknown error in a measurement with zero counts. Furthermore, in bins with low statistics, weighted averages bias the result to artificially low values because of underestimation of the statistical errors in fluctuations to small values. This difficulty is avoided and the correct weighting is achieved by simply summing the numerator and the denominator of Equation 5.2 over θ_8 before dividing.

Radiative effects in the data produce distortions in the measured spectral functions (Equations 4.5 and 4.6), which are difficult to remove. Currently, radiative effects have not been removed from the measured $S(E_m, p_m)$, which therefore do not represent the true (unradiated) $S(E_s, p)$ described in Section I.A.1. Fortunately, the $S(E_m, p_m)$ data can still be used to verify the validity of the PWIA/IPSM model and therefore, of the transparency analysis. When comparing the measured values with the model spectral function, radiative effects are instead added to the model spectral function as described earlier in Section IV.A.

In the following graphs, the comparison is usually shown for $S(E_m, p_m)$ integrated

over the p_m or E_m ranges (listed in Table 11) used to measure the transparency. For example, Figure 47 shows the deuteron momentum distribution $n(p_m)$, obtained by integrating the $S(E_m, p_m)$ measured at $Q^2 = 1$–$7\,(\mathrm{GeV/c})^2$ over dE_m for $-30 < E_m < 100\,\mathrm{MeV}$. The error bars shown in this and the following graphs are statistical only. For the systematic errors, see Section V.C. Also shown is a histogram giving the integral of the $S(E_m, p_m)$ extracted from the PWIA Independent Particle Shell Model prediction, calculated using the Bonn potential wave function [42]. In this and the following graphs, the PWIA result is scaled by the measured transparency (see Section V.B). The statistics of the PWIA $S(E_m, p_m)$ are generally $\gtrsim 10$ times higher than the data, so its error bars are not shown. The graph exhibits, at all Q^2, good agreement over several orders of magnitude between the data and the PWIA prediction.

Figure 48 shows the deuteron E_m distribution $P(E_m)$, obtained by integrating the $S(E_m, p_m)$ measured at $Q^2 = 1$–$7\,(\mathrm{GeV/c})^2$ over $d^3p_m = 2\pi p_m^2 dp_m$ for $-170\,\mathrm{MeV/c} < \mathrm{p_m} < 170\,\mathrm{MeV/c}$. In the absence of radiation and resolution, the E_m distribution would be a delta function at 2.2 MeV, the deuteron binding energy. The difference in the heights and widths of the data and PWIA peaks is due to imperfect simulation of the spectrometer resolutions in the PWIA calculation. One sees that the resolution degrades with increasing Q^2 due to the larger momenta involved in the measurement of E_m and p_m. The peak is followed by a tail due to internal and external radiation. Because $S(E_m, p_m)$ is highly peaked at $p_m \simeq 0$ (see Figure 47), the tails satisfy $|p_m| \sim E_m$ (see Equations 4.5 and 4.6). Thus, even though the radiative strength dies rapidly with increasing E_m, the p_m^2 weighting causes the tail height to look almost constant. The absence of strength at $E_m \gtrsim 120\,\mathrm{MeV}$ is due to the lack of E_m acceptance there.

Figure 49 shows the carbon $P(E_m)$ measured at $Q^2 = 1\,(\mathrm{GeV/c})^2$ for $0 < p_m < 250\,\mathrm{MeV/c}$. The range extends beyond the fermi momentum $p_f \sim 220\,\mathrm{MeV/c}$, so

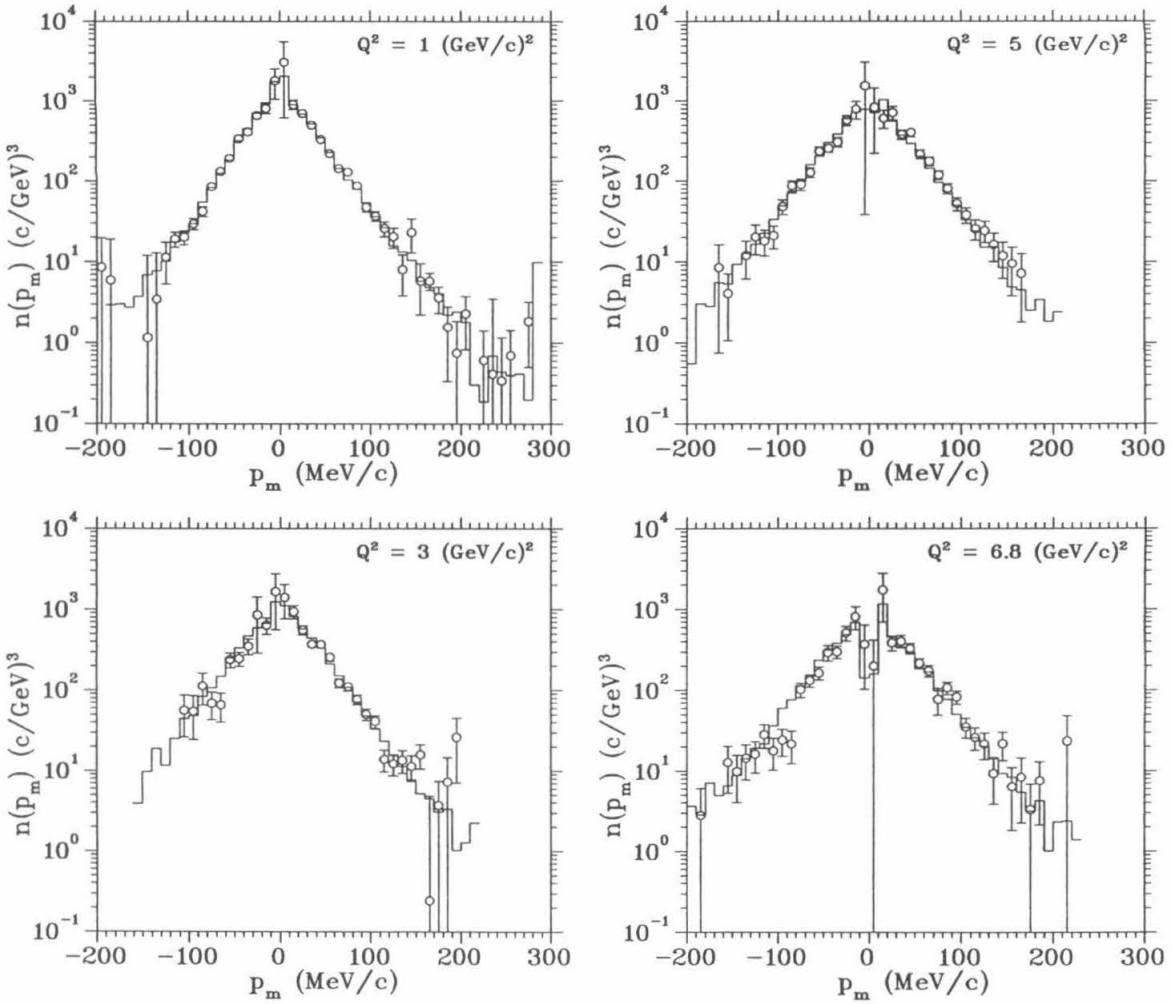

FIG. 47. ^{2}H p_m distribution at $Q^2 = 1$–$7\,(\mathrm{GeV/c})^2$. **Points with error bars are the integral over $-30 < E_m < 100\,\mathrm{MeV}$ of $S(E_m, p_m)$ extracted from the data and the histogram is the integral of $S(E_m, p_m)$ extracted from the PWIA calculation, scaled by the measured transparency. The error bars shown in this and the following graphs are statistical only.**

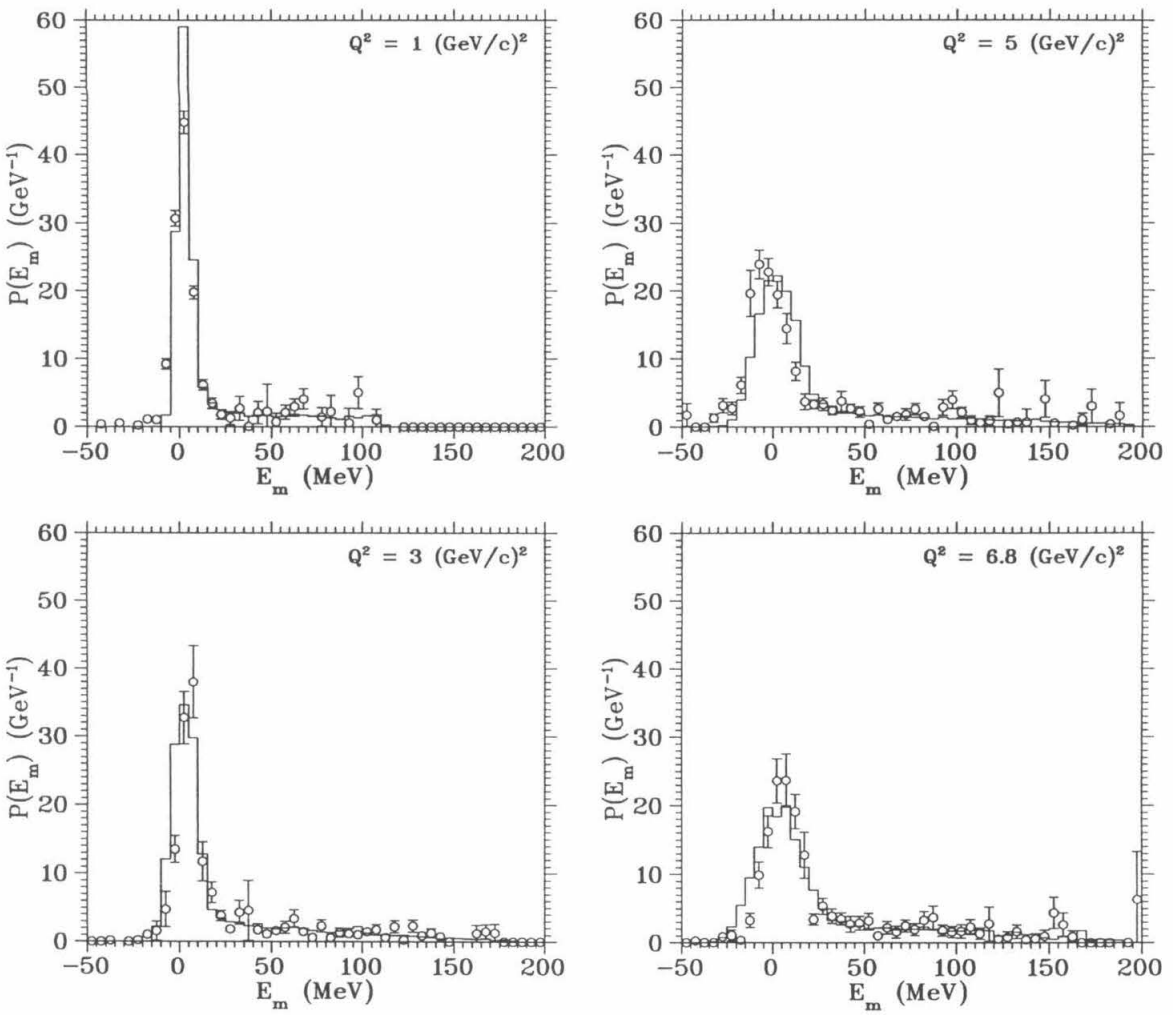

FIG. 48. ^{2}H E_m distribution at Q^2 = 1–7 $(\mathrm{GeV/c})^2$ for $|p_m| < 170\,\mathrm{MeV/c}$. The histogram is the PWIA result, scaled by the transparency.

most of the spectral function strength is included. The narrow peak at $E_m \simeq 17\,\mathrm{MeV}$ due to the carbon $1p$ nuclear shell and the broad peak at $E_m \simeq 38\,\mathrm{MeV}$ due to the $1s$ shell seen in this figure are more clearly exhibited in Figure 50 because of finer binning. This figure shows the data counts binned in E_m for the $Q^2 = 1\,(\mathrm{GeV/c})^2$, $\theta_8 = 43.4°$ kinematics. In Figure 49 a shift of $-2.5\,\mathrm{MeV}$ is applied to the PWIA result. This is done to cancel disagreement with the data on the position of the $1p$ peak, apparently produced by changes in offset matrix elements (the position used in the PWIA is known to better than 1 MeV). The shift is not applied in Figure 51, which shows the measured E_m distribution at each value of Q^2. As Q^2 increases, the peaks become broader and the relative height of the radiative tail increases due to the larger momenta involved.

One observes that the $1s$ shell in the PWIA has more strength at low E_m than does the data. Previous $A(e,e'p)$ experiments have indicated that the energy distribution of the nuclear shells are skewed to high E_s (see Figure 6) but for simplicity the IPSM spectral function uses a symmetric Lorentzian. The asymmetry is not due to multi-nucleon effects (such as correlations) at large E_m because it is observed even in the valence orbitals of ^{208}Pb. Fortunately, the discrepancies in the data and PWIA E_m distributions due to this and the E_m shift mentioned above do not bias the measurement of transparency, which is largely insensitive to the details of the energy distribution. This is because $P(E_m)$ is small at the edges of the $0 < E_m < 100\,MeV$ range used to measure T and because the range includes the majority of the spectral function strength.

In fact, the PWIA Independent Particle Shell Model input spectral function has very little strength at $E_m \gtrsim 60\,\mathrm{MeV}$ (Figure 52). The high-E_m strength in the ^{12}C PWIA/IPSM curves is caused by the radiative tails of the single-particle strength at $E_m \lesssim 60\,\mathrm{MeV}$. Note the radiative effects are more pronounced than in low-Q^2 measurements because E, E', and E'_p are large compared to E_m. The good

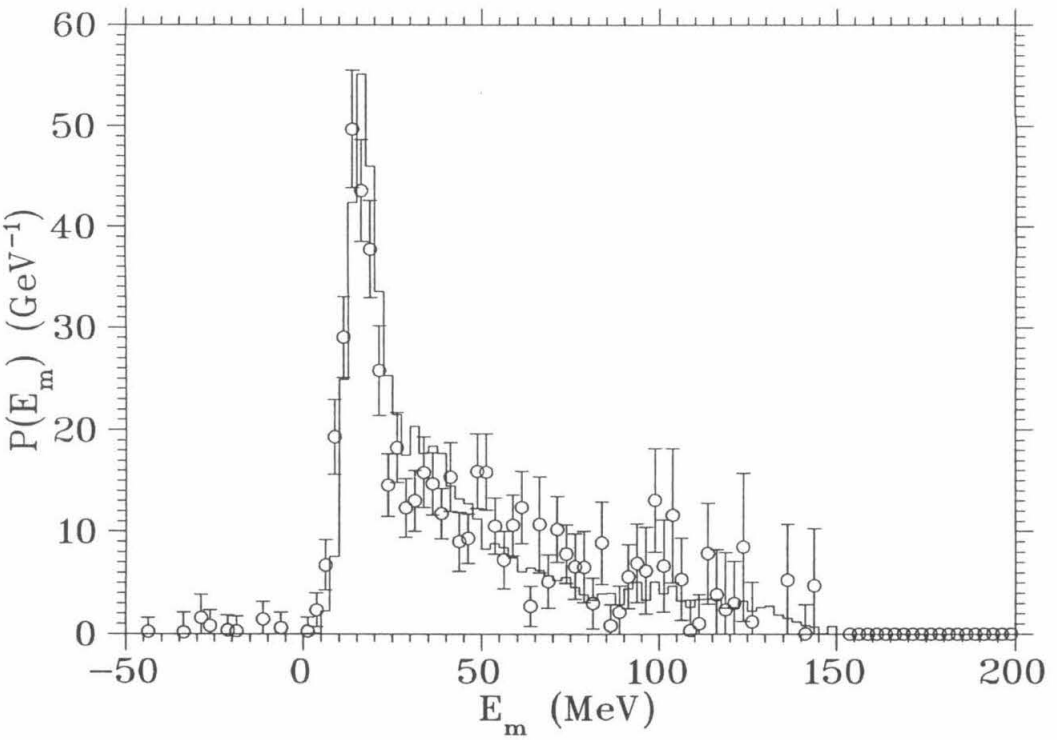

FIG. 49. ^{12}C E_m **distribution at** $Q^2 = 1\,(\mathrm{GeV/c})^2$ **for** $0 < p_m < 250\,\mathrm{MeV/c}$. **The two curves are as in Figure 47.**

agreement of the data and PWIA/IPSM E_m distributions for $E_m \gtrsim 60\,\mathrm{MeV}$ indicates that there is not a great deal of strength from multi-nucleon processes (*e.g.*, dynamic correlations) in the measured range of p_m, in spite of the concerns mentioned in reference [14]. Presumably these effects are more important at $p_m > p_f$. As was the case for the nucleus ^{2}H, the importance of the radiative tail is enhanced in the $P(E_m)$ distribution because of the p_m^2 weighting in the integral over p_m. The significance of the correlation tail at high p_m and E_m is also increased.

The single-particle nature of the observed strength is dramatically confirmed by the separate momentum distributions of the $1p$ and $1s$ shells, shown in Figure 53. These were obtained by integrating the $S(E_m, p_m)$ measured at $Q^2 = 1\,(\mathrm{GeV/c})^2$ over

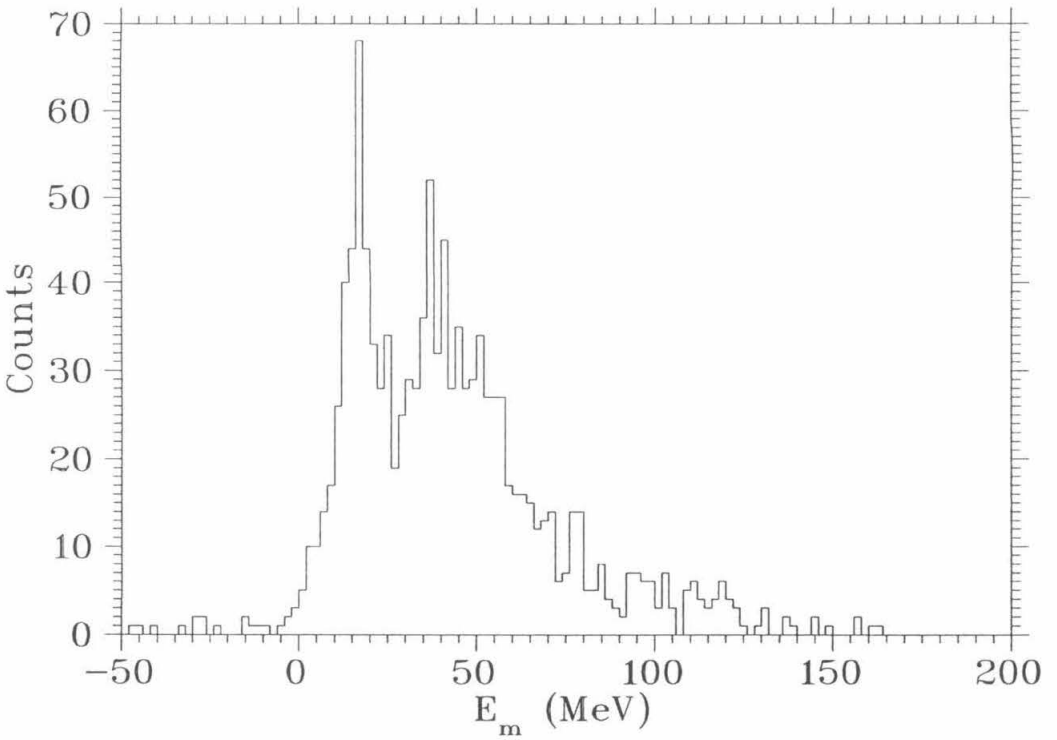

FIG. 50. ^{12}C E_m **counts at** $Q^2 = 1\,(\mathrm{GeV/c})^2$ **and** $\theta_8 = 43.4°$ **(no** p_m **cut). Background from accidental coincidences has not been subtracted. The prominence of the** $1s$ **shell peak is enhanced by the low values of missing momenta accepted at this angle** ($|p_m| \lesssim 100\,\mathrm{MeV/c}$).

$-20 < E_m < 25\,\mathrm{MeV}$ and $35 < E_m < 70\,\mathrm{MeV}$, respectively (after the -2.5 MeV shift in the PWIA E_m). The data clearly exhibits the p and s shell behavior present in the PWIA/IPSM calculation: peaks at $|p_m| \simeq 100\,\mathrm{MeV/c}$ and $p_m \simeq 0$, respectively. The gap in the $1s$ momentum distribution at $p_m \simeq 0$ is due to the absence of measurement phase space there ($d^3p_m = 2\pi p_m^2 dp_m \simeq 0$ for small p_m). Note that to reduce systematic errors at the edge of the (E_m, p_m) acceptance, bins with $I_{PS} < 10\%$ of its maximum value at each θ_8 are not included in the integrals over the $S(E_m, p_m)$ of solid targets. This exclusion is not practiced for ^{2}H, which is highly peaked at $p_m = 0$.

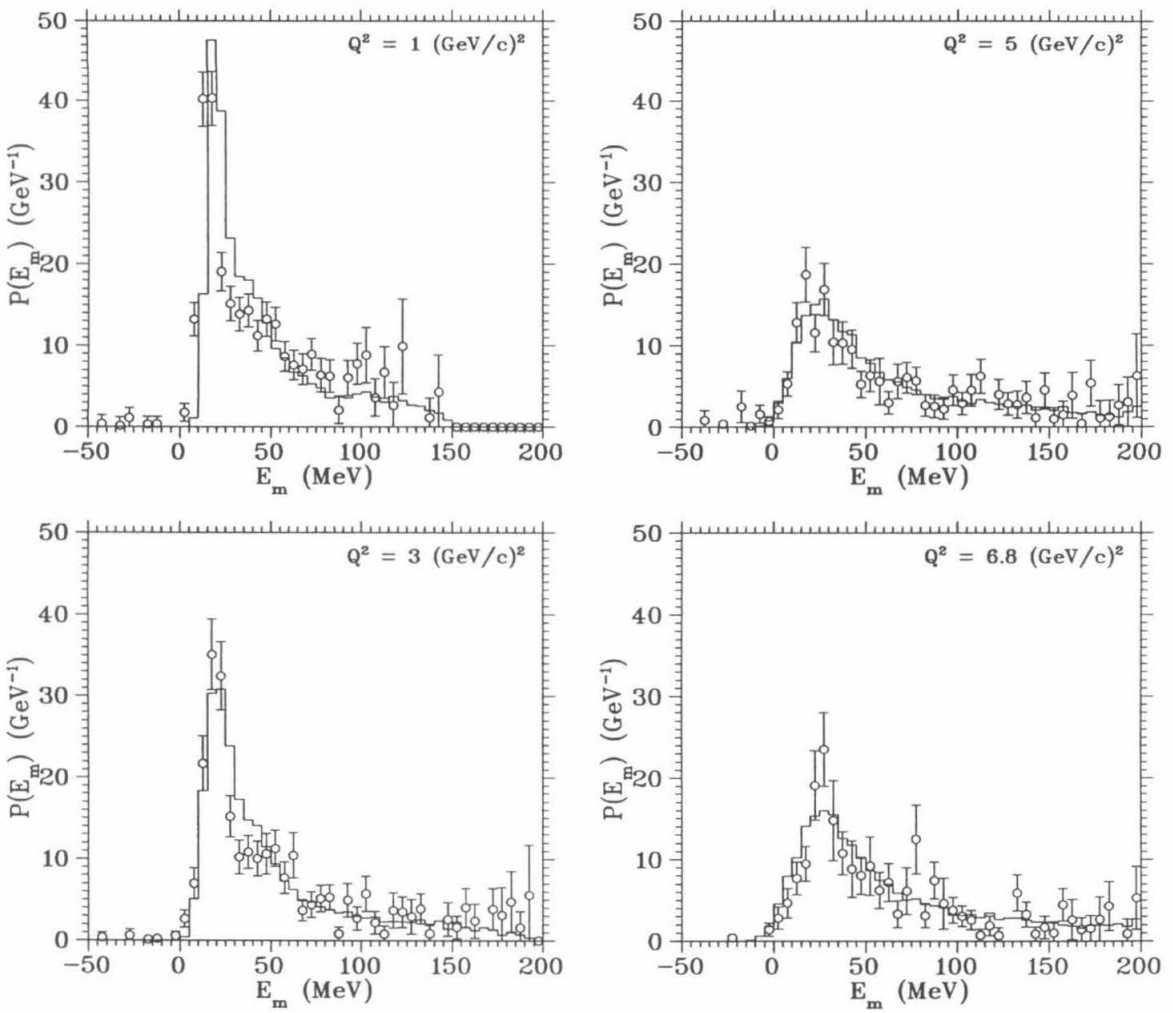

FIG. 51. ^{12}C E_m distribution at $Q^2 = 1$–$7\,(\mathrm{GeV/c})^2$ for $0 < p_m < 250\,\mathrm{MeV/c}$. The two curves are as in Figure 47.

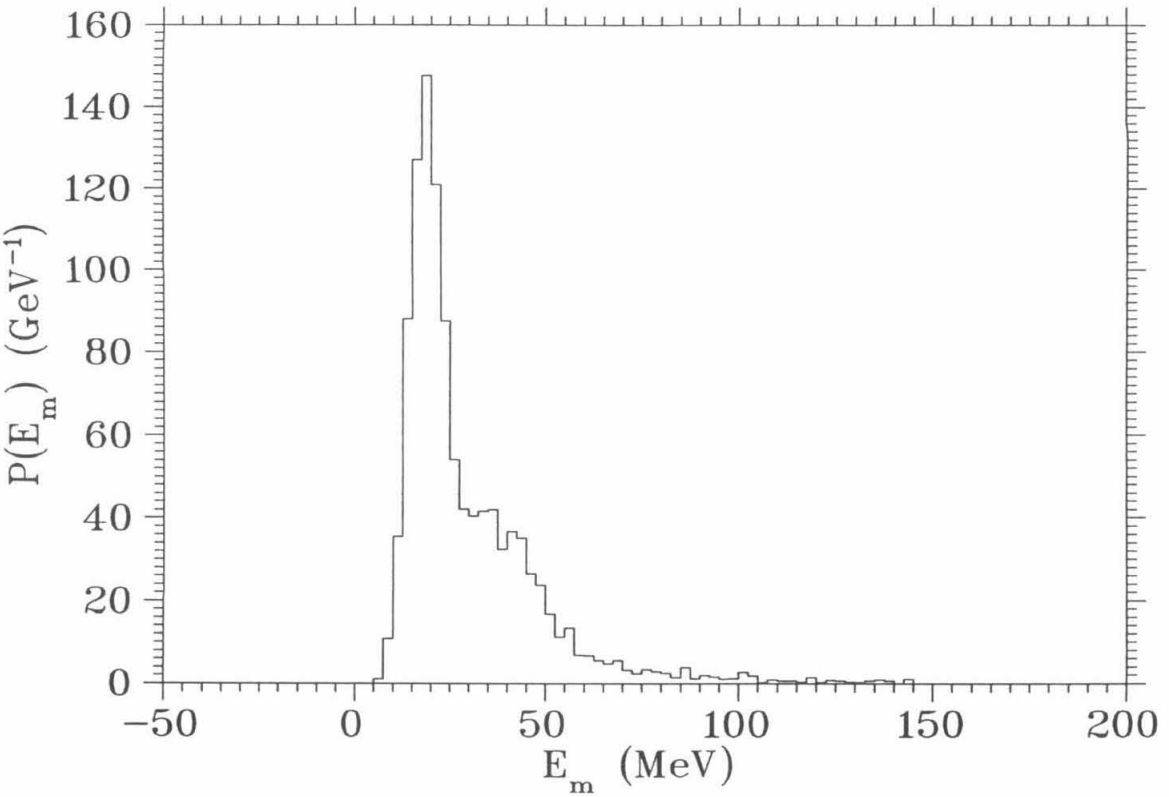

FIG. 52. E_m **distribution for** ^{12}**C at** $Q^2 = 1\,(\mathrm{GeV/c})^2$ **from the PWIA calculation with radiative effects disabled.**

The total ^{12}C momentum distribution, shown in Figure 54, is obtained by integrating $S(E_m, p_m)$ over $-30 < E_m < 100\,\mathrm{MeV}$. The data exhibit good agreement with the PWIA/IPSM at all p_m and Q^2. One observes that, due to time constraints during the experiment, the distribution was not as well-measured at $p_m < 0$.

The data on ^{56}Fe and ^{197}Au were taken with fewer statistics, but also indicate the success of the single-particle PWIA description. In Figures 55 and 56, one observes that the E_m resolution is not sufficient to distinguish the more-closely spaced energy levels of Fe and Au. But the PWIA/IPSM adequately describes the general shape of the E_m distributions. At $Q^2 \geq 5\,(\mathrm{GeV/c})^2$ in both nuclei, the statistics are so bad that the data can hardly be called a measurement of the spectral function.

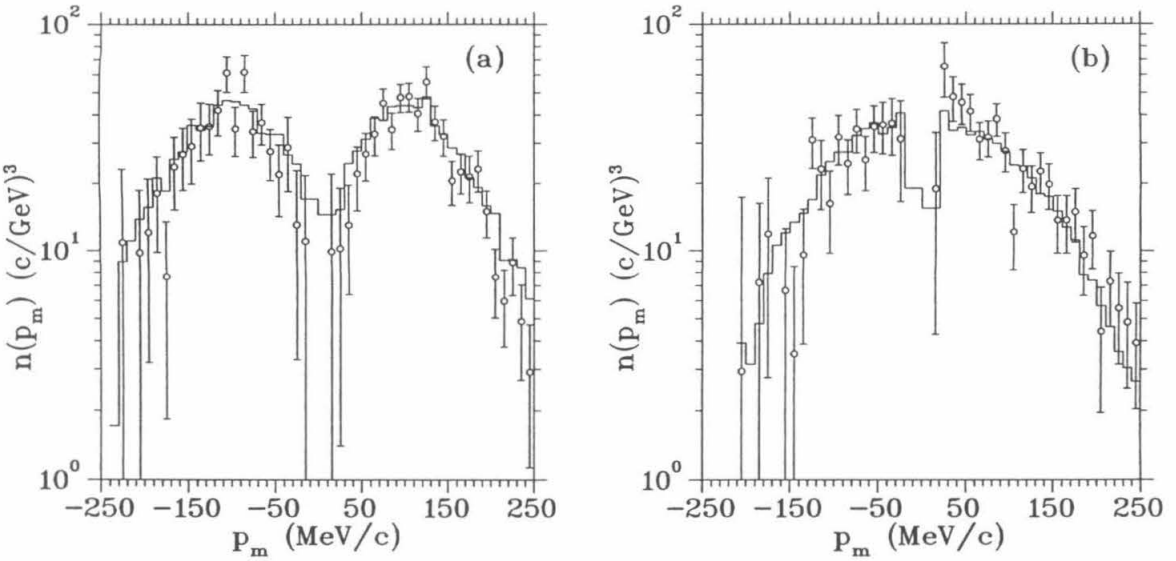

FIG. 53. ^{12}C **(a)** $1p$ **and (b)** $1s$ p_m **distributions at** $Q^2 = 1\,(\mathrm{GeV/c})^2$ **for** $-20 < E_m < 25\,\mathrm{MeV}$ **and** $35 < E_m < 70\,\mathrm{MeV}$ **respectively. The points and histogram are as in Figure 47.**

The Fe and Au p_m distributions, presented in Figures 57 and 58, also indicate the continued success of the PWIA/IPSM description. It is important to note, however, that the momentum distributions used in the PWIA/IPSM calculation is narrower than those used to fit $A(e,e'p)$ measurements at low Q^2. The apparent discrepancy in the measured p_m widths is probably due to uncertainties at low Q^2 in the corrections for proton FSI and Coulomb distortions (see Appendix E).

In conclusion, one observes excellent overall agreement between the data and the PWIA/IPSM model. The agreement indicates that the single-particle PWIA description of the scattering describes the dominant contribution to the scattering. The observed disagreements do not greatly influence the transparency measurement and could be removed by refining the IPSM model. The $S(E_m, p_m)$ of Fe and Au are measured for the first time, with errors comparable to the previous, low-Q^2 measurements

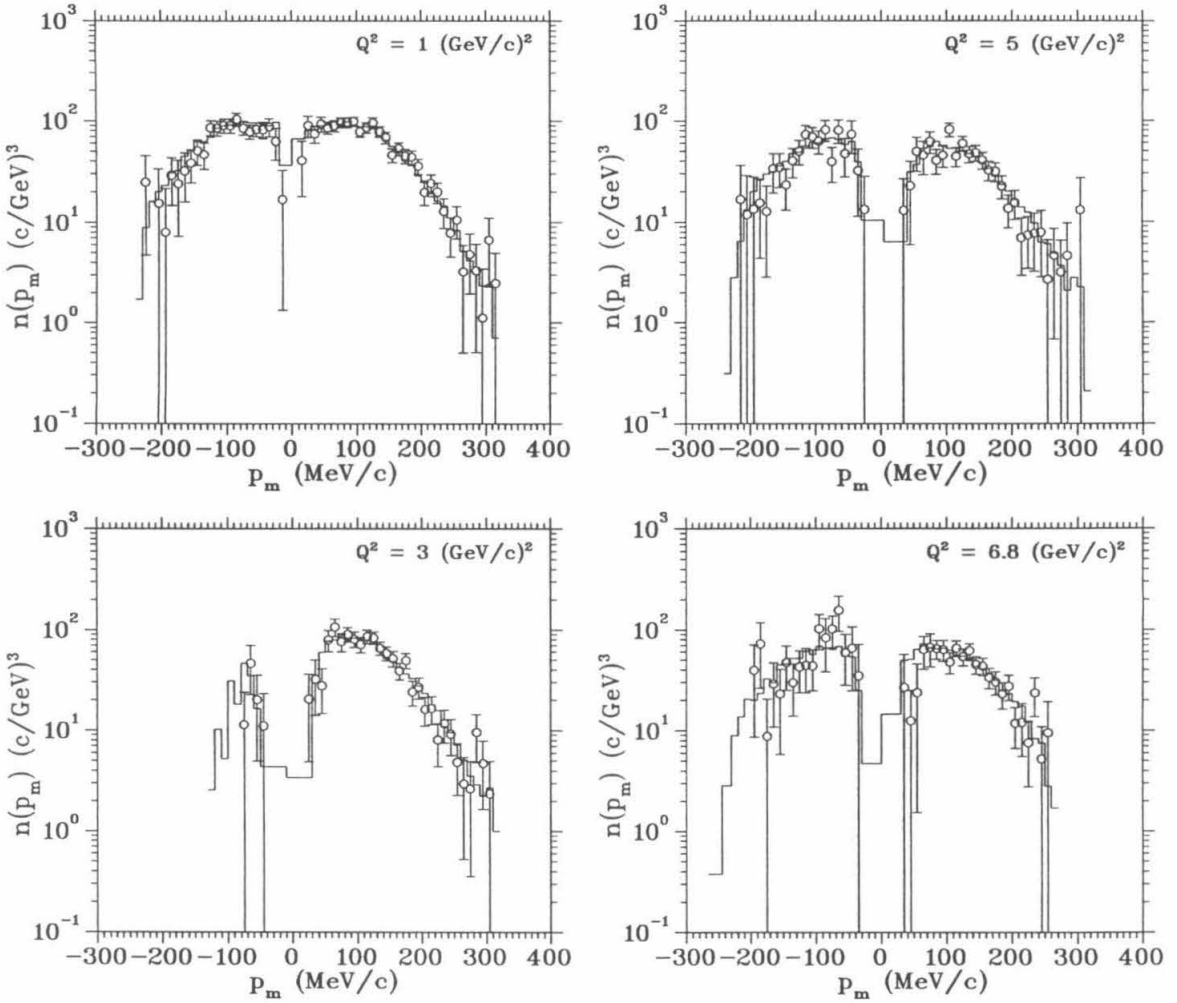

FIG. 54. ^{12}C p_m distribution at $Q^2 = 1$–$7\,(\mathrm{GeV/c})^2$ for $-30 < E_m < 100\,\mathrm{MeV}$. The two curves are as in Figure 47.

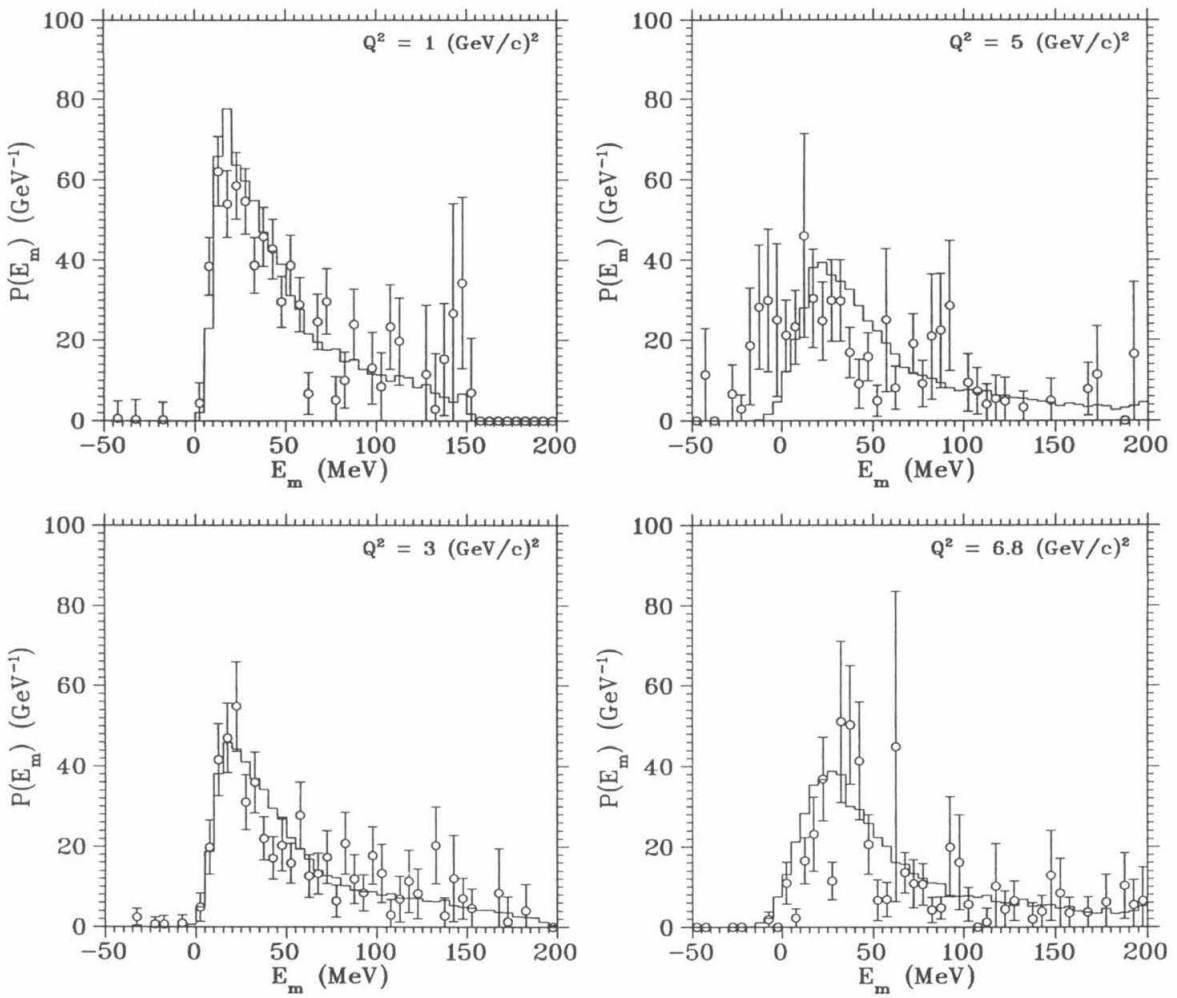

FIG. 55. ^{56}**Fe** E_m **distribution at** $Q^2 = 1$–$7\,(\mathrm{GeV/c})^2$ **for** $0 < p_m < 250\,\mathrm{MeV/c}$. **The two curves are as in Figure 47.**

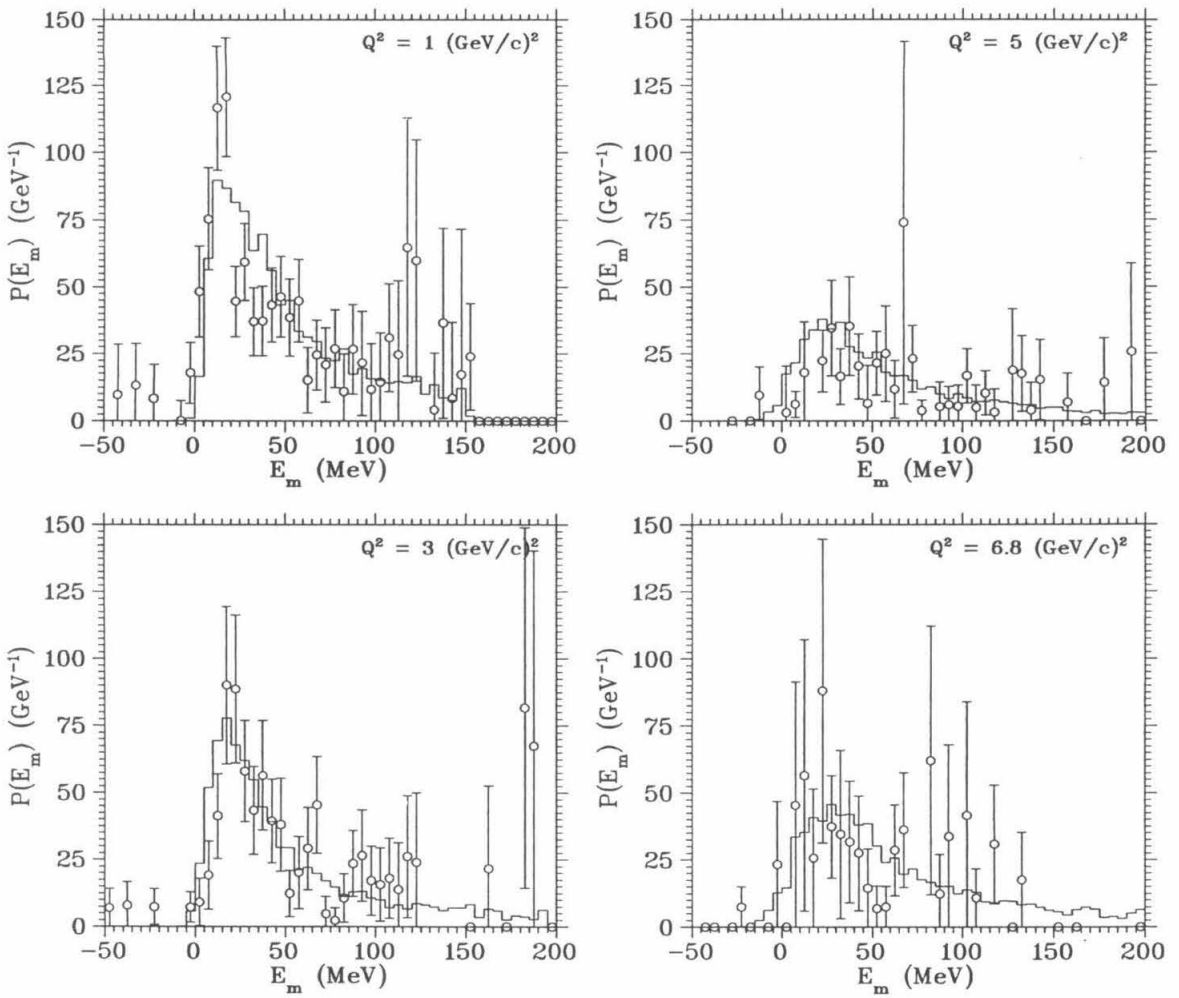

FIG. 56. ^{197}Au E_m distribution at $Q^2 = 1$–$7\,(\mathrm{GeV/c})^2$ for $0 < p_m < 210\,\mathrm{MeV/c}$. The two curves are as in Figure 47.

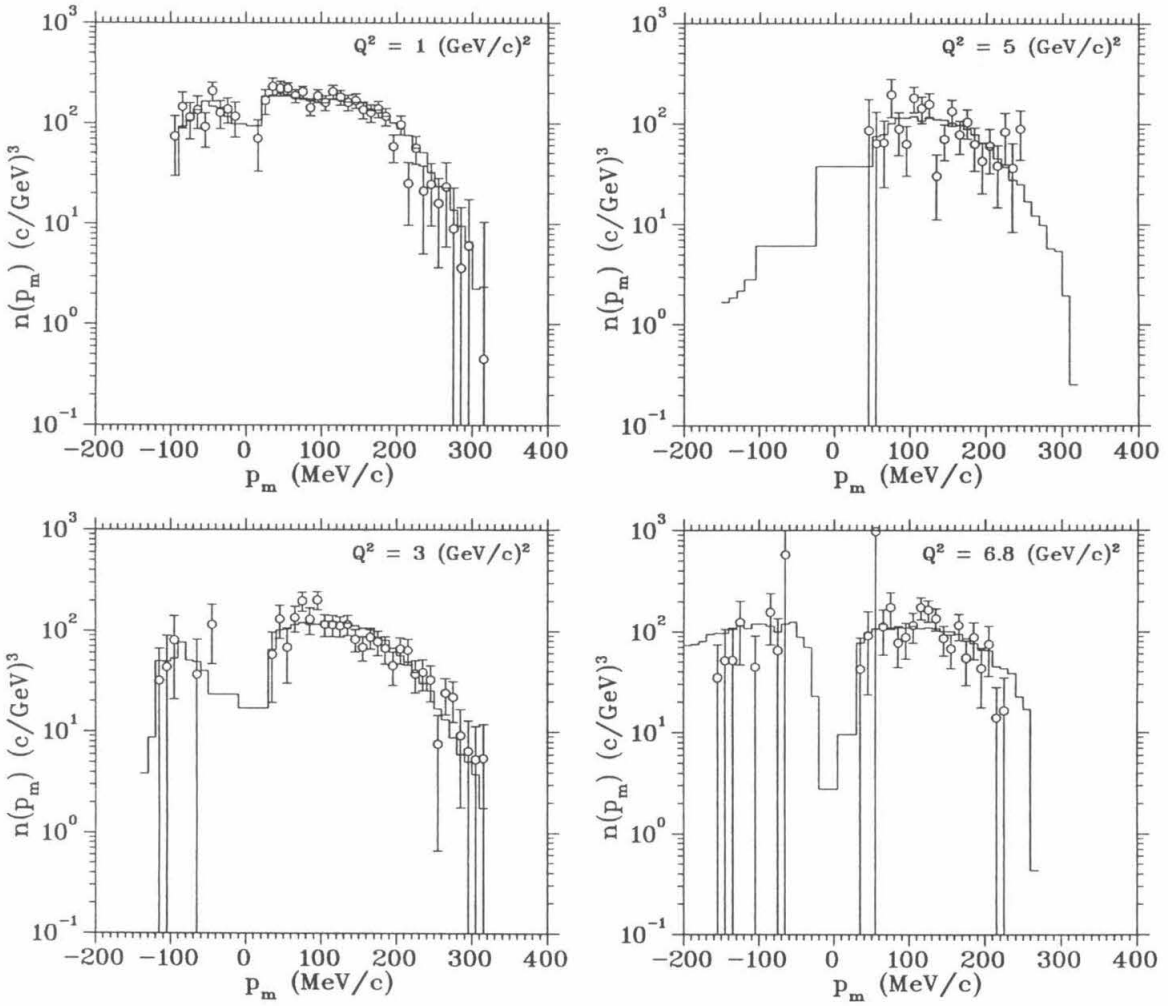

FIG. 57. ^{56}**Fe** p_m **distribution at** $Q^2 = 1$–$7\,(\mathrm{GeV/c})^2$ **for** $-30 < E_m < 100\,\mathrm{MeV}$. **The two curves are as in Figure 47.**

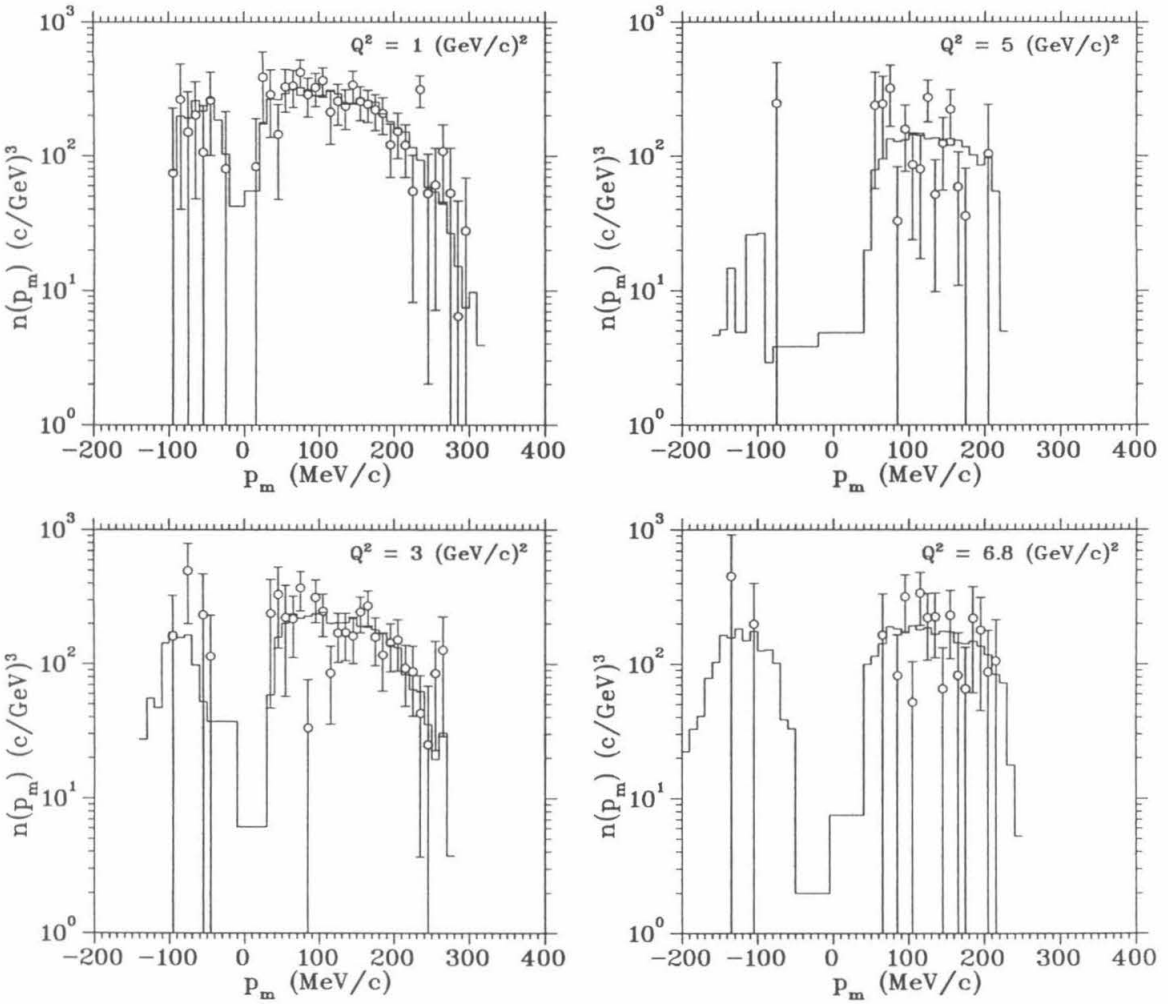

FIG. 58. ^{197}Au p_m **distribution at** $Q^2 = 1$–$7\,(\mathrm{GeV/c})^2$ **for** $-30 < E_m < 100\,\mathrm{MeV}$. **The two curves are as in Figure 47.**

of nearby nuclei. Due to the higher momenta involved, the current measurements have poorer (E_m, p_m) resolution than the low-Q^2 data. Interestingly, the momentum distributions of Fe and Au appear to be narrower than observed in the low-Q^2 experiments for nearby nuclei. As expected, the data show no evidence of distortion due to the FSI of the proton (excluding the re-normalization due to absorption) or of significant multi-nucleon effects at $|p_m| < 250\,\mathrm{MeV/c}$. The success of the PWIA/IPSM description of the scattering justifies the use of this model in the calculation of the nuclear transparency T.

V.B. Measurement of $T(Q^2)$

At low Q^2 the fraction of saturation of the spectroscopic sum rule (Equation 1.10) was given by the integral of the measured $S(E_m, p_m)$,

$$Z_{eff} = \int_0^\infty dE_m \int_0^\infty d^3p_m S(E_m, p_m), \tag{5.4}$$

divided by Z. As discussed in Section I.A.2, one shortcoming of this approach is that $S(E_m, p_m)$ is only measured in a finite range of (E_m, p_m), so the integral over the measured region is artificially low. Ideally, a correction would be applied based on a model for the amount of the Z_{eff} strength outside of the experimental acceptance. In addition to this model dependence, measurement of $S(E_m, p_m)$ also assumes the validity of the PWIA cross section (see Equation 5.2). (Although in the low-Q^2 experiments, the approximation is improved by dividing Z_{eff} by the prediction of the Distorted Wave Impulse Approximation instead of Z.)

For the current experiment, the use of $T = Z_{eff}/Z$ would be further complicated by the presence of radiative effects in the measured $S(E_m, p_m)$. The presence of internal bremsstrahlung and internal virtual photons changes both the distribution and the magnitude of $S(E_m, p_m)$. Except through the use of a full radiative correction procedure, the correction for these effects would also depend on the model of $S(E_s, \mathbf{p})$.

Use of Equation 5.4 would generate additional problems common to measurements which require binning the data. First, the statistical error is increased by unequal weighting of counts. The presence of $d^3p_m = 4\pi p_m^2 dp_m$ in the Z_{eff} integral makes the $S(E_m, p_m)$ measurement especially sensitive to the values at high p_m, where the statistical errors are large. The method is likely to be very unreliable at $Q^2 \geq 5\,(\mathrm{GeV/c})^2$ for the Fe and Au nuclei, where the statistics are especially poor.

Second, the biases introduced by reconstruction errors (offsets and resolution) are amplified by the binning. For example, the width of the p_m distribution increases

TABLE 11. The (E_m, p_m) range $\mathcal{R}$

Targets	$E_{m,min}$	$E_{m,max}$	$p_{m,min}$	$p_{m,max}$
^{1}H, ^{2}H	-30 MeV	100 MeV	-170 MeV/c	170 MeV/c
C, Fe	-30 MeV	100 MeV	0 MeV/c	250 MeV/c
Au	-30 MeV	100 MeV	0 MeV/c	210 MeV/c

with Q^2 due to the degraded resolution. Thus, the p_m^2-weighted integral also increases, mimicking the onset of CT. Third, errors in the acceptance function are amplified by the binning since the uncertainty in $A_{16}A_8$ at the edge of the acceptance is larger than the error in the product of the spectrometers' solid angles.

In light of the preceding discussion, the technique used in the current experiment is division of the measured rate in a large (E_m, p_m) range $\mathcal{R}$ (given in Table 11) by the rate calculated in the PWIA/IPSM. Although still dependent on the model for $S(E_s, \mathbf{p})$, the PWIA calculation is more accurate than the standard PWIA used in Equation 5.4. Furthermore, the method maximizes the use of the data statistics by weighting the counts equally and is sensitive only to the broad structure of the spectral function and acceptance functions.

The extraction of T only uses data where the acceptance of the spectrometers and the shape of the spectral function are well described. In order to maximize statistics and minimize sensitivity to details of the spectral function model, the range $\mathcal{R}$ is chosen to be as large as possible without including (E_m, p_m) bins where I_{PS} is $< 10\%$ of its maximum value for all θ_8. Rejecting events with $E_m \gtrsim 140\,\mathrm{MeV} \simeq \mathrm{m}_\pi$ ensures that no inelastic processes have occurred. Use of $|p_m| < 250\,\mathrm{MeV/c}$ for the solid targets minimizes the contribution of the correlation tail.

At each kinematic setting, the measured transparency is:

$$T(Q^2, \theta_8) = N_{true}/N_{PWIA}. \tag{5.5}$$

Here N_{true} (calculated using Equation 3.1) and N_{PWIA} are the measured and calculated number of coincidences for the experimental integrated luminosity $\mathcal{L}$. The $T(Q^2, \theta_8)$ are shown in Figures 59 through 62 for each kinematics. In most cases, the measured $T(Q^2, \theta_8)$ are consistent within errors at each Q^2. They are combined in a weighted average:

$$T(Q^2) = < T(Q^2, \theta_8) >_{\theta_8} . \tag{5.6}$$

The rise in $T(Q^2, \theta_8)$ with increasing θ_8 in the ^{2}H$(e, e'p)$, $Q^2 = 1\,(\mathrm{GeV/c})^2$ data is probably due to a p_m shift introduced by imperfect offset matrix elements. This data is very sensitive to such shifts because it is highly peaked in p_m. The effect of the shift averages out when combining the angles, so there should be no degradation of the error in $T(Q^2)$ (in particular, the measurement is dominated by the $\theta_8 = 41.3°$ kinematics, which is centered at $p_m = 0$ and so is not sensitive to the shift).

The IPSM spectral function does not include the effects of short-range nuclear correlations, which move strength to $|p_m| > p_f$. The measured T must be corrected by the ratio of $\int S d^3p dE_s$ for the IPSM and correlated spectral functions, integrated over the (E_m, p_m) range $\mathcal{R}$:

$$C_{correl} = \frac{1}{I_{correl}} \int_{\mathcal{R}} dE_s d^3p S(E_s, \mathbf{p}). \tag{5.7}$$

The correction assumes the correlations produce a uniform suppression of the uncorrelated spectral function strength at $|p_m| < 250\,\mathrm{MeV/c}$. This strength appears at larger $|p_m|$ but, since this region is excluded from the transparency measurement, the form does not need to be specified. Due to uncertainties in the amount of correlated spectral function strength at large E_m, the integral over the range $\mathcal{R}$ is averaged with the integral over all E_m:

$$I_{correl} = 0.5 \left(\int_{\mathcal{R}} dE_s d^3p S_{correl}(E_s, \mathbf{p}) + \int_0^{\infty} dE_s \int_{p_{m,min}}^{p_{m,max}} d^3p S_{correl}(E_s, \mathbf{p}) \right). \tag{5.8}$$

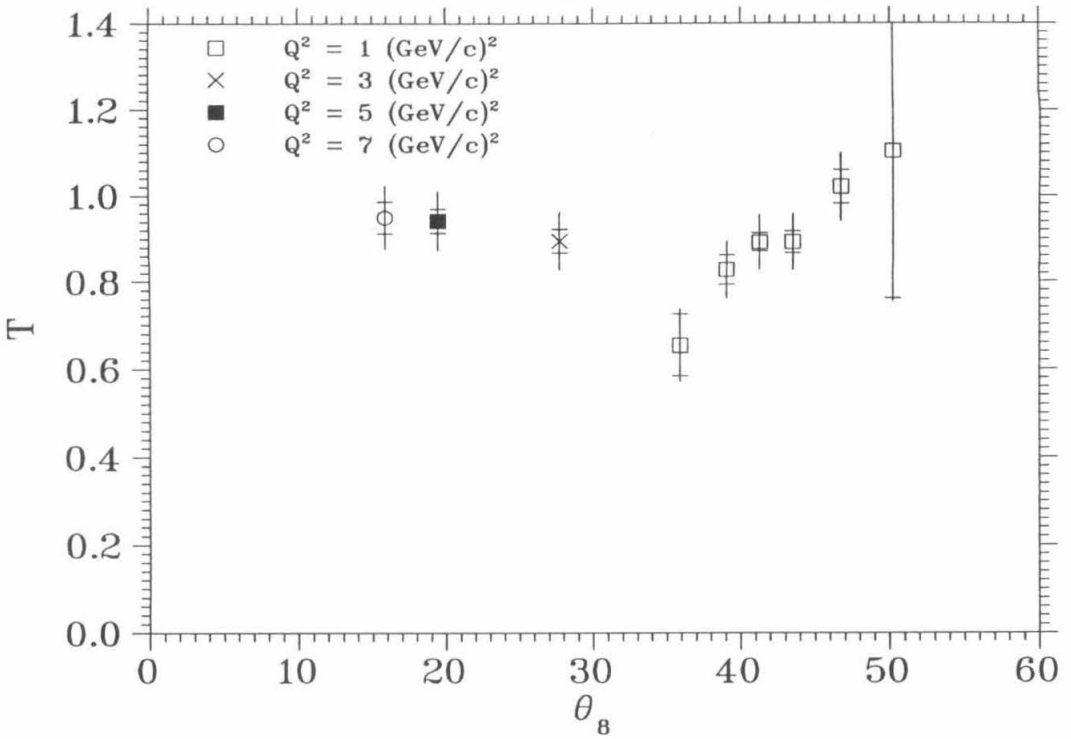

FIG. 59. **Nuclear transparency $T(Q^2, \theta_8)$ measured in ^{2}H$(e, e'p)$. values with multiple θ_8 kinematic settings. The inner error bars are statistical only and the outer error bars give the total error (statistical plus systematic, combined in quadrature).**

For ^{12}C, the integral over $\mathcal{R}$ is calculated using $S_{correl}(E_s, \mathbf{p})$ calculated for ^{12}C [52] and the other integral is calculated using $S_{correl}(E_s, \mathbf{p})$ calculated for ^{16}O [53]. For Fe and Au the integrals were calculated using a correlated nuclear matter spectral function corrected for finite nucleus effects [54]. The fraction of strength at $E_m > 100$ MeV for this spectral function is 21%, which is quite possibly an overestimate. Vonderfecht *et al.* [55] claim that the fraction should only be 13%. This discrepancy motivates the use of Equation 5.8. The resulting correction factors are given in Table 12. The quoted errors are based on the difference between the two integrals in Equation 5.8. It is expected that the error in the correlation correction will be reduced through

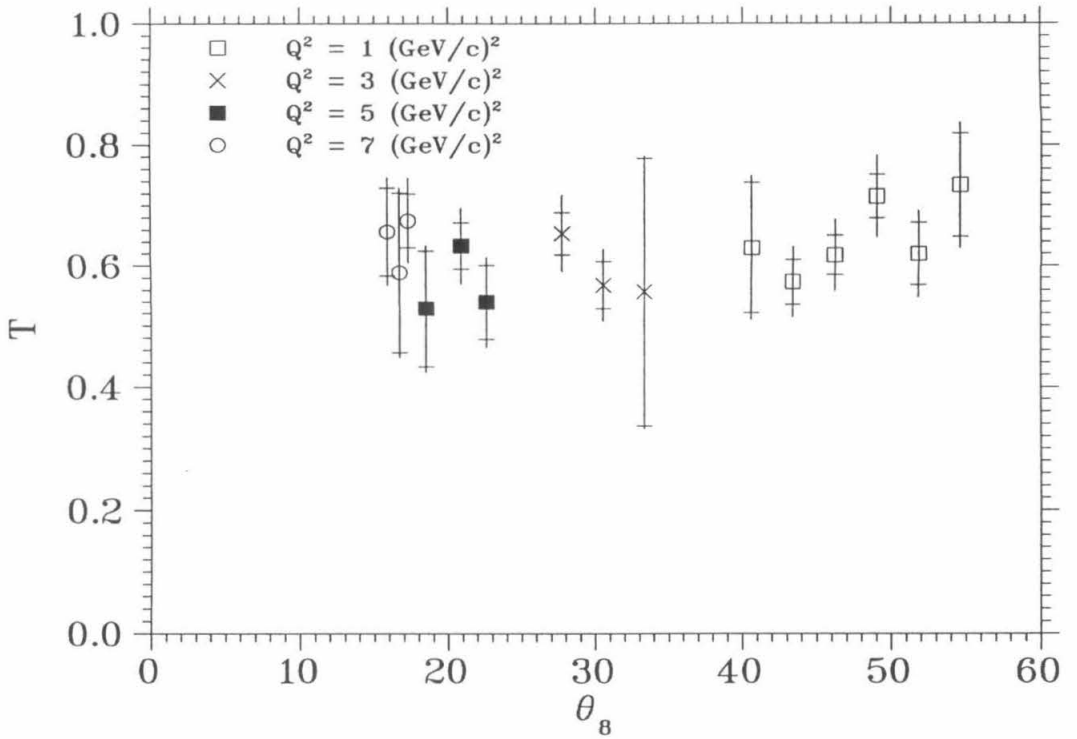

FIG. 60. **Nuclear transparency $T(Q^2, \theta_8)$ measured in $^{12}\mathbf{C}(e, e'p)$.**

further study of available correlated spectral functions. Based on comparisons of transparency calculated with different IPSM spectral functions, the Q^2 dependent variations associated with the correlation correction are only half as large as the quoted error in C_{correl}. Thus, most of the error in C_{correl} does not affect the search for a Q^2 dependence in $T(Q^2)$.

The correlation correction assumes the absence of CT, which suppresses the Initial State Interactions of the proton and could therefore reduce the effect of the short-range correlations. However, if the onset of CT were to suppress the correlations, it would bias the measured T to artificially high values. This phenomenon would therefore *increase* the sensitivity of the transparency measurement to the onset of CT. The degree of reduction of the correlation tail depends on the relative time scales for the

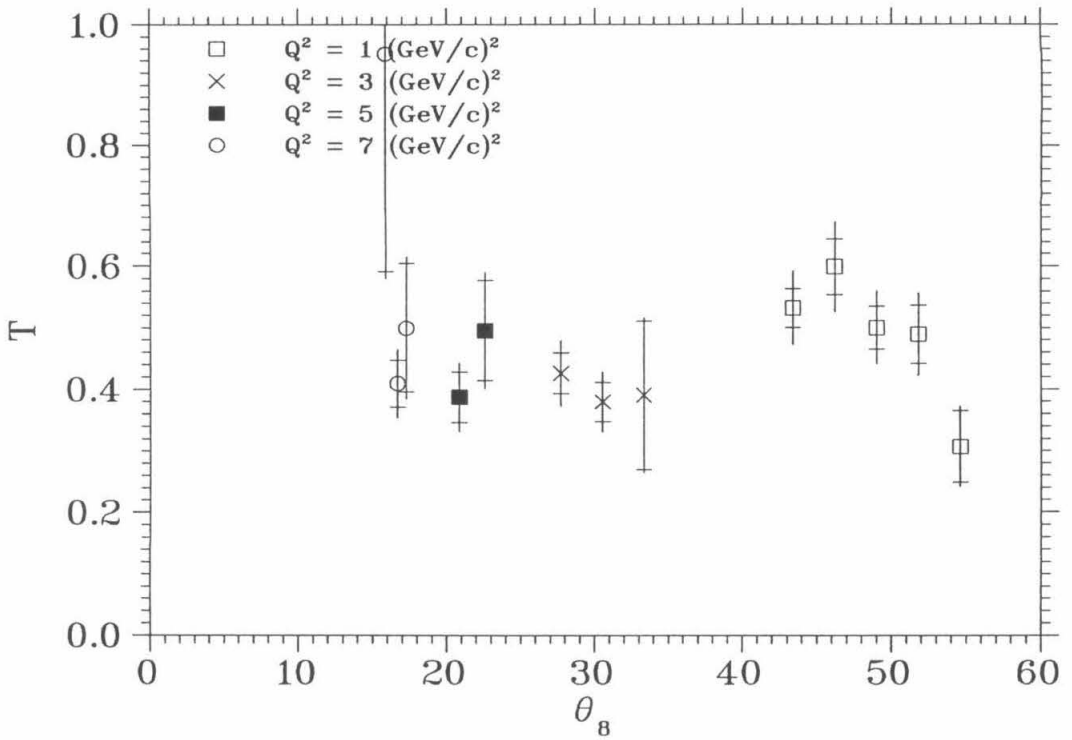

FIG. 61. **Nuclear transparency $T(Q^2, \theta_8)$ measured in ^{56}Fe$(e, e'p)$.**

TABLE 12. Correlation tail correction to the PWIA calculation

A	C_{correl}
^{1}H, ^{2}H	1.00
^{12}C	1.11 ± 0.03
^{56}Fe	1.26 ± 0.08
^{197}Au	1.32 ± 0.08

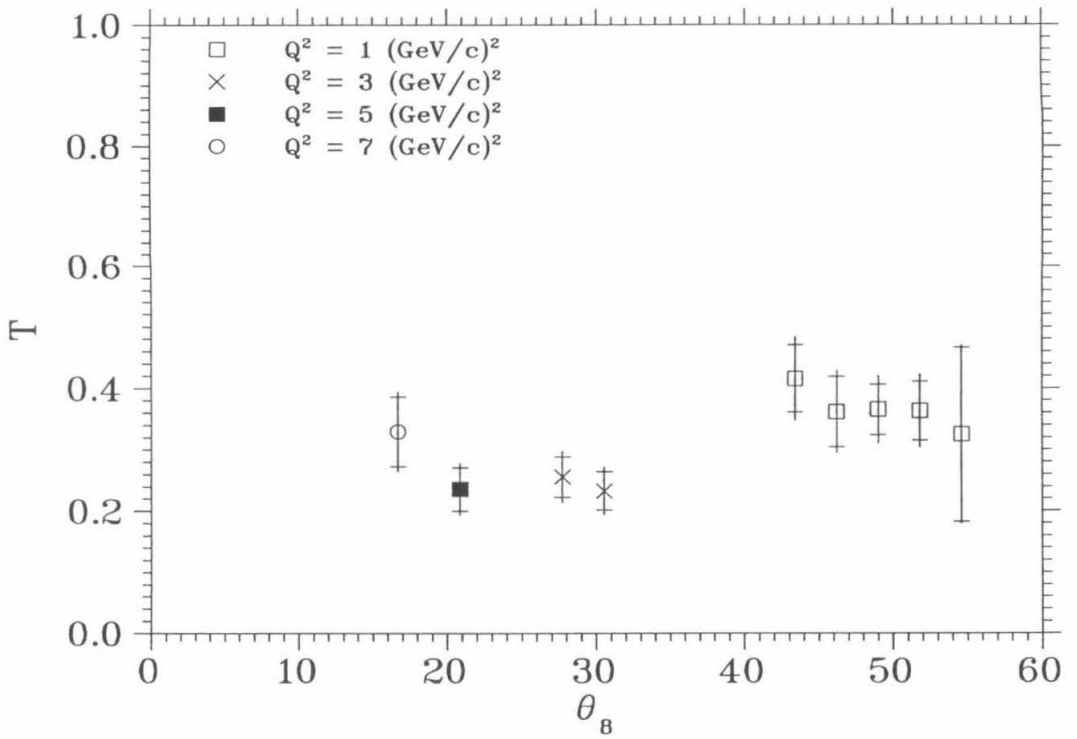

FIG. 62. **Nuclear transparency $T(Q^2, \theta_8)$ measured in ^{197}Au$(e, e'p)$.**

formation of a Point Like Configuration (t_{PLC}) and the occurrence of a short-range correlation (t_{src}). In the PLC rest frame, the formation time t_{PLC} should be the same as the expansion time $\gamma\tau \simeq l_h/c$. The naive parton model gives the largest value, $\tau = R_p/c$. Time dilation from the Fermi motion is negligible, and $t_{PLC} \lesssim 0.8\,\mathrm{fm/c}$. The correlation time scale t_{src} can be estimated as the crossing time of two nucleons' hard cores, roughly 1 fm divided by the relative velocity ($0.21c$ for a typical relative momentum $\sim 200\,\mathrm{MeV/c}$): $t_{src} \simeq 5\,\mathrm{fm}$. Thus, it appears that the correlation occurs before the formation of the PLC and persists until the electron-proton interaction.

The resulting transparency values are given in Figure 63 and Table 13. Values are not identical to those published in reference [56], where these results are averaged with values from an independent analysis [57] that was performed as a consistency

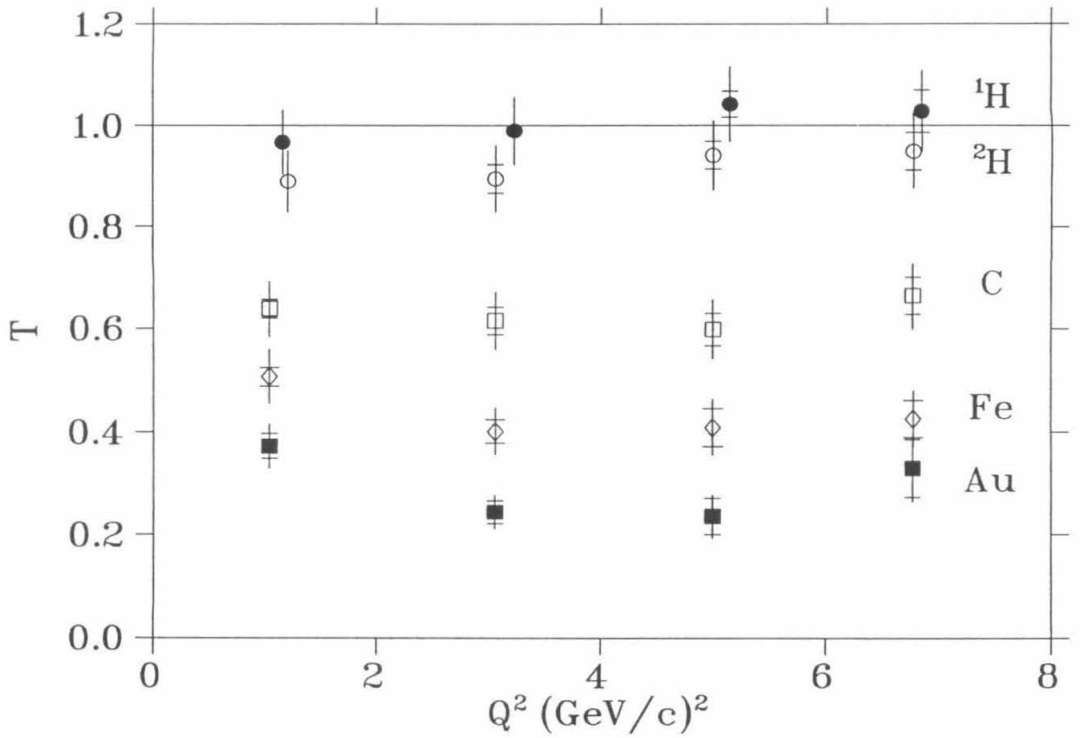

FIG. 63. **Nuclear transparency $T(Q^2)$ Measured in Experiment NE-18. The inner error bars are statistical only and the outer error bars give the total error (statistical plus systematic, combined in quadrature).**

check. The ^{1}H results are consistent with the expected $T = 1$ (no FSI). In addition, the measured inclusive H(e, e') cross sections agree with the exclusive H$(e, e'p)$ values to within 2%.

The measured transparency is insensitive ($< 2\%$) to large changes ($\lesssim 40$ MeV in E_m and $\lesssim 50$ MeV/c in p_m) in the range $\mathcal{R}$, indicating once again the successful description of the data by the PWIA/IPSM model and the absence of large multi-nucleon effects at $E_m \gtrsim 60$ MeV.

The nuclear targets show decreasing proton transmission for increasing A, as expected. The $T(Q^2)$ measured on ^{2}H varies between about 0.9 and 0.95, indicating the

TABLE 13. **Nuclear transparency T Measured in Experiment NE-18, with statistical and systematic errors.**

	$T(Q^2)$				Systematic
A	$Q^2 = 1\,(\mathrm{GeV/c})^2$	$Q^2 = 3\,(\mathrm{GeV/c})^2$	$Q^2 = 5\,(\mathrm{GeV/c})^2$	$Q^2 = 7\,(\mathrm{GeV/c})^2$	Error
^{1}H	0.967 ± 0.006	0.990 ± 0.013	1.042 ± 0.025	1.028 ± 0.041	0.066
^{2}H	0.889 ± 0.014	0.894 ± 0.028	0.941 ± 0.028	0.949 ± 0.037	0.067
^{12}C	0.637 ± 0.018	0.614 ± 0.026	0.598 ± 0.031	0.663 ± 0.037	0.080
^{56}Fe	0.506 ± 0.018	0.401 ± 0.023	0.409 ± 0.037	0.425 ± 0.036	0.097
^{197}Au	0.372 ± 0.024	0.244 ± 0.023	0.236 ± 0.036	0.329 ± 0.056	0.097

presence of weak FSI effects. For Fe, and Au one observes an enhanced transparency at $Q^2 = 1\,(\mathrm{GeV/c})^2$. This is at least partially due to the smaller nucleon-nucleon inelastic cross section at momenta $\simeq 1\,\mathrm{GeV/c}$ [6]. The effect is smaller in C, and cannot be resolved within the error bars.

Color Transparency is expected to produce an increase in T with increasing Q^2 for the nuclear targets. In testing for this increase, the $Q^2 = 1\,(\mathrm{GeV/c})^2$ data should not be used because of its enhanced T. None of the nuclei exhibit an increase larger than the error bars in range $Q^2 = 3$–$7\,(\mathrm{GeV/c})^2$, so the measured transparency is consistent with the absence of CT. The solid target data can be used to rule out some models of CT, as will be discussed in Section V.D. [The ^{2}H data cannot be used to test for the presence of CT, since the errors are consistent with $T_{^2\mathrm{H}}(7\,(\mathrm{GeV/c})^2) = 1$ (full CT) and $T_{^2\mathrm{H}}(Q^2) =$ constant (no CT).]

V.C. Systematic Errors

Systematic errors in the calculation of $S(E_m, p_m)$ and $T(Q^2)$ are caused by uncertainties such as those in the efficiency corrections, the kinematics, the luminosity, and the PWIA calculation. These errors are discussed throughout the text, but are summarized here for convenience. The systematic errors are indicated in the graphs of $T(Q^2)$, but not in those of $S(E_m, p_m)$.

The errors in the PWIA calculation are given in Table 14. The PWIA calculation of I_{PS} used in the extraction of $S(E_m, p_m)$ has a unit spectral function, no radiative effects, and no correlation tail correction. In this case the third, forth, and fifth lines of the table do not apply. The measurement of $T(Q^2)$ involves the full PWIA calculation, and all five error sources are relevant. The error on the radiation is an upper limit derived by comparing transparency values for different radiation length targets. The error in the correlation tail correction is given in Section V.B and the remaining errors are discussed in Section IV.B.

The uncertainty in the $S(E_s, \mathbf{p})$ energy distributions is characterized by two spectral function models with E_s distributions based on shell locations from Hartree-Fock calculations or from $A(e, e'p)$ and $A(p, 2p)$ measurements at low Q^2 (see Appendix E). The Hartree-Fock E_s distributions agree with the current data, and the low Q^2 distribution should be considered as an extreme model to test the sensitivity to the E_s distribution. The transparency calculated using the two models disagrees by 4% in Fe and 5% in Au, but the Hartree-Fock E_s distribution is probably more accurate than the disagreement between the models. The systematic uncertainty in $T(Q^2)$ is therefore estimated to be $< 2\%$. The insensitivity of the transparency measurement to rearrangements of the strength in E_m is due to the large range of E_m used in the measurement.

Note the systematic error on the model $S(E_s, \mathbf{p})$ does not include the model-

dependence of the **p** distributions. The Fe and Au transparency are sensitive to the width of the PWIA/IPSM spectral function in p_m, since there is still moderate strength at the high p_m cut. This model-dependence is mostly independent of Q^2 (see the discussion following Equation 5.8) and so does not effect the search for Color Transparency presented in this paper. Note that the IPSM momentum distributions used in the analysis do not agree with those measured in nearby nuclei at low Q^2 (for details, see Appendix E). If these spectral functions are used instead, the measured Fe and Au transparencies increase by a factor of ~ 1.05 and ~ 1.15 respectively.

Table 15 lists the systematic errors from other sources (*i.e.*, the apparatus and analysis procedures). These errors are common to any quantity derived from the measured $A(e,e'p)$ cross section. The total errors in the $S(E_m,p_m)$ and $T(Q^2)$ measurements are given in Table 16.

One of the main sources of error is the 5% uncertainty in the experimental acceptance. The uncertainty is greatest for the 8 GeV/c spectrometer, which was run in the

TABLE 14. Fractional uncertainties in the PWIA calculation. The first two rows apply to both the $S(E_m,p_m)$ and $T(Q^2)$ measurements. The following three rows apply to the measurement of $T(Q^2)$ only.

Source	^{1}H	^{2}H	^{12}C	^{56}Fe, ^{197}Au
Off-shell σ_{ep}	0.00	0.01	0.02	0.02
G_E^p and G_M^p	0.02	0.02	0.02	0.02
Model $S(E_s,\mathbf{p})$	0.00	0.005	0.02	0.02
Radiation	0.02	0.02	0.03	0.03
Correlation tail[a]	0.000	0.000	0.027	0.061
Total $S(E_m,p_m)$	0.020	0.022	0.028	0.028
Total $T(Q^2)$	0.028	0.030	0.053	0.068

[a]Error is almost entirely independent of Q^2.

TABLE 15. Experimental systematic errors

Source	Value	Notes
Kinematic uncertainties	0.01	
Beam charge	0.005	
Dead times	0.003	Appendix C
Proton absorption	0.02	Table 10
1.6 GeV/c track ID	0.01	Table 10
1.6 GeV/c multiple tracks	0.01	Section III.B
8 GeV/c track ID	0.01	Table 10
8 GeV/c multiple tracks	0.01	Section III.B
Coincidence identification	0.01	Table 10
Spectrometer Acceptances	0.05	Section IV.G
Target thickness	0.007	Maximum value [a]
Total	0.060	

[a]Liquid targets 0.007; solid targets 0.002

TABLE 16. Total systematic errors. The final column indicates the error in the Q^2 dependence of $T(Q^2)$, obtained by subtracting the Q^2-independent portion of the error in the correlation correction.

Source	^{1}H	^{2}H	^{12}C	^{56}Fe, ^{197}Au
$S(E_m, p_m)$	0.063	0.064	0.072	0.083
$T(Q^2)$	0.066	0.067	0.080	0.097
Q^2-dependent $T(Q^2)$	0.066	0.067	0.076	0.081

previously untested large acceptance tune. In the current experiment, the acceptance functions of the spectrometers were constrained mostly with elastic electron-proton scattering, which provides limited illumination. Use of deep inelastic scattering to provide nearly structureless illumination of the spectrometers could help constrain the acceptance functions at the edges of the spectrometers. Experiment E-140X, which ran immediately before NE-18, took some deep inelastic scattering data using the large acceptance tune of the 8 GeV/c spectrometer. Further study of the acceptance may reduce the acceptance systematic.

Another large uncertainty is the width of the momentum distributions of Fe and Au, which seem to be narrower then observed at low Q^2. High statistics, high resolutions $S(E_m, p_m)$ measurements at $Q^2 > 1\,(\mathrm{GeV/c})^2$ would be valuable to confirm this apparent disagreement and to fine-tune the PWIA/IPSM model spectral functions.

V.D. Comparison of $T(Q^2)$ with Theory

V.D.1. The Glauber Predictions

Before considering predictions including the Color Transparency effect, it is worth comparing the data with the predictions of standard nuclear physics, generically referred to as the Glauber prediction. The following semiclassical model of the FSI of the outgoing proton illustrates the necessary considerations in a simple way. The model is developed to predict $T(Q^2)$ for the $Q^2 \geq 3\,(\mathrm{GeV/c})^2$ data. In this energy regime, due to the small ($< 0.1\,\mathrm{fm}$) de Broglie wavelength of the proton, the FSI can be treated as interactions with the individual nucleons in the recoiling $A-1$ system. Furthermore the inelastic and total proton-nucleon cross sections are approximately constant (within about $\pm 5\,\mathrm{mb}$) at $\sigma_{in} \simeq 26\,\mathrm{mb}$ and $\sigma_{tot} \simeq 43\,\mathrm{mb}$ (see Figure 64). Almost all elastic nucleon-nucleon interactions knock the proton outside of the experimental acceptance [50], so the total pN cross section is most relevant.

The probability that a proton struck at position $\mathbf{r} = (x, y, z)$ escapes the nucleus without interacting is,

$$\mathcal{P}(\mathbf{r}) = \exp\left(-\int_z^\infty dz' \sigma_{tot} \rho_{A-1}(\mathbf{r}')\right), \tag{5.9}$$

where the z axis is parallel to $\mathbf{p}'$ and $\rho_{A-1}(\mathbf{r}')$ is the nucleon number density of the recoil $A-1$ system at the position $\mathbf{r}' = (x, y, z')$ on the proton's path. The transparency is this probability, averaged over the position of the struck proton:

$$T_{classical} = \frac{1}{A} \int d^3r \rho_A(\mathbf{r}) \mathcal{P}(\mathbf{r}). \tag{5.10}$$

Here $\rho_A(\mathbf{r})$ is the number density in the nucleus A.

For simplicity we take A and $A-1$ to be uniform spheres of radius R_0 given in Table 5. The resulting proton mean free path, $\lambda \equiv 1/(\rho_{A-1}\sigma_{tot})$, is 2.984, 2.021, and 1.618 fm respectively for C, Fe, Au. Substituting $r_\perp = \sqrt{x^2 + y^2}$, one finds:

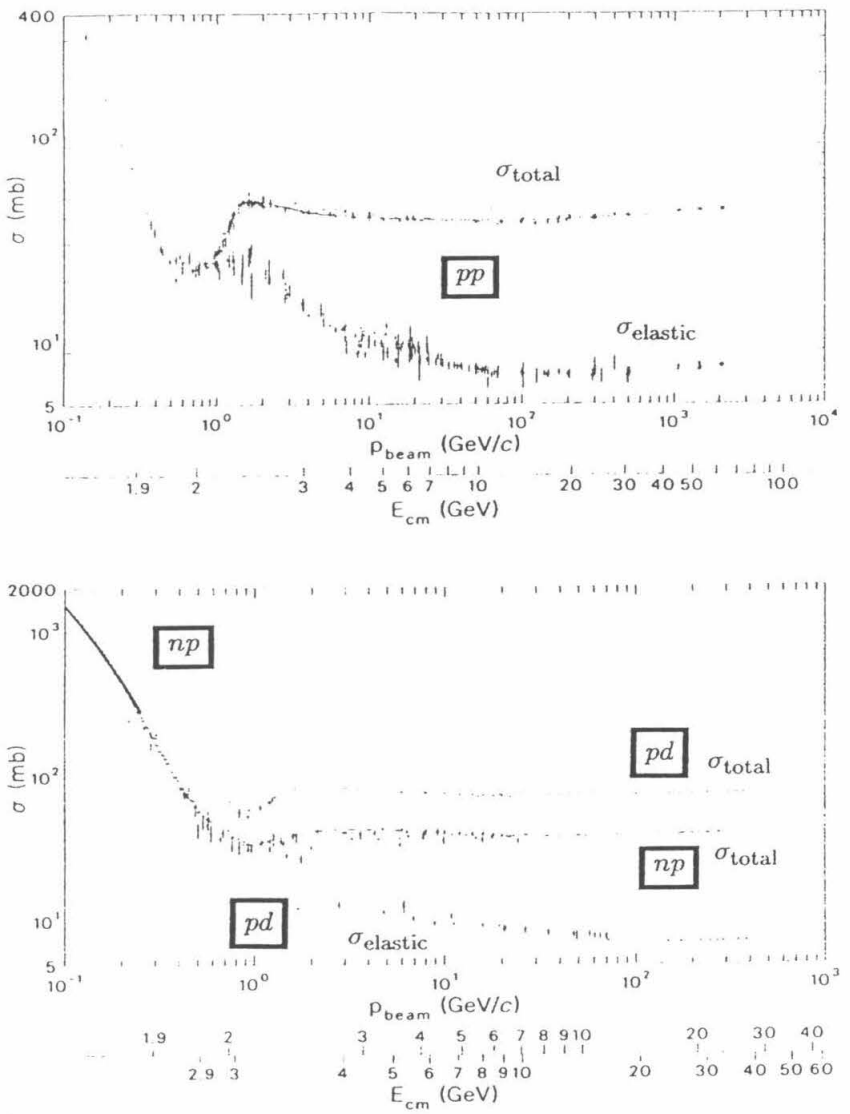

FIG. 64. Nucleon-nucleon total and elastic cross sections vs. laboratory beam momentum p_{beam} and total center-of-mass energy E_{cm}, from [38].

$$\mathcal{P}(\mathbf{r}) = \exp\left[\left(\sqrt{R_0^2 - r_\perp^2} - z\right)/\lambda\right]. \tag{5.11}$$

This factors into a z-dependent piece and a $r_\perp$-dependent piece, and the 3-dimensional integration can be performed in two steps: integration over dz with limits $\pm\sqrt{R_0^2 - r_\perp^2}$ and integration over $d^2r_\perp = 2\pi r_\perp dr_\perp$. The result is:

$$T_{classical} = \frac{3}{4}\left(\frac{\lambda}{R_0}\right)\left[1 - \frac{1}{2}\left(\frac{\lambda}{R_0}\right)^2 + \frac{1}{2}\left(\frac{\lambda}{R_0}\right)\left(2 + \frac{\lambda}{R_0}\right)e^{-2R_0/\lambda}\right]. \tag{5.12}$$

The resulting transparency predictions for C, Fe, and Au are 0.52, 0.29, and 0.17, respectively. These are 15–30% below the values measured at $Q^2 = 3$ and $5\,(\mathrm{GeV/c})^2$, which is not surprising in light of the semiclassical approximation and the grossly simplified model of the nuclear density. The nuclei Fe and Au approach the limit $R_0 \gg \lambda$, where the expression simplifies to $T_{classical} \simeq 3\lambda/4R_0$. This is easily understood by noting that escaping protons come from a region with z within λ of the nuclear surface. The transparency is the volume of this region, $\pi R_0^2\lambda$, divided by the volume of the entire nucleus, $4\pi R_0^3/3$.

The data are compared to more sophisticated models of the transparency in Figures 65 through 67. Because the predictions vary so much (up to 40%), the differences in their assumptions will be discussed in some detail.

Farrar *et al.* [2] used the semiclassical approximation with $\sigma_{tot} = 40\,\mathrm{mb}$ and a more realistic Woods-Saxon shape for the nuclear density, and obtained T uniformly higher than the above estimates.

In general, the other calculations are performed using some variation on the Glauber multiple scattering theory [60]. As in the semiclassical model above, the struck proton propagates without distortion between interactions with individual nucleons, but now the calculation is (ideally) performed quantum-mechanically.

For example, Jennings and Miller [3,4] calculate the transparency in the eikonal approximation, assuming that any FSI resulting in excitation of the $A - 1$ system

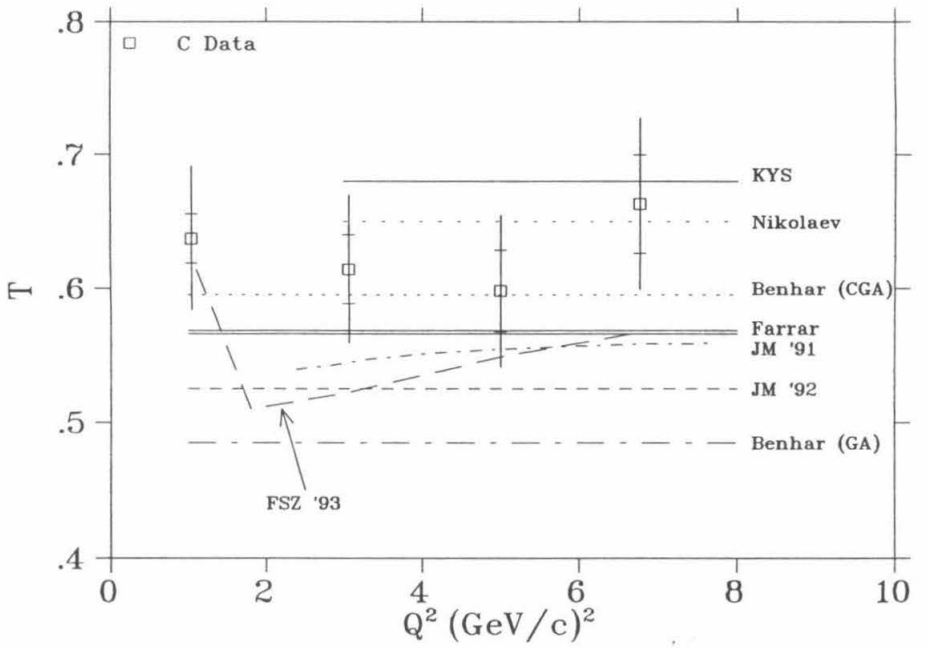

FIG. 65. **Standard T predictions for ^{12}C. Curves are from references [2–4,6,5,58,59].**

prevents detection of the proton (similar to the use of σ_{tot} instead of σ_{in} in the semiclassical calculation above). To lowest order in the Glauber expansion, the wave function of the outgoing proton is [3]:

$$\psi(\mathbf{r}) = \frac{e^{i\mathbf{p}\cdot\mathbf{r}}}{(2\pi)^{3/2}} \exp\left(-\frac{\sigma_{tot}}{2}\int_z^\infty dz' \rho_{A-1}(\mathbf{r}')\right). \tag{5.13}$$

Here the use of $\sigma_{tot}/2$ instead of σ_{tot} indicates that the attenuation of the amplitude is just the square root of the attenuation of the probability given by Equation 5.11. The amplitude for different initial positions z of the struck proton are allowed to interfere, yielding:

$$T_{eikonal} = \left|\int d^3r \sqrt{\rho_A(\mathbf{r})} \exp\left(-\frac{\sigma_{tot}}{2}\int_z^\infty dz' \rho_{A-1}(\mathbf{r}')\right)\right|^2. \tag{5.14}$$

Jennings and Miller also calculated the transparency using the semiclassical approximation and found agreement with the eikonal to within a few percent [3]. They used

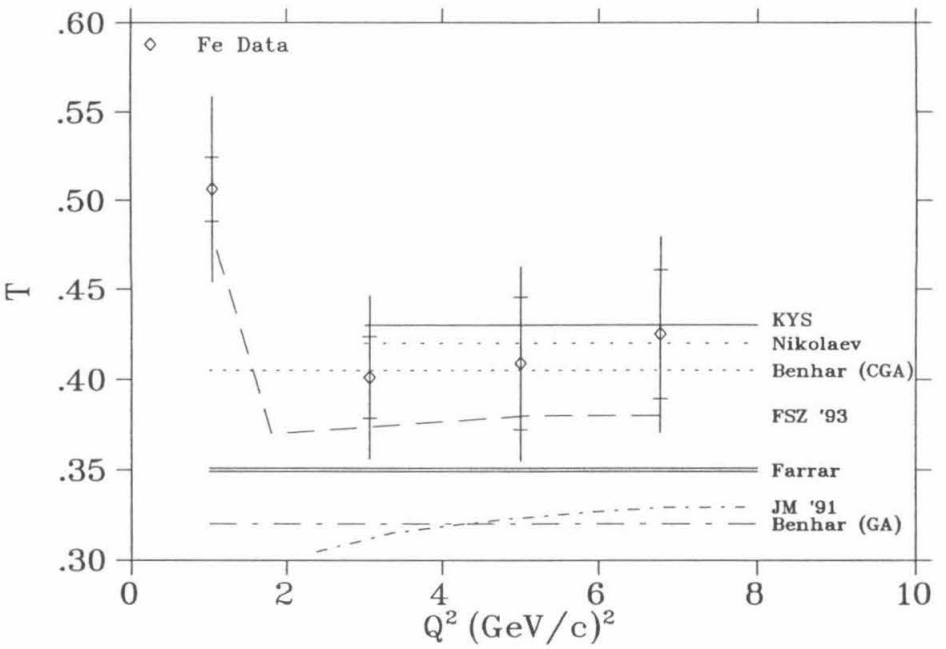

FIG. 66. **Standard T predictions for ^{56}Fe. Curves are from references [2,3,6,5,58,59].**

$\sigma_{tot} = 40\,\mathrm{mb}$ and the Woods-Saxon (Fermi) form for the densities.

Use of the total cross section is not strictly correct. Kohama *et al.* [58] argue that because the E_m acceptance includes the most important excited states of the $A-1$, it is more appropriate to apply a closure sum over the state of the $A-1$ system. (See, for example, the discussion following Equation 1.10.) In a Glauber model neglecting the $A-1$ recoil (justified for large A) and nucleon-nucleon correlations, they find a form for the d^3p'-integrated transparency identical to Equation 5.10 except with σ_{in} in place of σ_{tot}. The connection is understood by noting that the classical calculation effectively performs the closure sum on the $A-1$ system by ignoring its excitations. Furthermore, σ_{in} occurs because protons undergoing only elastic interactions are included in the d^3p' integral. Unfortunately, the integral over d^3p' is not well-justified in the current experiment because the finite $\mathbf{p}'$ acceptance excludes most

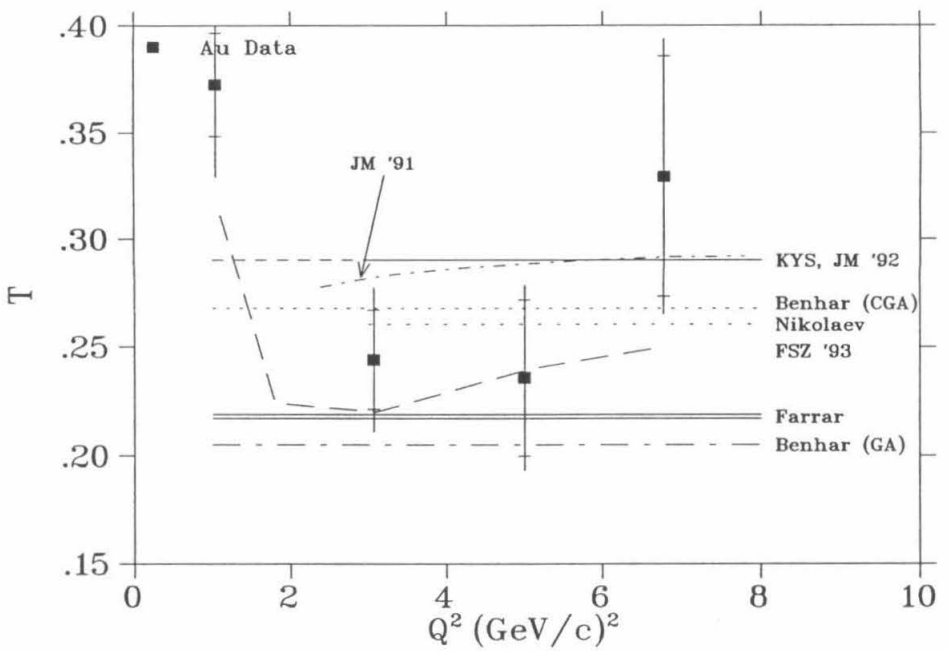

FIG. 67. **Standard T predictions for ^{197}Au. Curves are from references [2–4,6,5,58,59].**

elastically-scattered protons. This is the reason why σ_{tot} was used in the semiclassical derivation. Note that it is difficult to estimate the error made in performing the d^3p' integral because if it is not performed, the result is not simply Equation 5.10. The truth probably lies somewhere between the eikonal and the closure approach. Kohama *et al.* use $\sigma_{in} = 28$ mb and the Woods-Saxon form for the densities [58]. Because this analysis includes excitations of the $A-1$ system (or equivalently, because $\sigma_{in} < \sigma_{tot}$), the resulting transparency is higher than the Jennings and Miller value.

Benhar *et al.* [5] also begin with Equation 5.13, but apparently do not allow interference between the different initial positions. They publish two curves, with the lower values (GA = Glauber Approximation) calculated as:

$$T_{benhar} = \int d^3r \rho_A(\mathbf{r}) |\psi(\mathbf{r})|^2, \tag{5.15}$$

which is clearly equivalent to the classical expression, Equation 5.10. They use nuclear

density distributions obtained by fitting elastic electron-nucleus scattering data and $\sigma_{tot} = 43.3\,\mathrm{mb}$. Their upper curve (CGA = Correlated Glauber Approximation) includes the suppression of nuclear density near the initial position $\mathbf{r}$ due to nucleon-nucleon correlations (*i.e.*, other nucleons are excluded from the immediate region by the hard core of the nucleon-nucleon potential). They find the correlations enhance the transparency by 20–30%, but Kohama *et al.* [58] and Nikolaev *et al.* [59] argue that the effect is much smaller.

Nikolaev *et al.* [59] independently arrived at the same transparency equation as Kohama *et al.* through the use of the same closure and d^3p'-integration arguments. Like Benhar *et al.*, they then included the correlation of the other nucleons with the struck proton but found that the effect was reduced by $r_c^2/(r_c^2 + b_{pN}) \simeq 1/3$ by the finite range of the pN interaction (here $r_c \simeq 0.5\,\mathrm{fm}$ is the standard deviation of their assumed gaussian 2-nucleon correlation function and $b_{pN} \simeq 0.5\,\mathrm{fm}^2$ is the pN elastic slope parameter). Crudely speaking, the blurring introduced by the finite range "fills in" the correlation hole. They also included the 2-body correlations of the spectator nucleons and found that these *raised* the transparency, because the correlation reduces the shadowing of one spectator nucleon by the other. The two correlation effects partly cancel each other, for a net transparency increase of only 2–3% [59]. Nikolaev *et al.* use $\sigma_{in} = 32\,\mathrm{mb}$ and a Fermi nuclear density. The smaller value of σ_{in} used in Kohama *et al.* is at least partly responsible for their larger transparency prediction.

Frankfurt, Strikman, and Zhalov were the first to publish a prediction for $A(e, e'p)$ that took the variation of the pN cross section into account, leading to a Q^2-dependent Glauber prediction [6]. They used a more general version of the eikonal approximation, with the distortion modelled by an optical model potential (with phase shift and absorption) rather than just by an absorbing cross section (cf. Equation 5.14). For σ_{tot} they used 26 mb at $p' \simeq 1\,\mathrm{GeV/c}$, increasing to the maximum

of 43 mb at $p' \simeq 2\,\mathrm{GeV/c}$, and slowly decreasing and becoming constant at 40 mb at $p' \gg 3\,\mathrm{GeV/c}$. The value at $p' \simeq 1\,\mathrm{GeV/c}$ is 4 mb less than the free-nucleon value, based on observed disagreements between Glauber calculations and the pA cross sections measured at momenta of 1 GeV/c. (Such a correction is not applied at higher Q^2 because the Glauber approximation is expected to be more accurate at higher energy.) This model does a good job of reproducing the measured transparency drop between $Q^2 = 1$ and $3\,(\mathrm{GeV/c})^2$.

The main conclusions from the graphs of the Glauber predictions are: 1) the transparency expected using standard nuclear physics is uncertain by $\sim \pm 20\%$, and 2) the $Q^2 \geq 3\,(\mathrm{GeV/c})^2$ data is within the range of the theories, and 3) the enhanced transparency at $Q^2 = 1\,(\mathrm{GeV/c})^2$ is at least partly due to the lower pN cross section.

Conclusion (1) indicates that the average magnitude of T cannot be used to test for the presence of CT. In comparing with any of the CT predictions, one can easily imagine improving (or destroying) the agreement with the data by a 20–40% renormalization of the theory. Currently, the only fair test of the presence of CT is in the Q^2 dependence of the data. If an accurate theoretical consensus on the Glauber prediction arises, then much more stringent tests of CT will be possible. Currently the main uncertainties in the Glauber prediction are the treatment of elastic interactions (*i.e.*, whether or not to include the excited states of the $A-1$ system) and the treatment of nucleon-nucleon correlations.

Conclusion (2) indicates that the present data may not be subject to the incomplete saturation of the spectroscopic sum rule observed in $A(e,e'p)$ at $Q^2 < 1\,(\mathrm{GeV/c})^2$. Given the current dispersion in the theoretical predictions, this question also cannot be resolved with certainty. But it is suggestive that the $Q^2 \geq 3\,(\mathrm{GeV/c})^2$ data generally lie at the high end of the Glauber predictions. As discussed in Section I.A.2, there were many reasons to think that the problem would not persist in the current experiment: use of a large measurement range $\mathcal{R}$, the use of a correction

for strength in the correlation tail, the increased single-particle nature of the reaction at $Q^2 \gtrsim 1\,(\mathrm{GeV/c})^2$, and the simpler theoretical description of the proton FSI. This simpler description should allow for decreased uncertainty in the FSI predictions.

The significance of conclusion (3) is that the various Glauber calculations can be tested more rigorously if the authors repeat their work taking the change in cross section into account. Then the high-statistics $Q^2 = 1\,(\mathrm{GeV/c})^2$ data can be used to set the highly uncertain normalization of the predictions. Thus, the entire data set provides an excellent opportunity for the refinement of the Glauber predictions.

V.D.2. The Color Transparency Predictions

This section includes comparisons between the data and models of the transparency with and without the Color Transparency effect, as presented in several different calculations. As described in the previous section, the uncertainty in the Glauber predictions hampers use of the data to discriminate between the various models. Because of this, the interpretation of these comparisons is necessarily limited. Also, for models that do not include the enhancement of the transparency at $Q^2 = 1\,(\mathrm{GeV/c})^2$ by the decreased pN cross section, the comparison is restricted to the data at $Q^2 \geq 3\,(\mathrm{GeV/c})^2$.

In calculating the effect of CT, the general approach has been to use a reduced value σ_{eff} for the pN cross section in the Glauber model transparency calculations (presented in the previous section). The physics content of the CT models is in the Q^2 and time dependence of the reduced cross section, based on the considerations discussed in Section I.B.

Figure 68 shows the predictions of Farrar *et al.* [2] in the naive parton and quantum diffusion models discussed in Section I.B.3. They assume that the transverse extent of the Point Like Configuration is $b \sim (n < k_t^2 >^{1/2}) R_p/Q^2$ at the time of the interaction

and that it propagates a distance l_h while expanding back to the normal proton size. Here $n = 3$ is the number and $< k_t^2 >^{1/2} \simeq 0.35\,\mathrm{GeV/c}$ is the RMS transverse momentum of the constituents of the proton. Using $\sigma_{eff} \simeq \sigma_{tot} b^2/R_p^2$ (Equation 1.15), they arrive at the following effective cross section during the expansion of the PLC:

$$\sigma_{eff} = \sigma_{tot}\left[\delta^\kappa + \frac{< n^2 k_t^2 >}{Q^2}(1 - \delta^\kappa)\right] \tag{5.16}$$

where $\delta = (z' - z)/l_h$ is the distance $z' - z$ traveled since the interaction in units of l_h. The term in brackets, which represents $(b/R_h)^2$ during the expansion, increases from the initial value at $\delta = 0$ to 1 at $\delta = 1$. The expansion length for the naive parton model ($\kappa = 2$) is $l_h = \gamma\tau c \simeq (E_p'/M_p)R_p$, where τ is the expansion time in the PLC rest frame and $\gamma = E_p'/M_p$ is the time dilation factor. In the naive parton model, b increases linearly with time due to free expansion of the partons. For the quantum diffusion model ($\kappa = 1$), the expansion length is $l_h \simeq 2\hbar p'/c^2\Delta M^2$, where $\Delta M^2 = 0.7\,\mathrm{GeV^2/c^4}$. (See Section I.B.3 for more details.) As can be seen in Figure 68, the quantum diffusion model is consistent with the C and Au data at $Q^2 \gtrsim 3\,(\mathrm{GeV/c})^2$. However, the data clearly rules out the naive parton model.

Jennings and Miller [3] treat the PLC as being the superposition of states in a hadronic basis (see Section I.B.3). They argue that the PLC-nucleus FSI are soft and can only connect low-lying excitations with a proton in the final state. They assume that the proton final state is dominated by contributions from the nucleon $|N>$ and a low-lying nucleonic excitation $|N_1>$ of mass M_1. The authors consider the two states to have the same energy E_p' but different momenta p' and $p_1' = \sqrt{p'^2 + M_p^2c^2 - M_1^2c^2} \simeq p' - (M_1^2 - M_p^2)c^3/(2E_p')$. For definiteness, they model the transverse wave functions with the ground state and first excited state of a two-dimensional harmonic oscillator,

$$< r_\perp|N >= \frac{1}{R_p\sqrt{\pi}} e^{-r_\perp^2/2R_p^2} \tag{5.17}$$

and

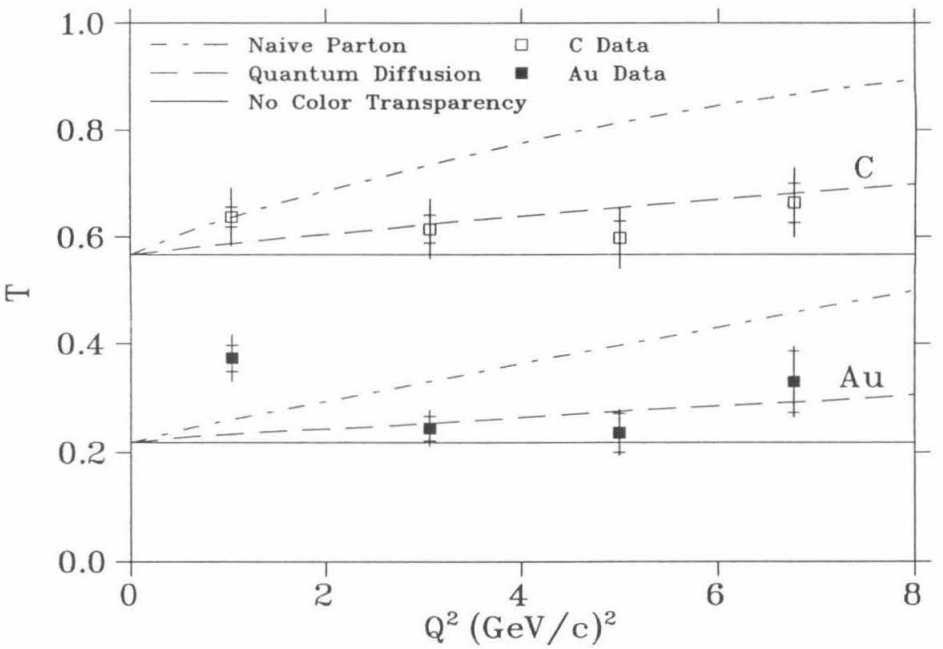

FIG. 68. **Farrar *et al.* [2] C, Au T predictions**

$$< r_\perp | N_1 >= (1 - r_\perp^2/R_p^2) < r_\perp | N > \tag{5.18}$$

where $r_\perp$ is the transverse coordinate ($b =< r_\perp^2 >^{1/2}$). Introducing the associated operator $\hat{r}_\perp$, one observes that this choice of wave functions results in the convenient relation:

$$\hat{r}_\perp^2 | N >= R_p^2(|N> - |N_1>). \tag{5.19}$$

In calculating the effective cross section $\sigma_{eff} \simeq \sigma_{tot} b^2/R_p^2$ one must include the longitudinal part $e^{ip'z'}$ of the wave function:

$$\sigma_{eff} = \sigma_{tot} \left[1 - \frac{p'}{p'_1} e^{i(p'-p'_1)(z'-z)} \right] \tag{5.20}$$

$$\simeq \sigma_{tot} \left[1 - e^{i(p'-p'_1)(z'-z)} \right]. \tag{5.21}$$

Here the longitudinal wave functions were assumed to be in phase at the time of scattering ($z' = z$), giving $\sigma_{eff} = 0$. As the PLC propagates, it expands to full size

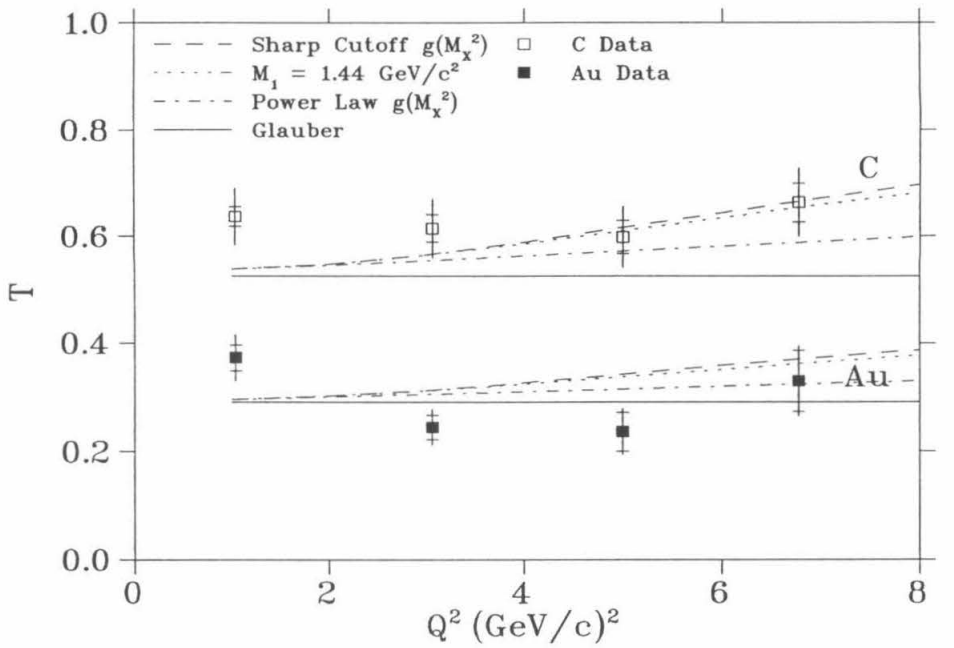

FIG. 69. **Jennings and Miller 1992 [4] C, Au T predictions**

and full σ_{tot} because the phase decoherence of the $|N>$ and $|N_1>$ state destroys the cancellation of the $\hat{r}_\perp^2$ expectation value. This is the model used to calculate the $M_1 = 1.44\,\mathrm{GeV/c^2}$ curve in Figure 69. In 1992 the authors generalized the technique to include contributions from more than two hadron states, with the decreasing importance of higher-mass resonances characterized by a function $g(M_X^2)$, where M_X is the resonance mass [4]. The function is given by a sharp cutoff $g(M_X^2) = 0.6\theta(M_c^2 - M_X^2)$ or by a power law $g(M_X^2) = (M/M_X)^\beta$ (see Figure 69). Here $M_c^2 \simeq 2.2\,\mathrm{GeV^2/c^4}$ and β ranges from 2.4 to 4.0. These values are constrained using the measured proton diffractive dissociation and electron deep inelastic scattering cross sections. Any of these models can be made consistent with the data by renormalization within the theoretical uncertainty of the Glauber approximation.

The Benhar *et al.* [5] calculations (Figure 70) are performed in the Correlated

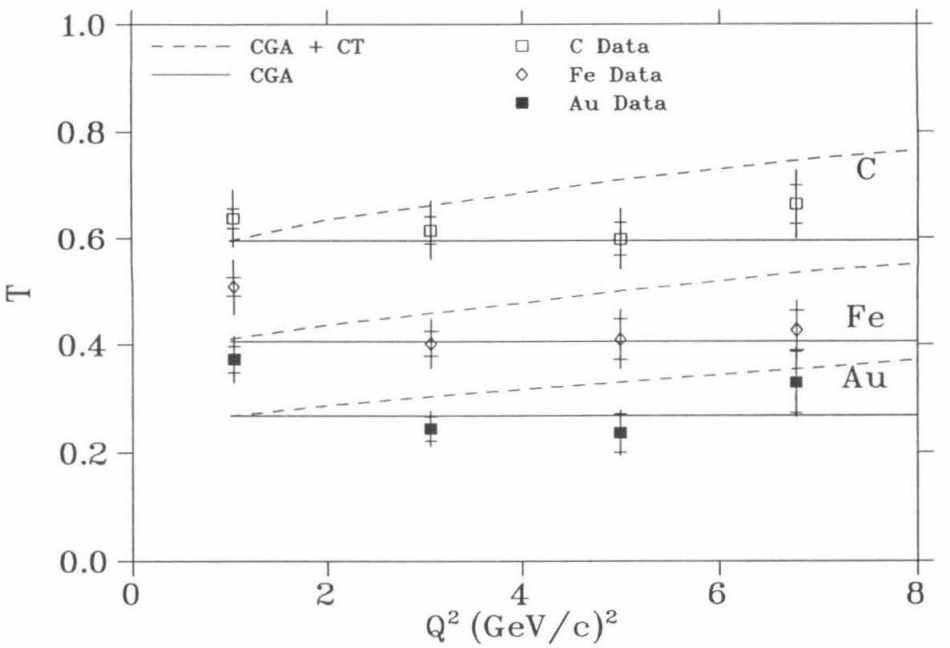

FIG. 70. **Benhar** *et al.* **[5] C, Au** T **predictions**

Glauber Approximation (CGA, which includes nucleon-nucleon correlations). For the CT curves, they use the Farrar *et al.* quantum diffusion model (Equation 5.16 with $\kappa = 1$ and $\Delta M^2 = 0.7\,\mathrm{GeV}^2/\mathrm{c}^4$). Within the uncertainties in the Glauber approximation, the data cannot rule out either CGA + CT or CGA.

The CT predictions of Frankfurt, Strikman and Zhalov [6] in Figure 71 were calculated using their Glauber model and the Farrar *et al.* quantum diffusion model of σ_{eff} (Equation 5.16 with $\kappa = 1$ and ΔM^2 labelled in the figure). The label "CSE" refers to the inclusion of the Color Screening Effect, which causes suppression of the PLC in the nuclear environment: the PLC has a smaller interaction with nearby nucleons and therefore a smaller binding energy. Hence, it is energetically unfavorable and, for $Q^2 > Q_0^2$, is suppressed by the factor:

$$\delta(k) = \left[1 + \left(\frac{1 - Q_0^2}{Q^2}\right) \frac{k^2/M_p^2 + 2\varepsilon_A}{\Delta E}\right]^{-2}. \tag{5.22}$$

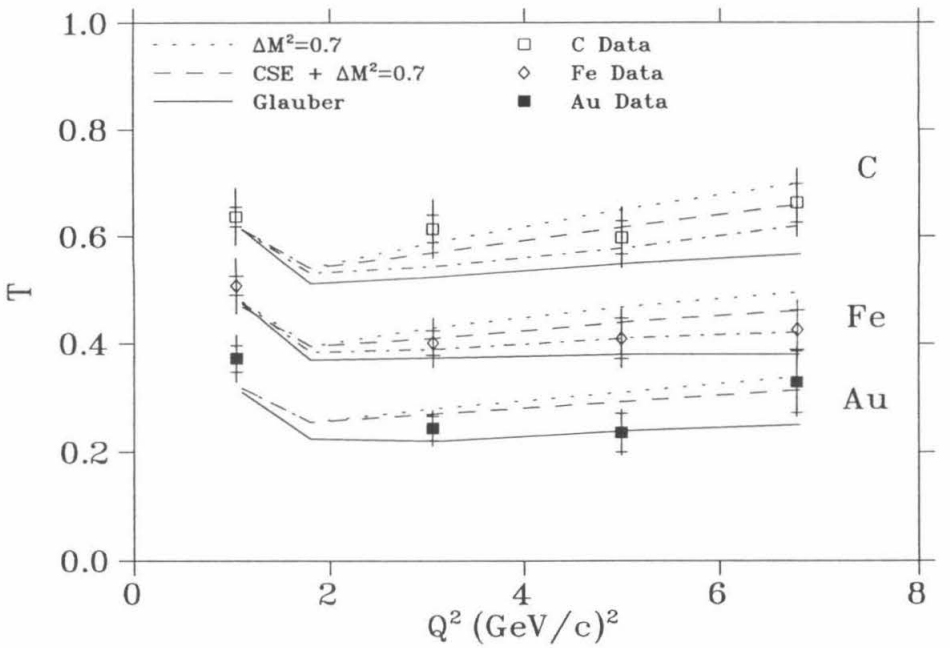

FIG. 71. **Frankfurt, Strikman, and Zhalov [6] C, Fe, Au T predictions**

Here $\varepsilon_A \simeq 8\,\mathrm{MeV}$ is the mean binding energy, $\Delta E \simeq 0.6\,\mathrm{GeV}$ based on the EMC effect, and $Q_0^2 \simeq 2\,(\mathrm{GeV/c})^2$ based on the SLAC $^2\mathrm{H}(e,e')$ data at $x \geq 1$ and large Q^2 [6]. Comparing the calculations to the $Q^2 \geq 3\,(\mathrm{GeV/c})^2$ data, one again observes that none of the curves can be ruled out within the accuracy of the Glauber approximation. However, unlike the other predictions, these include the effect of the variations in σ_{tot} and should also reproduce the $Q^2 = 1\,(\mathrm{GeV/c})^2$ data. One observes that, regardless of the renormalization of the authors' Glauber prediction, the $\Delta M^2 = 0.7$ and $CSE + \Delta M^2 = 0.7$ curves are inconsistent at the two sigma level with either the $Q^2 = 1\,(\mathrm{GeV/c})^2$ or the $Q^2 = 5\,(\mathrm{GeV/c})^2$ Au data. The disagreement of these curves with the data indicate either a failure of the CT model or an underestimate in the drop in the Glauber value from $Q^2 = 1\,(\mathrm{GeV/c})^2$ to $Q^2 = 3\,(\mathrm{GeV/c})^2$.

In summary, the data has ruled out the naive parton Color Transparency model

of Farrar *et al.* [2] and both of the Frankfurt, Strikman, and Zhalov [6] ^{197}Au$(e,e'p)$ CT predictions. It is important to realize that the exclusion of the latter results was made possible only through the use of the $Q^2 = 1\,(\mathrm{GeV/c})^2$ data, which serves to fix the very uncertain normalization of the Glauber model. Because of this, the failure of the predictions could be evidence of shortcomings in the Glauber model at $Q^2 = 1\,(\mathrm{GeV/c})^2$ rather than the CT model.

Since the Frankfurt, Strikman, and Zhalov calculations were the only predictions with a realistic treatment of the FSI at $Q^2 = 1\,(\mathrm{GeV/c})^2$, it was the only theory that could be subject to this more rigorous test. If the other calculations were improved to include the variation in σ_{tot} with Q^2, it is possible that other CT predictions could be ruled out as well. As an alternative, a more rigorous test of the CT predictions would also be allowed by the reduction of the uncertainty in the Glauber predictions.

Finally, it is worth considering the general state of the theory predictions. Clearly none of the CT predictions represent a realistic QCD dynamical model of the electron-proton scattering and subsequent Final State Interactions. The models are instead largely *ad hoc* and crudely justified, and so contain a large degree of adjustability (*e.g.*, through the mass scales ΔM^2 and M_1). This is underscored by the continual discovery and controversy over new effects (*e.g.*, the charge screening effect, nucleon-nucleon correlations, and the suppression of the effect of nucleon-nucleon correlations through the spectator effect and the finite range of the nucleon-nucleon interaction) that are argued to produce large changes in the measured values of T. Thus, while the presence of a strong Q^2 dependence in an experiment like NE-18 would be evidence of Color Transparency, the absence thereof does not rule out CT. However, because the CT effect is expected to increase with Q^2, its absence in a higher Q^2 experiment would be more convincing.

A decisive test of the phenomenon of Color Transparency in $A(e,e'p)$ awaits either a truly realistic prediction of $T(Q^2)$, the measurement of a Q^2 dependence larger than

the experimental errors, or the measurement of no Q^2 dependence in an accurate experiment at much higher Q^2.

VI. CONCLUSIONS

The $A(e,e'p)$ reaction has been measured at quasielastic kinematics for A =^{1}H, ^{2}H, ^{12}C, ^{56}Fe, and ^{197}Au and Q^2 = 1, 3, 5, and 6.8 $(\mathrm{GeV/c})^2$. This represents an increase by an order of magnitude of the range of Q^2 measured in $A(e,e'p)$ experiments. The effective spectral functions $S(E_m, p_m)$ extracted from the data exhibit the shell structure expected in the nuclear shell model. The shapes of the measured $S(E_m, p_m)$ agree well with those predicted using an Independent Particle Shell Model spectral function input and the Plane Wave Impulse Approximation. The agreement confirms the expected single-particle nature of the quasielastic knockout reaction at $Q^2 \geq$ 1 $(\mathrm{GeV/c})^2$. There is no evidence of significant multi-particle effects at $p_m < p_f$ and $E_m < m_\pi$.

The nuclear transparency T is extracted as the ratio of the measured rate to the rate expected in the absence of Final State Interactions, which is calculated in the PWIA/IPSM model. Thus, T is a measure of the absorption and deflection of the protons by the FSI. The T at $Q^2 = 1,3\,(\mathrm{GeV/c})^2$ is compared with the expectation using the standard nuclear physics model of the FSI (called the Glauber model) in order to test the saturation of the spectroscopic sum rule. The data is within the range of the Glauber calculations, indicating full saturation of the sum rule within the $\pm$20% uncertainty in the Glauber predictions. This is in contrast to the situation at low Q^2, where there is only $\sim$ 70% saturation of the spectroscopic sum rule. The data can also be used to better constrain the Glauber predictions.

Future experiments at the Continuous Electron Beam Facility (CEBAF) should result in higher-statistics and higher-resolution measurements of $S(E_m, p_m)$ at this Q^2 range. These are particularly interesting in light of the apparent disagreement of the Fe and Au momentum distributions measured in the current experiment with those measured for nearby nuclei at low Q^2. It is important to accurately test the earlier

results with measurements at $Q^2 \gtrsim 1\,(\mathrm{GeV/c})^2$, where the model of the FSI simplifies to independent proton-nucleon collisions and where the distortion to the shape of $S(E_m, p_m)$ is minimized by the large angular deflection in elastic interactions and by the decreasing value of the elastic proton-nucleon cross section. Although $S(E_m, p_m)$ measurements at much higher Q^2 would have even smaller distortions due to elastic FSI, they would be hampered by the degraded (E_m, p_m) resolution and larger radiative effects resulting from the increased experimental momenta. Because of this, it is likely that the optimal value for a precise measurement of $S(E_m, p_m)$ is within the Q^2 range of the present experiment.

Measurements of the nuclear transparency in $A(p, 2p)$ have indicated the possible onset of the Color Transparency effect [28]. The limitations in the interpretation of these data are intrinsic to the $A(p, 2p)$ reaction, so it is important to examine the issue with the theoretically simpler and better-understood $A(e, e'p)$ reaction. Within the total errors, the T measured in the present experiment does not exhibit the increase with Q^2 that would indicate the onset of Color Transparency. The data rule out three calculations of $T(Q^2)$ which include Color Transparency effects. The use of the data to rule out additional Color Transparency models is inhibited by the uncertainties in the Glauber predictions. More stringent limits on the Color Transparency models would result by reducing the theoretical uncertainty in the Glauber predictions. As an alternative, stricter limits could be obtained by normalizing the Glauber predictions to the T observed at $Q^2 = 1\,(\mathrm{GeV/c})^2$. At present this is not possible for the majority of Color Transparency models because they do not account for the reduced proton-nucleon cross section at $Q^2 = 1\,(\mathrm{GeV/c})^2$.

Many of the systematic errors in the current analysis are due to fundamental limitations in the understanding of the $A(e, e'p)$ reaction and to the increased difficulties inherent in the measurement of coincidence reactions. It would be difficult for future experiments to greatly improve the systematic error in T. Thus, the chances for ob-

servation of the Color Transparency effect in $A(e, e'p)$ seem best at higher Q^2, where the models predict larger changes in T.

APPENDIX A: COORDINATES

A schematic of the experiment is shown in Figure 72 with 3-momenta corresponding to the $Q^2 = 1\,(\mathrm{GeV/c})^2$, $\theta_8 = 35°$ carbon kinematics. The figure indicates the coordinate systems used in this document, which are defined in Tables 17–19.

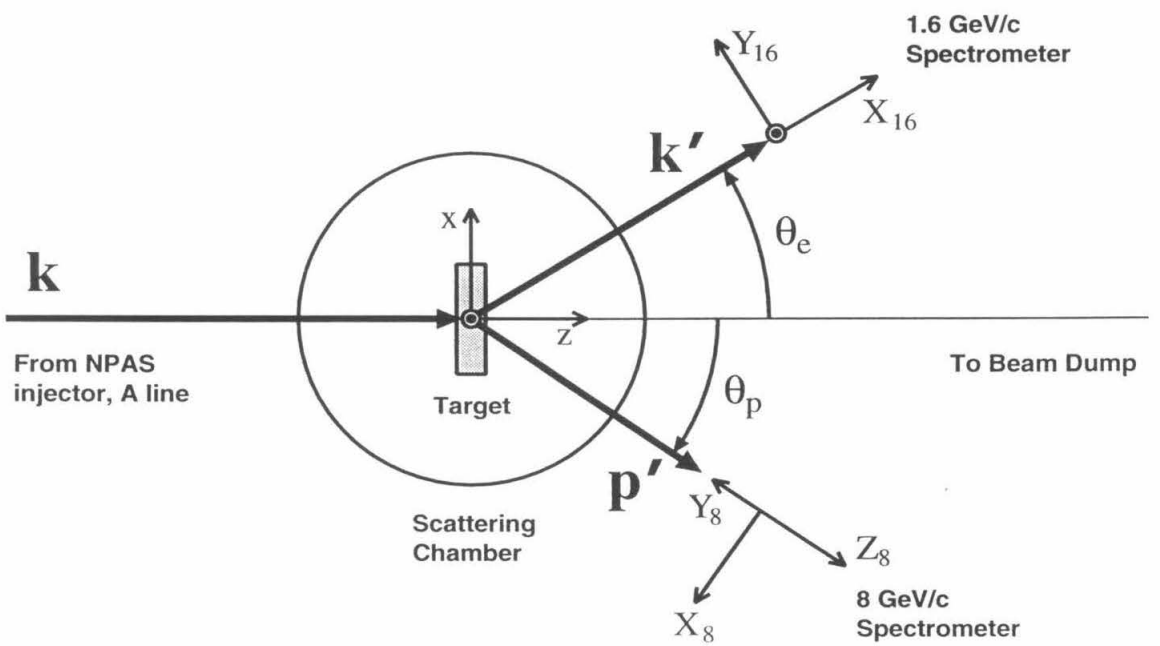

FIG. 72. Plan view of experiment NE-18. The coordinates y and Z_{16} are vertical (out of the page, as indicated by the bulls-eyes). Due to the tilt of the 8 GeV/c hut, Y_8 and Z_8 are inclined at 30° to the vertical and the horizontal, respectively.

TABLE 17. Laboratory coordinates. The angle variables Ω, θ, and ϕ generally have a subscript giving which 3-momentum they refer to. If not, they refer to the direction of the scattered electron (*i.e.*, $\Omega = \Omega_{k'}$, etc.).

Name	Description
x	Horizontal (the 1.6 GeV/c is at $x > 0$ and the 8 GeV/c is at $x > 0$)
y	Vertical, pointing up
z	Downstream along the beam line
θ, ϕ	Polar angles
Ω	Solid angle, $\Omega = (\theta, \phi)$
θ_{16}	Central angle of 1.6 GeV/c (electron) spectrometer
θ_8	Central angle of 8 GeV/c (proton) spectrometer

TABLE 18. Spectrometer (Transport [35]) coordinates. Coordinates are often accompanied by a subscript 16 or 8 to specify which spectrometer they refer to.

Name	Description
δ	Fractional deviation of momentum from central value
$\Delta\Theta$	Angle in the horizontal (xz) plane with respect to the beam line (minus central value)
Φ	Angle in vertical plane; larger values are up
Z_{targ}	z of scattering, as measured by one of the spectrometers

TABLE 19. Focal plane (hut) coordinates Coordinates at the "focal plane" of the detector hut. The focal plane ($Z = 0$) is orthogonal to the optical axis and does not necessarily correspond exactly to the momentum or angle focal planes of the spectrometers, which can be tilted. For convenience, the coordinates $(X, Y, Z)_8$ are given in a left-handed system.

Name	Description
X_{16}	In dispersive direction (increasing momentum)
Y_{16}	Orthogonal to X_{16}, Z_{16} (right handed)
Z_{16}	Along the optical axis; note $Z_{16} \parallel y$
X_8	Orthogonal to Y_8, Z_8 (left handed)
Y_8	In the negative dispersive direction
Z_8	Along the optical axis
$dX_{8,16}$	Shorthand for $(dX/dZ)_{8,16}$ (track slope)
$dY_{8,16}$	Shorthand for $(dX/dZ)_{8,16}$

APPENDIX B: TRACK PURGING

The track identification algorithms described in Section III.B often result in the identification of more than one track in an event. The purpose of the track purging software is to remove this ambiguity through the use of each spectrometer's position-sensitive detector elements. If a given track fails any one in the series of tests, it is discarded. The tests are applied either as "purges" or as "cuts." Purges are not applied unless at least one track would survive. Cuts are applied regardless of whether or not they reject all of the tracks. If all of the tracks in either spectrometer are cut, then the event is discarded. Such events are accounted for in the tracking efficiency correction, described below.

The purges and cuts are adjusted to minimize the number of true coincidence events rejected, as measured with the coincidence timing peak. In the 1.6 GeV/c spectrometer this was accomplished with spot checks of the data. In the 8 GeV/c each purge was adjusted to produce $\lesssim 0.1\%$ coincidence rejection in *every* run, even if it is applied as a cut. In Tables 20 and 21 and below, we describe the track purging tests.

The purpose of the 1.6 GeV/c and 8 GeV/c fiducial cuts is to ensure that the tracks are restricted to a region of constant detector efficiency, thus avoiding position-dependent biases. In the 8 GeV/c the test restricted tracks to at least 1 cm inside the $(X,Y)_8$ extents of the SF, NBS, and SR planes. In the 1.6 GeV/c, the cuts are:

$$|dX_{16}| < 0.25\,\text{rad}, |X_{vac}| < 100\,\text{cm}, |X_{PA}| < 100\,\text{cm}, \tag{B1}$$

$$|dY_{16}| < 0.20\,\text{rad}, \ |Y_{vac}| < 15\,\text{cm}, \ |Y_{PA}| < 100\,\text{cm}, \tag{B2}$$

where $(X,Y)_{vac}$ is the track position projected back to the exit of the dipole and $(X,Y)_{PA}$ is the position projected to the first shower counter layer. The cut on $|Y_{vac}|$ is used to throw out tracks where the electron suffered a grazing interaction with the

TABLE 20. Purge tests applied to tracks in the 1.6 GeV/c to remove tracking ambiguities.

Name	Type	Description
Fiducial	Cut	Track is in detector volume
Transv. Scint.	Cut	Track points at scintillators that fired
Shower Track	Purge	Track points at an electromagnetic shower in the segmented lead glass detector
Long. Scint.	Purge	Track points at location inferred from scintillator PMT time difference
Reconstruction	Cut	Track inside loose $(\delta, \Delta\Theta, \Phi)$ cuts
Nearby	Purge	Decides between multiple nearby tracks, assumes they are due to same particle
χ^2	Purge	Hits are co-linear
Most Wires	Purge	Take track with most wires
Most Pairs	Purge	Take track with most pairs
Best χ^2	Purge	Take track with best χ^2

beam pipe inside the dipole. Studies with ^{1}H$(e, e'p)$ demonstrate that these events entered the hut with randomized momenta and lower energies: they are broadly distributed in E_m and p_m, they appeared at artificially low Δt_{p-e} (and are therefore slower than they should be), and they deposited less energy in the shower counter. It is important to discard these because the acceptance model of the spectrometer assumes that an electron is lost if it hit the beam pipe.

The χ^2 tests are used to discard spurious tracks that arise when the track identification software connects up unrelated chamber hits. The transverse and longitudinal scintillator tests use the position and timing information of PMTs that fired to limit the $(X, Y)_{16,8}$ position of the detected particle. The reconstruction test is used to

TABLE 21. Purge tests applied in the 8 GeV/c to remove tracking ambiguities.

Name	Type	Description
χ^2	Purge	Hits are co-linear
Fiducial	Cut	Track is in detector volume
Scintillator	Purge	Like Transv. and Long. Scint test in 1.6 GeV/c
NBS	Purge	Track points at NBS counter that fired
Combined	Purge	Track passes a restrictive scintillator OR a restrictive NBS test
X_8–dX_8	Purge	Track satisfies observed correlation
Reconstruction	Cut	Track inside loose $(\delta, \Delta\Theta, \Phi)$ cuts
Z_{targ}	Purge	Track reconstructs back to target
Most Chambers	Purge	Take track with most chambers
Best χ^2	Purge	Take track with best χ^2
Best X_8–dX_8	Purge	Take track with best correlation

throw out tracks clearly outside the spectrometer acceptance. The last three purges in both spectrometers are used to select only one track out of any that remained.

The 1.6 GeV/c software also contains a purge on the "shower track" value. The value is the gain-matched sum of the signal heights in the shower counter blocks within 4 cm (the approximate width of an electromagnetic shower) of the track. Electrons are identified by large shower track values and pions, the main source of multiple tracks, by small values. The 1.6 GeV/c software also makes a series of purges on nearby tracks, assuming they are caused by the same particle, to decide which of them is best. It is safe to take only one of several nearby tracks because choosing the wrong one only results in worse resolution for that event.

In the 8 GeV/c, the scintillator tests are supplemented by the analogous NBS test and also the new combined test. In the combined test, the track is required to pass restrictive versions of either the scintillator OR the NBS tests. While the

individual inefficiencies of these restrictive tests is 1–5%, the combined inefficiency is $\lesssim 0.1\%$. Similarly, the 8 GeV/c reconstruction test is supplemented by a purge on Z_{targ} to throw out particles that could not have come from the target. The purge on the X_8–dX_8 correlation, produced by the 8 GeV/c spectrometer magnetic optics, is largely redundant with the Z_{targ} purge. It might seem that the final purge, on the best X_8–dX_8 correlation, would never be necessary because it is preceded by a purge on best χ^2. However, due to the discrete nature of the track angle measurement, two tracks that are parallel within the wire chamber resolution could have the same χ^2.

APPENDIX C: DEAD-TIME CORRECTIONS

The measured coincidence rate is corrected for the computer dead-time f_{coin}, giving the number of events missed because the computer could read out only one event per beam pulse. The dead-time is inferred from scalers measuring the rates of the various pretriggers. The computer dead-time cannot generally be calculated as simply the ratio of pretriggers to triggers because some of the pretriggers have temporal correlations.

We will use the conventions of Section II.D, where "$\mathcal{M}$" refers to a module and "$\mathcal{P}$" refers to a pretrigger. We also adopt new notations whereby "$\mathcal{T}_{pretrig}$" refers to a trigger resulting from the pretrigger *pretrig*, and "$\sum \mathcal{M}$" is a scaler counting the number of times module $\mathcal{M}$ fired.

The computer dead-time correction for electrons in the 1.6 GeV/c spectrometer is given by the total number of electrons divided by the number of electrons giving triggers. These values are given by the scalers $\sum \mathcal{M}_{cab}$ (corrected for hardware dead-time, below) and $\sum \mathcal{T}_{cab}$, see Figure 73. The $\mathcal{M}_{cab}$ scalers are used instead of $\mathcal{P}_{el}$ scalers because of their smaller π^- contamination. This is necessary because the correction is applied to the measured number of *true* electrons (in the coincidence peak), not to the measured number of $\mathcal{T}_{el}$ triggers (which includes π^- contamination).

In the 8 GeV/c, the computer dead-time is more subtle. When the rate of $\mathcal{M}_{2/3}$ signals is high, the dead-time can different dramatically depending on the status of the beam gate prescaler. For a prescaling fraction of ϵ_{pre} (typically $< 2^{-8}$), $\mathcal{P}_{2/3,pre}$ pretriggers were blocked during $1 - \epsilon_{pre}$ of the beam gates. During these beam gates only the pretriggers $\mathcal{P}_{coin}$, $\mathcal{P}_{longcoin}$, and $\mathcal{P}_{ran}$ could occur. Since these always occur in concert with a 1.6 GeV/c pretrigger ($\mathcal{P}_{el}$ or $\mathcal{P}_{ran}$), the computer dead-time for these beam bursts is already accounted for by $\sum \mathcal{M}_{cab} / \sum \mathcal{T}_{cab}$.

In the remaining fraction ϵ_{pre} of the beam spills, every $\mathcal{M}_{2/3}$ signal generates a

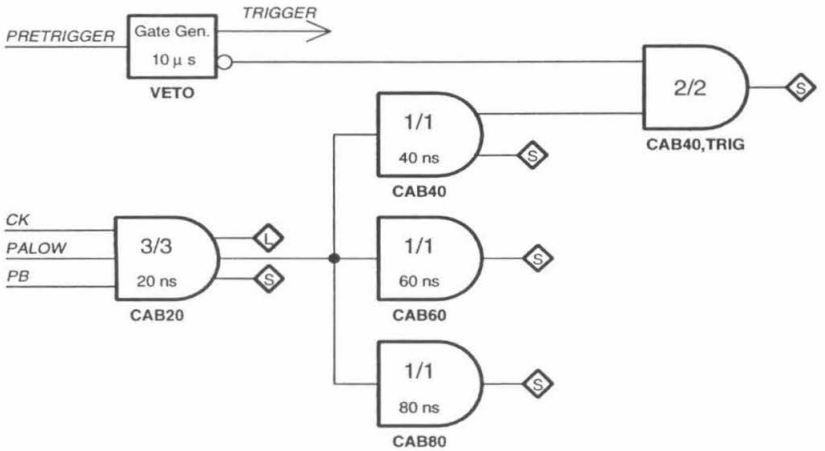

FIG. 73. **Formation of the 1.6 GeV/c $\mathcal{M}_{cab}$ (labelled CAB20–CAB80) and $\mathcal{T}_{cab}$ (labelled CAB40,TRIG) signals. The module $\mathcal{M}_{cab}$ requires signals in the Čerenkov and both shower counter layers (PA, PB), and has therefore has a lower π^- contamination than $\mathcal{P}_{el}$. The module $\mathcal{T}_{cab}$ is vetoed by the inverted trigger signal, and therefore indicates a $\mathcal{P}_{el}$ that came in concert with a trigger. See Figure 28 for the origins of the input signals.**

pretrigger $\mathcal{P}_{2/3,pre}$. The scaler $\sum \mathcal{P}_{2/3,pre}$ ($\sum \mathcal{T}_{2/3,pre}$) counts the number of these pretriggers (triggers). (See Figure 74.) In fact, these scalers count all possible pretriggers (triggers) that occur during the prescaled beam gates, except for the extremely small fraction caused by $\mathcal{P}_{ran}$. This is because $\mathcal{P}_{coin}$ and $\mathcal{P}_{longcoin}$ both require $\mathcal{M}_{prot}$, which is a subset of $\mathcal{M}_{2/3}$. The number of triggers due solely to the pretrigger $\mathcal{P}_{2/3}$ is measured by the scaler $\sum \mathcal{T}_{2/3,only}$ (see Figure 74). During prescaled beam gates, the fraction of triggers due to $\mathcal{P}_{coin}$, $\mathcal{P}_{longcoin}$, and $\mathcal{P}_{ran}$ is $1 - \sum \mathcal{T}_{2/3,only} / \sum \mathcal{T}_{2/3,pre}$. The presence of the pretrigger $\mathcal{P}_{2/3,pre}$ has not prevented the firing of these triggers, and their dead-time is again correctly given by $\sum \mathcal{M}_{cab} / \sum \mathcal{T}_{cab}$. In the remaining fraction $\sum \mathcal{T}_{2/3,only} / \sum \mathcal{T}_{2/3,pre}$ of the triggers, due only to the pretrigger $\mathcal{P}_{2/3,pre}$, the additional

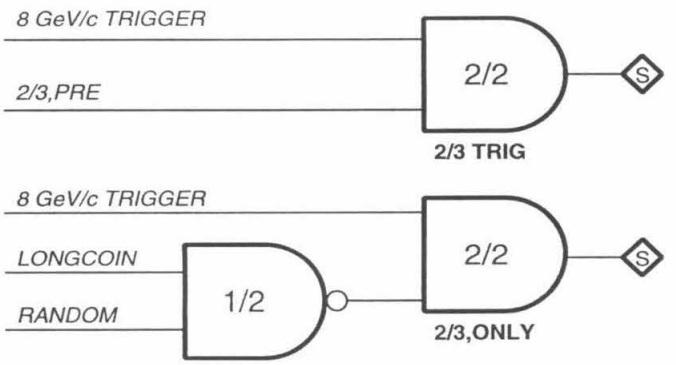

FIG. 74. **Formation of the 8 GeV/c $\mathcal{T}_{2/3}$ (labelled 2/3,TRIG) and $\mathcal{T}_{2/3,only}$ (labelled 2/3,ONLY) signals. See Figure 30 for the origin of the input signals.**

8 GeV/c dead-time is given by the pretrigger to trigger ratio for the prescaled beam gates, $\sum \mathcal{P}_{2/3,pre} / \sum \mathcal{T}_{2/3,pre}$. Thus the dead-time correction for the prescaled beam gates is:

$$f_{pre} = \frac{\sum \mathcal{M}_{cab}}{\sum \mathcal{T}_{cab}} \left[\left(1 - \frac{\sum \mathcal{T}_{2/3,only}}{\sum \mathcal{T}_{2/3,pre}} \right) + \frac{\sum \mathcal{T}_{2/3,only}}{\sum \mathcal{T}_{2/3,pre}} \frac{\sum \mathcal{P}_{2/3,pre}}{\sum \mathcal{T}_{2/3,pre}} \right] . \tag{C1}$$

The coincidence live time (1/dead-time) for both classes of beam gate is the weighted average of f_{pre}^{-1} and the live time for non-prescale beam gates. The total coincidence dead-time is therefore:

$$f_{coin} = \frac{\sum \mathcal{M}_{cab}}{\sum \mathcal{T}_{cab}} \left[(1 - \epsilon_{pre}) + \frac{\epsilon_{pre}}{\left(1 - \frac{\sum \mathcal{T}_{2/3,only}}{\sum \mathcal{T}_{2/3,pre}} \right) + \frac{\sum \mathcal{T}_{2/3,only}}{\sum \mathcal{T}_{2/3,pre}} \frac{\sum \mathcal{P}_{2/3,pre}}{\sum \mathcal{T}_{2/3,pre}}} \right] . \tag{C2}$$

For the large majority of runs, this formula agrees to within 1% with the dead-time expected from the measured rates and Poisson statistics. The disagreement is almost certainly due to the statistical error in the expected rate, which was not calculated. Equation C2 should be accurate to much better than 1%, even though it is only an approximate form, The approximations are assuming a statistical distribution of events between the prescaled and non-prescaled beam gates (negligible error for the

two cases used, $\epsilon_{pre} = 1$ and $\epsilon_{pre} \ll 1$) and neglecting the (tiny) fraction of $\mathcal{P}_{ran}$ triggers. The dead-time f_{coin} is usually $< 20\%$.

In the above, the signals $\mathcal{M}_{cab}$ and $\mathcal{P}_{2/3,pre}$ can occur more than once a beam burst and must be corrected for hardware dead-time, wherein the finite width of input logic gates (typically $\tau = 20\,\text{ns}$) prevents the scalers from distinguishing two nearly simultaneous firings. The measured rate ω_{scaler} is reduced from the true rate ω by the probability of simultaneous firing:

$$\omega_{scaler} = \omega e^{-\omega\tau} \simeq \omega(1 - \omega\tau). \tag{C3}$$

The linear approximation never under-estimates the hardware dead-time by more than 0.04% in the 8 GeV/c and 0.08% in the 1.6 GeV/c. The scalers used to calculate the computer dead-time are measured using $\tau = 20, 40, 60, 80\,\text{ns}$. The measured scaler counts vs. τ shows a linear relationship for all but $\tau = 20\,\text{ns}$, probably because of double pulsing. Thus, only the $\tau > 20\,\text{ns}$ scalers can be used to perform the linear extrapolation to the true counts at $\tau = 0$.

The total error of the dead time corrections is estimated to be $< 0.3\%$, based on comparisons of the measured dead times with values expected using Poisson statistics.

APPENDIX D: COINCIDENCE IDENTIFICATION

The time difference $\Delta t_{8-16} = t_8 - t_{16}$ between the triggers was measured by two TDCs, a 50 ps/channel TDC started by the 8 GeV/c coincidence trigger (T_{16-8}) and a 100 ps/channel TDC started by the 1.6 GeV/c trigger (T_{8-16}). (See Table 22 for the naming conventions used to refer to times.) Figure 75 shows non-linear response in both TDCs for small values, and describes how they were linearized for the analysis. During the $Q^2 = 7\,(\mathrm{GeV/c})^2$ data-taking, the stop signal to the 1.6 GeV/c TDC became erratic, causing the TDC to time out. The 8 GeV/c TDC was used at all kinematics to identify coincidences.

TABLE 22. Timing conventions, including times commonly referred to in the discussion of coincidence identification. Many statements apply equally to the 1.6 GeV/c and the 8 GeV/c spectrometers. In these cases the 8 GeV/c spectrometer will be taken as an example. Constant time offsets are generally suppressed, but should be viewed as being carried along. For our purposes, all of these constants can be treated as being absorbed in the C of Equation D4.

Name	Description
t_{16}	1.6 GeV/c trigger time (leading edge)
t_8	8 GeV/c trigger time
t_e	time of electron at target
t_p	time of proton at target
t_{fp8}	particle time at spectrometer focal plane, 8 GeV/c
t_{fp16}	particle time at spectrometer focal plane, 1.6 GeV/c
t_{PMT}	time discriminator fires and stops PMT's TDC
Δt_{a-b}	$t_a - t_b$, where a, b are two of the subscripts above
T_{a-b}	TDC measurement of Δt_{a-b} ($b = 8$ or 16 starts the TDC and a stops it)

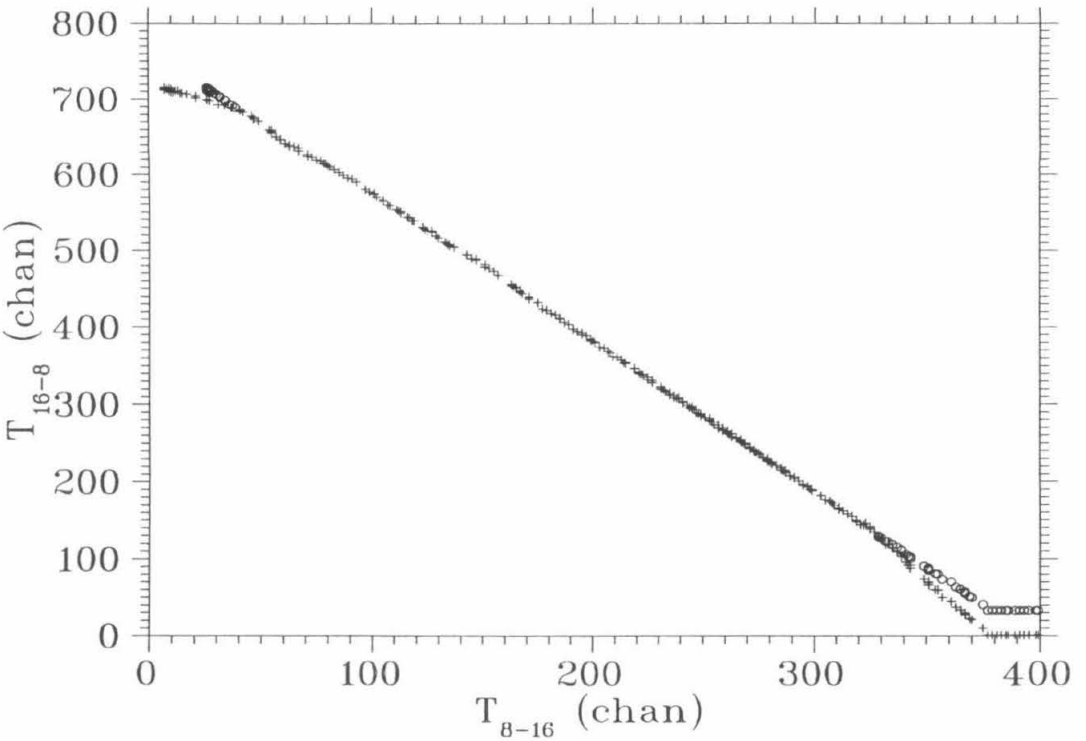

FIG. 75. **Coincidence TDC non-linearities. Comparison of the two coincidence TDC values for 1/100 of the $Q^2 = 1\,(\mathrm{GeV/c})^2$ carbon data. The plus signs are the raw values, and the circles show the linearized values (when different). Both raw TDCs behave non-linearly for small values. The 8 GeV/c TDC T_{16-8} is fit as having three slopes (for values < 45, 45–130, and ≥ 130) and the 1.6 GeV/c TDC T_{8-16} is fit as having two slopes (for values < 40 and ≥ 40). The linearized values, obtained by applying a piecewise linear correction derived from the fit slopes, are used in the analysis and all other graphs.**

The signal delay lines were adjusted so coincidence proton pre-triggers would arrive, on average, about 20 ns into the gate (see Figure 76). This time was made as short as possible to minimize dead-time caused by non-coincidence 8 GeV/c pre-triggers occurring during the gate before true coincidence protons. The time was not made shorter to prevent loss of true coincidences due to the $\sim \pm 5$ ns width of the Δt_{8-16} coincidence peak.

Variations in path length through the spectrometer and scintillator response time are responsible for the $\sim \pm 5$ ns width. The value Δt_{8-16} was converted into a time difference Δt_{p-e} between the proton and electron at the target by removing these effects (see Figure 78 and Equation D4). The path length corrections were made in each spectrometer using the Z matrix elements of the reverse Transport model, adjusted to produce the best timing resolution. The matrix elements specify the path length Z from the target to the spectrometer focal plane. The time it takes the particle to reach the focal plane is

$$\Delta t_{p-fp8} = Z/\beta_8 c, \tag{D1}$$

where Z is the path length. Here the particle velocity $\beta_8 c$ is inferred from the measured momentum p_8 and the assumed mass M_8:

$$\beta_8 = p_8/\sqrt{p_8^2 + M_8^2 c^2}. \tag{D2}$$

For $(e, e'p)$ the masses were $M_{16} = m_e$ and $M_8 = M_p$. Errors in Δt_{p-fp8} (or Δt_{e-fp16}) for particles of mass $\neq M_8$ (M_{16}) do not effect the measured coincidence rate because these particles are always accidentals and are therefore uniformly distributed in Δt_{p-e}. The scintillator response times Δt_{8-fp8} were determined using measurements of the Time-of-Flight (TOF) between scintillators for particles of known velocity (see Appendix D.2). Combining this with the path length correction Δt_{8-fp8}, one obtains the time it takes the particle to cause a trigger:

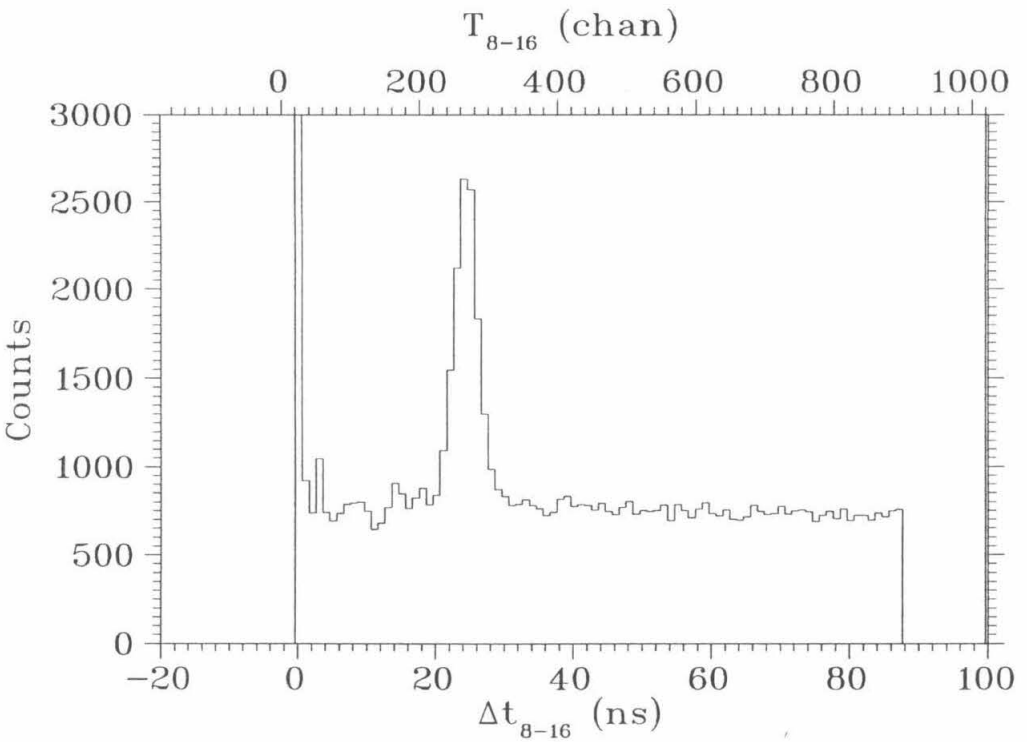

FIG. 76. **Time difference Δt_{8-16} between the 1.6 GeV/c electron trigger and the 8 GeV/c COIN trigger, as measured by the 1.6 GeV/c coincidence TDC T_{8-16}. The peak at $\Delta t_{8-16} \simeq 20\,ns$ is due to true $(e, e'p)$ coincidences, which occur 20 ns after the opening of the coincidence gate. The peak at $\Delta t_{8-16} = 0$ is due to accidentals occurring at the beginning of the coincidence gate. For these events, the time of the coincidence trigger was determined by the the 1.6 GeV/c electron pre-trigger instead of by the 8 GeV/c proton pre-trigger. This occurred when the 18 ns wide 8 GeV/c proton pre-trigger was already true when the 1.6 GeV/c electron pre-trigger occurred. For these events T_{16-8} is still a valid measurement of Δt_{8-16}.**

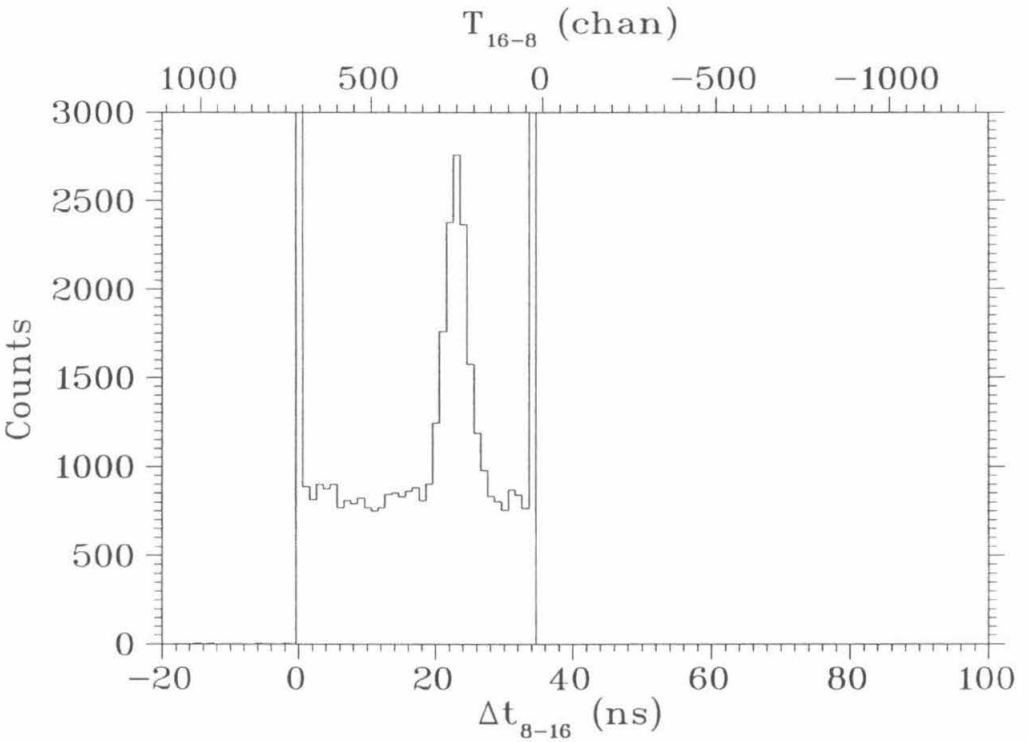

FIG. 77. Δt_{8-16} as measured by the 8 GeV/c TDC T_{16-8}. For this TDC a smaller value corresponds to a *larger* time difference between the triggers (the top and bottom axes run in opposite directions). The peak at $T_{16-8} = 0$ is due to underflow of the TDC for accidentals with $\Delta t_{8-16} > 34$ ns. For these events, T_{16-8} is *not* a valid measurement of Δt_{8-16}.

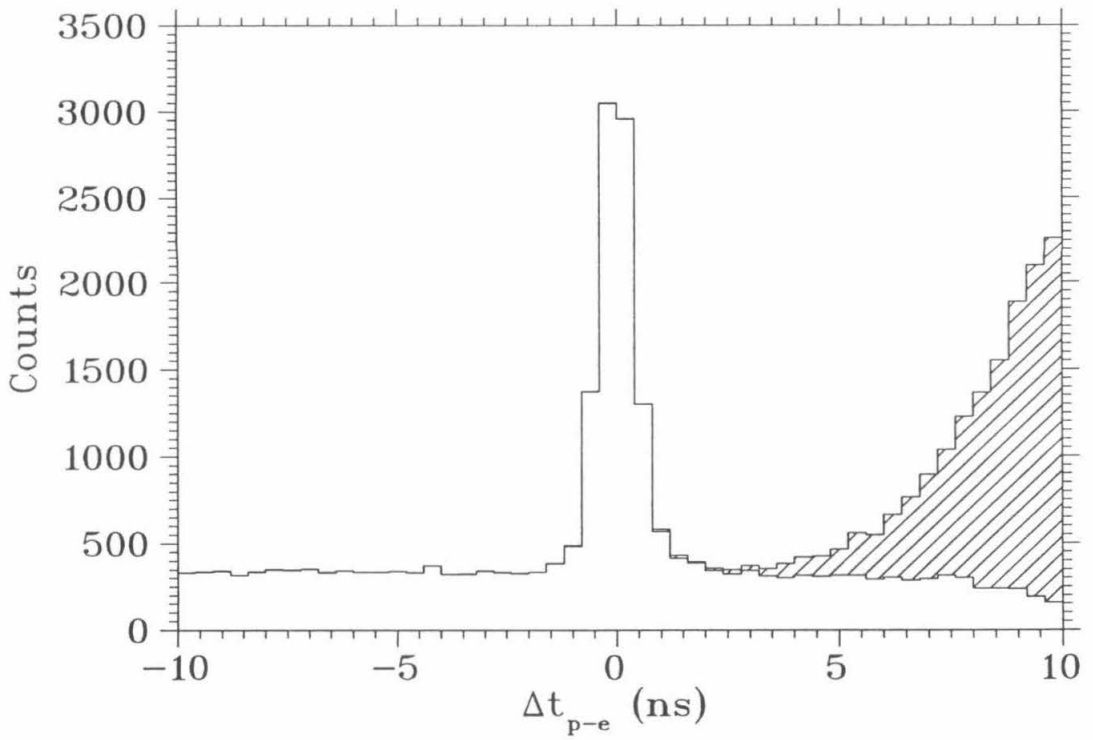

FIG. 78. **Time difference Δt_{p-e} between the electron and proton at target, calculated from the data in Figure 77 by removing the effects of path length through the spectrometer and scintillator response time. The peak at $\Delta t_{p-e} = 0$ is due to true $(e, e'p)$ coincidences. The shaded region are the data at $T_{16-8} = 0$, where TDC underflow prevents a valid measurement of Δt_{8-16} (see Figure 77).**

$$\Delta t_{p-8} = Z/\beta_8 c - \Delta t_{8-fp8}. \tag{D3}$$

True coincidences are identified by calculating the difference between the times of the electron and proton at target:

$$\begin{aligned} \Delta t_{p-e} &= \Delta t_{p-8} + \Delta t_{8-16} - \Delta t_{e-16} \\ &= \Delta t_{p-8} + C - T_{16-8} - \Delta t_{e-16}. \end{aligned} \tag{D4}$$

The 1.6 and 8 GeV/c trigger delay line lengths were varied as Q^2 was changed to account for the variation in proton flight time. The constant C was determined at each Q^2 by centering the coincidence peak at $\Delta t_{p-e} = 0$.

To prevent contamination by the tails of the coincidence peak, the accidental rate must be measured using events with $|\Delta t_{p-e}| > 5\,\mathrm{ns}$. The rate is determined using only the data in the range $-20\,\mathrm{ns} < \Delta \mathrm{t_{p-e}} < -6\,\mathrm{ns}$ ($\Delta t_{win} = 14\,\mathrm{ns}$, below). The measurement could be extended to more negative Δt_{p-e}, but this would provide minimal improvement to the statistics of the accidental subtraction. The shaded events in Figure 78 prevent determination of the accidental rate using the data at $\Delta t_{p-e} > 0$.

To prevent contamination by events with incorrect time determinations, the number of coincidences is determined without the 8 GeV/c TDC underflow events (the shaded region in Figure 78). A further efficiency factor is applied to correct for true coincidences in the underflow channel. This correction is determined by calculating Δt_{p-e} with the 1.6 GeV/c TDC, which does not have the underflow problem.

The 8 GeV/c TDC underflow problem could have been prevented by increasing the delay of the 1.6 GeV/c trigger signal into the TDC. During the design of the experiment, it was incorrectly thought that doing so would increase the dead-time. It would not have, in fact, because the TDC gave time differences between triggers and the electronics guaranteed that only one 8 GeV/c and one 1.6 GeV/c trigger could occur during a beam burst. Thus there were no signals competing to start or stop the TDC.

D.1. Scintillator Timing Corrections

A PMT's TDC measured T_{PMT-8}, the time the PMT fired with respect to the trigger. The ns/chan scale of each TDC channel was measured using a pulser. We

convert to the trigger response time,

$$\Delta t_{8-fp8} = \Delta t_{PMT-fp8} - T_{PMT-8}, \tag{D5}$$

needed in Equation D3 by correction for the scintillator response time $\Delta t_{PMT-fp8}$. This is calculated based on the particle tracking information:

$$\Delta t_{PMT-fp8} = C_{PMT} + Z_{PMT}\sqrt{1 + dX^2 + dY^2}/\beta_8 c - \Delta L/v_{scint} - P\sqrt{\max(A_{PMT}, A_0)}. \tag{D6}$$

The constant C_{PMT} represents cable lengths and PMT response times that can vary from PMT to PMT.

The term $Z_{PMT}\sqrt{1 + dX^2 + dY^2}/\beta_8 c$ is the particle drift time from the focal plane ($Z_8 = 0$) to the scintillator ($Z_8 = Z_{PMT}$). (Note that for $Z_{PMT} < 0$ this time can be negative.) The factor $\sqrt{1 + dX^2 + dY^2}$ represents the small ($< 0.1\%$) increase in drift length due to the track hut angles dX and dY.

Within a constant, $-\Delta L/v_{scint}$ is the time it takes the scintillation light travelling at velocity v_{scint} to propagate the distance $L/2 - \Delta L$ along the scintillator from the particle track to the PMT. Here L is the length of the scintillator and $\Delta L = X_8$ or Y_8 is the track coordinate in the longitudinal direction of the scintillator.

The pulse height correction is $-P\sqrt{\max(A_{PMT}, A_0)}$, which corrects for the fact that the discriminator that stops the T_{PMT-8} TDC fires earlier for large PMT pulses than for small ones. Here A_{PMT} is the value of the PMT's area-integrating ADC after pedestal subtraction. The procedure for determining the values of the adjustable parameters v_{scint}, C_{PMT}, P, and A_0 is described in Appendix D.2.

Each PMT that fired and is also on the particle track can be considered to provide a nearly independent measurement of Δt_{8-fp8}. In the 1.6 GeV/c most events had 8 measurements of $\Delta t_{16-fp16}$ (two per plane, because the scintillators are read out on both sides) and in the 8 GeV/c most provided at least 6 measurements of Δt_{8-fp8} (two

per plane, or more for tracks in the overlap regions of the SM and SR). The TOF software averages together the Δt_{8-fp8} measurements for all PMTs satisfying: 1) the X_8, Y_8 of the track at $Z_8 = Z_{PMT}$ are inside the extent of the PMT's scintillator, 2) both PMTs on the scintillator fired, and measured the same value of Δt_{8-fp8} within a tolerance. The tolerance was 0.8 (SF), 1.0 (SM,SR), or 1.5 ns (all 1.6 GeV/c scintillators).

Condition (1) guards against the inclusion of scintillator hits not associated with the particle track and which are likely to have occurred at a different time. The X_8 and Y_8 extent of each scintillator was determined using the track coordinates at $Z_8 = Z_{PMT}$ when the scintillator PMTs fired, coupled with the known width and length. If no scintillator satisfying directly on the track had a PMT that fired then, to allow for tracking resolution, condition (1) is relaxed. At this point the track must point within 1 cm (0.5 cm in the 1.6 GeV/c) of the scintillator for the PMTs to be included in the Δt_{8-fp8} measurement.

Calculation of Δt_{8-fp8} requires good TDC and ADC values. For the purposes of the TOF software, a PMT is considered to have fired if $2 < T_{PMT-8} < 1500$ chan (TDC finite but not timed out) and $A_{PMT} > 30$ chan (at least a small pulse). (For the 1.6 GeV/c spectrometer the ranges are $2 < T_{PMT-16} < 600$ chan and $A_{PMT} > 30$ chan. The 8 GeV/c TDCs had 0.05 ns/chan resolution and the 1.6 GeV/c TDCs had 0.1 ns/chan resolution.) The two-PMT requirement in condition (2) was motivated by studies of events where the PMTs' Δt_{8-fp8} values did not agree within resolution. Most of the Δt_{8-fp8} outliers were from scintillators where either: a) only one PMT fired or b) two PMTs fired but disagreed on Δt_{8-fp8}. Either case indicates an increased probability that the PMT firing was not associated with the particle track. In case (a) the PMT firing may have been spurious or due to a neutral particle. In case (b) the scintillator was probably hit by a particle at a different longitudinal position than the track. After applying condition (2) the fraction of events

with Δt_{8-fp8} outliers was less than 1%.

D.2. Scintillator Timing Parameters

As mentioned above, the parameters v_{scint}, C_{PMT}, P, and A_0 were required for each PMT to make the scintillator timing corrections (Equation D6). The pulse height correction was not very sensitive to A_0 and a value of $A_0 = 50\,\text{chan}$ was adopted for all PMTs. The parameters were fit using measurements of the Time-of-Flight between scintillators for $(e, e'p)$ events and assuming the velocity $\beta_8 c$ given in Equation D2. In order to prevent biasing of the fits, only loose cuts on Δt_{p-e} were used to identify the coincidences. The fitting data came from kinematics with good Δt_{p-e} true-to-accidental ratio to ensure minimal contamination by particles of mass $\neq M_8$.

In addition, it proved convenient (see Appendix D.3) to measure the attenuation length λ and the ADC value A_1 for a particle passing through the center of the scintillator by the following fit:

$$A_{PMT} = A_1 e^{-\Delta L/\lambda}. \tag{D7}$$

In this case no time differences needed to be calculated.

The parameters were fit for each PMT independently. Due to the uniformity of the scintillators and PMTs, the fits generally gave consistent values of v_{scint}, P, λ and A_1 for the PMTs in a given scintillator plane. For these parameters, adopting the global values given in Table 23 yielded adequate timing resolution. This is because small uncorrelated errors in the corrections for individual PMT's averaged out over the large ($\gtrsim 6$) number of Δt_{8-fp8} measurements for each event. It was far more important to have accurate, individual values of C_{PMT}, because of the significant differences in cable lengths and PMT response times. Best timing resolution was

TABLE 23. Timing parameter values used to make the scintillator timing corrections in Equation D6. The scintillator thickness is included to demonstrate its effect on v_{scint} and λ. The inferior condition of the 1.6 GeV/c scintillator material results in lower values of v_{scint} and λ than for SM and SR in the 8 GeV/c. For comparison with v_{scint}, the speed of light in vacuum is $c = 30.0$ cm/ns. The value of $A_0 = 50$ chan is used for all scintillator planes. Rough values for A_1 and λ in the 8 GeV/c are given for comparison, but are not used in the data analysis. The reference planes are those used in fitting the coefficients for the fit plane. The values of σ given are rough indications of the timing resolution of each plane, as inferred from the scatter in the difference of Δt_{8-fp8} between pairs of planes.

Fit Plane	Thick. cm	v_{scint} cm/ns	P ns/chan$^{1/2}$	A_1 chan	λ cm	Reference Planes	σ ns
SF	0.9525	13.7	0.19	400	90	SM, SR	0.13
SM	1.27	14.3	0.09	220	250	SF	0.16
SR	1.27	14.3	0.09	190	250	SF	0.19
YD	1.27	13.6	0.12	460	50	XU	0.21
XD	1.27	13.6	0.10	460	50	YU	0.22
YU	1.27	13.6	0.15	460	50	XD	0.26
XU	1.27	13.6	0.12	460	50	YD	0.26

obtained by refitting the 8 GeV/c C_{PMT} at each Q^2, because of changes in β_8 and the energy loss rate (and therefore A_{PMT}) with energy.

Rather than make a global fit of all of the v_{scint}, C_{PMT}, and P simultaneously, we used an iterative procedure that allowed each value to be fit independently. (The global fit was considered to be more likely to be unstable and more prone to correlations between the different corrections. For example, the pulse height correction, coupled with the attenuation length of the scintillator material, could give a false value for v_{scint}.) For the starting values of v_{scint} and P we used parameters measured

in a cosmic ray telescope before the experiment. The offsets C_{PMT} were fit parameters and did not need to be specified. In this procedure each parameter was measured for one PMT at a time by comparison with the timing information from reference scintillators in different planes.

The events used in the fitting were those where a reference scintillator r satisfied conditions (1) and (2), above and where the PMT being fit fired and satisfied condition (1). For fitting, $\Delta t_r = \Delta t_{8-fp8}$ was calculated as the average of the value given by the PMTs on reference scintillator r. To improve the statistics and protect against systematic errors in Δt_r each correction was fit against several reference scintillators simultaneously. Incorrect values of v_{scint} and P in the reference plane could introduce position-correlated biases that could mimic additional v_{scint} and P dependence in the fit plane. To remove the correlation between ΔL in the fit and reference scintillators, the reference scintillators were chosen to be orthogonal to the fit scintillator and separated by at least 80 cm (see Table 23).

When measuring v_{scint}, the value $\Delta t_{fit} = \Delta t_{8-fp8}$ for the PMT being fit was calculated, except that ΔL was set to zero in Equation D6 to disable the v_{scint}-dependent correction. Then the fit $\Delta t_{fit} - \Delta t_r = \Delta L / v_{scint} + \Delta C_r$ versus ΔL was performed, with fit parameters v_{scint} and ΔC_r. Here $\Delta C_r = C_{fit} - C_r$ is the difference between the offsets of the fit PMT and reference scintillator r. Note that this fit is only used to obtain v_{scint}, and the values of C_{PMT} resulting from this fit were not adopted (see below).

Inside a scintillator, most light propagates to the PMT through a series of internal reflections and the propagation speed v_{scint} is less than c divided by the index of refraction of the scintillator. In thicker scintillators light takes a more direct path, and v_{scint} is higher. The age of the 1.6 GeV/c scintillator material probably reduced v_{scint} because crazed patches could block more direct propagation paths. (See Table 23.)

Note that when the Δt_{8-fp8} average is calculated, the correction $\Delta L / v_{scint}$ for

the two PMTs on a given scintillator cancel. Thus the value of v_{scint} only effects the determination of whether the two PMTs give consistent timing information (condition 2, above).

A similar fit was performed to extract P. In this case Δt_{fit} was calculated with P set to zero in Equation D6 to disable the pulse height correction. The fit was $\Delta t_{fit} - \Delta t_r = \Delta C_r - P\sqrt{\max(A_{PMT}, A_0)}$.

The need for the pulse height correction can be seen by a simple model. Scintillator pulses are asymmetric, with fast rise times ($\sim$ 10 ns) and long decay times ($\sim$ 20 ns). The leading edge, however, is approximately Lorentzian shaped:

$$\text{For } t < t_0 : P(t) \simeq \frac{kA_{PMT}}{(t - t_0)^2 + \Gamma^2/4}. \tag{D8}$$

Here t_0 is the time of maximum value, Γ is the FWHM of the peak, and k expresses the conversion between the ADC value and the peak height. Note that k varies slightly with variations in the pulse shape because the ADCs are area-integrating rather than pulse-height sampling. The PMT's TDC T_{PMT-8} is stopped by the signal of a discriminator set at a level D. In the above approximation, this occurs at the time:

$$t_{PMT} = t_0 - \sqrt{\frac{kA_{PMT}}{D} - \Gamma^2/4}. \tag{D9}$$

The form of the correction actually used was only approximately equal to this (Equation D6), but gave sufficient resolution. Better resolution could have been obtained by the correction $-P\sqrt{\max(0, A_{PMT} - A_0)}$, equivalent to the above. Rough fits to this form gave the following values of (P, A_0): (1.08,129) for SF, (0.73,107) for SM and SR, and (-1.04,312). These correspond to rise times $\sim \Gamma/2 = P\sqrt{A_0}$ of 12, 8, and 18 ns, respectively. These values are not intended to represent accurate measurements, but are merely to indicate the reasonableness of the model.

The values of C_{PMT} used were determined separately after all of the other parameters were finalized. This was done by averaging $\Delta t_{fit} - \Delta t_r$, where in this case

Δt_{fit} is given by Equation D6 with $C_{PMT} = 0$. Of course the fit only determines the difference in the offsets and the values are undetermined up to a common offset of all PMTs. The common offset affects only the choice of C in Equation D4, and is therefore chosen arbitrarily.

D.3. 1.6 GeV/c Scintillator ADC Malfunctions

Generally, the TDC and ADC of a scintillator PMT agree on whether or not the PMT fired. However, two classes of events were found for which the ADC values for the 1.6 GeV/c PMTs do not correspond to the TDC values. Fortunately both classes were marked by strong patterns in the ADC values so these events could be identified based on the ADC values alone. When the scintillator response time (Appendix D.1) was calculated for these events, the ADC value was replaced with an approximate value inferred from Equation D7 (if the TDC fired). After this correction, the Δt_{p-e} distribution for these events was nearly as good as for events where the ADCs functioned correctly. Even if this were not so, the coincidence timing efficiency correction would ensure that these events were counted correctly.

The scintillator ADCs were contained in three different LeCroy 2249 modules. These malfunctioned simultaneously, even though all other modules in the Camac crate continued to function correctly. Hence, the malfunction was probably due to the discriminator (or cable) providing the gate to these three modules. In the first class of events, possibly due to a too-wide gate signal, every channel in a given module gave the same large value (1185, 1997, or 1114) to within a few channels. In the second class of events, possibly due to a missing gate signal, some channels would read pedestal or below and others would exhibit more complicated but reproducible patterns.

APPENDIX E: THE MODEL SPECTRAL FUNCTION

The nuclear transparency T is determined by division of the measured $A(e,e'p)$ rate by that predicted in the PWIA calculation. The nuclear structure used in the calculation is specified by the model of the nuclear spectral function $S(E_s,\mathbf{p})$. The model $S(E_s,\mathbf{p})$ is calculated in the Independent Particle Shell Model approximation, with parameters adjusted to reproduce data from elastic electron-nucleus scattering and low-Q^2 $A(e,e'p)$ and $A(p,2p)$. This section specifies the parameters used for the nuclei C, Fe, and Au. The $S(E_s,\mathbf{p})$ of ^{1}H and ^{2}H are discussed in Section IV.B.

The IPSM spectral function used in the PWIA calculation is given in Equation 1.11. In the calculation, the energy profile of each nuclear shell i is given by a Lorentzian $L_i(E_s)$, which characterizes the energy width Γ_i due to the finite lifetime of the one-hole state:

$$L_i'(E_s) = \frac{1}{\pi}\frac{\Gamma_i/2}{(E_s-E_i)^2+\Gamma_i^2/4}. \tag{E1}$$

This formula must be modified, however, since the separation energy cannot be less than the one-proton removal energy of the nucleus, $E_{rem} = M_p + M_{A-1} - M_A$ (here M_A and M_{A-1} are the masses of the initial and recoil nuclei). Therefore the Lorentzian $L_i'(E_s)$ is cut off below E_{rem} and rescaled to ensure that the spectroscopic sum rule will still be satisfied:

$$L_i(E_s) = \begin{cases} L_i'(E_s)/\int_{E_{rem}}^{\infty} L_i'(E_s)dE_s, & E_s \geq E_{rem} \\ 0, & E_s < E_{rem} \end{cases} \tag{E2}$$

The momentum-space wave functions $\varphi_i(\mathbf{p})$ are the solutions to the bound-state Schrödinger equation with potential:

$$V(\mathbf{r}) = -V_0 f(r) + V_{SO}\left(\frac{\hbar}{m_\pi c}\right)^2 \frac{2}{r}\frac{df}{dr}\mathbf{l}\cdot\mathbf{s} + V_C(r). \tag{E3}$$

The parameter V_0 is the depth of a Woods-Saxon well with radius R_0 and diffuseness a:

$$f(r) = \left[1 + \exp\left(\frac{r - R_0}{a}\right)\right]^{-1}, \tag{E4}$$

where

$$R_0 = r_0(A-1)^{1/3}. \tag{E5}$$

The parameter V_{SO} is the strength of the Thomas spin-orbit term, and $V_C(r)$ is the Coulomb potential energy of a uniform sphere of radius $R_c = r_c(A-1)^{1/3}$. The $\varphi_i(\mathbf{p})$ are obtained as Fourier-transforms of the wave functions $\psi(\mathbf{r})$ calculated by the program described in reference [61].

Elton and Swift [15] found that for Ca nuclei and heavier, it was necessary to account for the non-locality of the nucleon-nucleon potential. Rather than calculate the wave function $\psi_{NL}(\mathbf{r})$ in a full non-local potential, it is sufficient to correct the wave function $\psi_L(\mathbf{r})$ from the local potential, Equation E3, in an effective mass approximation [61,51]:

$$\psi_{NL}(\mathbf{r}) = \psi_L(\mathbf{r})\left[1 + \frac{M_p}{2\hbar}\beta^2 V_0 f(r)\right]^{-1/2}. \tag{E6}$$

The resulting $\psi_{NL}(\mathbf{r})$ is then renormalized. For $\beta > 0$ (Fe, Au), the non-locality correction reduces the wave function at $r \lesssim R_0$ (where $f(r)$ is large) and increases it at large r. Consequently, the width of the momentum distribution $|\varphi_i(\mathbf{p})|^2$ is reduced by the non-locality correction. For $\beta = 0$ (C), the local-potential result is unchanged.

The parameters used to calculate $L_i(E_s)$ and $\varphi_i(\mathbf{p})$ are listed in Tables 24 and 25. The $\varphi_i(\mathbf{p})$ parameters for ^{12}C were derived by Elton and Swift [15] using charge-distributions from elastic electron-nucleus scattering and well depths from $A(p,2p)$. These were verified (and $V_0(1s)$ fine-tuned) with $^{12}\mathrm{C}(e,e'p)$ at Saclay [11,9], which provided what is probably the highest-quality $S(E_m,p_m)$ measurement of ^{12}C (see Figures 6 and 7).

The parameters for $L_i(E_s)$ of ^{12}C are also based on the Saclay [11,9] experiment. The *1s* shell experimental energy distribution is not symmetric about the peak, but is

TABLE 24. Shell-independent parameters of IPSM $S(E_s, \mathbf{p})$

Nucleus	a (fm)	r_c (fm)	β
^{12}C	0.55	1.3	0.0
^{56}Fe	0.60	1.3	0.85
^{197}Au	0.65	1.2	0.85

skewed to higher E_m. Since we approximate this with a nearly symmetric Lorentzian, it is best to use for E_{1s} the measured centroid at 38.1 ± 0.3 MeV rather than the peak at 35.6 ± 0.3 MeV. Because the $1p$ peak is so close to the one-proton removal energy $E_{rem} = 15.96$ MeV, $L_i(E_s)$ is also highly asymmetric and the peak is more appropriate than the centroid. The PWIA/IPSM uses $E_{1p} = 16.2$ MeV, based on inspection of the Saclay data and also on peak positions reported in other experiments [9]. The FWHM measured in the Saclay experiment were $\Gamma_{1s} = 21.4$ MeV [9] and $\Gamma_{1p} \simeq 2.5$ (estimated from the graph in reference [9]). The PWIA/IPSM uses $\Gamma_{1s} = 20$ MeV and $\Gamma_{1p} = 5$ MeV (which is effectively $\Gamma_{1p} \simeq 2.5$ MeV due to the E_{rem} cut-off). Note that the transparency is insensitive ($< 2\%$) to uncertainties in the energy distribution.

The $\varphi_i(\mathbf{p})$ parameters for ^{56}Fe are based on those measured for the nearby nucleus ^{58}Ni in $A(e, e'p)$ at Saclay [11,9]. The ^{58}Ni-based momentum distributions are wider than those measured in the present experiment, and have to be modified to produce agreement. The first modification is the use of the non-locality correction $\beta = 0.85$, which is recommended by Elton and Swift [15] for $A \gtrsim 40$. The second modification is the use of $r_0 = 1.3$ fm instead of 1.26 fm.

The parameters for the $L_i(E_s)$ of ^{56}Fe are also based on the Saclay ^{58}Ni$(e, e'p)$ [11,9] experiment, with E_i values corrected for the 2 MeV difference in the E_{rem} of ^{58}Ni (8.17 MeV) and ^{56}Fe (10.18 MeV). The experiment did not resolve the individual j states of the $1p$ and $1d$ orbitals, so the magnitude of the spin-orbit splitting was determined by the Woods-Saxon calculation. Due to the overlap of energy distributions

TABLE 25. Shell-dependent parameters of IPSM $S(E_s, \mathbf{p})$. The two sets of V_0, E_i, and Γ_i values presented for the deeper shells of Fe and Au are given by Hartree-Fock (smaller values) calculations and $A(e, e'p)$ data (larger values). The Hartree-Fock values are used in the analysis, with the data values as a check on the sensitivity to the E_s distribution.

Nucleus	i	V_0 (MeV)	r_0 (fm)	V_{SO} (MeV)	E_i (MeV)	Γ_i (MeV)
^{12}C	$1s_{1/2}$	66.0	1.36		38.1	20.0
	$1p_{3/2}$	55.0	1.36	9	16.2	5
^{56}Fe	$1s$	80.7	1.3		50/64	19/21
	$1p_{3/2}$	69.0	1.3	40	39.5/49.5	16/19
	$1p_{1/2}$	69.0	1.3	40	32.1/42.1	13/17
	$1d_{5/2}$	58.2	1.3	23.5	27.2	10
	$1d_{3/2}$	58.2	1.3	23.5	16.7	3.2
	$2s$	52.7	1.3		16.7	3.2
	$1f_{7/2}$	52.7	1.3	13.8	11.3	3
^{197}Au	$1s$	71.9/93.2	1.31		46/65	18/21
	$1p$	71.3/80.7	1.31		41/50	17/19
	$1d$	67.8/76.3	1.31		32/40	13/18
	$2s$	66.5	1.31		28	11
	$1f$	65.1	1.31		22.9	9.4
	$2p$	63.2	1.31		17.2	7.9
	$1g$	63.7	1.272		12.5	6.0
	$2d_{5/2}$	62.0	1.317	6	8.3	3.7
	$1h_{11/2}$	67.0	1.288	6	7.7	4.0
	$2d_{3/2}$	57.2	1.361	6	6.2	3

and uncertainties in the distortion corrections, the shell structure is somewhat ambiguous for the deepest orbitals. For these orbitals, Hartree-Fock calculations on ^{58}Ni [62] provide a more accurate indication of the actual shell energies. The Lorentzian widths are calculated according to the Brown and Rho [63] parameterization of Γ_i data for $A < 58$ [63]:

$$\Gamma_i = \frac{(24\,\mathrm{MeV})(E_i - E_F)^2}{(500\,\mathrm{MeV}^2) + (E_i - E_F)^2}. \tag{E7}$$

For Fe, $E_F = 8\,\mathrm{MeV}$ is used.

The $\varphi_i(\mathbf{p})$ parameters for ^{197}Au are modified versions of those measured for the nearby nucleus ^{208}Pb in $A(e,e'p)$ by Quint at NIKHEF [13]. There was some model-dependence in r_0 due to uncertainties in the calculation of the distortions in the DWIA, but an improved understanding of the distortions indicates that one should use the $\zeta = 0.5$ column of Quint's Table 4.5 [64]. Multiplication of the measured r_0 by 1.11 is necessary to produce agreement with the p_m distributions measured in the current experiment. The ^{208}Pb experiment did not measure r_0 for the deeper shells; they are assigned the typical value of 1.31 fm based on the valence shells. The V_0 values are chosen to reproduce the separation energies E_i. The values of the other parameters are from the discussion on page 15 of reference [13] or from private communication [64].

Most of the ^{197}Au separation energy centroids E_i and widths Γ_i are taken from Quint's Table 4.9 (or, for the $2s$ shell, from Figure 4.6), adjusted for the 2.2 MeV difference in the E_{rem} of ^{208}Pb (8.018 MeV) and ^{197}Au (5.77 MeV). The energy distributions of the deepest-lying energy levels ($1s$, $1p$, $1d$) were not measured. For these we use two models, one based on Hartree-Fock calculations on ^{208}Pb [62,13] and the other based on extrapolating the $1s$, $1p$, and $1d$ levels measured in $(p,2p)$ and $(e,e'p)$ [65] to $Z = 79$. The extrapolation from $Z \leq 30$ to $Z = 79$ is probably accurate to no better than $\pm 10\,\mathrm{MeV}$ for $1p$ and $1d$ and $\pm 20\,\mathrm{MeV}$ for 1s. The Γ_i measured by

Quint agree well with values calculated using Equation E7, so the equation is used to calculate the unmeasured ($1s$, $1p$, $1d$, $2s$) widths.

The Fe and Au spectral function models are subject to two ambiguities mentioned above: the need for the reduction in the width of the momentum distribution and the disagreement between Hartree-Fock calculations and $A(e,e'p)$ [and $A(p,2p)$] measurements on the E_s position of the deepest orbitals. Both are probably related to uncertainties in the correction of the measured distributions for the effects of proton FSI and Coulomb distortions. All indications are that the present experiment is not as sensitive to these effects. In fact distortions are not necessary to produce agreement between the PWIA calculation and the data. Furthermore, the Fe total momentum distribution cannot be considered to be well-constrained by the previous low-statistics measurement of only the outermost valence orbital (see Figure 79).

The ambiguity in the E_s of the deepest orbitals is resolved by investigating the Fe and Au E_m distributions measured at $Q^2 = 1\,(\mathrm{GeV/c})^2$ and $|p_m| < 100\,\mathrm{MeV/c}$, which are dominated by the $1s$ and $2s$ orbitals. The positions of the peaks agree with the PWIA calculation when the Hartree-Fock E_s distribution is used, but not when the values based on low Q^2 measurements are used. Thus, the Hartree-Fock E_s values are more correct, while the low Q^2 values provide an alternative spectral function model used to characterize the model-dependence of the PWIA calculation.

To summarize, the deep-shell E_s values and total momentum distributions measured in the current experiment are apparently inconsistent with those measured at low Q^2 in $A(e,e'p)$ and $A(p,2p)$. The discrepancy is probably due to errors in the distortion corrections at low Q^2.

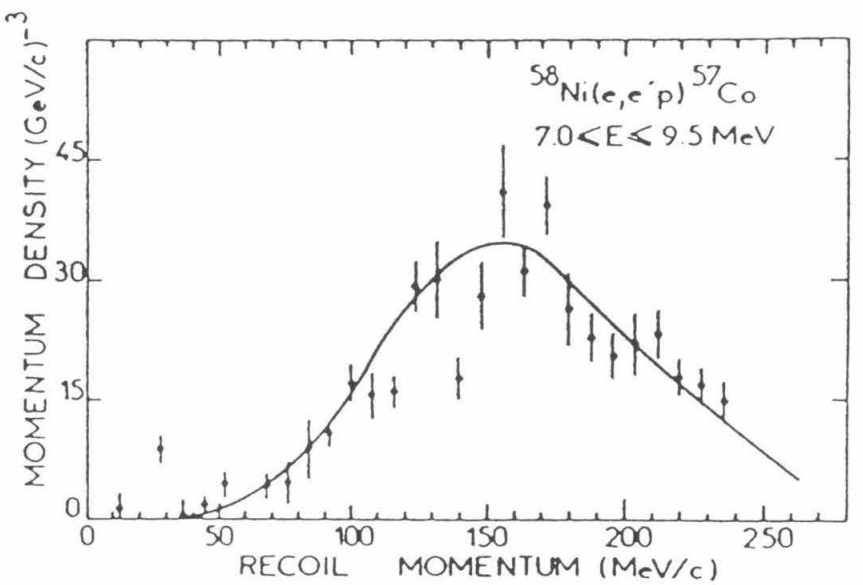

FIG. 79. p_m **distribution from** $^{58}\mathrm{Ni}(e,e'p)$ **at Saclay [11] for** $7 \leq E_m \leq 9.5\,\mathrm{MeV}$**. The solid line represents the DWIA calculation.**

APPENDIX F: RADIATION IN THE PWIA CALCULATION

In Section IV.E the equivalent radiator approximation is adjusted to reproduce the theoretical counting rates for H$(e, e'p)$. Sections F.1 and F.2 in this Appendix focus on the calculation of the counting rates in the equivalent radiator approximation. Most readers of these sections will probably only be interested in the results. Appendix F.1 details the calculation for radiation from two arms, specifically in the case of external radiation. Appendix F.2 uses this result to perform the calculation for three-arm radiation in the case of internal radiation.

Appendix F.3 discusses radiation in the one-photon limit, and helps explain why the modified equivalent radiator approximation is so successful. Appendix F.4 describes how the parameters of the equivalent radiator approximation are chosen. Appendix F.5 demonstrates the good agreement of the calculation and the data on the effects of radiation on the reaction kinematics.

F.1. Effect of External Radiation on Count Rate

In the PWIA calculation, the electron emits radiation ω and ω' before and after the collision, distributed according to Equation 4.7. The final electron energy is $E' = E'_{el} - \omega/R_k - \omega'$ where E'_{el} is the energy for elastic scattering ($\omega = \omega' = 0$). Because of the proton recoil, $R_k > 1$ and radiation by the incoming electron produces smaller changes in E' than radiation by the outgoing electron. For small ω, $R_k \approx (dE/dE')_{\omega=0} = (E/E')^2$.

The cross section for an electron to elastically scatter from E to $E' = E'_{el} - \Delta E'$ when there are t_i and t_f radiation lengths of material before and after scattering is:

$$\frac{d^2\sigma(E,E')}{d\Omega dE'} = \int_0^{R_k \Delta E'} d\omega \int_0^{\Delta E'} d\omega' I_b(\omega, t_i) I_b(\omega', t_f) \frac{d\sigma(E-\omega)}{d\Omega} \delta(\omega' + \omega/R_k - \Delta E'). \tag{F1}$$

Here $d\sigma(E)/d\Omega$ is the Born cross section for an electron of energy E scattering into the solid angle Ω, given by Equation 1.2. Since $I_b(\omega, t)$ is strongly peaked at $\omega = 0$, the double integral can be approximated as the sum of two double integrals, one near $\omega = 0$ and the other near $\omega' = 0$ (the energy peaking approximation):

$$\frac{d^2\sigma(E,E')}{d\Omega dE'} = \int_0^{R_k\Delta E'} d\omega I_b(\omega, t_i) I_b(\Delta E' - \omega, t_f) \frac{d\sigma(E-\omega)}{d\Omega} \tag{F2}$$

$$\approx I_b(\Delta E', t_f) \frac{d\sigma(E)}{d\Omega} \int_0^{R_k\Delta E'} d\omega I_b(\omega, t_i)$$

$$+ R_k I_b(R_k\Delta E', t_i) \frac{d\sigma(E - R_k\Delta E')}{d\Omega} \int_0^{\Delta E'} d\omega' I_b(\omega', t_f). \tag{F3}$$

We have used the fact that $I_b(\omega, t_i)$ and $I_b(\omega', t_f)$ dominate the ω and ω' dependence of the respective integrands by treating the other, slowly-varying, terms as being constant. The first term in Equation F3 is simply the probability that the outgoing electron radiates $\Delta E'$ and the incoming electron radiates less than $R_k\Delta E'$. The second term is similar, with the incoming electron dominating the radiation instead. In sum, the measured E' tail is the sum of two tails corresponding to photons emitted in two different directions.

The remaining integrals of I_b are dominated by the contribution near ω and $\omega' = 0$, so we can approximate $\phi(\omega/E) \approx 1$ to find:

$$\frac{d^2\sigma(E,E')}{d\Omega dE'} = \frac{1}{\Gamma(1+bt_i+bt_f)} \left(\frac{R_k\Delta E'}{E}\right)^{bt_i} \left(\frac{\Delta E'}{E'_{el}}\right)^{bt_f}$$

$$\times \left[\frac{bt_f}{\Delta E'}\phi\left(\frac{\Delta E'}{E'_{el}}\right)\frac{d\sigma}{d\Omega}(E) + \frac{bt_i}{\Delta E'}\phi\left(\frac{R_k\Delta E'}{E}\right)\frac{d\sigma}{d\Omega}(E - R_k\Delta E')\right], \tag{F4}$$

where we have combined the gamma functions $\Gamma(1 + bt_i)\Gamma(1 + bt_f)$ from $I_b(\omega, t_i)$ and $I_b(\omega', t_f)$ into $\Gamma(1 + bt_i + bt_f)$. This $\approx 0.2\%$ change is required so that in a trivial scattering process ($d\sigma/d\Omega = 1$, $R_k = 1$, $\Delta E' = \omega$) Equation F4 reduces to Equation 4.7 with $t = t_i + t_f$.

F.2. Effect of Internal Radiation on Count Rate

In the PWIA calculation, radiation by the proton affects E', even though the radiation occurs "after" the scattering. Radiation of massless photons changes the proton's energy and momentum equally. So in order to leave the proton on-shell after the radiation, it must be left off-shell by the scattering. The amount of proton radiation is decided *before* the scattering, and E' is chosen to leave the proton the correct amount off-shell. The quantity $\omega_p = R_p \Delta E'$ specifies the amount of energy the proton arm must radiate to make $E' = E'_{el} - \Delta E'$ (in the absence of other radiation). For small $\Delta E'$, $R_p = (M_p + 2E\sin^2(\theta/2))/(E'_p - p')$.

The equivalent radiator three-tail cross section is found in a generalization of the energy peaking approximation used to find Equation F4. Here the integral is split into three pieces, one for each arm dominating the total $\Delta E'$. The probability I_b for the other two arms to emit $\omega \approx 0$ is simply Equation F4 with $d\sigma/d\Omega = 1$ and the appropriate values of R_k, R_p and 1. The resulting cross section is:

$$\begin{aligned}\frac{d^2\sigma(E,E')}{d\Omega dE'} = \frac{1}{\Gamma(1+\lambda_k+\lambda_{k'}+\lambda_{p'})}&\left(\frac{R_k\Delta E'}{E}\right)^{\lambda_k}\left(\frac{\Delta E'}{E'_{el}}\right)^{\lambda_{k'}}\left(\frac{R_p\Delta E'}{E'_p}\right)^{\lambda_{p'}}\\ &\times\left[\frac{\lambda_k}{\Delta E'}\phi\left(\frac{\Delta E'}{E'_{el}}\right)\frac{d\sigma}{d\Omega}(E)+\frac{\lambda_{p'}}{\Delta E'}\phi\left(\frac{R_p\Delta E'}{E'_p}\right)\frac{d\sigma}{d\Omega}(E)\right.\\ &\left.+\frac{\lambda_{k'}}{\Delta E'}\phi\left(\frac{R_k\Delta E'}{E}\right)\frac{d\sigma}{d\Omega}(E-R_k\Delta E')\right]. \qquad \text{(F5)}\end{aligned}$$

The integral of the above over small $\Delta E'$ is easily found by setting $\phi(\omega/E) = 1$ and $d\sigma/d\Omega$ constant:

$$\left(\frac{d\sigma}{d\Omega}\right)^{PWIA}_{\Delta E'} = \frac{1}{\Gamma(1+\lambda_k+\lambda_{k'}+\lambda_{p'})}\left(\frac{R_k\Delta E'}{E}\right)^{\lambda_k}\left(\frac{\Delta E'}{E'_{el}}\right)^{\lambda_{k'}}\left(\frac{R_p\Delta E'}{E'_p}\right)^{\lambda_{p'}}\frac{d\sigma}{d\Omega}(E). \qquad \text{(F6)}$$

F.3. Internal Radiation in the One-Photon Limit

This section discusses internal radiation in the single-photon approximation in order to help explain the success of the modified equivalent radiator approximation described in Section IV.E.

We begin with the angular distribution $\Upsilon(\theta_\omega, \phi_\omega)$ of H$(e, e'p)$ radiation in the one photon exchange approximation and the soft photon (low ω) limit:

$$\omega^2 \frac{d^5\sigma}{d\Omega d^3\omega} = \frac{d^5\sigma}{d\Omega d\omega d\Omega_\omega} = \frac{\Upsilon(\theta_\omega, \phi_\omega)}{\omega} \left(\frac{d\sigma}{d\Omega}\right)_{Born}. \tag{F7}$$

The angular distribution $\Upsilon(\theta_\omega, \phi_\omega)$, which is calculated from the diagrams in Figure 43, is not a function of the magnitude ω [40]. The result is shown in Figures 80 and 81 for two of the NE-18 kinematics.

As in the case of external radiation, most of the radiation is emitted nearly parallel to k or k′. (In fact $\Upsilon(\theta_\omega, \phi_\omega)$ diverges in the k and k′ directions, although the integral over $d\Omega_\omega$ is finite.) Futhermore, the energy dependence of the radiation in a given direction is $1/\omega$, the same as for external radiation in the one-photon limit (Equation 4.10). Thus it is natural to simulate the angular distribution and energy dependence of the internal radiation by the equivalent radiator method.

The count rate in an H$(e, e')p$ experiment for $E'_{el} - \Delta E' < E' < E'_{el}$ can be calculated by the integral of the inelastic diagrams (Equation F7), plus the elastic diagrams (Figures 3 and 42). The $\ln\omega$ infrared divergence of the $1/\omega$ bremsstrahlung integral is cancelled by the soft-photon divergence in the virtual photon graphs, yielding [40]:

$$\left(\frac{d\sigma}{d\Omega}\right)_{\Delta E'}^{1-\gamma} = (1 + \delta_{E'}) \left(\frac{d\sigma}{d\Omega}\right)_{Born}. \tag{F8}$$

The correction factor $\delta_{E'}$ is a function of the scattering kinematics and the E' acceptance. It contains a cut-independent piece, due to elastic diagrams with hard virtual photons (Figure 42), and a cut-dependent piece describing the counts lost outside the

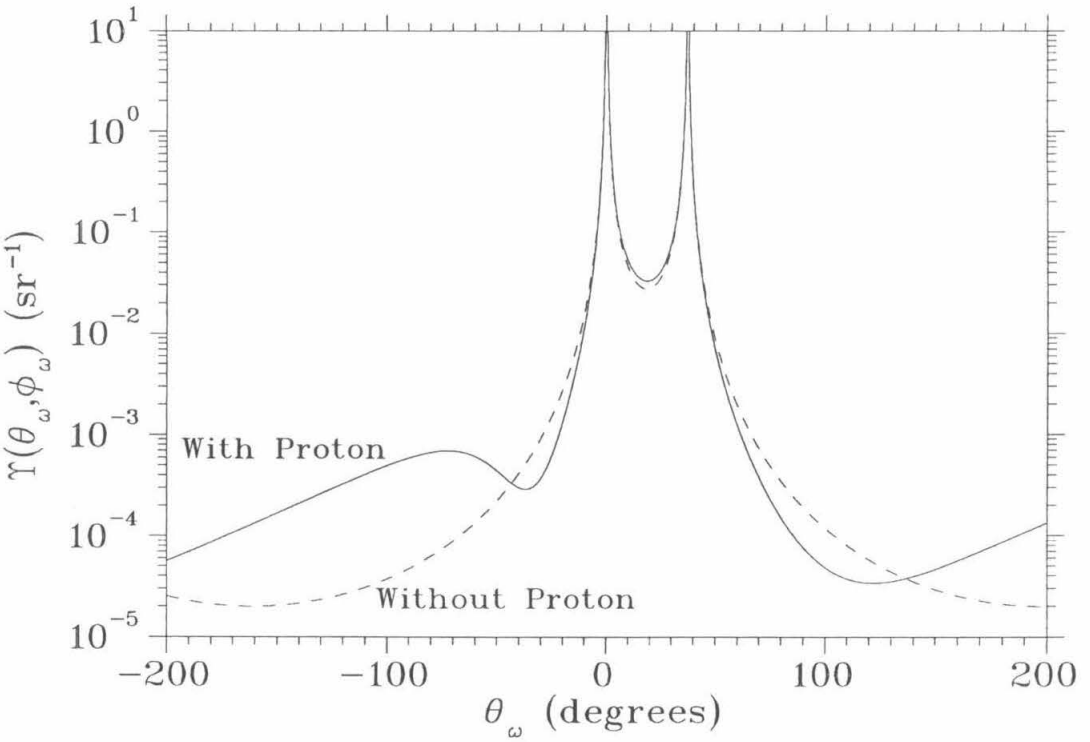

FIG. 80. **Single-photon angular distribution $\Upsilon(\theta_\omega, \phi_\omega)$ of H$(e, e'p)$ internal bremsstrahlung at $Q^2 = 1\,(\mathrm{GeV/c})^2$. The curves assume the emission of a single soft photon, and are valid in the soft photon (low ω) approximation. The dashed line shows the angular distribution when diagrams involving radiation by the proton are omitted.**

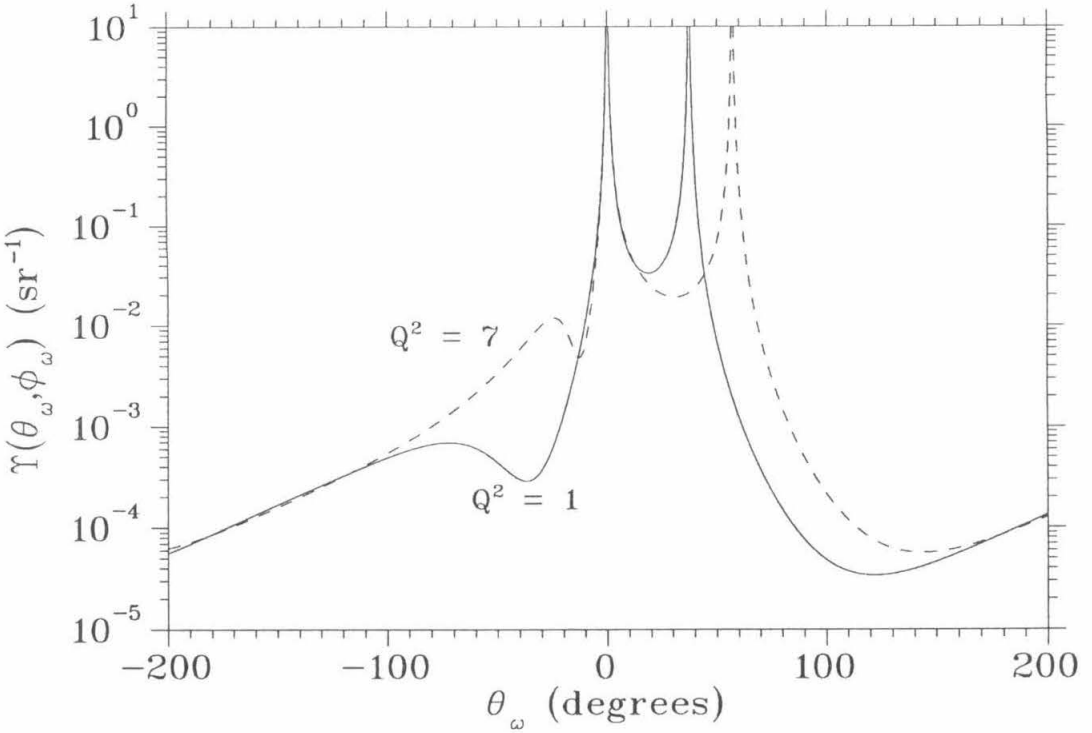

FIG. 81. **Single-photon $\Upsilon(\theta_\omega, \phi_\omega)$ at $Q^2 = 1, 7$ (GeV/c)^2**

acceptance due to internal bremsstrahlung (Figure 43). For the $\delta_{E'}$ given in Mo and Tsai, Equation F8 is only valid for $\Delta E' \ll E'/(1 + 2E/M_p)$ [48].

Above we noted that the single-photon expressions for internal and external radiation, Equations 4.10 and F7 had the same $1/\omega$ dependence. Agreement is maintained in the infinite-photon limit because the *coherent* multiple-photon exponentiation in Equation F6 serves the same role as the *incoherent* multiple-collision factor ω^{bt} in Equation 4.7. To see this, recall Equation 4.16, $e^\delta = N\omega^\lambda$ (we use $\omega = \Delta E_m$ and drop the E_m subscripts for compactness). The tail height (divided by the Born cross section) is $de^\delta/d\omega = N\lambda\omega^{\lambda-1}$. For $\lambda = bt$, this has the same ω dependence as Equation 4.7, the multi-collision form for external radiation. (For simplicity we compare with the one-tail version instead of the three-tail version, Equation F5. The number

of tails does not effect the ω dependence because $\Upsilon(\theta_\omega, \phi_\omega)$ is not a function of ω.)

Now consider the single-photon version of the above: $\delta = \lambda \ln \omega + \ln N$, with tail height $d\delta/d\omega = \lambda/\omega$. This is just the single-collision form for external radiation, Equation 4.10. Thus the conversion from the single-photon to the coherent multiple-photon form is mathematically identical to the conversion to the incoherent multiple-collision form.

From this we conclude that, to the accuracy of the exponential approximation, the PWIA calculation correctly includes multiple-photon internal radiation. This in spite of the fact that the calculation uses the multiple-collision form for external radiation. Furthermore, we conclude that if exponentiation approximates the higher-order diagrams of *external* radiation as well, then the Equation 4.7 is approximately correct to all orders of α.

F.4. Description of the Modified Equivalent Radiator Approximation

This section describes the selection method for the parameters of the equivalent radiator approximation, discussed in Section IV.E, used to simulate internal bremsstrahlung in the PWIA calculation. In order to reproduce the theoretical E' and E_m cut dependences, the equivalent radiator approximation must reproduce the theoretical values of $N_{E'}$, N_{E_m} and $\lambda_{E'}$ (see Equations 4.18 and 4.19).

Conveniently the equivalent radiator cut dependence, given by Equation F6, has the same $\Delta E'$ dependence as the theory [$\sim (\Delta E')^{\lambda_{E'}}$], so long as the calculation's λ^{PWIA} are chosen so that:

$$\lambda_k^{PWIA} + \lambda_{k'}^{PWIA} + \lambda_{p'}^{PWIA} = \lambda_{E'}. \tag{F9}$$

Multiplication of the cross section by the proper normalization factor, allows the calculation to satisfy Equation 4.18 at small $\Delta E'$. The normalization factor represents the contribution of the hard virtual photon diagrams in Figure 42.

The E_m cut dependence is given by Equation F6 with $R_e = R_p = 1$ (because of Equation 4.5). Thus, the calculation simultaneously satisfies Equations 4.18 and 4.19 at all (small) values of $\Delta E'$ and ΔE_m by using:

$$R_e^{\lambda_k} R_p^{\lambda_{p'}} = \frac{N_{E'}}{N_{E_m}} = e^{\delta_{E'} - \delta_{E_m}}. \tag{F10}$$

Reproducing the theoretical $N_{E'}$, N_{E_m} and $\lambda_{E'}$ places three conditions on the four unknowns (λ_k, $\lambda_{k'}$, $\lambda_{p'}$, and the normalization). The theoretical integral of the cross section over another observable (for instance E'_p) could provide a fourth condition ($N_{E'_p}$) and remove the remaining ambiguity. However, the PWIA calculation is insensitive at the $< 0.5\%$ level to the ratio of λ_k to $\lambda_{p'}$. For definiteness, we choose the value $\lambda_k^W / \lambda_{p'}^W$ given by the Wasson *et al.* [41] 3-tail peaking approximation:

$$\lambda_k^{PWIA} = f_t \lambda_k^W \tag{F11}$$

$$\lambda_{p'}^{PWIA} = f_t \lambda_{p'}^W \tag{F12}$$

where the fraction f_t varies between 0.88 and 0.89:

$$f_t = \frac{\delta_{E'} - \delta_{E_m}}{\ln(R_e^{\lambda_k^W} R_p^{\lambda_{p'}^W})}. \tag{F13}$$

The λ^{PWIA} values resulting from these prescriptions are listed in Table 26. The equivalent radiator parameters are evaluated for central kinematics, and are not adjusted for the kinematics of each event. The errors produced by neglecting variations in E and $\theta_{k'}$ are negligible ($< 0.04\%$ in the normalization and < 0.0012 in the λ values).

Wasson *et al.* [41] obtained the 3-tail peaking approximation λ^W used in Equation F13 by integrating the radiation's angular distribution over the peaks in the $\mathbf{k}$, $\mathbf{k}'$, and $\mathbf{p}'$ directions:

$$\lambda_k^W = \frac{\alpha}{\pi} \left[\ln \left(\frac{4k^2}{m_e^2} \right) - 1 \right] \tag{F14}$$

TABLE 26. Comparison of the equivalent radiator thicknesses λ for the ^{1}H kinematics. Values λ^{EQ} are from Equation 4.17, λ^W are from Equations F14–F15, and λ^{PWIA} are from Equations F9–F13.

Q^2	λ^{EQ}	λ^W_k	$\lambda^W_{k'}$	$\lambda^W_{p'}$	λ^{PWIA}_k	$\lambda^{PWIA}_{k'}$	$\lambda^{PWIA}_{p'}$
(GeV/c^2)	(%)	(%)	(%)	(%)	(%)	(%)	(%)
1.1538	3.322	3.936	3.767	0.042	3.502	3.614	0.037
3.2233	3.561	4.149	3.790	0.326	3.652	4.282	0.287
5.1459	3.669	4.279	3.790	0.485	3.786	4.619	0.429
6.8496	3.736	4.369	3.790	0.590	3.883	4.836	0.524

$$\lambda^W_{k'} = \frac{\alpha}{\pi}\left[\ln\left(\frac{4k'^2}{m_e^2}\right) - 1\right] \tag{F15}$$

$$\lambda^W_{p'} = \frac{\alpha}{\pi}\left[\ln\left(\frac{E'_p + p'}{E'_p - p'}\right) - 2\right]. \tag{F16}$$

This description, while an improvement over the standard method, does not satisfy Equations 4.18 and 4.19.

Due to approximations in the calculation of δ, Equations 4.14 and 4.16 are not valid for for $\Delta E' \gtrsim E'/(1 + 2E/M_p)$ [48]. The approximations neglect two effects, which are present in the modified equivalent radiator technique: $d\sigma(E - R_e\Delta E')/d\Omega > d\sigma(E)/d\Omega$, and $\phi(\omega/E) < 1$. Thus, the PWIA calculation maintains good agreement ($< 0.5\%$) with exact calculations of the radiation for large $\Delta E'$. (The comparison can be done in the one-photon limit.)

F.5. Internal Radiation and Kinematics

As discussed at the beginning of Section IV.D, events can also be cut by the finite momentum byte and solid angle of the 8 GeV/c spectrometer. Thus the PWIA calculation should correctly include the effect of the radiation on the kinematics of the

outgoing particles. The equivalent radiator procedure used in the calculation implicitly makes two assumptions about the effect of internal bremsstrahlung on kinematics: 1) photons can be treated as being emitted exactly parallel to the outgoing particles (the angle peaking approximation), and 2) photons emitted along one of the outgoing particles were effectively emitted by that particle.

We touched on the angle peaking approximation shortly after Equation F7, but wish to evaluate it more carefully here. In the single-photon limit, most of the radiation occurs within $\Delta\theta = (m_e/E)^{1/2}$ of the $\mathbf{k}$ direction and $(m_e/E')^{1/2}$ of the $\mathbf{k}'$ direction [40]. For E, $E' \geq 1.4\,\mathrm{GeV}$ and $\omega < 20\,\mathrm{MeV/c}$, $\Delta\theta < 19\,\mathrm{mr}$. The deflection of the electron is less than 0.3 mr, small enough to ignore. But for the few events with $\omega \simeq \omega_{max} = 200\,\mathrm{Mev/c}$, the deflection is 3 mr. Even though the average deflection is zero, this could conceivably have a small effect on the count rate. In Figure 82 one finds, however, that the calculation does a good job of reproducing the observed widths of the peaks in ϑ_ω for these $\omega > 20\,\mathrm{MeV/c}$ events. This is because, in *multi-photon* bremsstrahlung, the simultaneous emission of photons from all three arms produces most of the peak width. (Resolution broadening is not very important in Figure 82. This was checked by comparing with the same graph for $\omega > 40, 60\,\mathrm{MeV/c}$.) The events at $\vartheta \approx 15\,\mathrm{mr}$ are the result of radiation by the electron before and after the scattering. The incoherent addition of the radiation before and after the scattering in the equivalent radiator approximation underpredicts the strength given by the coherent interference of the corresponding radiative diagrams. The missing strength is less than 10% of the counts at $20\,\mathrm{MeV/c} < \omega < 200\,\mathrm{MeV/c}$—that is, less than 1% of the total counts. Since in only a fraction of these events would the exact photon angle make the difference between the outgoing particles being inside or outside of the experimental acceptance, the error is insignificant.

The validity of assumption (2), that photons emitted along one of the outgoing particles were emitted by that particle, is demonstrated in Figure 83. Here we see

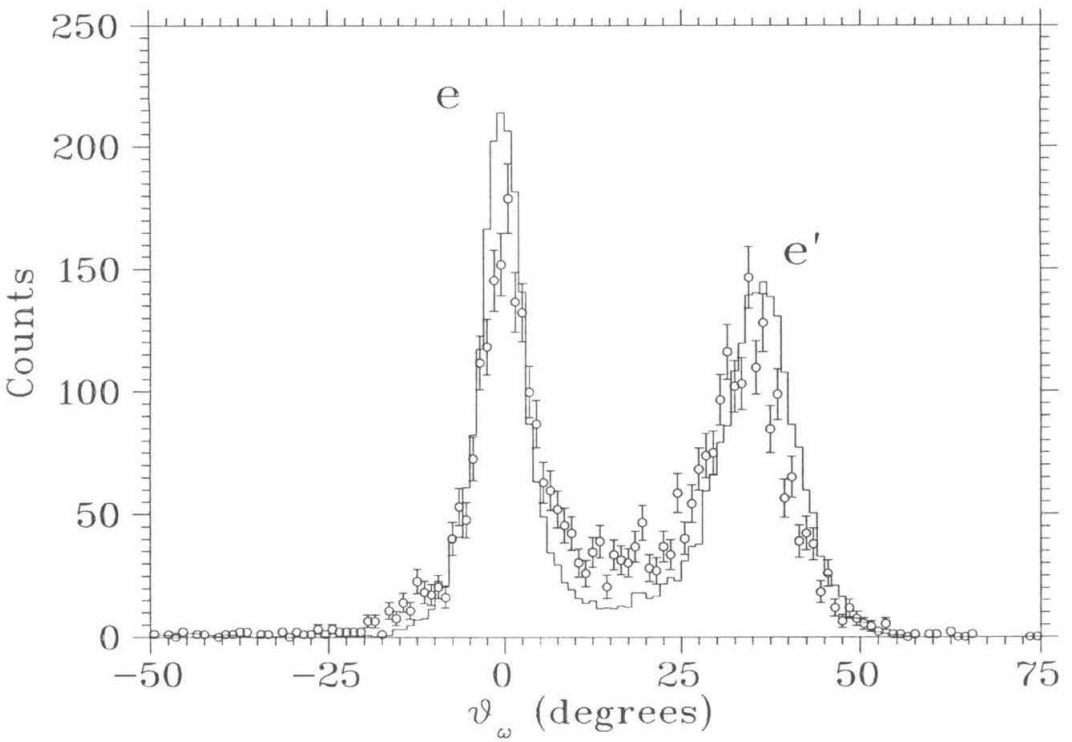

FIG. 82. **Comparison between the H$(e, e'p)$ data and PWIA prediction distributions for the angle $\vartheta_\omega = \tan^{-1}(P_{m,x}/P_{m,z})$ at $Q^2 = 1\,(\mathrm{GeV/c})^2$. Note that ϑ_ω is the projected angle of the radiation in the horizontal plane rather than the spherical coordinate θ_ω. To reduce the effects of the finite resolution, only events with $E_m > 20\,\mathrm{MeV}$ are displayed. The peaks from radiation directed along k and k′ are clearly visible at $\vartheta_\omega = \theta_k = 0$ and $\vartheta_\omega = \theta_{k'} = 37.296°$.**

that radiation in the $\mathbf{k}'$ direction has $R \approx R_{k'} = 1$, and radiation in the $\mathbf{k}$ direction has $R \approx R_e$. That is, radiation *along* $\mathbf{k}'$ has the same effect on the kinematics as radiation *by* the outgoing electron (and analogously for the incoming electron). In the figure, the cross over from the $\vartheta_\omega < 15°$ to $\vartheta_\omega > 15°$ occurs at $R \approx 1.4$ for both data and calculation. The calculation's underestimate of events at $\vartheta \approx 15\,\mathrm{mr}$, discussed above, maps here to an underestimate at $R \approx 1.4$.

In conclusion, the equivalent radiator procedure used in the PWIA calculation simulates the effect of internal radiation on the measured counting rates to good accuracy, as required for the extraction of the nuclear transparency.

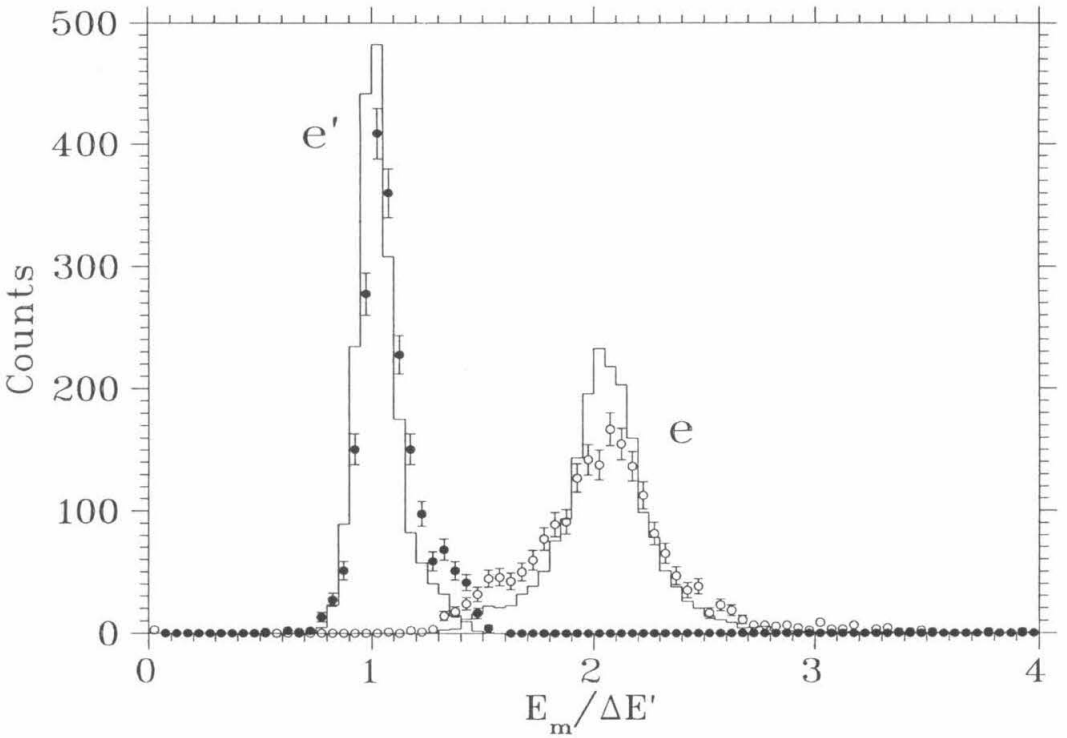

FIG. 83. **Comparison between the H$(e, e'p)$ data and the PWIA calculation for the recoil ratio $R = E_m/\Delta E'$ at $Q^2 = 1\,(\mathrm{GeV/c})^2$. To reduce the effects of the finite resolution, only events with $E_m > 20\,\mathrm{MeV}$ are displayed. The solid circles and left-hand histogram are the data points and PWIA prediction for $\vartheta_\omega > 15°$, corresponding to the peak at θ'_k in Figure 82. Note these events have the ratio $R \approx R_{k'} = 1$. The open circles and right-hand histogram are for the peak at $\theta_k = 0$ $(\vartheta_\omega < 15°)$, and have $R \approx R_k = 2.07$.**

REFERENCES

[1] A. H. Mueller, in *Proceedings of the XVII Rencontre de Moriond, 1982*, edited by J. Tran Thanh Van (Editions Frontieres, Gif-sur-Yvette, France, 1982), p. 13; S. J. Brodsky, in *Proceedings of the Thirteenth International Symposium on Multiparticle Dynamics*, edited by W. Kittel, W. Metzger, and A. Stergiou (World Scientific, Singapore, 1982), p. 963.

[2] G. R. Farrar *et al.*, Phys. Rev. Lett. **61**, 686 (1988).

[3] B. K. Jennings and G. A. Miller, Phys. Rev. **D44**, 692 (1991).

[4] B. K. Jennings and G. A. Miller, Phys. Rev. Lett. **69**, 3619 (1992).

[5] O. Benhar *et al.*, Phys. Rev. Lett. **69**, 881 (1992).

[6] L. L. Frankfurt, M. I. Strikman, and M. B. Zhalov, "Pitfalls in Looking for Color Transparency at Intermediate Energies" (unpublished).

[7] G. B. West, Phys. Rep. **18C**, 264 (1975).

[8] D. Day *et al.*, Phys. Rev. Lett. **43**, 1143 (1979).

[9] S. Frullani and J. Mougey, Advances in Nucl. Phys. **14**, Plenum Press, New York (1984).

[10] T. De Forest, Nucl. Phys. **A392**, 232 (1983).

[11] J. Mougey, Nucl. Phys. **A262**, 461 (1976).

[12] L. B. Weinstein, Ph. D. Thesis, Mass. Inst. of Tech. (1988).

[13] E. N. M. Quint, Ph. D. Thesis, U. Amsterdam (1988).

[14] R. W. Lourie *et al.*, Phys. Rev. **C47**, R444 (1993).

[15] L. R. B. Elton and A. Swift, Nucl. Phys. **A94**, 52 (1967).

[16] V. R. Pandharipande and S. C. Pieper, Phys. Rev. **C45**, 791 (1992).

[17] V. R. Pandharipande, private communication.

[18] D. B. Day *et al.*, Phys. Rev. Lett. **59**, 427 (1987).

[19] S. J. Brodsky and G. R. Farrar, Phys. Rev. Lett. **31**, 1153 (1973); S. J. Brodsky and G. R. Farrar, Phys. Rev. **D11**, 1309 (1975).

[20] J. E. Belz, Ph. D. Thesis, Caltech (1994).

[21] A. B. Bakulev and A. V. Radushkin, Phys. Lett. **B271**, 223 (1991).

[22] S. Rock *et al.*, Phys. Rev. Lett. **49**, 1139 (1982).

[23] R. G. Arnold *et al.*, Phys. Rev. Lett. **57**, 174 (1986).

[24] B. Povh and J. Hüfner, Phys. Rev. Lett. **58**, 1612 (1987).

[25] D. Geesaman, private communication.

[26] B. Z. Kopeliovich *et al.*, "Decisive Test of Color Transparency in Exclusive Electroproduction of Vector Mesons" (unpublished).

[27] L. Frankfurt, G. A. Miller, and M. Strikman, Comments Nucl. Part. Phys. **21**, 1 (1992).

[28] A. S. Carroll *et al.*, Phys. Rev. Lett. **61**, 1698 (1988).

[29] J. P. Ralston and B. Pire, Phys. Rev. Lett. **61**, 1823 (1988).

[30] D. Sivers *et al.*, Phys. Rep. **23C**, 1 (1976).

[31] NPAS Users Guide, SLAC Report No. 269, 1984 (unpublished).

[32] A. Lung, Ph. D. Thesis, American University (1992).

[33] R. Anderson *et al.*, Nucl. Instr. Meth. **66**, 328 (1968).

[34] P. N. Kirk *et al.*, Phys. Rev. **D8**, 63 (1973).

[35] K.L. Brown *et al.*, SLAC Report No. 91, Rev. 2, 1977 (unpublished).

[36] A. T. Katramatou, Ph. D. Thesis, American University (1988).

[37] R. M. Sternheimer *et al.*, Brookhaven National Laboratory Report No. BNL-31435 (1982). L. D. Landau, J. Phys. U.S.S.R. bf 8, 201 (1944).

[38] Review of Particle Properties, Phys. Rev. **D45**, Part 2 (1992).

[39] H. Überall, *Electron Scattering from Complex Nuclei*, vols. A and B (Academic Press, New York, 1971), p. 210.

[40] L. W. Mo and Y. S. Tsai, Rev. Mod. Phys. **41**, 205 (1969).

[41] D. A. Wasson, to be published (1993).

[42] R. Machleidt *et al.*, Phys. Rep. **149**, 1 (1987).

[43] M. F. Gari and W. Krümplemann, Z. Phys. **A322**, 689 (1985).

[44] P. E. Bosted *et al.*, Phys. Rev. Lett. **68**, 3841 (1992); A. Lung *et al.*, Phys. Rev. Lett. **70**, 718 (1993).

[45] R. A. Early, Nucl. Instr. Methods **109**, 93 (1973).

[46] Y. S. Tsai, Rev. Mod. Phys. **46**, 815 (1974).

[47] R. C. D. Walker, Ph. D. Thesis, Caltech (1989).

[48] Y. S. Tsai, Phys. Rev. **122**, 1898 (1961).

[49] D. Potterveld, Ph. D. Thesis, California Institute of Technology (1989).

[50] T. G. O'Neill, B. W. Filippone, and R. Seki (to be published).

[51] F. G. Perry and B. Buck, Nucl. Phys. **32**, 353 (1962); F. G. Perey, in *Direct*

Interactions and Nuclear Reaction Mechanisms, edited by E. Clementel and C. Villi (Gordon and Breach, New York, 1963), p. 125; H. Fiedeldey, Nucl. Phys. **77**, 149 (1966).

[52] I. Sick, private communication.

[53] J. W. Van Orden, W. Truex, and M. K. Banerjee, Phys. Rev. **C21**, 2628 (1980).

[54] X. Ji and J. Engel, Phys. Rev. **C40**, R497 (1989); X. Ji, private communication.

[55] B. E. Vonderfecht *et al.*, Phys. Rev. **C44**, R1265 (1991).

[56] N. C. R. Makins *et al.*, to be published (1994).

[57] N. C. R. Makins, Ph. D. Thesis, Mass. Inst. of Tech., to be published.

[58] A. Kohama, K. Yazaki, and R. Seki, Nucl. Phys. **A551**, 687 (1993).

[59] N. N. Nikolaev *et al.*, Phys. Lett. B **317**, 281 (1993).

[60] R. J. Glauber, in *Lectures in Theoretical Physics*, edited by W. E. Brittin *et al.* (Interscience, New York, 1959), p. 315.

[61] H. P. Blok and J. H. Heisenberg, in *Computational Nuclear Physics, vol. 1*, edited by K. Langanke, J. A. Marun, and S. E. Koonin (Springer-Verlag, Berlin/New York, 1989), p. 90.

[62] J. W. Negele, Phys. Rev. **C1**, 1260 (1970); J. W. Negele and D. Vautherin, Phys. Rev. **C5**, 1472 (1972).

[63] G. E. Brown and M. Rho, Nucl. Phys. **A372**, 397 (1981).

[64] L. Lapikás, private communication.

[65] G. Jacob and Th. A. J. Maris, Rev. Mod. Phys. **45**, 6 (1973).

[66] C. Mahaux and H. Ngô, Nucl. Phys. **A431**, 486 (1984).